UNIVERSITY OF CALIFORNIA SAN DIEGO

GPCRs as Next-Gen Targets for Immune Oncology

A dissertation submitted in partial satisfaction of the

requirements for the degree Doctor of Philosophy

in

Biomedical Sciences

by

Victoria H. Wu

Committee in charge:

Professor J. Silvio Gutkind, Chair
Professor Joan Heller Brown
Professor Ananda Goldrath
Professor Tracy Handel
Professor Pablo Tamayo

2021

The Dissertation of Victoria H. Wu is approved, and it is acceptable in quality and form for publication on microfilm and electronically.

University of California San Diego

2021

DEDICATION

This dissertation is dedicated to my family and friends, who have provided unwavering support throughout my graduate studies.

TABLE OF CONTENTS

LIST OF FIGURES

LIST OF TABLES

ACKNOWLEDGEMENTS

I am deeply grateful to my dissertation advisor, Dr. J. Silvio Gutkind, for his guidance, inspiration, and mentorship throughout my PhD program. I am also thankful to my committee members, Dr. Joan Heller Brown, Dr. Ananda Goldrath, Dr. Tracy Handel, and Dr. Pablo Tamayo.

Chapter 2, in full, has been accepted for publication of the material in “Illuminating the Onco-GPCRome: Novel G protein-coupled receptor-driven oncocrine networks and targets for cancer immunotherapy” in *Journal of Biological Chemistry*, 2019. Victoria H. Wu, Huwate Yeerna, Nijiro Nohata, Joshua Chiou, Olivier Harismendy, Francesco Raimondi, Asuka Inoue, Rob Russell, Pablo Tamayo, and J. Silvio Gutkind. The dissertation author was the primary investigator and author of this paper.

Chapter 3, in full, has been accepted for publication of the material in “Novel syngeneic animal model of tobacco-associated oral cancer reveals the activity of in situ anti-CTLA-4” in *Nature Communications*, 2019. Zhiyong Wang, Victoria H Wu, Michael M Allevato, Mara Gilardi, Yudou He, Juan Luis Callejas-Valera, Lynn Vitale-Cross, Daniel Martin, Panomwat Amornphimoltham, James Mcdermott, Bryan S Yung, Yusuke Goto, Alfredo A Molinolo, Andrew B Sharabi, Ezra EW Cohen, Qianming Chen, J Guy Lyons, Ludmil B Alexandrov, J. Silvio Gutkind. The dissertation author was the primary investigator and author of this paper.

Chapter 4, in full, is in preparation for submission for publication in “A chemogenetic approach reveals a GPCR-Gαs-PKA signaling axis promoting T cell dysfunction and cancer immunotherapy failure”. Victoria H. Wu, Bryan S. Yung, Farhoud Faraji, Robert Saddawi-Konefka, Zhiyong Wang, Miranda Song, Meghana S. Pagadala, Alexander T. Wenzel, Sanju Sinha, Marin Matic, Francesco Raimondi, Thomas S. Hoang, Rebecca Berdeux, Hannah Carter, Eytan Ruppin, Jill P. Mesirov, J. Silvio Gutkind. The dissertation author was the primary investigator and author of this paper.

VITA

University of California San Diego
Ph.D., Biomedical Sciences, 2021

San Jose State University
M.S. – Microbiology/Molecular Biology, 2014

University of California Davis
B.S. – Microbiology, 2012

FELLOWSHIPS

Ruth L. Kirschstein Predoctoral Individual NRSA F31 for NCI
NIH Grant number: 1F31CA250488-01
Funding period: (8/26/2020-8/25/2022)

UCSD Cancer Biology, Informatics & Omics (CBIO) T32 NRSA
NIH Grant number: 5T32CA067754-23
Funding period: (7/1/2019 – 7/1/2021)

PUBLICATIONS

2021

Wu, V.H., Yung, B.S., Saddawi-Konefka, R., Wenzel, A.T., Pagadala, M., Sinha, S., Wang, Z., Faraji, F., O'Farrell, A., Song, M., Mesirov, J.P., Carter, H., Ruppin, E., Gutkind, J.S. A novel GPCR-Gαs immune checkpoint axis promoting T cell exhaustion in cancer. (2021) *Submitted, Nature Immunology.*

Pagadala, M., **Wu, V.H.**, Perez-Guijarro, E., Kim, H., Castro, A., Talwar, J., Gonzalez-Colin, C., Cao, S., Schmiedel, B.J., Salem, R.M., Morris, G.P., Harismendy, O., Patel, S.P., Mesirov, J.P., Zanetti, M., Day, C.P., Fan, C.C., Thompson, W.K., Merlino, G., Gutkind, J.S., Vijayanand, P., Carter, H. Germline variants that influence the tumor immune microenvironment also drive response to immunotherapy. (2021) *Submitted, Cancer Discovery*.

Gilardi, M., **Wu, V.H.**, Saddawi-Konefka, R., Lopez-Ramirez, M.A., Wang, Z., Soto, F., Steffen, D.J., Proietto, M., Mikulski, Z., Miki, H., Sharabi, A., Kupor, D., Rueda, R., Wang, J., Gutkind, J.S. Microneedle-mediated intratumoral delivery of anti-CTLA-4 promotes cDC1-dependent eradication of oral squamous cell carcinoma with limited irAEs. (2021) *In revision, Molecular Cancer Therapeutics.*

Wang, Z., Goto, Y., Allevato, M.M., **Wu, V.H.**, Saddawi-Konefka, R., Gilardi, M., Alvarado, D., Yung, B.S., O'Farrell, A., Molinolo, A.A., Duvvuri, U., Grandis, J.R., Califano, J.A., Cohen, E.E.W., Gutkind, J.S. Disruption of the HER3-PI3K- mTOR oncogenic signaling axis and PD-1 blockade as a multimodal precision immunotherapy in head and neck cancer. Nature Communications (2021).

2019

Wang, Z., **Wu, V.**, Allevato, M., Gilardi, M., He, Y., Callejas-Valera, J., Vitale-Cross, L., Martin, D., Amornphimoltham, P., Mcdermott, J., Goto, Y., Molinolo, A., Sharabi, A., Cohen, E., Chen, Q., Lyons, G., Alexandrov, L., and Gutkind, J.S. (2019) Novel syngeneic animal model of tobacco-associated oral cancer reveals the activity of in situ anti-CTLA-4. Nature Communications, 10 (1): 5546. *Featured as Nature Communications' December Editor's Highlights*

Wu, V., Gutkind, J.S. (2019) Improving the Therapeutic Ratio in Head and Neck Cancer, Volume 6, 1st Edition (Chapter 10: Targeting GPCRs in HNC). Elsevier, October 2019.

Wu, V., Yeerna, H., Nohata, N., Chiou, J., Harismendy, O., Raimondi, F., Inoue, A., Russell, R. B., Tamayo, P., and Gutkind, J. S. (2019) Illuminating the Onco-GPCRome: Novel G protein-coupled receptor-driven oncocrine networks and targets for cancer immunotherapy. J Biol Chem, 294 (29): 11062-11086. *In the top 5% of all research outputs scored by Altmetric, one of the most read articles in JBC, July 2019*

Wu, X., Yeerna, H., Goto, Y., Ando, T., **Wu, V.**, Zhang, X., Wang, Z., Amornphimoltham, P., Murphy, A., Tamayo, P., Chen, Q., Lippman, S., and Gutkind, J.S. (2019) A Mitochondrial Complex I Rescue Approach Reveals that Metformin Acts Directly on Head and Neck Squamous Cell Carcinoma Initiating Cells. Cancer Res, 79 (17): 4360-4370.

Wang, Z., Feng, X., Molinolo, A. A., Martin, D., Vitale-Cross, L., Nohata, N., Ando, M., Wahba, A., Amornphimoltham, P., Wu, X., Gilardi, M., Allevato, M., **Wu, V.**, Steffen, D. J., Tofilon, P., Sonenberg, N., Califano, J., Chen, Q., Lippman, S. M., and Gutkind, J. S. (2019) 4E-BP1 Is a Tumor Suppressor Protein Reactivated by mTOR Inhibition in Head and Neck Cancer. Cancer Res 79, 1438-14.

Guram, K., Kim, S. S., **Wu, V.**, Sanders, P. D., Patel, S., Schoenberger, S. P., Cohen, E. E. W., Chen, S. Y., and Sharabi, A. B. (2019) A Threshold Model for T-Cell Activation in the Era of Checkpoint Blockade Immunotherapy. Front Immunol 10, 491.

2018

Naing, A., Infante, J. R., Papadopoulos, K. P., Chan, I. H., Shen, C., Ratti, N. P., Rojo, B., Autio, K. A., Wong, D. J., Patel, M. R., Ott, P. A., Falchook, G. S., Pant, S., Hung, A., Pekarek, K. L., **Wu, V.**, Adamow, M., McCauley, S., Mumm, J. B., Wong, P., Van Vlasselaer, P., Leveque, J., Tannir, N. M., and Oft, M. (2018) PEGylated IL-10 (Pegilodecakin) Induces Systemic Immune Activation, CD8(+) T Cell Invigoration and Polyclonal T Cell Expansion in Cancer Patients. Cancer Cell 34, 775-791 e773.

2016

Chan, I. H., **Wu, V.**, Bilardello, M., Jorgenson, B., Bal, H., McCauley, S., Van Vlasselaer, P., and Mumm, J. B. (2016) PEG-rIL-10 treatment decreases FoxP3(+) Tregs despite upregulation of intratumoral IDO. Oncoimmunology 5, e1197458

Wu, V., Smith, A. A., You, H., Nguyen, T. A., Ferguson, R., Taylor, M., Park, J. E., Llontop, P., Youngman, K. R., and Abramson, T. (2016) Plasmacytoid dendritic cell-derived IFNalpha modulates Th17 differentiation during early Bordetella pertussis infection in mice. Mucosal Immunol 9, 777-786

2015

Chan, I. H., **Wu, V.**, Bilardello, M., Mar, E., Oft, M., Van Vlasselaer, P., and Mumm, J. B. (2015) The Potentiation of IFN -gamma and Induction of Cytotoxic Proteins by Pegylated IL-10 in Human CD8 T Cells. J Interferon Cytokine Res 35, 948-955

Chan, I. H., **Wu, V.**, McCauley, S., Grimm, E. A., and Mumm, J. B. (2015) IL-10: Expanding the Immune Oncology Horizon. Receptors Clin Investig 2

2013

Parales, R. E., Luu, R. A., Chen, G. Y., Liu, X., **Wu, V.**, Lin, P., Hughes, J. G., Nesteryuk, V., Parales, J. V., and Ditty, J. L. (2013) Pseudomonas putida F1 has multiple chemoreceptors with overlapping specificity for organic acids. Microbiology 159, 1086-1096

2012

Nguyen, T. M., Ravindra, D., Kwong, B., Waheed, S., Ferguson, R., Tarlton, N., **Wu, V.**, Sequeira, C. S., Bremer, M., and Abramson, T. (2012) Differential expression of alpha 4 integrins on effector memory T helper cells during Bordetella infections. Delayed responses in Bordetella pertussis. PLoS One 7, e52903

ABSTRACT OF THE DISSERTATION

GPCRs as Next-Gen Targets for Immune Oncology

by

Victoria H. Wu

Doctor of Philosophy in Biomedical Sciences

University of California San Diego, 2021

Professor J. Silvio Gutkind, Chair

G-protein coupled receptors (GPCRs) are the most intensively studied drug targets since they play key roles in many physiological processes, and they have remained longstanding favorable pharmacological targets. GPCRs have become one of the top targets for pharmaceutical drug development, largely due to their known dysregulated expression and aberrant functions in some of the most prevalent human diseases. However, the study of the role of GPCRs in tumor biology has only just begun to make headway. Though recent advances have enriched our understanding of the contribution of GPCRs to tumorigenesis, angiogenesis, and immune evasion, drug development for GPCRs in oncology is still underexploited. Adding to his, although checkpoint blockade immunotherapies (CBI) inhibiting programmed death-1 (PD-1) and cytotoxic T-lymphocyte antigen-4 (CTLA-4) have revolutionized cancer treatment, the limited response rates in most cancers suggest that new approaches, targets, and animal models that more faithfully recapitulate human cancers are clearly needed to fully elucidate the underlying biology of resistance to cancer immunotherapies. Here, we first developed a full, comprehensive analysis of GPCRs across multiple tumor types to highlight GPCRs that may be important to target on the global tumor level. Next, we explored whether a carcinogen-induced mouse model of oral cancer can better model mutational signatures and response to immunotherapies of human head and neck cancers. With these novel tools and analyses, we aimed to uncover new GPCR targets for immune oncology with cutting edge chemogenetic approaches to investigate the role of downstream $G\alpha_s$-signaling in CD8 T cells that infiltrate tumors. Altogether, our work here provides a platform to identify emerging GPCR targets that when blocked concomitant with PD-1 and CTLA-4, can enable achieving a higher response rate and more durable responses (cure). Ultimately, our studies provide novel therapeutic interventions as part of multimodal precision immunotherapies for oncology.

Chapter 1: Introduction (of dissertation)

1.1 Illuminating the Onco-GPCRome

The G protein-coupled receptor (GPCR) family is a 7-transmembrane domain family of proteins that includes over 800 members and makes up ~4% of the human genome (1). GPCRs participate in a plethora of physiological processes, including vision, olfaction, neurotransmission, hormone and enzyme release, immune response, hemostasis, cardiac response and blood pressure regulation, epithelial cell renewal, stem cell fate decisions, tissue development, and homeostasis (2). In fact, dysfunction of GPCRs contributes to some of the most prevalent human diseases, which is reflected by the 475 currently approved drugs that target 108 unique GPCRs and represent 34% of all FDA-approved drugs (3). Although drugs for GPCRs represent 34% of the global therapeutic drug market, only a handful of these are drugs for oncology; of the current FDA-approved anti-cancer drugs, only eight of these target GPCRs. A comprehensive analysis of the landscape of GPCR expression, mutations, and copy number variations can shed light on important GPCRs to target for oncology.

1.2 Syngeneic animal models of tobacco-associated oral cancer

Head and neck squamous cell carcinoma (HNSCC) ranks 6th in cancer incidence worldwide and has a five-year survival rate of only 63% (4). Immune checkpoint inhibitors (ICI), like anti-PD-1 and anti-CTLA-4 antibodies that restore functional capacity of cytotoxic T cells have shown great promise for HNSCC treatment, but have not shown durable responses (5). Tobacco use is the main risk factor for HNSCC, but mouse models that accurately mimic the mutational landscape of human HNSCC is limited (6). By developing a carcinogen-induced mouse model of oral cancer, we aim to accelerate the identification of new targets for precision therapies in immunotherapy.

1.3 A chemogenetic approach reveals a GPCR-Gαs-PKA signaling axis promoting T cell dysfunction and cancer immunotherapy failure

Successful response to immunotherapy in cancer depends on the infiltration of cytotoxic T cells into the tumor, but immunosuppressive molecules at the tumor microenvironment dampen this response through immune checkpoints, namely programmed death-1 (PD-1) and cytotoxic T-lymphocyte-associated protein 4 (CTLA-4) (8, 9, 10). Though breakthrough discoveries in cancer immunotherapy have led to remarkable response across multiple cancer types, the lack of complete responses suggest additional targets that need to be blocked in order to restore T cell anti-tumor immunity. G-protein coupled receptors (GPCRs) are the most targeted class of cell surface receptors in the drug market, primarily due to their roles in most physiological processes (3). However, GPCRs have been underexploited in immune oncology, as only 1 current FDA-approved drug targets a GPCR in immunotherapy (11). Most GPCRs studied in immune oncology are $G\alpha_i$-coupled chemokine receptors that promote activation and infiltration of cytotoxic T cells to the tumor (12). These receptors inhibit cyclic AMP (cAMP) production, while $G\alpha_s$-coupled receptors activate adenylyl cyclases, thereby stimulating the production of cAMP and downstream protein kinase A (PKA) signaling (13). With this, the study of the interplay between signaling circuitries from GPCRs expressed on T cells that bind ligands abundant in the tumor microenvironment may uncover new targets for immune oncology.

1.4 References

1. Pierce, K. L., Premont, R. T., and Lefkowitz, R. J. (2002) Seven-transmembrane receptors. *Nature reviews. Molecular cell biology* 3, 639-650
2. Hauser, A. S., Attwood, M. M., Rask-Andersen, M., Schioth, H. B., and Gloriam, D. E. (2017) Trends in GPCR drug discovery: new agents, targets and indications. *Nat Rev Drug Discov* 16, 829-842
3. Santos, R., Ursu, O., Gaulton, A., Bento, A. P., Donadi, R. S., Bologa, C. G., Karlsson, A., Al-Lazikani, B., Hersey, A., Oprea, T. I., and Overington, J. P. (2017) A comprehensive map of molecular drug targets. *Nat Rev Drug Discov* 16, 19-34
4. Siegel, R. L., Miller, K. D., and Jemal, A. (2019) Cancer statistics, 2019. *CA Cancer J Clin* 69, 7-34
5. Ferris, R. L., Blumenschein, G., Jr., Fayette, J., Guigay, J., Colevas, A. D., Licitra, L., Harrington, K., Kasper, S., Vokes, E. E., Even, C., Worden, F., Saba, N. F., Iglesias Docampo, L. C., Haddad, R., Rordorf, T., Kiyota, N., Tahara, M., Monga, M., Lynch, M., Geese, W. J., Kopit, J., Shaw, J. W., and Gillison, M. L. (2016) Nivolumab for Recurrent Squamous-Cell Carcinoma of the Head and Neck. *N Engl J Med* 375, 1856-1867
6. Agudo, A., Bonet, C., Travier, N., Gonzalez, C. A., Vineis, P., Bueno-de-Mesquita, H. B., Trichopoulos, D., Boffetta, P., Clavel-Chapelon, F., Boutron-Ruault, M. C., Kaaks, R., Lukanova, A., Schutze, M., Boeing, H., Tjonneland, A., Halkjaer, J., Overvad, K., Dahm, C. C., Quiros, J. R., Sanchez, M. J., Larranaga, N., Navarro, C., Ardanaz, E., Khaw, K. T., Wareham, N. J., Key, T. J., Allen, N. E., Trichopoulou, A., Lagiou, P., Palli, D., Sieri, S., Tumino, R., Panico, S., Boshuizen, H., Buchner, F. L., Peeters, P. H., Borgquist, S., Almquist, M., Hallmans, G., Johansson, I., Gram, I. T., Lund, E., Weiderpass, E., Romieu, I., and Riboli, E. (2012) Impact of cigarette smoking on cancer risk in the European prospective investigation into cancer and nutrition study. *J Clin Oncol* 30, 4550-4557
7. Dong H, Strome SE, Salomao DR, Tamura H, Hirano F, Flies DB*, et al.* Tumor-associated B7-H1 promotes T-cell apoptosis: a potential mechanism of immune evasion. Nat Med 2002;8(8):793-800 doi 10.1038/nm730.
8. Ishida Y, Agata Y, Shibahara K, Honjo T. Induced expression of PD-1, a novel member of the immunoglobulin gene superfamily, upon programmed cell death. EMBO J 1992;11(11):3887-95.
9. Wei SC, Levine JH, Cogdill AP, Zhao Y, Anang NAS, Andrews MC*, et al.* Distinct Cellular Mechanisms Underlie Anti-CTLA-4 and Anti-PD-1 Checkpoint Blockade. Cell 2017;170(6):1120-33.e17 doi 10.1016/j.cell.2017.07.024.
10. Willingham SB, Hotson AN, Miller RA. Targeting the A2AR in cancer; early lessons from the clinic. Curr Opin Pharmacol 2020;53:126-33 doi 10.1016/j.coph.2020.08.003.
11. Tokunaga R, Zhang W, Naseem M, Puccini A, Berger MD, Soni S*, et al.* CXCL9, CXCL10, CXCL11/CXCR3 axis for immune activation - A target for novel cancer therapy. Cancer Treat Rev 2018;63:40-7 doi 10.1016/j.ctrv.2017.11.007.
12. Pierce KL, Premont RT, Lefkowitz RJ. Seven-transmembrane receptors. Nat Rev Mol Cell Biol 2002;3(9):639-50 doi 10.1038/nrm908.

Chapter 2: Illuminating the Onco-GPCRome: Novel G protein-coupled receptor-driven oncocrine networks and targets for cancer immunotherapy

2.1 Abstract

G protein–coupled receptors (GPCRs) are the largest gene family of cell membrane–associated molecules mediating signal transmission, and their involvement in key physiological functions is well-established. The ability of GPCRs to regulate a vast array of fundamental biological processes, such as cardiovascular functions, immune responses, hormone and enzyme release from endocrine and exocrine glands, neurotransmission, and sensory perception (e.g. vision, odor, and taste), is largely due to the diversity of these receptors and the layers of their downstream signaling circuits. Dysregulated expression and aberrant functions of GPCRs have been linked to some of the most prevalent human diseases, which renders GPCRs one of the top targets for pharmaceutical drug development. However, the study of the role of GPCRs in tumor biology has only just begun to make headway. Recent studies have shown that GPCRs can contribute to the many facets of tumorigenesis, including proliferation, survival, angiogenesis, invasion, metastasis, therapy resistance, and immune evasion. Indeed, GPCRs are widely dysregulated in cancer and yet are underexploited in oncology. We present here a comprehensive analysis of GPCR gene expression, copy number variation, and mutational signatures.

2.2 Introduction

The G protein– coupled receptor (GPCR) family of proteins includes over 800 members and comprises ~4% of the encoded human genome, making it the largest gene family involved in signal transduction (1,2). Common to all GPCRs is the 7-transmembrane domain structure, which has an extracellular N terminus and an intracellular C terminus. The importance of the multiple biological roles GPCRs is reflected in the range of key physiological processes that they regulate, including vision, olfaction, neurotransmission, hormone and enzyme release, immune response, hemostasis, cardiac response and blood pressure regulation, epithelial cell renewal, stem cell fate decisions, tissue development, and homeostasis.

A defining feature of GPCRs is the ability to activate one or multiple Gα proteins, which can be subdivided into four major families based on sequence similarity: Gαs, Gαi, Gαq/11, and Gα12/13 (**Figure 2.1**). As reviewed previously (3,4), Gαs activates adenylyl cyclases to catalyze the conversion of ATP to cAMP, which is produced as a second messenger and activates protein kinase A (PKA) and in some cells guanine nucleotide exchange factors (GEFs) for the small GTPase RAP1. Members of the Gαi family primarily inhibit cAMP production, activate a variety of phospholipases and phosphodiesterases, and promote the opening of several ion channels. The Gαq/11 family converts phosphatidylinositol 4,5-bisphosphate to DAG and inositol 1,4,5-trisphosphate to activate PKC and elevates intracellular Ca2+ levels. In a noncanonical fashion, Gαq/11 also stimulates Rho GEFs thereby stimulating Rho GTPases (5,6), whereas DAG activates Ras-GEFs (7). Gα12/13 signaling involves a family of RhoGEFs harboring an RGS domain by which they associate with active Gα12/13 and stimulate Rho GTPase (8).

Dysfunction of GPCRs contributes to some of the most prevalent human diseases, which is reflected by the 475 currently approved drugs that target 108 unique GPCRs and represent 34% of all FDA-approved drugs (https://www.centerwatch. com/drug-information/fda-approved-drugs) (9,10). Although drugs for GPCRs represent ~34% of the global therapeutic drug market (9,10), only a handful of these are drugs for oncology; of the current FDA-approved anti-cancer

drugs, only eight of these target GPCRs, as described in detail below. Here, we summarize the current knowledge of how GPCRs are altered in cancer and how these aberrations can contribute to cancer initiation and progression. We also bring forth an emerging role of GPCRs as part of autocrine and paracrine signaling processes, which we refer to collectively as oncocrine networks that drive tumor formation, growth, and immune evasion. We also highlight the potential benefits of targeting GPCRs in the new era of precision cancer immunotherapies.

2.3 Results

2.3.1 Mutational landscape of G proteins and GPCRs in cancer

The Cancer Genome Atlas (TCGA) is a comprehensive, publicly available database launched by the National Institutes of Health, which includes large-scale genome sequencing analyses through multiple omics platforms for a variety of cancer types (11). In addition to this, the TCGA database also includes array-based DNA methylation sequencing for methylation profiling and reverse-phase protein array for large-scale protein expression profiling. These platforms can add a multidimensional view to the landscape of GPCRs and G proteins in cancer. Here, we built on our prior cancer genome-wide study (12), performing an in-depth omics analysis of the mutational land- scape of 33 cohorts of cancer patients in TCGA by new bioinformatics approaches (**Table 2.1**).

The power of this analysis revealed that 20% of all human tumors sequenced contained mutations in genes encoding GPCRs. In particular, we used MutSig2CV, a now widely used computational biology tool that takes mutations discovered by DNA sequencing to illuminate genes that are statistically more frequently mutated relative to the background mutation rate of individual lesions (13). Many G proteins and GPCRs were found to be mutated. For visualizing the data, we used a very stringent criterion (MutSig2CV q-value <0.25) to identify the most statistically significant mutated genes in each cancer type. An unexpected observation was that among all cancer cohorts, cancers arising in the gastrointestinal (GI) tract, including colon adenocarcinoma (COAD), stomach adenocarcinoma (STAD), and pancreatic adenocarcinoma (PAAD) displayed the highest number of significantly mutated GPCRs and G proteins (**Figure 2.2 and Tables 2.2 and 2.3**). This may be independent of the mutational burden of these tumors, which are lower than that of other typical highly-mutated cancers such as melanoma and lung cancer, for example (14). However, the phenotypic and biological outcome of these mutations remains largely unknown, and thus these findings provide a wealth of information for the development of hypothesis-driven approaches to investigate their cancer relevance.

2.3.2 Significantly mutated G proteins in cancer

Whereas the contribution of each GPCR mutation in cancer is still under evaluation, the recent discovery of hot spot mutations in G proteins as oncogenic drivers in multiple highly prevalent cancer types has accelerated tremendously the research in this field. Indeed, many G protein genes (GNAS, GNA11, GNAQ, and GNA13) are part of the current ~400 gene panels of cancer-associated genes sequenced routinely by clinical oncology services in many cancer centers and by all large cancer genomic testing providers and institutional genomics cores. Among them, the summary of our MutSig2CV analysis revealed that GNAS is the most highly mutated G protein in human cancer (**Table 2.3**). From this analysis, GNAS is significantly mutated in COAD (6.19%), PAAD (5.09%), and STAD (7.52%). As described above, GNAS is a known oncogene that was first described in growth hormone–secreting pituitary adenomas and has since been found to be mutated in a number of neoplasms, predominantly at the codon 201 hotspot (12,15). Mutations occurring at arginine 201 of GNAS activate adenylate cyclase and lead to constitutive cAMP signaling by reducing the rate of GTP hydrolysis of the active GTP-bound G□s, as well as by adopting an active-like conformation even when bound to GDP (12,16). In COAD, a synergistic effect with the MAPK pathway is likely, as GNAS is co-mutated with KRAS in a large portion of adenomas and carcinomas. Similarly, GNAS mutations are found in ~50% of low-grade appendiceal mucinous neoplasms (17) and are highly prevalent in a subset of pancreatic tumors, including intraductal papillary mucinous neoplasms and adenocarcinomas (18). In this regard, recent mouse models revealed that GNAS and KRAS mutations arenecessary and sufficient to initiate this particular subtype of pancreatic adenocarcinomas (19,20).

2.3.3 Mutated oncoGPCRome

The most frequently mutated GPCRs in each cancer type are depicted in **Figure 2.2** and are listed in **Table 2.2** with the corresponding statistical significance (q-value) and frequency. As mentioned above, the high frequency of GPCR mutations specifically in tumors arising from the gastrointestinal tract is intriguing as it likely reflects their ability to stimulate organ- specific growth-

promoting pathways in these cancers. Although a discussion of each specific GPCR is beyond our goals, we will discuss new emerging concepts and specific cases that may exemplify the challenges and opportunities for future exploration in this area and its potential for drug discovery.

Whether mutations in GPCRs result in GOF or LOF, or rep- resent passenger mutations with little impact on cancer progression, in most cases is still unknown. A complicating factor is that most GPCRs do not harbor hotspot mutations, meaning that mutations in each GPCR do not occur with high frequency in a single or limited numbers of codons, and in addition, each tumor exhibits a different repertoire of mutated GPCRs. To address this daunting question, we have recently developed new bioinformatics approaches analyzing GPCR mutations in the context of multiple sequence alignments (MSA) defining the conserved seven-transmembrane (7TM) domain, as well as considering 3D structures and interaction partners (21). We have used this approach to model the most significantly mutated GPCRs (**Table 2.2**). Remarkably, visualization of the most mutated 7TM positions on a representative GPCR 3D structure revealed that most mutations occur in "hotspot structural motifs" rather than being randomly distributed (**Figure 2.3**). This includes frequent mutations in the DRY arginine motif, which is as important for class A GPCR activation as it is responsible for the intramolecular polar contacts that keep the receptor inactive until ligand binding (22). Other structural mutation hotspots are found at or nearby highly-conserved GPCR regions, including the ligand and G protein–binding sites, as well as the NPXXY and other conserved motifs that regulate in an allosteric way receptor's activation (23). Collectively, this supports that most cancer-associated mutations in GPCRs occur in "structural hotspots," similar to other oncogenes and tumor suppressor genes, a property that could have not been predicted from the analysis of individual GPCRs.

Although the functional impact of these alterations may need to be investigated for each GPCR, our recent computational analysis of cancer genomes indicates that most Gαi-linked GPCRs exhibit DRY mutations that are inhibitory in nature (inhibit function), which typically occur mutually exclusively with GNAS-activating mutations (21). This suggests the exciting possibility

that mutations in Gαi–GPCRs may mimic *GNAS* mutants leading to higher cAMP activity to drive tumorigenesis (21).

The analysis of the mutational landscape of GPCRs suggest that COAD harbors the highest incidence of significantly mutated receptors. Among them, thyroid-stimulating hormone receptor (TSHR) was the most frequently mutated GPCR, involving ~14% of COAD patients. Mutations in the P2Y purinoceptor 13 (P2RY13) gene were the most statistically significant in this cancer type and occurred in ~5% of COAD patients. P2RY13 encodes for a purine receptor and has been shown to be overexpressed in acute myeloid leukemia samples but not involved in other nonhematologic malignancies (24). On a related note, mucosal biopsies from the colon of Crohn's disease and ulcerative colitis patients have shown abnormalities in P2RY13, which may suggest a role for the receptor in GI inflammatory diseases (25). The importance of TSHR-activating mutations in human neoplasia was first demonstrated in thyroid adenomas (26) and are also found in some thyroid carcinomas. However, the roles of both TSHR and P2Y13 in COAD remain largely unexplored.

Recently, analysis of hotspot mutations in oncogenes uncovered a mutation in cysteinyl leukotriene receptor 2 (CYSLTR2) in a UVM cohort. This GOF mutation results in an L129Q substitution and leads to the Gαq-coupled receptor to be constitutively active (27). This mutant protein is insensitive to leukotriene stimulation, constitutively activates Gαq, and can promote tumorigenesis in melanocytes in vivo (27). According to MutSig2CV analysis, CysLT2 is the most frequently mutated GPCR (3.75%) in UVM. While representing a small fraction of all UVM cases, these mutations in CYSLTR2 are mutually exclusive with known drivers in UVM (GNA11 and GNAQ) (27). Therefore, CYSLTR2 mutations promote persistent Gαq activation substituting for GNA11 and GNAQ mutations to drive aberrant Gαq signaling in UVM. This receptor is also mutated in COAD at a distinct amino acid, and hence its con- sequences (GOF or LOF) are still unknown. Recently, small molecules have been discovered and utilized against WT CysLT2, but

development of higher-affinity molecules or antibodies that can stabilize the mutated receptor in its inactive state will be required to explore the therapeutic benefit of targeting CysLT2 in UVM.

Our current analysis also identified many adhesion receptors and class A GPCRs that are mutated with high frequency in cancer. The former includes GPR98, BAI3, ADGRL1, CELSR1, GPR125, GPR110, GPR112, and GPR126, which can now be prioritized for their individual analysis. A recent comprehensive mutagenesis screen in ADGRL1 revealed that many cancer-associated mutations result in GOF alterations and persistent activity (28).

Among the typical class A GPCRs, some of the more frequently mutated genes are muscarinic receptors M2 and M3 (CHRM2 and CHRM3), multiple P2Y receptors, serotonin receptors (HTR1E, HTR1F, HTR2A, and HTR7), and adenosine receptors (ADORA3), among others, all of which could be activated by locally produced ligands as well. Notable mutated GPCRs also include the PAR2 receptor (F2RL1), which is often amplified and will be discussed below, as well as multiple orphan GPCRs whose coupling specificity and biological activity is still largely unknown.

2.3.4 Gene copy number alterations and G protein and GPCR expression in cancer

In addition to mutations, alterations in gene expression and copy number of G protein and GPCR genes have been detected. Determining the contribution of such alterations to cancer initiation and progression remains a significant challenge, yet it may be critical both for the discovery of driver oncogenic processes and for the development of targeted therapeutics. Indeed, aberrant expression of many WT G proteins and GPCRs can contribute to cancer growth even if not mutated, often as part of oncocrine signaling networks (see below).

Somatic alterations are acquired at random during cell division, and some of these participate in tumorigenesis or tumor growth. Here, we used GISTIC (Genomic Identification of Significant Targets in Cancer), an algorithm that identifies genes targeted by somatic CNVs that may contribute to tumorigenesis by evaluating the frequency and amplitude of observed events (29). To illuminate the most relevant GPCR candidates in tumorigenesis, we also filtered the large

list of CNVs for those that correlated with mRNA expression. Our analysis revealed that 28 out of 33 TCGA cancer cohorts included alterations of GPCR and G protein that are significantly correlated with mRNA expression of the corresponding genes (R > 0.33) (**Figure 2.4**).

Among the G proteins, copy number gain in GNA12 is remarkably significant in ovarian cancer (OV). This cancer type is characterized by few driver mutations and by the accumulation of high concentrations of LPA in ascites fluids, which may work through Gα12 to promote growth and metastasis (30). Similarly, GNAI1 (encoding Gαi1) is significantly amplified in breast-invasive carcinoma (BRCA), a cancer type in which many Gαi-coupled GPCRs, including CXCR4, are well-established as metastatic drivers (see below). The significance of other genomic alterations in G proteins, including copy number gains in Gβ subunits (GNAB1, GNAB2, GNAB3, and GNAB5) and Gγ (GNG4, GNG5, GNG7, GNG12, and GNGT1) in multiple cancers likely reflect the broad signaling capacity of G$\beta\gamma$ dimers (**see Figure 2.1**).

Testicular germ cell tumor displayed the most genomic alterations in genes encoding GPCRs, which included mostly orphan, taste, and adhesion receptors. In contrast, F2RL1, the gene encoding -activated receptor (PAR) 2, was the most significantly altered gene in OV. PAR2 is a protease-activated receptor and is expressed in many organs. Another unexpected observation was that most kidney cancers (KIPAN) exhibit highly-significant copy number gains in genes for multiple chemokine receptors (CCR2, CCR5, CCR6, CCR9, CX3CR1, and CXCR6) and histamine receptors (HRH2), among others. The frizzled family of GPCRs and LPA receptors (in particular LPAR6) were also genetically altered in multiple cancer types. Overall, although gene copy gains and losses may reflect cancer-associated genomic instability, most cancers exhibit a very specific pattern of copy number variations in G protein and GPCR genes, whose biological relevance can now be examined.

2.3.5 pan-Cancer GPCRs expression

In addition to mutations, normal GPCRs can play a key role in cancer progression, and they can be targeted pharmacologically for therapeutic purposes. A typical problem when analyzing gene expression changes in cancer is that often both normal and cancerous tissues are heterogeneous, including multiple cell types. Hence, relative changes (fold changes and over- and underexpression) may reflect cellular heterogeneity more than the progression from a normal cell to its distinct cancer states. For example, comparison of GPCRs expressed in cutaneous melanoma with normal skin may grossly overestimate the relative changes in expression between normal and cancerous melanocytes, as the normal skin includes a very limited number of melanocytes. Moreover, although fold changes can provide useful information, this takes attention away from GPCRs that may exert important functions for cancer transformation through increased local ligand secretion or aberrant down- stream signaling activity. A recent study has documented relative changes in GPCR expression in cancer (31). Instead, we focus here on illuminating absolute expression levels of each GPCR and provide visual representations to gauge absolute GPCR levels. Certainly, a limitation of this analysis is that the precise cells that express each GPCR within the tumors, such as cancer and tumor stromal cells (e.g. cancer associated fibroblasts, blood vessels, and immune infiltrating cells), will need to be established in future efforts, for example by the use of modern single cell sequencing approaches. Nonetheless, we expect that we can gain an unprecedented new perspective on GPCR expression patterns in human malignancies by utilizing information gained from this analysis.

Specifically, as shown in **Figure 2.5**, an intriguing area of study is the expression of orphan GPCRs in cancer. The endogenous ligands of more than 140 of these receptors remain unidentified and/or poorly understood, thus, their natural function is currently largely unknown (32). Nevertheless, according to our pan-cancer analysis, orphan GPCRs are differentially expressed across cancer types, and they may exert multiple functions during cancer progression. For example, since a decrease in extracellular pH is a major tumor-promoting factor in the tumor microenvironment, an intriguing area of research is the group of proton-sensing GPCRs: GPR132,

GPR65, GPR68, and GPR4, which are highly expressed in a large range of human cancers. Both GPR4 and TDAG8 (GPR65) have been shown to be overexpressed in many cancers and can cause malignant transformation of cells in vitro (33). Interestingly, in our recent G protein–coupling predictor trained by a large experimental dataset, orphan GPCRs tend to show a higher proportion of coupling toward Gα12/13 than other GPCR classes (34) further suggesting potential importance of orphan GPCRs in cancers that involve aberrant Gα12/13 signaling.

Interestingly, many class A orphan GPCRs are rarely expressed across cancer types. These include the MAS oncogene, which can explain the limitations in analyzing its role in human cancer despite its initial identification during transfection experiments several decades ago. Others are expressed in a single cancer (e.g. GPR22 in pheochromocytoma and paraganglioma) or a few cancers (e.g. GPR17 and GPR37L1 that are expressed only in GBM and brain lower grade glioma), whereas others are expressed in most cancers, such as OPN3 and LGR4. These studies de-orphaning GPCRs and uncovering the function of additional overexpressed GPCRs may provide promising candidates for therapeutic intervention in cancer. Although this review will not provide a comprehensive analysis of each GPCR, a few concepts may be worth discussing. For example, expression of the purinergic P2Y11 and adenosine A2A receptors is widespread in all cancers, whereas GBM tumors express high levels of ADORA1, ADORA2, and ADORA3, all of which can be activated by adenosine in the tumor microenvironment. Multiple lipid receptors for S1P (S1P1–3) and LPA (LPA1, LPA2 , and LPA6) are widely expressed as well. These receptors are intriguing because ligands for these receptors have been shown to accumulate in the tumor microenvironment (35,36). Conserved residues in these receptors also display a high mutational rate, which suggests that they may play vital roles in receptor signaling initiation, termination, and coupling specificity (12).

This is also highly relevant for the 17 known GPCRs that specifically recognize intermediates or (by)products of cellular metabolism, which are often involved in nutrient sensing

(37). These include receptors sensing amino acids and amino acid metabolites (GPR142, CasSR, GPR35, TAAR1, and FOPR1/2), bile acid (TGR5/GPBAR1), triglyceride metabolites (e.g. FFA1/ GPR40, FFA4/GPR120, and GPR119), products of the intermediary metabolism and small carboxylic metabolites such as acetate and propionate (FFA2/GPR43 and FFA3/GPR41), butyrate (FFA2/GPR43, FFA3/GPR41, and HCA2/GPR109A), β-hy- droxybutyrate (HCA2/GPR109A), β -hydroxyoctanoate (HCA3/ GPR109B), lactate (HCA1/GPR81), succinate (GPR91), and capric acid (GPR84) receptors, as well as gut microbiota-derived products (e.g. short-chain fatty acids, such as acetate, propionate, and butyrate) (37). These receptors are highly expressed in multiple organs of the digestive tract and immune cells (38), and they may be persistently activated in the tumor microenvironment due to the high metabolic rate that characterizes most solid tumors.

The EP4 (PTGER4) and EP2 (PTGER2) receptors for the typical inflammatory mediator PGE2 (see below) are also widely expressed, whereas EP3 (PTGER3) is mainly expressed in kidney cancer.

Among the class of GPCRs for proteins (**Figure S2.1**), which includes chemokine receptors, CXCR4 is the most widely expressed. This may include many cancers that express CXCR4 under hypoxic conditions, as well as in blood vessels and immune cells (see below) (39-41). Other chemokine receptors that are highly expressed in immune cells (see below) were less well-represented, suggesting a more limited impact of immune infiltrating cells to the overall mRNA expression patterns in our pan-cancer analysis. The analysis of GPCRs activated by peptides (**Figure S2.2**) show a clear widespread expression in genes for thrombin PAR1 (F2R) and PAR2 (F2RL1) receptors and endothelin receptors (EDNRB), the latter with particularly higher expression in SKCM and uveal (UM) melanomas. HRH1, encoding H1 histamine receptor, is the most widely expressed aminergic GPCR (**Figure S2.3**), whereas M1 muscarinic receptors (CHRM1) and β1-adrenergic receptors (ADRB1) are highly expressed in prostate cancer, the

latter receptor being of unexpected importance for the most highly prevalent cancer among males (see below). Another interesting finding was the high level of expression of dopamine receptor 2 (DRD2) in a well-defined set of cancers, including GBM, considering that a new family of antagonists for this receptor has exhibited encouraging anti-tumor activity in multiple cancer types (42,43).

Interestingly, from our analysis of Frizzled GPCRs, SMO is widely expressed in most cancers, beyond its initial main role in BCC. This might be due to SMO being expressed in cancer stromal cells that are present in most solid tumors (Fig. S1G) (44,45). There is also widespread expression of FZD6 and a more cancer-restricted expression of FZD1 and FZD4 (**Figure S2.4**).

Intriguingly, analysis of the sensory GPCRs revealed a high level of expression of the taste receptor, TAS1R3, across most cancer types, which has not been previously investigated **(Figure S2.5**).

The adhesion GPCR family has mainly been studied in immunological and developmental functions, but they have recently been linked to cancer (**Figure S2.6**). For example, EMR2 (ADGRE2) is overexpressed in human breast cancer, and increased nuclear expression of EMR2 is negatively correlated with tumor grade (46). Additionally, CD97 (ADGRE5) and GPR56 (ADGRG1) are the highest expressed adhesion GPCRs across all cancers, but they have only been studied in the con- text of melanoma, gastric, esophageal, and thyroid cancers (47-49). Additionally, GPR65 (TDAG8) and GPR133 (ADGRD1) have also been associated with human cancers and linked to tumor promotion (33,50), but the role of this highly-expressed family of GPCRs in tumor initiation and metastasis is still not fully understood.

Overall, we expect that the emerging pan-cancer information on GPCR expression will ignite new interest on their study in human malignancies.

2.3.6 Key role for GPCRs in cancer immunology

In the last few years, cancer immunotherapy became one of the most exciting breakthroughs in cancer treatment. Recent revolutionary discoveries have highlighted the

importance of the tumor microenvironment and its associated immune cells in cancer development and therapeutic resistance. Tumors can deploy multiple mechanisms to avoid immune recognition and an anti-tumor immune response, including the recruitment of myeloid-derived suppressor cells (MDSC) and conditioning of the surrounding microenvironment to become highly immune-suppressive by expressing cytokines, such as IL-6, IL-10, and transforming growth factor β (51). This can lead to the accumulation of suppressive regulatory T cells (Tregs) and the polarization of macrophages toward an immune-suppressive phenotype, which is often referred to as M2 or tumor-associated macrophage (TAM) phenotype (52). A key emerging mechanism of tumor immunosuppression involves the induction of T-cell exhaustion through activation of T-cell checkpoints, including programmed death 1 (PD-1). Its ligand, programmed death-ligand 1 (PD-L1), is expressed by macrophages and some cancer cells, which can restrain T-cell activation and induce immunosuppresion (53-55). Together, these conditions contribute to the suppression of cytotoxic CD8+ T lymphocyte recruitment, survival, and function, and ultimately to the loss of an effective anti-tumor immune response. Although the aberrant function and dysregulated expression of GPCRs is now beginning to be linked directly to the tumor itself, the role of GPCRs on immune cells infiltrating tumors is still not fully understood and grossly underappreciated. Given the diversity of GPCRs and the variety of GPCR families, current studies have only scratched the surface of delineating GPCRs on immune cells in cancer. The importance of studying GPCRs in the context of cancer immunology is reflected by the multiple roles that this receptor family plays in inflammation, orchestrating immune cell trafficking and regulating the tumor microenvironment, as summarized in **Figure 6**. A crucial first step in anti-tumor immunity is the migration of cytotoxic cells recognizing tumor antigens to the tumor, and this is mediated largely by chemokine receptors.

2.3.7 Modulation of immunosuppressive GPCRs by the tumor microenvironment

The immunosuppressive and hypoxic nature of the tumor microenvironment can also largely influence the function of cytotoxic immune cells and the success of cancer

immunotherapies. A driving force behind the malignancy and morbidity of cancer is its ability to proliferate unrestrained, by creating an immunosuppressive environment favoring tumor growth. The nucleoside adenosine is a potent physiologic and pharmacologic regulator that is released from injured and necrotic cells by extracellular breakdown of ATP by the action of the ectonucleotidases CD39 and CD73 (56). Typical extracellular adenosine levels are low, but at injury sites with tissue breakdown and hypoxia, the adenosine levels can rise from nanomolar to micromolar concentrations. Extracellular adenosine can signal through four GPCRs: A1, A2A, A2B, and A3 adenosine receptors (ADORA1, ADORA2A, ADORA2B, and ADORA3, respectively) (57). A1 and A3 receptors signal through Gαi and lead to decreased cAMP. Activation of A2A and A2B receptors, which are expressed on immune and endothelial cells, leads to signaling through Gαs proteins, and A2B can also signal through Gαq (58). Of the four adenosine receptors, A2A receptor (encoded by the ADORA2A gene) is the predominantly expressed subtype in most immune cells. In general, stimulation of the A2A receptor provides an immunosuppressive signal in T cells (57), NK cells (59), DCs (60), and neutrophils (61). A2A receptor stimulation interferes with trafficking of T cells and NK cells by desensitizing chemokine receptors and reducing levels of pro-inflammatory cytokines (62). Blocking the adenosine-generating pathway has shown tumor regression in breast cancer, colorectal cancer, and melanoma (56,63), and small molecule inhibitors of A2A receptor as well as blocking antibodies anti-CD73 and anti-CD39 are under current evaluation for combination cancer immunotherapies (56,64). Although these immunotherapies aim to boost immune cell activity in the immunosuppressive tumor microenvironment, it is also important to consider the effects of tumor-driven inflammation, largely driven by prostaglandins and prostaglandin receptors.

2.3.8 GPCRs link inflammation to cancer immune evasion

Inflammation occurs as the immune system responds to infection and injury to beneficially remove the offending factors and restore tissue structure and physiological function. However, with subsequent tissue injury, cells that have sustained DNA damage or mutagenic assault will

continue to proliferate in microenvironments rich in inflammatory cells and growth/survival factors that support their growth. Prostaglandins are a group of physiologically-active lipid compounds found in almost every tissue in humans and animals, and they play a key role in the generation of an inflammatory response (65). They are enzymatically derived from arachidonic acid by the COX isoforms, COX1 and COX2, and are powerful vasodilators (66). PGE2 is the most abundant prostaglandin produced in cancers, and the prostanoid receptor family, which are GPCRs, includes the following: E prostanoid receptor 1 (EP1, PTGER1), EP2 (PTGER2), EP3 (PTGER3), and EP4 (PTGER4). Of these, EP1 is coupled to Gαq; EP3 is coupled to Gαi, and both EP2 and EP4 are coupled to Gαs (66). PGE2 binding to different EP receptors can regulate the function of many immune cell types, including macrophages, DCs, T cells, and B cells, as will be discussed here.

PGE2 produced by cancer cells has been linked to increased expression of FOXP3 in Treg cells, promoting the immune-suppressive activity of Tregs (67). In addition to Tregs, PGE2 has also been linked to increased recruitment of MDSCs (68), decreased CD8 T-cell activation (69,70), and increased expression of inhibitory markers, like PD-1 (68,69,71). PGE2 alters the differentiation, maturation, and cytokine secretion of DCs by up-regulating CD25 and indoleamine-pyrrole 2,3-dioxygenase and decreased expression of CD80, CD86, and MHCI maturation markers (72). Recently, NSAIDs that block COX2 and/or COX1 and COX2 were found to have beneficial effects on reducing the risk of developing esophageal, stomach, skin, and breast cancers, in addition to their best-established function in preventing colorectal cancer (73,74). Hence, EP receptors may represent exciting targets for cancer immune prevention and treatment.

2.4 Discussion

Emerging studies have begun to explain the functional impact of GNAS mutations. In 1991, GNAS mutations were discovered in McCune-Albright syndrome and pituitary tumors (75). In cancer, GNAS has been linked to pro-inflammatory functions, which could mimic the impact of

chronic inflammation on tumor development. Gαs is well-documented to mediate the effects of inflammatory mediators like cyclooxygenase (COX) 2-derived prostaglandins. Its inflammatory role in cancer is best shown in colon neoplasia where COX2-derived prostaglandin E2 (PGE2) enhances colon cancer progression via activation of PI3K and AKT and relieving the inhibitory phosphorylation of β-catenin as part of Gαs oncogenic signaling (76). Activating mutations in GNAS have also been found in gastric adenocarcinomas, leading to activation of the Wnt/β-catenin signaling pathway (77).

Mutations in GNAQ and GNA11 are most relevant in uveal melanoma (UVM) incidence, as 93% of patients harbor mutations in these genes encoding constitutively active Gαq family members (78,79). All cancer mutations in Gαq or Gα11 occur at either glutamine 209 or, in a smaller proportion, arginine 183 (Gln-209 and Arg-183, respectively; Arg-183 is the identical position to Arg-201 in Gαs) (78,79). Mutations affecting Gln- 209 in GNAQ or GNA11 are present in most primary UVM lesions and their metastases (79). Mutated residues impair GTPase activity (diminish GTP hydrolysis), which ultimately leads to prolonged signaling. Although initial studies supported a role of ERK signaling in UVM development, targeting this pathway did not improve the survival of UVM metastatic patients (80). Instead, our genome-wide RNAi screens revealed that the noncanonical activation of RhoGEFs, specifically TRIO, by Gαq mediates UVM progression (81). Furthermore, we discovered that the activation of YAP, the most downstream target of the Hippo pathway, by the novel TRIO–RHO signaling arm is essential for UVM, thus identifying a druggable target downstream from mutated Gαq (81).

GNAQ mutations are also associated with a smaller proportion of skin cutaneous melanoma (SKCM) and have been recently described in vascular tumors, such as hemangiomas and angiosarcomas (82,83). GNAQ R183Q mutations are also specifically responsible for a frequent congenital neurocutaneous disorder characterized by port wine skin lesions that are vascularly-derived, which is known as Sturge-Weber syndrome (84). Thus, mutations in GNAQ

appear to be responsible for numerous disease conditions for which there are no current targeted therapeutic options.

Mutations in GNA13 have been characterized in both liquid and solid tumors and are present at high frequency in bladder carcinoma. In addition, recent genome-wide sequencing efforts have unveiled the presence of frequent mutations in GNA13 in lymphomas, specifically Burkitt's lymphoma and diffuse large B-cell lymphoma (DLBCL) (85-87). These mutations in GNA13 as well as in RhoA, a downstream target of Gα13, have been shown to be inhibitory in nature, suggesting a tumor-suppressive role for Gα13 and RhoA in Burkitt's lymphoma and DLBCL (85). In this case, loss–of–function (LOF) mutations rather than gain–of–function (GOF) mutations underlie the oncogenic activity of GNA13, likely by disrupting the normal differentiation program of B cells (85). In contrast, WT GNA13 overexpression has been implicated in many solid tumors, such as in gastric cancer (88), nasopharyngeal carcinoma (89), prostate cancer (90), and breast cancer (91). Furthermore, GNA13 levels modulate drug resistance and tumor-initiation phenotypes in patient-derived head and neck squamous cell carcinoma cells in vitro and in vivo (92). In this case, GNA13 or GNA12 overexpression may enhance the proliferative and pro-migratory function of multiple GPCRs that converge to activate these G protein α subunits. A causal role of excessive Gα12 signaling may be elucidated by a use of a recently developed Gα12-coupled chemogenetic designer GPCR (Designer Recep- tors Exclusively Activated by Designer Drugs (DREADD)) (34).

Mutations in Gα subunits are infrequent, and yet activating mutations in Gβ1 and Gβ2 (GNB1 and GNB2, respectively) has been identified in myeloid and B-cell neoplasms, which act as an oncogenic driver and confer resistance to kinase inhibitors targeting typically mutated kinases in these malignancies, including BCR–ABL, BRAF, and JAK2 (93). Certainly, this information suggests that other Gα subunit mutations may also harbor tumorigenic potential.

A particular challenge when analyzing the potential impact of cancer mutations is that longer genes exhibit a higher number of mutations, which would achieve statistical significance (MutSig2CV analysis) only when higher than the background mutation rate of individual lesions. This is well-exemplified by GPR98, which is the most frequently mutated GPCR across all cancer types and, concomitantly, is the GPCR with the highest number of amino acids. GPR98 is an adhesion receptor, and its ligand and physiological functions are currently poorly understood. GPR98 mutations are known to cause febrile seizures and one form of Usher syndrome, the most common genetic cause of combined blindness and deafness (94,95). GPR98 has been shown to have significant association with glioblastoma (GBM) (96) and lymphoblastic leukemia (97), and the evaluation of the impact of GPR98 mutations in cancer warrants further investigation. The family of metabotropic glutamate GPCRs, GRM1– 8, are also frequently mutated in many cancer cohorts. Mutations of GRM1, GRM5, and GRM3 have been shown in breast cancer and melanoma (98-100). In addition, their transforming potential and increased secretion of their ligand, glutamate, by the tumor microenvironment makes the GRM receptor family an intriguing area of study.

Given the emerging studies supporting the notion that aberrant GPCR activity leads to tumor initiation and progression, we expect that the emerging mutational information will guide new cancer-relevant studies addressing each of these frequently mutated GPCRs. Given that many ligands of GPCRs may be produced in significantly higher amounts in the hypoxic, metabolic, and acidic tumor microenvironment, the tumorigenic synergism between ligand availability and activating mutations in receptors should also be explored.

GPR132 (also known as G2A) was previously shown to have tumor suppressor properties, as it prevents oncogenic transformations of pre-B cells by the BCR–ABL oncogene, similar to the role of GNA13 in these cell types (101). However, GPR132 has been shown to be highly transforming in fibroblasts (102). Thus, proton-sensing GPCRs may display tumor-promoting or

suppressive functions depending on the cancer cell of origin and may also display pro-tumorigenic activity when activated in the tumor stroma (31).

The leucine-rich repeat-containing GPCRs (LGR) LGRs 4 – 8 are known for their role in development, bone formation, and remodeling, but LGR4 and LGR5 are also up-regulated in several cancer types (103). These receptors are expressed in multiple tissue-resident stem cells, and their overexpression may reflect the expansion of this cellular compartment as well as the establishment of cancer stem cell niches (103). Overexpression of LGR4 and LGR5 in colon and ovarian tumors most likely enhances cell proliferation and metastasis (104,105).

The ability of pro- teases to degrade extracellular matrices and to activate PARs render them important in the facilitation of tumor growth and metastasis (106,107). Overexpression of F2RL1 has been linked to some of the most diagnosed cancers, including lung, breast, colon, and pancreatic cancers (106,108,109). Functionally, PAR2 has also been linked to cancer cell migration and stimulates vascular endothelial growth factor (VEGF) production for angiogenesis (110,111).

PGE2 plays a critical role in epithelial regeneration following tissue injury and cancer growth, which occurs via PI3K/Akt and β-catenin pathways (76,112). COX2 overexpression and enhanced PGE2 production is most notable in colorectal cancer, and COX2 blockade can help explain the cancer chemopreventive activity of aspirin and other nonsteroidal anti-inflammatory drugs (NSAIDs) (113). However, direct roles for PGE2 in tumorigenesis have been demonstrated for many other human malignancies, including breast, lung, liver, and gastric cancers, among others. For example, in laboratory models of breast and gastric cancers, COX2 overexpression and alterations in Wnt signaling both led to increased tumorigenesis (114,115). Moreover, EP3 has been shown to be involved in angiogenesis in lung cancer cell lines by increasing VEGF and metalloproteinase-9 (MMP-9) expression (116).

Chapter 2, in full, has been accepted for publication of the material in “Illuminating the Onco-GPCRome: Novel G protein-coupled receptor-driven oncocrine networks and targets for

cancer immunotherapy" in *Journal of Biological Chemistry*, 2019. Victoria H. Wu, Huwate Yeerna, Nijiro Nohata, Joshua Chiou, Olivier Harismendy, Francesco Raimondi, Asuka Inoue, Rob Russell, Pablo Tamayo, and J. Silvio Gutkind. The dissertation author was the primary investigator and author of this paper.

2.5 Figures

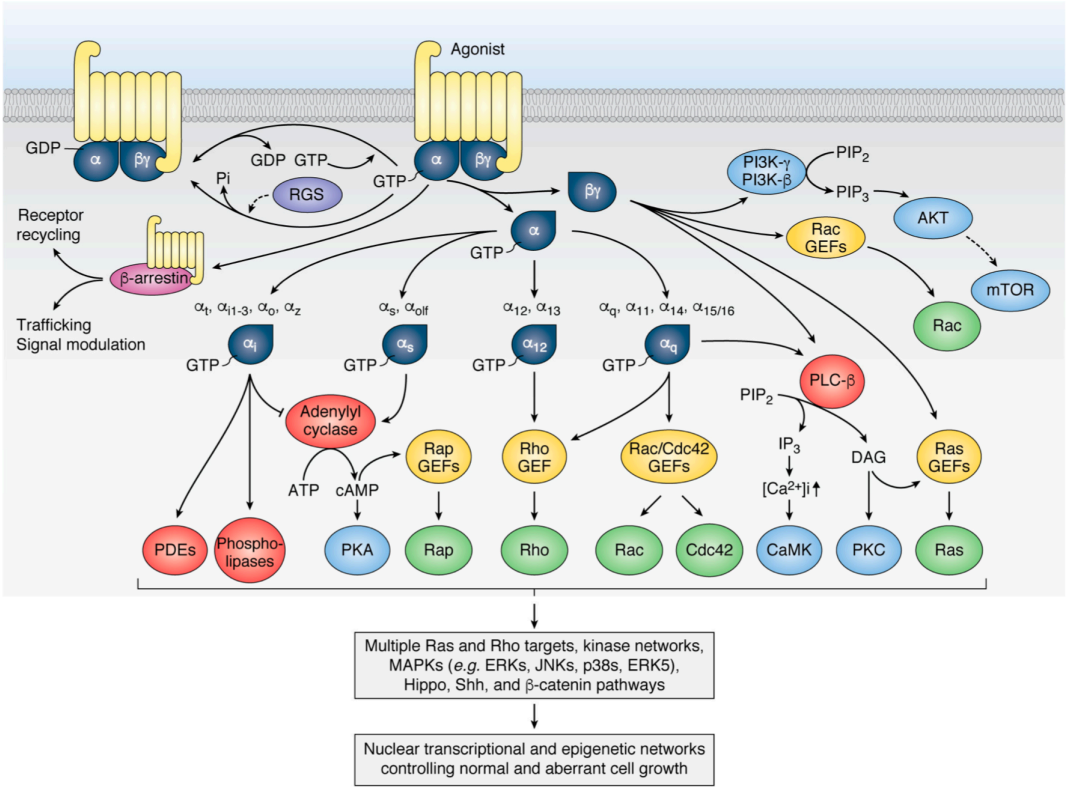

Figure 2.1. GPCR signaling.

Agonist-activated GPCRs promote the dissociation of GDP bound to the α subunit of heterotrimeric G proteins and its replacement by GTP. Gα and Gβγ subunits can then activate numerous downstream effectors. The 16 human G protein subunits can be divided into the four subfamilies, and a single GPCR can couple to one or more families of Gα subunits. Downstream effectors regulated by their targets include a variety of second messenger systems (red), GEFs (yellow), and Rho and Ras GTPases (green), which will result in the stimulation of multiple kinase cascades (blue) regulating key cellular functions. These include members of the MAPK, AKT, and mTOR, second messenger regulated kinases and phosphatases, and multiple kinases regulated by Rho and Ras GTPases. In addition, Gαs-coupled receptors inhibit and Gα12/13-, Gαi-, and Gαq/11-coupled receptors activate the transcription coactivator YAP and its related protein TAZ, the most downstream targets of the Hippo kinase cascade, as well as β-catenin and the Shh pathway, among others. Ultimately, these large numbers of effector molecules can have multiple effects in the cytosol and nucleus to regulate gene expression, cell metabolism, migration, proliferation, and survival by GPCRs, which can contribute to normal and malignant cell growth. See text for details.

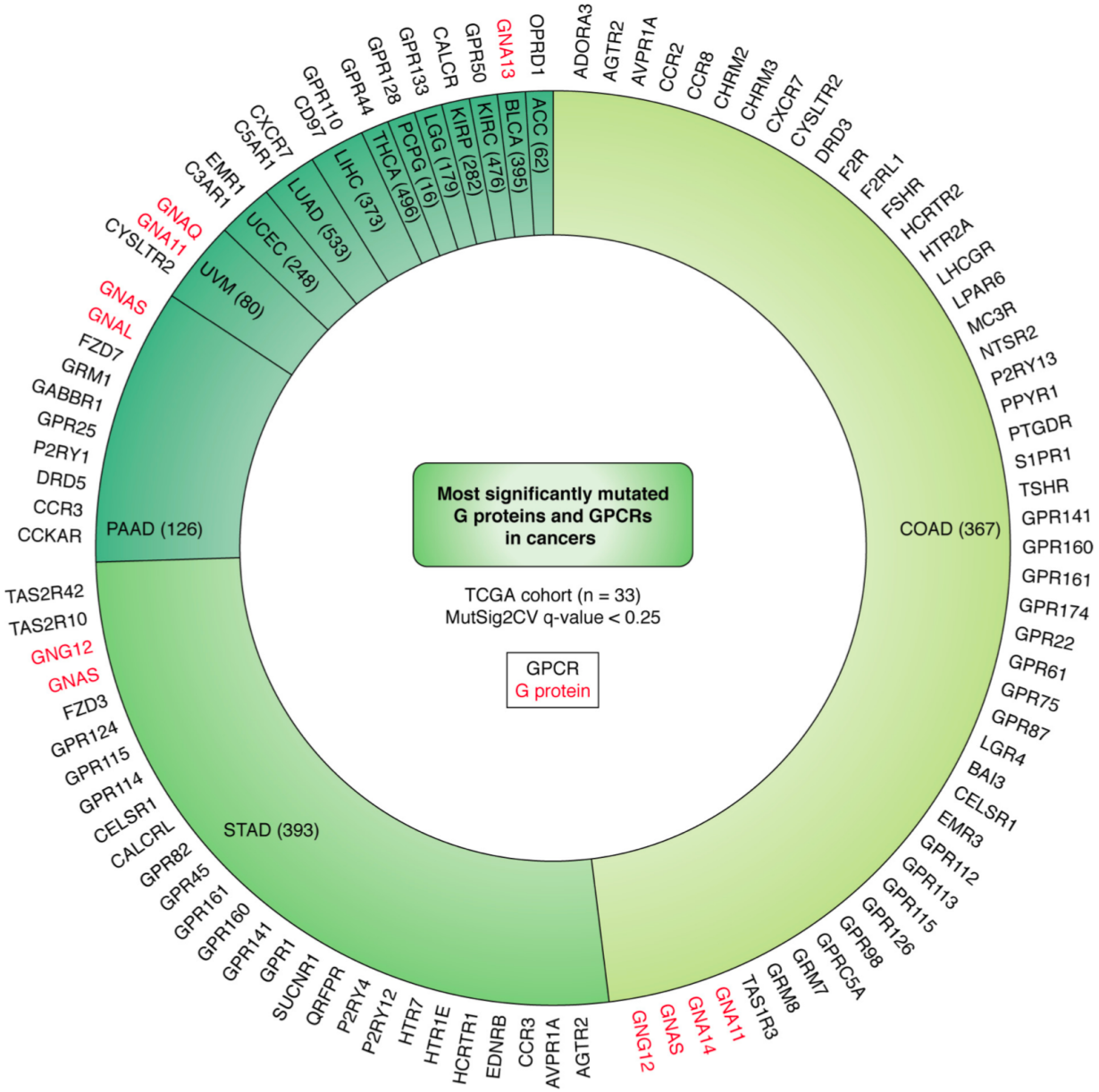

Figure 2.2. Top significant mutations of GPCRs and G proteins in cancer.

From MutSig2CV analysis, the proportion of TCGA cohorts (sample number) with highly-significant (MutSig2CV q-value <0.25) mutations in genes encoding GPCRs (black) and G proteins (red) are shown. The statistically significant mutated genes for each cohort are plotted outside of the pie; cohorts are colored based on number of significant genes.

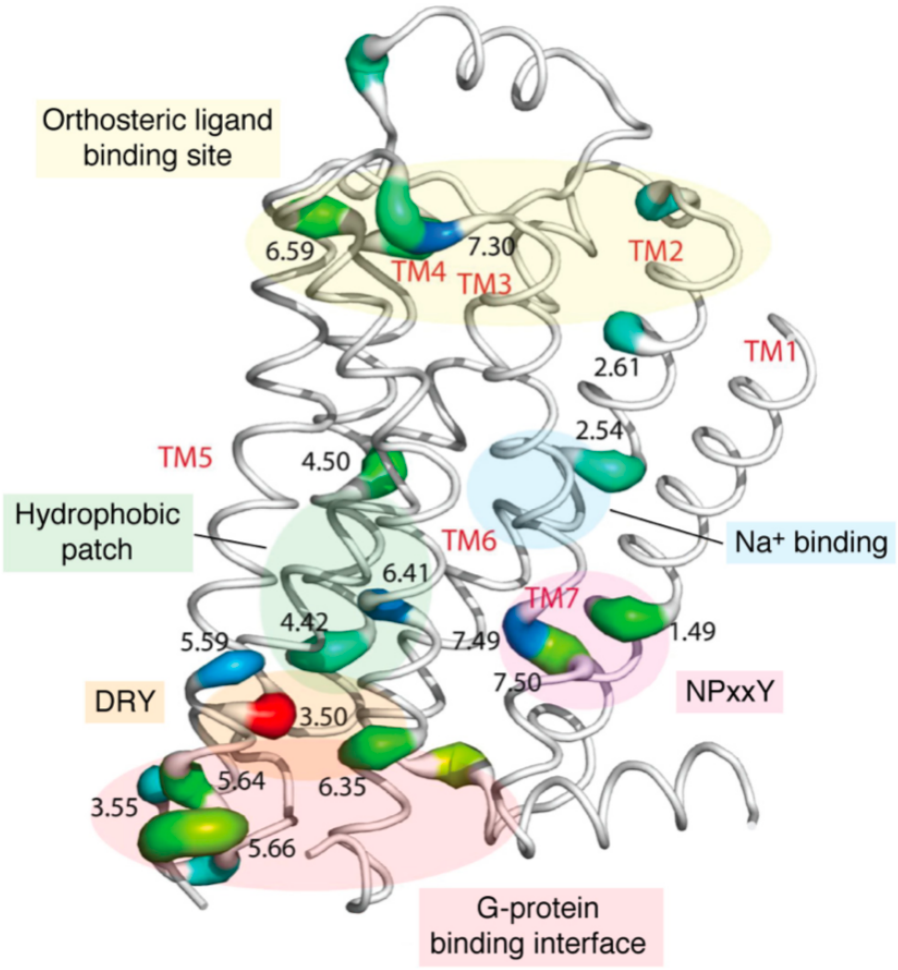

Figure 2.3. Significantly mutated genes in 7TM positions.

3D “putty” drawing of most mutated 7TM positions in significantly mutated genes from the TCGA database is shown. A prototypical GPCR structure (i.e. ADRB2, Protein Data Bank code 3NYA) is used for representation. Cartoon diameter and coloring (blue to red) are directly proportional to the number of unique samples carrying mutations at given 7TM positions. To identify these, mutated receptor sequences were aligned (using PFAM 7tm_1 Hidden Markov Model), and Ballesteros/Weinstein numberings were assigned (see Table S3). Conserved functional motives are highlighted and labeled.

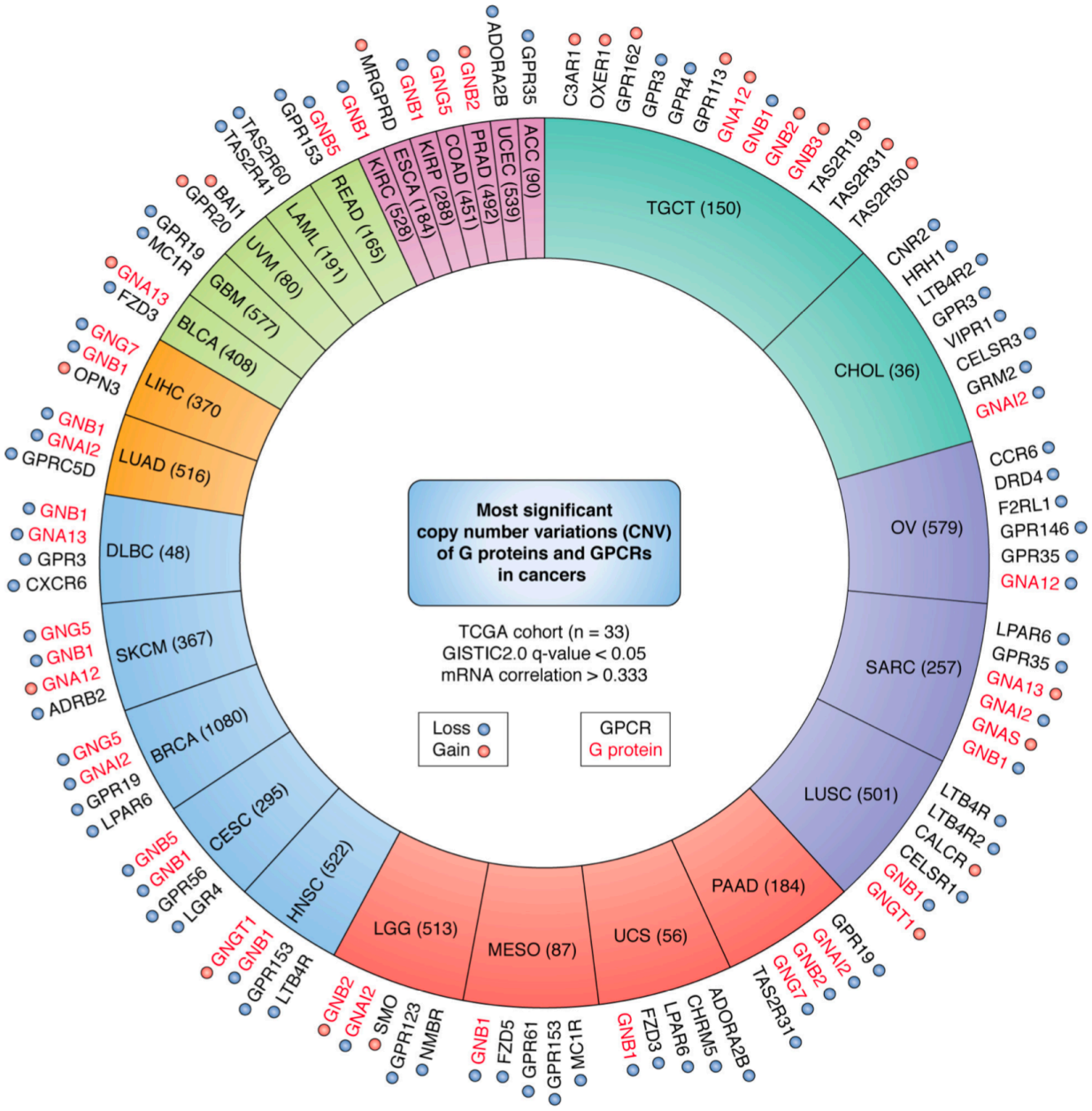

Figure 2.4. Top significant CNVs of GPCRs and G proteins in cancer.

From GISTIC analysis, the proportion of TCGA cohorts (sample number) with highly significant (GISTIC q-value <0.05 and mRNA correlation >0.333) CNVs in genes encoding GPCRs (black) and G proteins (red) are shown. The significant genes for each cohort are plotted outside of the cohort pie; cohorts are colored based on the number of significant genes, and amplification is denoted by red highlighting, and deletion is denoted by a blue highlighting.

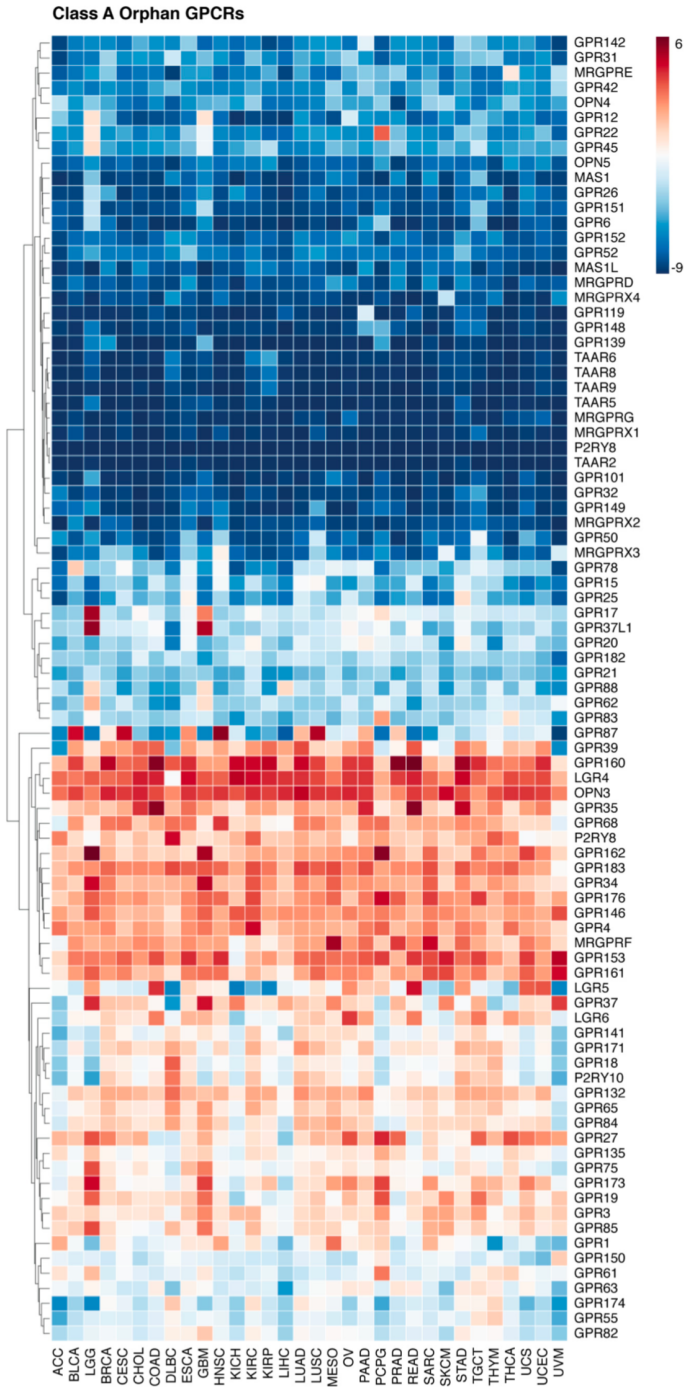

Figure 2.5. Expression of class A orphan receptors in cancer.

Gene expression for class A orphan GPCRs from the UCSC TCGA PanCan Cohort RNA-seq dataset is shown. Expression values are summarized by defining transcripts per million (TPM), which normalizes for both gene length and sequencing depth. Expression values are log2(TPM + 0.001) averaged within the primary tumor samples of each cancer. GPCRs are clustered based on similarity across cancer types.

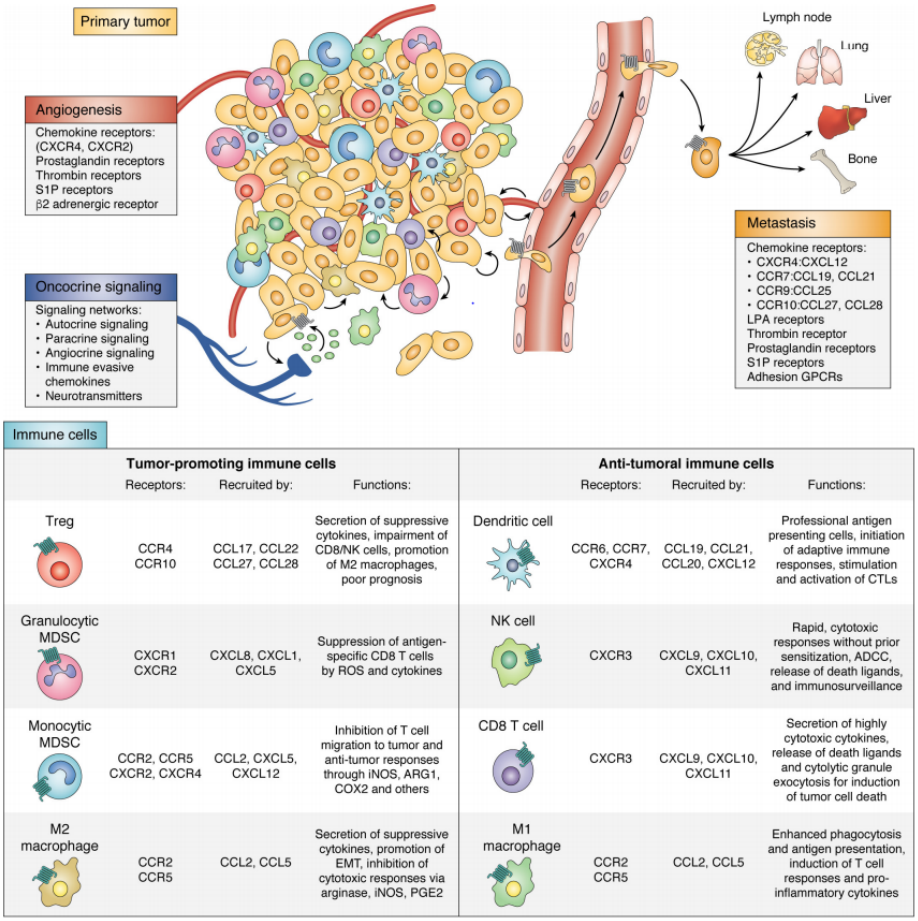

Figure 2.6. Function of GPCRs in cancer.

Top, GPCRs contribute to both tumor promotion, angiogenesis, metastasis, and immune evasive functions in the tumor microenvironment. Multiple GPCR agonists released by the tumors or accumulating in the tumor microenvironment promote angiogenesis by stimulating GPCRs on endothelial cells. GPCRs play multiple roles in cell communication between tumors cells, tumor stroma, endothelial cells, and blood vessels and immune cells, as well as in response to neurotransmitters released as a consequence of tumor-induced axonogenesis and tumor innervation as part of autocrine and paracrine (oncocrine) signaling networks that drive tumorigenesis. GPCRs present on tumor cells assist in extravasation and migration of circulating tumor cells to promote metastasis to distant organ destinations. Bottom, chemokine receptors recruit a variety of immune cells to the primary tumor and release agents that both promote and suppress immune functions. Immune-suppressive cells promote tumor growth by inhibiting functions of cytotoxic immune cells or secreting hypoxic and anti-inflammatory molecules to sculpt the suppressive tumor microenvironment. Anti-tumor immune cells that are recruited to the tumor secrete highly cytotoxic molecules for tumor cell destruction. See text for details. (Abbreviations used are as follows: ROS, reactive oxygen species; iNOS, inducible nitric-oxide synthase; ARG1, arginase 1; EMT, epithelial to mesenchymal transition; ADCC, antibody-dependent cellular cytotoxicity.

2.6 Supplementary Figures

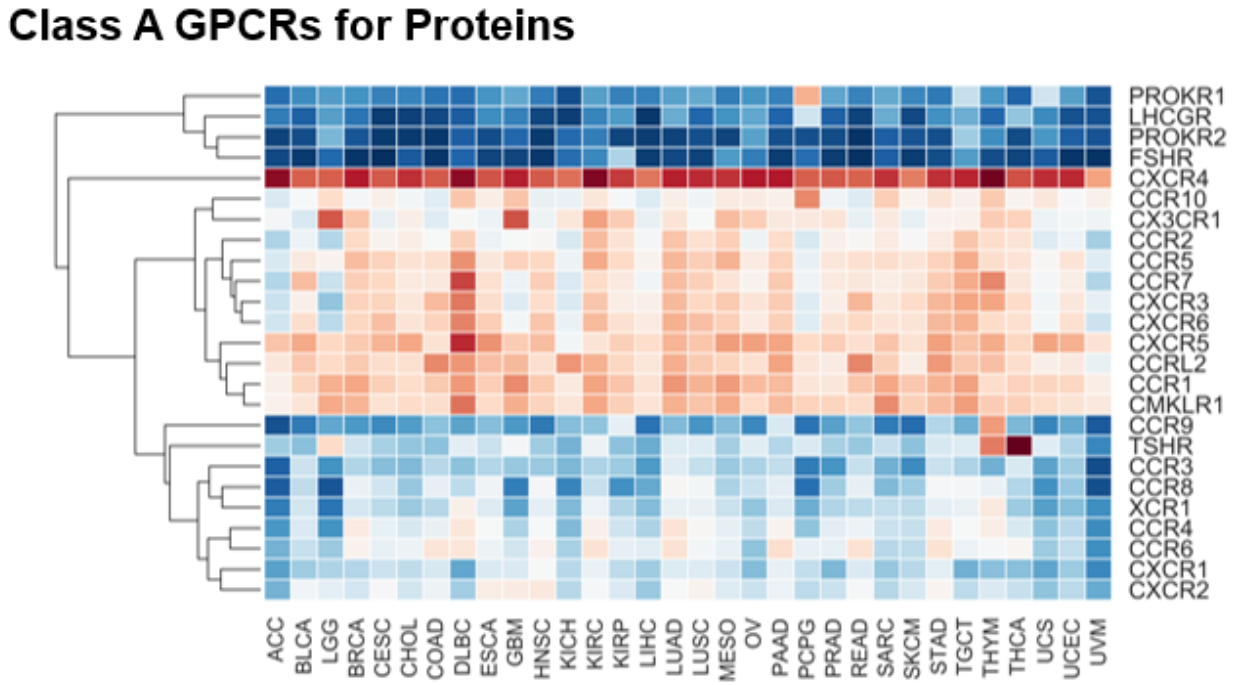

Figure S2.1. Relative expression of Class A GPCRs for proteins GPCRs across TCGA cancer types

Gene expression for class A GPCRs for proteins from the UCSC TCGA PanCan Cohort RNA-seq dataset is shown. Expression values are summarized by defining transcripts per million (TPM), which normalizes for both gene length and sequencing depth. Expression values are log2(TPM + 0.001) averaged within the primary tumor samples of each cancer. GPCRs are clustered based on similarity across cancer types.

Class A GPCRs for Peptides

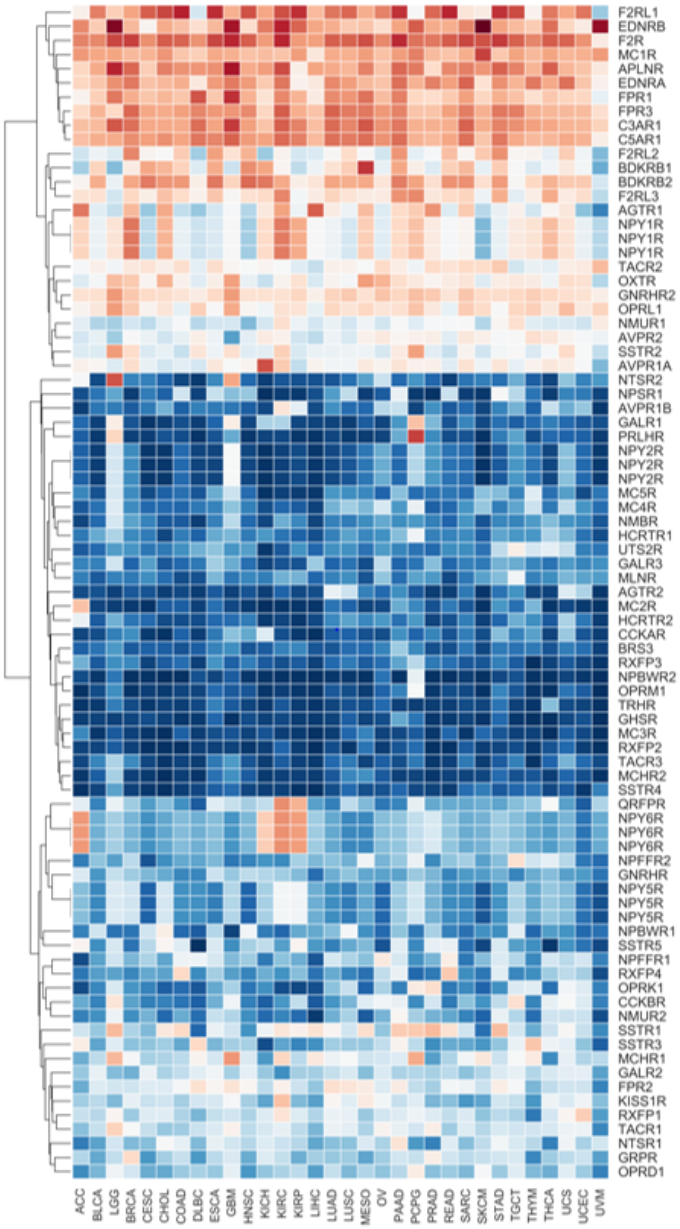

Figure S2.2. Relative expression of Class A GPCRs for peptides GPCRs across TCGA cancer types

Gene expression for class A GPCRs for peptides from the UCSC TCGA PanCan Cohort RNA-seq dataset is shown. Expression values are summarized by defining transcripts per million (TPM), which normalizes for both gene length and sequencing depth. Expression values are log2(TPM + 0.001) averaged within the primary tumor samples of each cancer. GPCRs are clustered based on similarity across cancer types.

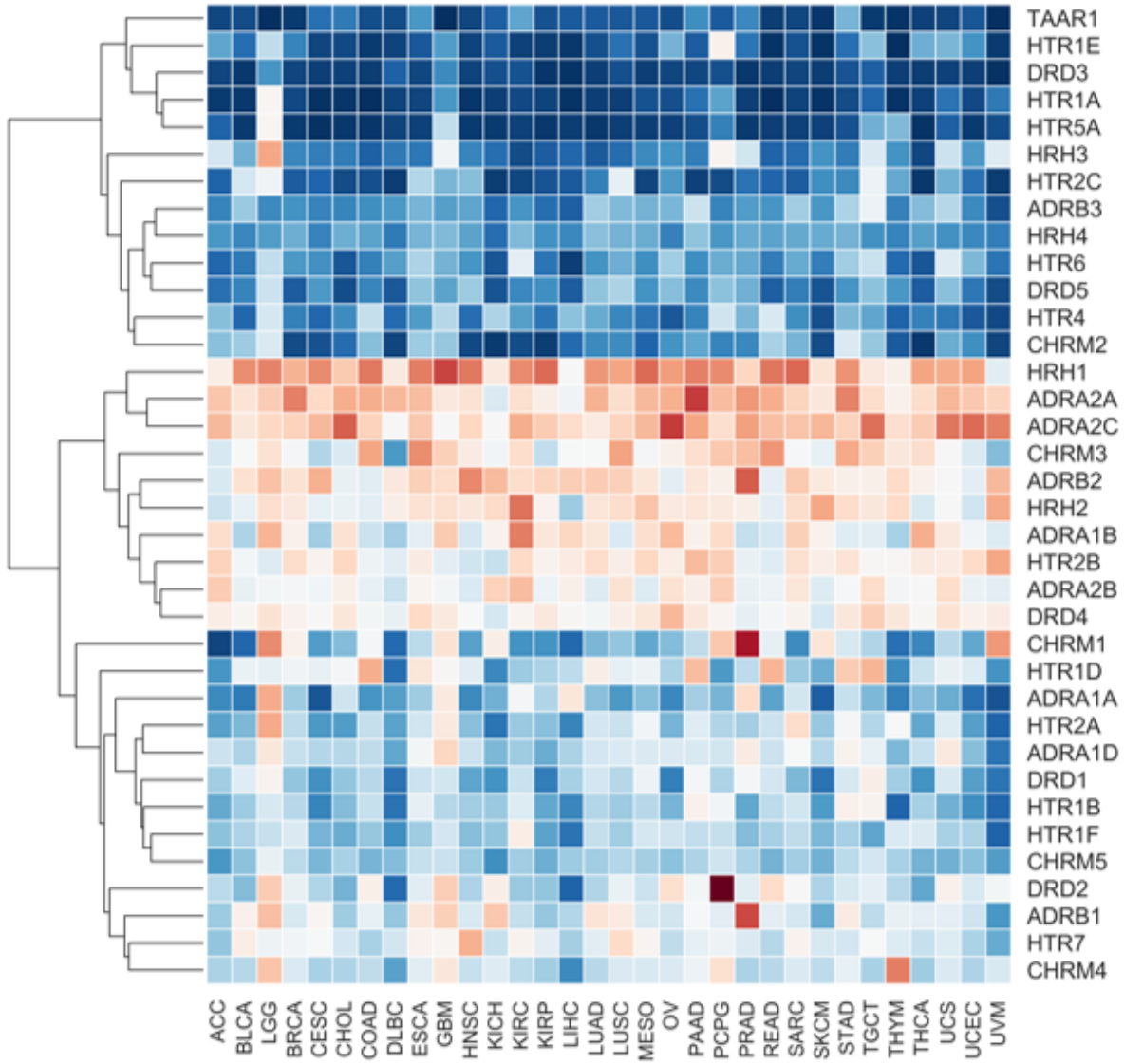

Figure S2.3. Relative expression of Class A aminergic GPCRs across TCGA cancer types

Gene expression for class A aminergic GPCRs from the UCSC TCGA PanCan Cohort RNA-seq dataset is shown. Expression values are summarized by defining transcripts per million (TPM), which normalizes for both gene length and sequencing depth. Expression values are log2(TPM + 0.001) averaged within the primary tumor samples of each cancer. GPCRs are clustered based on similarity across cancer types.

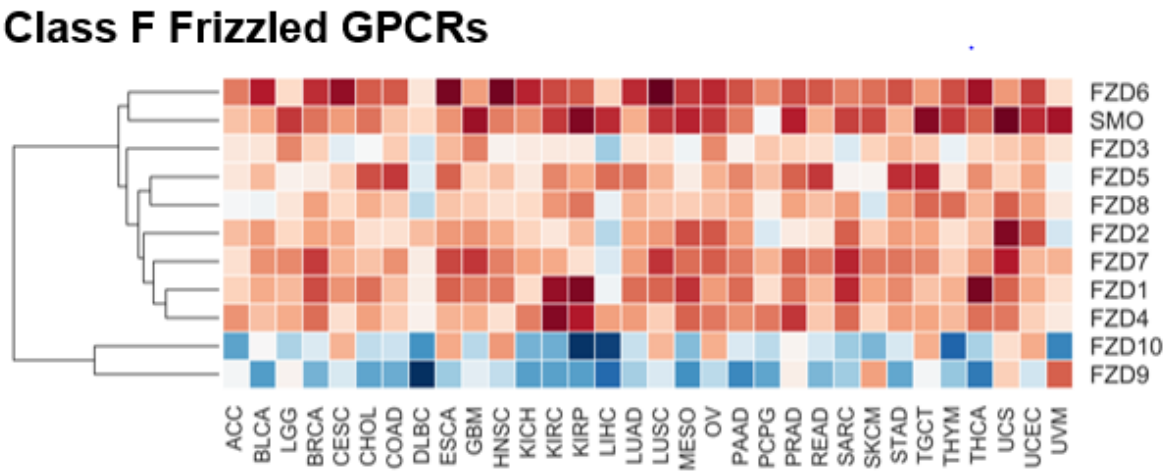

Figure S2.4. Relative expression of Class F Frizzled GPCRs across TCGA cancer types

Gene expression for class F Frizzled GPCRs from the UCSC TCGA PanCan Cohort RNA-seq dataset is shown. Expression values are summarized by defining transcripts per million (TPM), which normalizes for both gene length and sequencing depth. Expression values are log2(TPM + 0.001) averaged within the primary tumor samples of each cancer. GPCRs are clustered based on similarity across cancer types.

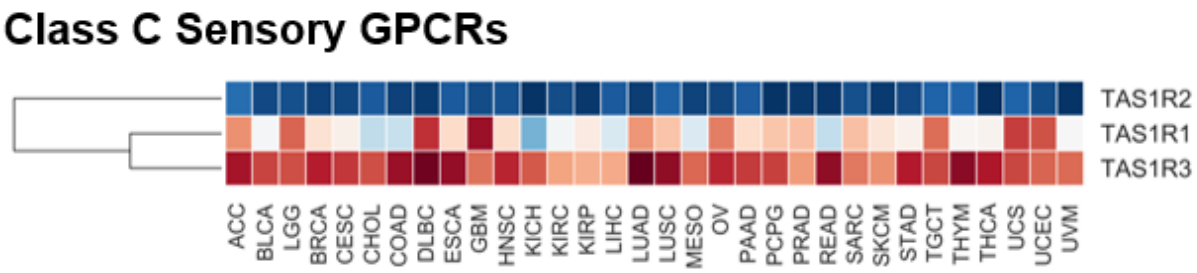

Figure S2.5. Relative expression of Class C Sensory GPCRs across TCGA cancer types

Gene expression for class C Sensory GPCRs from the UCSC TCGA PanCan Cohort RNA-seq dataset is shown. Expression values are summarized by defining transcripts per million (TPM), which normalizes for both gene length and sequencing depth. Expression values are log2(TPM + 0.001) averaged within the primary tumor samples of each cancer. GPCRs are clustered based on similarity across cancer types.

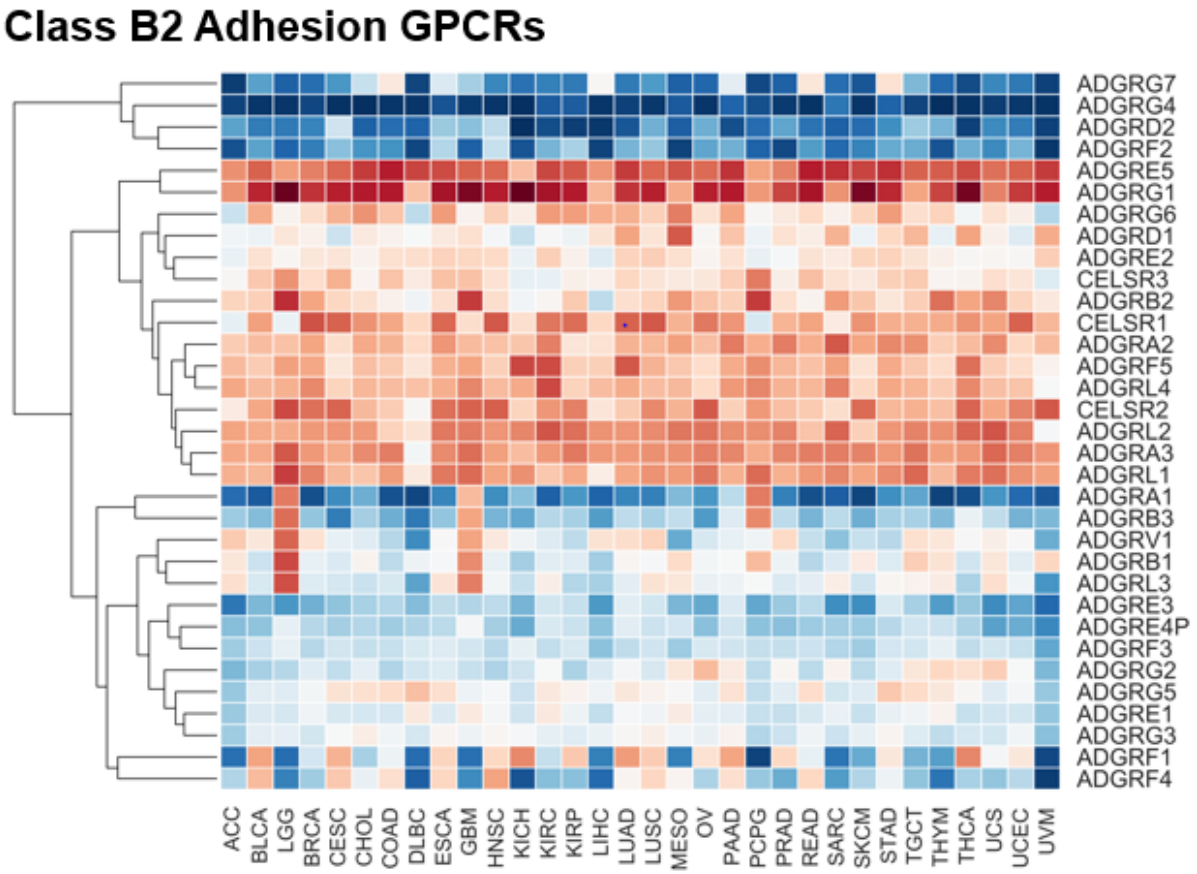

Figure S2.6. Relative expression of Class B2 adhesion GPCRs across TCGA cancer types

Gene expression for class B2 adhesion GPCRs from the UCSC TCGA PanCan Cohort RNA-seq dataset is shown. Expression values are summarized by defining transcripts per million (TPM), which normalizes for both gene length and sequencing depth. Expression values are log2(TPM + 0.001) averaged within the primary tumor samples of each cancer. GPCRs are clustered based on similarity across cancer types.

2.7 Tables

Table 2.1 G Proteins and GPCR genes

Abbreviation	Cancer Type
LAML	Acute Myeloid Leukemia
ACC	Adrenocortical carcinoma
BLCA	Bladder Urothelial Carcinoma
LGG	Brain Lower Grade Glioma
BRCA	Breast invasive carcinoma
CESC	Cervical squamous cell carcinoma and endocervical adenocarcinoma
CHOL	Cholangiocarcinoma
COAD	Colon adenocarcinoma
DLBC	Diffuse large B cell lymphoma
ESCA	Esophageal carcinoma
GBM	Glioblastoma multiforme
HNSC	Head and Neck squamous cell carcinoma
KICH	Kidney Chromophobe
KIRC	Kidney renal clear cell carcinoma
KIRP	Kidney renal papillary cell carcinoma
LIHC	Liver hepatocellular carcinoma
LUAD	Lung adenocarcinoma
LUSC	Lung squamous cell carcinoma
MESO	Mesothelioma
OV	Ovarian serous cystadenocarcinoma
PAAD	Pancreatic adenocarcinoma
PCPG	Pheochromocytoma and Paraganglioma
PRAD	Prostate adenocarcinoma
READ	Rectum adenocarcinoma
SARC	Sarcoma
SKCM	Skin Cutaneous Melanoma
STAD	Stomach adenocarcinoma
TGCT	Testicular Germ Cell Tumors
THYM	Thymoma
THCA	Thyroid carcinoma
UCS	Uterine Carcinosarcoma
UCEC	Uterine Corpus Endometrial Carcinoma
UVM	Uveal Melanoma

Table 2.2. Significantly mutated GPCRs in cancer (MutSig2CV)
q-value < 0.25

Cohort	Gene	q-value	Frequency (%)
ACC	*OPRD1*	3.56E-05	20.97%
COAD	*P2RY13*	1.11E-05	4.63%
COAD	*CYSLTR2*	0.000472768	4.90%
COAD	*PTGDR*	0.000538427	1.91%
COAD	*HTR2A*	0.001053684	5.99%
COAD	*LHCGR*	0.002315267	7.63%
COAD	*F2RL1*	0.003449761	2.72%
COAD	*TSHR*	0.00400722	13.90%
COAD	*CCR2*	0.005056044	2.45%
COAD	*CHRM2*	0.006076699	7.08%
COAD	*HCRTR2*	0.02244983	3.00%
COAD	*ADORA3*	0.02318246	4.09%
COAD	*AGTR2*	0.03024169	4.36%
COAD	*CCR8*	0.06467115	2.72%
COAD	*LPAR6*	0.07117763	2.45%
COAD	*FSHR*	0.08378402	5.18%
COAD	*PPYR1*	0.08815879	1.36%
COAD	*CHRM3*	0.09655267	4.90%
COAD	*CXCR7*	0.1261582	5.99%
COAD	*F2R*	0.1482772	4.36%
COAD	*MC3R*	0.1644041	5.45%
COAD	*NTSR2*	0.1659019	2.18%
COAD	*S1PR1*	0.1677213	3.27%
COAD	*AVPR1A*	0.1691768	4.36%
COAD	*DRD3*	0.236229	2.18%
COAD	*GPR174*	0.00099668	2.18%
COAD	*GPR87*	0.005206213	2.72%
COAD	*GPR141*	0.007351373	3.54%
COAD	*GPR75*	0.0127943	3.00%
COAD	*GPR22*	0.01728688	3.00%
COAD	*GPR161*	0.09250785	3.54%
COAD	*GPR61*	0.1963423	2.72%
COAD	*GPR160*	0.2046627	1.63%
COAD	*LGR4*	0.2132763	4.63%
COAD	*GPR112*	0.005092901	12.26%
COAD	*GPR115*	0.01545525	5.72%
COAD	*BAI3*	0.02382248	13.62%
COAD	*GPR126*	0.03070161	5.18%
COAD	*EMR3*	0.05560063	5.72%
COAD	*GPR98*	0.06315749	21.25%
COAD	*GPR113*	0.07351878	5.45%
COAD	*CELSR1*	0.1498409	8.45%
COAD	*GRM7*	0.005207256	8.17%
COAD	*GRM8*	0.005207256	7.36%
COAD	*GPRC5A*	0.2197412	1.91%
COAD	*TAS1R3*	0.2227904	1.91%
KIRC	*GPR50*	0.0496251	0.63%

Table 2.2. Significantly mutated GPCRs in cancer (MutSig2CV) q-value < 0.25, continued.

Cohort	Gene	q-value	Frequency (%)
LGG	*CALCR*	0.1331555	1.06%
LIHC	*GPR133*	0.1736967	0.97%
LIHC	*GPR110*	0.01166817	1.88%
LUAD	*CD97*	0.1084244	1.88%
LUAD	*CXCR7*	0.09869265	2.63%
PAAD	*C5AR1*	0.1908224	1.69%
PAAD	*CCR3*	0.001406141	3.17%
PAAD	*CCKAR*	0.001833062	3.17%
PAAD	*P2RY1*	0.001902382	4.76%
PAAD	*DRD5*	0.03199904	3.97%
PAAD	*GPR25*	3.66E-08	3.97%
PAAD	*GABBR1*	8.13E-05	7.94%
PAAD	*GRM1*	0.09842003	7.14%
PCPG	*FZD7*	0.07270165	4.76%
STAD	*GPR128*	0.1014237	2.23%
STAD	*HTR7*	0.005851123	4.07%
STAD	*EDNRB*	0.01163884	8.14%
STAD	*HTR1E*	0.01927706	3.82%
STAD	*P2RY4*	0.02174705	3.31%
STAD	*QRFPR*	0.03319128	3.31%
STAD	*HCRTR1*	0.1254579	2.04%
STAD	*SUCNR1*	0.1514292	1.02%
STAD	*AVPR1A*	0.184545	4.33%
STAD	*P2RY12*	0.1849948	2.80%
STAD	*AGTR2*	0.2158861	1.53%
STAD	*CCR3*	0.2263208	3.05%
STAD	*GPR141*	0.006552625	3.05%
STAD	*GPR161*	0.009878479	3.56%
STAD	*GPR82*	0.0130167	2.29%
STAD	*GPR160*	0.02612271	2.04%
STAD	*GPR45*	0.03595802	5.09%
STAD	*GPR1*	0.05628878	1.53%
STAD	*CALCRL*	0.03494575	2.54%
STAD	*CELSR1*	0.000118461	11.20%
STAD	*GPR124*	0.05187925	4.58%
STAD	*GPR114*	0.07458871	3.31%
STAD	*GPR115*	0.1809458	2.04%
STAD	*FZD3*	1.49E-05	3.56%
STAD	*TAS2R10*	0.004125855	1.53%
THCA	*TAS2R42*	0.00449062	1.53%
UCEC	*GPR44*	5.84E-07	0.81%
UCEC	*C3AR1*	0.1401939	2.82%
UVM	*EMR1*	0.1890719	5.65%
	CYSLTR2	0.005856445	3.75%

Table 2.3. Significantly mutated G Proteins in cancer (MutSig2CV)
q-value < 0.25

Cohort	Gene	q-value	Frequency (%)
UVM	*GNA11*	6.08E-13	45.00%
UVM	*GNAQ*	6.08E-13	50.00%
STAD	*GNG12*	2.05E-10	3.31%
PAAD	*GNAS*	0.00095559	7.14%
BLCA	*GNA13*	0.00281375	3.54%
COAD	*GNAS*	0.00344976	9.81%
COAD	*GNA11*	0.01406654	2.45%
PAAD	*GNAL*	0.01769679	2.38%
COAD	*GNA14*	0.02929533	3.54%
COAD	*GNG12*	0.1012602	2.18%
STAD	*GNAS*	0.1662342	9.16%

2.8 References

1. Fredriksson, R., Lagerstrom, M. C., Lundin, L. G., and Schioth, H. B. (2003) The G-protein-coupled receptors in the human genome form five main families. Phylogenetic analysis, paralogon groups, and fingerprints. *Mol Pharmacol* **63**, 1256-1272
2. Pierce, K. L., Premont, R. T., and Lefkowitz, R. J. (2002) Seven-transmembrane receptors. *Nature reviews. Molecular cell biology* **3**, 639-650
3. O'Hayre, M., Degese, M. S., and Gutkind, J. S. (2014) Novel insights into G protein and G protein-coupled receptor signaling in cancer. *Current opinion in cell biology* **27**, 126-135
4. Dorsam, R. T., and Gutkind, J. S. (2007) G-protein-coupled receptors and cancer. *Nat Rev Cancer* **7**, 79-94
5. Vaque, J. P., Dorsam, R. T., Feng, X., Iglesias-Bartolome, R., Forsthoefel, D. J., Chen, Q., Debant, A., Seeger, M. A., Ksander, B. R., Teramoto, H., and Gutkind, J. S. (2013) A genome-wide RNAi screen reveals a Trio-regulated Rho GTPase circuitry transducing mitogenic signals initiated by G protein-coupled receptors. *Molecular cell* **49**, 94-108
6. Chikumi, H., Vazquez-Prado, J., Servitja, J. M., Miyazaki, H., and Gutkind, J. S. (2002) Potent activation of RhoA by Galpha q and Gq-coupled receptors. *J Biol Chem* **277**, 27130-27134
7. Chen, X., Wu, Q., Depeille, P., Chen, P., Thornton, S., Kalirai, H., Coupland, S. E., Roose, J. P., and Bastian, B. C. (2017) RasGRP3 Mediates MAPK Pathway Activation in GNAQ Mutant Uveal Melanoma. *Cancer Cell* **31**, 685-696 e686
8. Vazquez-Prado, J., Basile, J., and Gutkind, J. S. (2004) Modular architecture and novel protein-protein interactions regulating the RGS-containing Rho guanine nucleotide exchange factors. *Methods in enzymology* **390**, 259-285
9. Hauser, A. S., Attwood, M. M., Rask-Andersen, M., Schioth, H. B., and Gloriam, D. E. (2017) Trends in GPCR drug discovery: new agents, targets and indications. *Nat Rev Drug Discov* **16**, 829-842
10. Santos, R., Ursu, O., Gaulton, A., Bento, A. P., Donadi, R. S., Bologa, C. G., Karlsson, A., Al-Lazikani, B., Hersey, A., Oprea, T. I., and Overington, J. P. (2017) A comprehensive map of molecular drug targets. *Nat Rev Drug Discov* **16**, 19-34
11. Hoadley, K. A., Yau, C., Hinoue, T., Wolf, D. M., Lazar, A. J., Drill, E., Shen, R., Taylor, A. M., Cherniack, A. D., Thorsson, V., Akbani, R., Bowlby, R., Wong, C. K., Wiznerowicz, M., Sanchez-Vega, F., Robertson, A. G., Schneider, B. G., Lawrence, M. S., Noushmehr, H., Malta, T. M., Cancer Genome Atlas, N., Stuart, J. M., Benz, C. C., and Laird, P. W. (2018) Cell-of-Origin Patterns Dominate the Molecular Classification of 10,000 Tumors from 33 Types of Cancer. *Cell* **173**, 291-304 e296
12. O'Hayre, M., Vazquez-Prado, J., Kufareva, I., Stawiski, E. W., Handel, T. M., Seshagiri, S., and Gutkind, J. S. (2013) The emerging mutational landscape of G proteins and G-protein-coupled receptors in cancer. *Nat Rev Cancer* **13**, 412-424
13. Lawrence, M. S., Stojanov, P., Polak, P., Kryukov, G. V., Cibulskis, K., Sivachenko, A., Carter, S. L., Stewart, C., Mermel, C. H., Roberts, S. A., Kiezun, A., Hammerman, P. S., McKenna, A., Drier, Y., Zou, L., Ramos, A. H., Pugh, T. J., Stransky, N., Helman, E., Kim, J., Sougnez, C., Ambrogio, L., Nickerson, E., Shefler, E., Cortes, M. L., Auclair, D., Saksena, G., Voet, D., Noble, M., DiCara, D., Lin, P., Lichtenstein, L., Heiman, D. I., Fennell, T., Imielinski, M., Hernandez, B., Hodis, E., Baca, S., Dulak, A. M., Lohr, J.,

Landau, D. A., Wu, C. J., Melendez-Zajgla, J., Hidalgo-Miranda, A., Koren, A., McCarroll, S. A., Mora, J., Crompton, B., Onofrio, R., Parkin, M., Winckler, W., Ardlie, K., Gabriel, S. B., Roberts, C. W. M., Biegel, J. A., Stegmaier, K., Bass, A. J., Garraway, L. A., Meyerson, M., Golub, T. R., Gordenin, D. A., Sunyaev, S., Lander, E. S., and Getz, G. (2013) Mutational heterogeneity in cancer and the search for new cancer-associated genes. *Nature* **499**, 214-218

14. Alexandrov, L. B., Nik-Zainal, S., Wedge, D. C., Aparicio, S. A., Behjati, S., Biankin, A. V., Bignell, G. R., Bolli, N., Borg, A., Borresen-Dale, A. L., Boyault, S., Burkhardt, B., Butler, A. P., Caldas, C., Davies, H. R., Desmedt, C., Eils, R., Eyfjord, J. E., Foekens, J. A., Greaves, M., Hosoda, F., Hutter, B., Ilicic, T., Imbeaud, S., Imielinski, M., Jager, N., Jones, D. T., Jones, D., Knappskog, S., Kool, M., Lakhani, S. R., Lopez-Otin, C., Martin, S., Munshi, N. C., Nakamura, H., Northcott, P. A., Pajic, M., Papaemmanuil, E., Paradiso, A., Pearson, J. V., Puente, X. S., Raine, K., Ramakrishna, M., Richardson, A. L., Richter, J., Rosenstiel, P., Schlesner, M., Schumacher, T. N., Span, P. N., Teague, J. W., Totoki, Y., Tutt, A. N., Valdes-Mas, R., van Buuren, M. M., van 't Veer, L., Vincent-Salomon, A., Waddell, N., Yates, L. R., Australian Pancreatic Cancer Genome, I., Consortium, I. B. C., Consortium, I. M.-S., PedBrain, I., Zucman-Rossi, J., Futreal, P. A., McDermott, U., Lichter, P., Meyerson, M., Grimmond, S. M., Siebert, R., Campo, E., Shibata, T., Pfister, S. M., Campbell, P. J., and Stratton, M. R. (2013) Signatures of mutational processes in human cancer. *Nature* **500**, 415-421

15. Vallar, L., Spada, A., and Giannattasio, G. (1987) Altered Gs and adenylate cyclase activity in human GH-secreting pituitary adenomas. *Nature* **330**, 566-568

16. Hu, Q., and Shokat, K. M. (2018) Disease-Causing Mutations in the G Protein Galphas Subvert the Roles of GDP and GTP. *Cell* **173**, 1254-1264 e1211

17. Alakus, H., Babicky, M. L., Ghosh, P., Yost, S., Jepsen, K., Dai, Y., Arias, A., Samuels, M. L., Mose, E. S., Schwab, R. B., Peterson, M. R., Lowy, A. M., Frazer, K. A., and Harismendy, O. (2014) Genome-wide mutational landscape of mucinous carcinomatosis peritonei of appendiceal origin. *Genome medicine* **6**, 43

18. Wu, J., Matthaei, H., Maitra, A., Dal Molin, M., Wood, L. D., Eshleman, J. R., Goggins, M., Canto, M. I., Schulick, R. D., Edil, B. H., Wolfgang, C. L., Klein, A. P., Diaz, L. A., Jr., Allen, P. J., Schmidt, C. M., Kinzler, K. W., Papadopoulos, N., Hruban, R. H., and Vogelstein, B. (2011) Recurrent GNAS mutations define an unexpected pathway for pancreatic cyst development. *Sci Transl Med* **3**, 92ra66

19. Patra, K. C., Kato, Y., Mizukami, Y., Widholz, S., Boukhali, M., Revenco, I., Grossman, E. A., Ji, F., Sadreyev, R. I., Liss, A. S., Screaton, R. A., Sakamoto, K., Ryan, D. P., Mino-Kenudson, M., Castillo, C. F., Nomura, D. K., Haas, W., and Bardeesy, N. (2018) Mutant GNAS drives pancreatic tumourigenesis by inducing PKA-mediated SIK suppression and reprogramming lipid metabolism. *Nat Cell Biol* **20**, 811-822

20. Ideno, N., Yamaguchi, H., Ghosh, B., Gupta, S., Okumura, T., Steffen, D. J., Fisher, C. G., Wood, L. D., Singhi, A. D., Nakamura, M., Gutkind, J. S., and Maitra, A. (2018) GNAS(R201C) Induces Pancreatic Cystic Neoplasms in Mice That Express Activated KRAS by Inhibiting YAP1 Signaling. *Gastroenterology* **155**, 1593-1607 e1512

21. Raimondi, F., Inoue, A., Kadji, F. M. N., Shuai, N., Gonzalez, J. C., Singh, G., de la Vega, A. A., Sotillo, R., Fischer, B., Aoki, J., Gutkind, J. S., and Russell, R. B. (2019) Rare, functional, somatic variants in gene families linked to cancer genes: GPCR signaling as a paradigm. *Oncogene* **38**, 6491-6506

22. Rosenbaum, D. M., Rasmussen, S. G., and Kobilka, B. K. (2009) The structure and function of G-protein-coupled receptors. *Nature* **459**, 356-363

23. Thal, D. M., Glukhova, A., Sexton, P. M., and Christopoulos, A. (2018) Structural insights into G-protein-coupled receptor allostery. *Nature* **559**, 45-53

24. Maiga, A., Lemieux, S., Pabst, C., Lavallee, V. P., Bouvier, M., Sauvageau, G., and Hebert, J. (2016) Transcriptome analysis of G protein-coupled receptors in distinct genetic subgroups of acute myeloid leukemia: identification of potential disease-specific targets. *Blood cancer journal* **6**, e431

25. Rybaczyk, L., Rozmiarek, A., Circle, K., Grants, I., Needleman, B., Wunderlich, J. E., Huang, K., and Christofi, F. L. (2009) New bioinformatics approach to analyze gene expressions and signaling pathways reveals unique purine gene dysregulation profiles that distinguish between CD and UC. *Inflammatory bowel diseases* **15**, 971-984

26. Parma, J., Duprez, L., Van Sande, J., Cochaux, P., Gervy, C., Mockel, J., Dumont, J., and Vassart, G. (1993) Somatic mutations in the thyrotropin receptor gene cause hyperfunctioning thyroid adenomas *Nature* **365**, 649-651

27. Moore, A. R., Ceraudo, E., Sher, J. J., Guan, Y., Shoushtari, A. N., Chang, M. T., Zhang, J. Q., Walczak, E. G., Kazmi, M. A., Taylor, B. S., Huber, T., Chi, P., Sakmar, T. P., and Chen, Y. (2016) Recurrent activating mutations of G-protein-coupled receptor CYSLTR2 in uveal melanoma. *Nat Genet* **48**, 675-680

28. Nazarko, O., Kibrom, A., Winkler, J., Leon, K., Stoveken, H., Salzman, G., Merdas, K., Lu, Y., Narkhede, P., Tall, G., Promel, S., and Arac, D. (2018) A Comprehensive Mutagenesis Screen of the Adhesion GPCR Latrophilin-1/ADGRL1. *iScience* **3**, 264-278

29. Mermel, C. H., Schumacher, S. E., Hill, B., Meyerson, M. L., Beroukhim, R., and Getz, G. (2011) GISTIC2.0 facilitates sensitive and confident localization of the targets of focal somatic copy-number alteration in human cancers. *Genome Biol* **12**, R41

30. Fang, X., Gaudette, D., Furui, T., Mao, M., Estrella, V., Eder, A., Pustilnik, T., Sasagawa, T., Lapushin, R., Yu, S., Jaffe, R. B., Wiener, J. R., Erickson, J. R., and Mills, G. B. (2000) Lysophospholipid growth factors in the initiation, progression, metastases, and management of ovarian cancer. *Annals of the New York Academy of Sciences* **905**, 188-208

31. Insel, P. A., Sriram, K., Wiley, S. Z., Wilderman, A., Katakia, T., McCann, T., Yokouchi, H., Zhang, L., Corriden, R., Liu, D., Feigin, M. E., French, R. P., Lowy, A. M., and Murray, F. (2018) GPCRomics: GPCR Expression in Cancer Cells and Tumors Identifies New, Potential Biomarkers and Therapeutic Targets. *Frontiers in pharmacology* **9**, 431

32. Wacker, D., Stevens, R. C., and Roth, B. L. (2017) How Ligands Illuminate GPCR Molecular Pharmacology. *Cell* **170**, 414-427

33. Sin, W. C., Zhang, Y., Zhong, W., Adhikarakunnathu, S., Powers, S., Hoey, T., An, S., and Yang, J. (2004) G protein-coupled receptors GPR4 and TDAG8 are oncogenic and overexpressed in human cancers. *Oncogene* **23**, 6299-6303

34. Inoue, A., Raimondi, F., Kadji, F. M. N., Singh, G., Kishi, T., Uwamizu, A., Ono, Y., Shinjo, Y., Ishida, S., Arang, N., Kawakami, K., Gutkind, J. S., Aoki, J., and Russell, R. B. (2019) Illuminating G-Protein-Coupling Selectivity of GPCRs. *Cell* **177**, 1933-1947 e1925

35. Nagahashi, M., Ramachandran, S., Kim, E. Y., Allegood, J. C., Rashid, O. M., Yamada, A., Zhao, R., Milstien, S., Zhou, H., Spiegel, S., and Takabe, K. (2012) Sphingosine-1-phosphate produced by sphingosine kinase 1 promotes breast cancer progression by stimulating angiogenesis and lymphangiogenesis. *Cancer Res* **72**, 726-735

36. Xu, Y., Fang, X. J., Casey, G., and Mills, G. B. (1995) Lysophospholipids activate ovarian and breast cancer cells. *Biochem J* **309 (Pt 3)**, 933-940

37. Husted, A. S., Trauelsen, M., Rudenko, O., Hjorth, S. A., and Schwartz, T. W. (2017) GPCR-Mediated Signaling of Metabolites. *Cell Metab* **25**, 777-796

38. Offermanns, S. (2014) Free fatty acid (FFA) and hydroxy carboxylic acid (HCA) receptors. *Annu Rev Pharmacol Toxicol* **54**, 407-434

39. Staller, P., Sulitkova, J., Lisztwan, J., Moch, H., Oakeley, E. J., and Krek, W. (2003) Chemokine receptor CXCR4 downregulated by von Hippel-Lindau tumour suppressor pVHL. *Nature* **425**, 307-311

40. Liu, Y. L., Yu, J. M., Song, X. R., Wang, X. W., Xing, L. G., and Gao, B. B. (2006) Regulation of the chemokine receptor CXCR4 and metastasis by hypoxia-inducible factor in non small cell lung cancer cell lines. *Cancer biology & therapy* **5**, 1320-1326

41. Schioppa, T., Uranchimeg, B., Saccani, A., Biswas, S. K., Doni, A., Rapisarda, A., Bernasconi, S., Saccani, S., Nebuloni, M., Vago, L., Mantovani, A., Melillo, G., and Sica, A. (2003) Regulation of the chemokine receptor CXCR4 by hypoxia. *J Exp Med* **198**, 1391-1402

42. Arrillaga-Romany, I., Chi, A. S., Allen, J. E., Oster, W., Wen, P. Y., and Batchelor, T. T. (2017) A phase 2 study of the first imipridone ONC201, a selective DRD2 antagonist for oncology, administered every three weeks in recurrent glioblastoma. *Oncotarget* **8**, 79298-79304

43. Kline, C. L. B., Ralff, M. D., Lulla, A. R., Wagner, J. M., Abbosh, P. H., Dicker, D. T., Allen, J. E., and El-Deiry, W. S. (2018) Role of Dopamine Receptors in the Anticancer Activity of ONC201. *Neoplasia* **20**, 80-91

44. Xie, J., Murone, M., Luoh, S. M., Ryan, A., Gu, Q., Zhang, C., Bonifas, J. M., Lam, C. W., Hynes, M., Goddard, A., Rosenthal, A., Epstein, E. H., Jr., and de Sauvage, F. J. (1998) Activating Smoothened mutations in sporadic basal-cell carcinoma. *Nature* **391**, 90-92

45. Walter, K., Omura, N., Hong, S. M., Griffith, M., Vincent, A., Borges, M., and Goggins, M. (2010) Overexpression of smoothened activates the sonic hedgehog signaling pathway in pancreatic cancer-associated fibroblasts. *Clin Cancer Res* **16**, 1781-1789

46. Davies, J. Q., Lin, H. H., Stacey, M., Yona, S., Chang, G. W., Gordon, S., Hamann, J., Campo, L., Han, C., Chan, P., and Fox, S. B. (2011) Leukocyte adhesion-GPCR EMR2 is aberrantly expressed in human breast carcinomas and is associated with patient survival. *Oncol Rep* **25**, 619-627

47. Aust, G., Eichler, W., Laue, S., Lehmann, I., Heldin, N. E., Lotz, O., Scherbaum, W. A., Dralle, H., and Hoang-Vu, C. (1997) CD97: a dedifferentiation marker in human thyroid carcinomas. *Cancer Res* **57**, 1798-1806

48. Yang, L., Chen, G., Mohanty, S., Scott, G., Fazal, F., Rahman, A., Begum, S., Hynes, R. O., and Xu, L. (2011) GPR56 Regulates VEGF production and angiogenesis during melanoma progression. *Cancer Res* **71**, 5558-5568

49. Xu, L., Begum, S., Hearn, J. D., and Hynes, R. O. (2006) GPR56, an atypical G protein-coupled receptor, binds tissue transglutaminase, TG2, and inhibits melanoma tumor growth and metastasis. *Proc Natl Acad Sci U S A* **103**, 9023-9028

50. Bayin, N. S., Frenster, J. D., Kane, J. R., Rubenstein, J., Modrek, A. S., Baitalmal, R., Dolgalev, I., Rudzenski, K., Scarabottolo, L., Crespi, D., Redaelli, L., Snuderl, M., Golfinos, J. G., Doyle, W., Pacione, D., Parker, E. C., Chi, A. S., Heguy, A., MacNeil, D. J., Shohdy,

N., Zagzag, D., and Placantonakis, D. G. (2016) GPR133 (ADGRD1), an adhesion G-protein-coupled receptor, is necessary for glioblastoma growth. *Oncogenesis* **5**, e263

51. Veglia, F., Perego, M., and Gabrilovich, D. (2018) Myeloid-derived suppressor cells coming of age. *Nat Immunol* **19**, 108-119

52. Devaud, C., John, L. B., Westwood, J. A., Darcy, P. K., and Kershaw, M. H. (2013) Immune modulation of the tumor microenvironment for enhancing cancer immunotherapy. *Oncoimmunology* **2**, e25961

53. Sharma, P., and Allison, J. P. (2015) The future of immune checkpoint therapy. *Science* **348**, 56-61

54. Wei, S. C., Duffy, C. R., and Allison, J. P. (2018) Fundamental Mechanisms of Immune Checkpoint Blockade Therapy. *Cancer Discov* **8**, 1069-1086

55. Thommen, D. S., and Schumacher, T. N. (2018) T Cell Dysfunction in Cancer. *Cancer Cell* **33**, 547-562

56. Young, A., Mittal, D., Stagg, J., and Smyth, M. J. (2014) Targeting cancer-derived adenosine: new therapeutic approaches. *Cancer Discov* **4**, 879-888

57. Cekic, C., and Linden, J. (2016) Purinergic regulation of the immune system. *Nature reviews. Immunology* **16**, 177-192

58. Borea, P. A., Gessi, S., Merighi, S., Vincenzi, F., and Varani, K. (2018) Pharmacology of Adenosine Receptors: The State of the Art. *Physiological reviews* **98**, 1591-1625

59. Young, A., Ngiow, S. F., Gao, Y., Patch, A. M., Barkauskas, D. S., Messaoudene, M., Lin, G., Coudert, J. D., Stannard, K. A., Zitvogel, L., Degli-Esposti, M. A., Vivier, E., Waddell, N., Linden, J., Huntington, N. D., Souza-Fonseca-Guimaraes, F., and Smyth, M. J. (2018) A2AR Adenosine Signaling Suppresses Natural Killer Cell Maturation in the Tumor Microenvironment. *Cancer Res* **78**, 1003-1016

60. Novitskiy, S. V., Ryzhov, S., Zaynagetdinov, R., Goldstein, A. E., Huang, Y., Tikhomirov, O. Y., Blackburn, M. R., Biaggioni, I., Carbone, D. P., Feoktistov, I., and Dikov, M. M. (2008) Adenosine receptors in regulation of dendritic cell differentiation and function. *Blood* **112**, 1822-1831

61. Visser, S. S., Theron, A. J., Ramafi, G., Ker, J. A., and Anderson, R. (2000) Apparent involvement of the A(2A) subtype adenosine receptor in the anti-inflammatory interactions of CGS 21680, cyclopentyladenosine, and IB-MECA with human neutrophils. *Biochemical pharmacology* **60**, 993-999

62. Leone, R. D., Lo, Y. C., and Powell, J. D. (2015) A2aR antagonists: Next generation checkpoint blockade for cancer immunotherapy. *Computational and structural biotechnology journal* **13**, 265-272

63. Ohta, A. (2016) A Metabolic Immune Checkpoint: Adenosine in Tumor Microenvironment. *Frontiers in immunology* **7**, 109

64. Antonioli, L., Yegutkin, G. G., Pacher, P., Blandizzi, C., and Hasko, G. (2016) Anti-CD73 in cancer immunotherapy: awakening new opportunities. *Trends Cancer* **2**, 95-109

65. Ricciotti, E., and FitzGerald, G. A. (2011) Prostaglandins and inflammation. *Arterioscler Thromb Vasc Biol* **31**, 986-1000

66. Sugimoto, Y., and Narumiya, S. (2007) Prostaglandin E receptors. *J Biol Chem* **282**, 11613-11617

67. Baratelli, F., Lin, Y., Zhu, L., Yang, S. C., Heuze-Vourc'h, N., Zeng, G., Reckamp, K., Dohadwala, M., Sharma, S., and Dubinett, S. M. (2005) Prostaglandin E2 induces FOXP3 gene expression and T regulatory cell function in human CD4+ T cells. *J Immunol* **175**, 1483-1490

68. Obermajer, N., and Kalinski, P. (2012) Key role of the positive feedback between PGE(2) and COX2 in the biology of myeloid-derived suppressor cells. *Oncoimmunology* **1**, 762-764

69. Iniguez, M. A., Punzon, C., and Fresno, M. (1999) Induction of cyclooxygenase-2 on activated T lymphocytes: regulation of T cell activation by cyclooxygenase-2 inhibitors. *J Immunol* **163**, 111-119

70. Sreeramkumar, V., Fresno, M., and Cuesta, N. (2012) Prostaglandin E2 and T cells: friends or foes? *Immunology and cell biology* **90**, 579-586

71. Wang, J., Zhang, L., Kang, D., Yang, D., and Tang, Y. (2018) Activation of PGE2/EP2 and PGE2/EP4 signaling pathways positively regulate the level of PD-1 in infiltrating CD8(+) T cells in patients with lung cancer. *Oncology letters* **15**, 552-558

72. von Bergwelt-Baildon, M. S., Popov, A., Saric, T., Chemnitz, J., Classen, S., Stoffel, M. S., Fiore, F., Roth, U., Beyer, M., Debey, S., Wickenhauser, C., Hanisch, F. G., and Schultze, J. L. (2006) CD25 and indoleamine 2,3-dioxygenase are up-regulated by prostaglandin E2 and expressed by tumor-associated dendritic cells in vivo: additional mechanisms of T-cell inhibition. *Blood* **108**, 228-237

73. Drew, D. A., Cao, Y., and Chan, A. T. (2016) Aspirin and colorectal cancer: the promise of precision chemoprevention. *Nat Rev Cancer* **16**, 173-186

74. Fischer, S. M., Hawk, E. T., and Lubet, R. A. (2011) Coxibs and other nonsteroidal anti-inflammatory drugs in animal models of cancer chemoprevention. *Cancer prevention research* **4**, 1728-1735

75. Weinstein, L. S., Shenker, A., Gejman, P. V., Merino, M. J., Friedman, E., and Spiegel, A. M. (1991) Activating mutations of the stimulatory G protein in the McCune-Albright syndrome [see comments]. *N Engl J Med* **325**, 1688-1695

76. Castellone, M. D., Teramoto, H., Williams, B. O., Druey, K. M., and Gutkind, J. S. (2005) Prostaglandin E2 promotes colon cancer cell growth through a Gs-axin-beta-catenin signaling axis. *Science* **310**, 1504-1510

77. Nomura, R., Saito, T., Mitomi, H., Hidaka, Y., Lee, S. Y., Watanabe, S., and Yao, T. (2014) GNAS mutation as an alternative mechanism of activation of the Wnt/beta-catenin signaling pathway in gastric adenocarcinoma of the fundic gland type. *Hum Pathol* **45**, 2488-2496

78. Van Raamsdonk, C. D., Griewank, K. G., Crosby, M. B., Garrido, M. C., Vemula, S., Wiesner, T., Obenauf, A. C., Wackernagel, W., Green, G., Bouvier, N., Sozen, M. M., Baimukanova, G., Roy, R., Heguy, A., Dolgalev, I., Khanin, R., Busam, K., Speicher, M. R., O'Brien, J., and Bastian, B. C. (2010) Mutations in GNA11 in uveal melanoma. *N Engl J Med* **363**, 2191-2199

79. Van Raamsdonk, C. D., Bezrookove, V., Green, G., Bauer, J., Gaugler, L., O'Brien, J. M., Simpson, E. M., Barsh, G. S., and Bastian, B. C. (2009) Frequent somatic mutations of GNAQ in uveal melanoma and blue naevi. *Nature* **457**, 599-602

80. Carvajal, R. D., Piperno-Neumann, S., Kapiteijn, E., Chapman, P. B., Frank, S., Joshua, A. M., Piulats, J. M., Wolter, P., Cocquyt, V., Chmielowski, B., Evans, T. R. J., Gastaud, L., Linette, G., Berking, C., Schachter, J., Rodrigues, M. J., Shoushtari, A. N., Clemett, D.,

Ghiorghiu, D., Mariani, G., Spratt, S., Lovick, S., Barker, P., Kilgour, E., Lai, Z., Schwartz, G. K., and Nathan, P. (2018) Selumetinib in Combination With Dacarbazine in Patients With Metastatic Uveal Melanoma: A Phase III, Multicenter, Randomized Trial (SUMIT). *J Clin Oncol* **36**, 1232-1239

81. Feng, X., Degese, M. S., Iglesias-Bartolome, R., Vaque, J. P., Molinolo, A. A., Rodrigues, M., Zaidi, M. R., Ksander, B. R., Merlino, G., Sodhi, A., Chen, Q., and Gutkind, J. S. (2014) Hippo-independent activation of YAP by the GNAQ uveal melanoma oncogene through a trio-regulated rho GTPase signaling circuitry. *Cancer Cell* **25**, 831-845

82. Parish, A. J., Nguyen, V., Goodman, A. M., Murugesan, K., Frampton, G. M., and Kurzrock, R. (2018) GNAS, GNAQ, and GNA11 alterations in patients with diverse cancers. *Cancer* **124**, 4080-4089

83. Ayturk, U. M., Couto, J. A., Hann, S., Mulliken, J. B., Williams, K. L., Huang, A. Y., Fishman, S. J., Boyd, T. K., Kozakewich, H. P., Bischoff, J., Greene, A. K., and Warman, M. L. (2016) Somatic Activating Mutations in GNAQ and GNA11 Are Associated with Congenital Hemangioma. *Am J Hum Genet* **98**, 789-795

84. Shirley, M. D., Tang, H., Gallione, C. J., Baugher, J. D., Frelin, L. P., Cohen, B., North, P. E., Marchuk, D. A., Comi, A. M., and Pevsner, J. (2013) Sturge-Weber syndrome and port-wine stains caused by somatic mutation in GNAQ. *N Engl J Med* **368**, 1971-1979

85. O'Hayre, M., Inoue, A., Kufareva, I., Wang, Z., Mikelis, C. M., Drummond, R. A., Avino, S., Finkel, K., Kalim, K. W., DiPasquale, G., Guo, F., Aoki, J., Zheng, Y., Lionakis, M. S., Molinolo, A. A., and Gutkind, J. S. (2016) Inactivating mutations in GNA13 and RHOA in Burkitt's lymphoma and diffuse large B-cell lymphoma: a tumor suppressor function for the Galpha13/RhoA axis in B cells. *Oncogene* **35**, 3771-3780

86. Love, C., Sun, Z., Jima, D., Li, G., Zhang, J., Miles, R., Richards, K. L., Dunphy, C. H., Choi, W. W., Srivastava, G., Lugar, P. L., Rizzieri, D. A., Lagoo, A. S., Bernal-Mizrachi, L., Mann, K. P., Flowers, C. R., Naresh, K. N., Evens, A. M., Chadburn, A., Gordon, L. I., Czader, M. B., Gill, J. I., Hsi, E. D., Greenough, A., Moffitt, A. B., McKinney, M., Banerjee, A., Grubor, V., Levy, S., Dunson, D. B., and Dave, S. S. (2012) The genetic landscape of mutations in Burkitt lymphoma. *Nat Genet* **44**, 1321-1325

87. Lohr, J. G., Stojanov, P., Lawrence, M. S., Auclair, D., Chapuy, B., Sougnez, C., Cruz-Gordillo, P., Knoechel, B., Asmann, Y. W., Slager, S. L., Novak, A. J., Dogan, A., Ansell, S. M., Link, B. K., Zou, L., Gould, J., Saksena, G., Stransky, N., Rangel-Escareno, C., Fernandez-Lopez, J. C., Hidalgo-Miranda, A., Melendez-Zajgla, J., Hernandez-Lemus, E., Schwarz-Cruz y Celis, A., Imaz-Rosshandler, I., Ojesina, A. I., Jung, J., Pedamallu, C. S., Lander, E. S., Habermann, T. M., Cerhan, J. R., Shipp, M. A., Getz, G., and Golub, T. R. (2012) Discovery and prioritization of somatic mutations in diffuse large B-cell lymphoma (DLBCL) by whole-exome sequencing. *Proc Natl Acad Sci U S A* **109**, 3879-3884

88. Zhang, J. X., Yun, M., Xu, Y., Chen, J. W., Weng, H. W., Zheng, Z. S., Chen, C., Xie, D., and Ye, S. (2016) GNA13 as a prognostic factor and mediator of gastric cancer progression. *Oncotarget* **7**, 4414-4427

89. Liu, S. C., Jen, Y. M., Jiang, S. S., Chang, J. L., Hsiung, C. A., Wang, C. H., and Juang, J. L. (2009) G(alpha)12-mediated pathway promotes invasiveness of nasopharyngeal carcinoma by modulating actin cytoskeleton reorganization. *Cancer Res* **69**, 6122-6130

90. Kelly, P., Stemmle, L. N., Madden, J. F., Fields, T. A., Daaka, Y., and Casey, P. J. (2006) A role for the G12 family of heterotrimeric G proteins in prostate cancer invasion. *J Biol Chem* **281**, 26483-26490

91. Kelly, P., Moeller, B. J., Juneja, J., Booden, M. A., Der, C. J., Daaka, Y., Dewhirst, M. W., Fields, T. A., and Casey, P. J. (2006) The G12 family of heterotrimeric G proteins promotes breast cancer invasion and metastasis. *Proc Natl Acad Sci U S A* **103**, 8173-8178

92. Rasheed, S. A. K., Leong, H. S., Lakshmanan, M., Raju, A., Dadlani, D., Chong, F. T., Shannon, N. B., Rajarethinam, R., Skanthakumar, T., Tan, E. Y., Hwang, J. S. G., Lim, K. H., Tan, D. S., Ceppi, P., Wang, M., Tergaonkar, V., Casey, P. J., and Iyer, N. G. (2018) GNA13 expression promotes drug resistance and tumor-initiating phenotypes in squamous cell cancers. *Oncogene* **37**, 1340-1353

93. Yoda, A., Adelmant, G., Tamburini, J., Chapuy, B., Shindoh, N., Yoda, Y., Weigert, O., Kopp, N., Wu, S. C., Kim, S. S., Liu, H., Tivey, T., Christie, A. L., Elpek, K. G., Card, J., Gritsman, K., Gotlib, J., Deininger, M. W., Makishima, H., Turley, S. J., Javidi-Sharifi, N., Maciejewski, J. P., Jaiswal, S., Ebert, B. L., Rodig, S. J., Tyner, J. W., Marto, J. A., Weinstock, D. M., and Lane, A. A. (2015) Mutations in G protein beta subunits promote transformation and kinase inhibitor resistance. *Nat Med* **21**, 71-75

94. Nakayama, J., Fu, Y. H., Clark, A. M., Nakahara, S., Hamano, K., Iwasaki, N., Matsui, A., Arinami, T., and Ptacek, L. J. (2002) A nonsense mutation of the MASS1 gene in a family with febrile and afebrile seizures. *Annals of neurology* **52**, 654-657

95. Mathur, P., and Yang, J. (2015) Usher syndrome: Hearing loss, retinal degeneration and associated abnormalities. *Biochim Biophys Acta* **1852**, 406-420

96. Sadeque, A., Serao, N. V., Southey, B. R., Delfino, K. R., and Rodriguez-Zas, S. L. (2012) Identification and characterization of alternative exon usage linked glioblastoma multiforme survival. *BMC medical genomics* **5**, 59

97. Nugent, A., and Proia, R. L. (2017) The role of G protein-coupled receptors in lymphoid malignancies. *Cellular signalling* **39**, 95-107

98. Pollock, P. M., Cohen-Solal, K., Sood, R., Namkoong, J., Martino, J. J., Koganti, A., Zhu, H., Robbins, C., Makalowska, I., Shin, S. S., Marin, Y., Roberts, K. G., Yudt, L. M., Chen, A., Cheng, J., Incao, A., Pinkett, H. W., Graham, C. L., Dunn, K., Crespo-Carbone, S. M., Mackason, K. R., Ryan, K. B., Sinsimer, D., Goydos, J., Reuhl, K. R., Eckhaus, M., Meltzer, P. S., Pavan, W. J., Trent, J. M., and Chen, S. (2003) Melanoma mouse model implicates metabotropic glutamate signaling in melanocytic neoplasia. *Nat Genet* **34**, 108-112

99. Choi, K. Y., Chang, K., Pickel, J. M., Badger, J. D., 2nd, and Roche, K. W. (2011) Expression of the metabotropic glutamate receptor 5 (mGluR5) induces melanoma in transgenic mice. *Proc Natl Acad Sci U S A* **108**, 15219-15224

100. Speyer, C. L., Smith, J. S., Banda, M., DeVries, J. A., Mekani, T., and Gorski, D. H. (2012) Metabotropic glutamate receptor-1: a potential therapeutic target for the treatment of breast cancer. *Breast Cancer Res Treat* **132**, 565-573

101. Lin, P., and Ye, R. D. (2003) The lysophospholipid receptor G2A activates a specific combination of G proteins and promotes apoptosis. *J Biol Chem* **278**, 14379-14386

102. Whitehead, I. P., Zohn, I. E., and Der, C. J. (2001) Rho GTPase-dependent transformation by G protein-coupled receptors. *Oncogene* **20**, 1547-1555

103. Barker, N., and Clevers, H. (2010) Leucine-rich repeat-containing G-protein-coupled receptors as markers of adult stem cells. *Gastroenterology* **138**, 1681-1696

104. Tanese, K., Fukuma, M., Yamada, T., Mori, T., Yoshikawa, T., Watanabe, W., Ishiko, A., Amagai, M., Nishikawa, T., and Sakamoto, M. (2008) G-protein-coupled receptor GPR49

is up-regulated in basal cell carcinoma and promotes cell proliferation and tumor formation. *Am J Pathol* **173**, 835-843

105. McClanahan, T., Koseoglu, S., Smith, K., Grein, J., Gustafson, E., Black, S., Kirschmeier, P., and Samatar, A. A. (2006) Identification of overexpression of orphan G protein-coupled receptor GPR49 in human colon and ovarian primary tumors. *Cancer biology & therapy* **5**, 419-426

106. Shi, X., Gangadharan, B., Brass, L. F., Ruf, W., and Mueller, B. M. (2004) Protease-activated receptors (PAR1 and PAR2) contribute to tumor cell motility and metastasis. *Mol Cancer Res* **2**, 395-402

107. Lopez-Otin, C., and Matrisian, L. M. (2007) Emerging roles of proteases in tumour suppression. *Nat Rev Cancer* **7**, 800-808

108. Su, S., Li, Y., Luo, Y., Sheng, Y., Su, Y., Padia, R. N., Pan, Z. K., Dong, Z., and Huang, S. (2009) Proteinase-activated receptor 2 expression in breast cancer and its role in breast cancer cell migration. *Oncogene* **28**, 3047-3057

109. Darmoul, D., Gratio, V., Devaud, H., and Laburthe, M. (2004) Protease-activated receptor 2 in colon cancer: trypsin-induced MAPK phosphorylation and cell proliferation are mediated by epidermal growth factor receptor transactivation. *J Biol Chem* **279**, 20927-20934

110. Dutra-Oliveira, A., Monteiro, R. Q., and Mariano-Oliveira, A. (2012) Protease-activated receptor-2 (PAR2) mediates VEGF production through the ERK1/2 pathway in human glioblastoma cell lines. *Biochem Biophys Res Commun* **421**, 221-227

111. Rasmussen, J. G., Riis, S. E., Frobert, O., Yang, S., Kastrup, J., Zachar, V., Simonsen, U., and Fink, T. (2012) Activation of protease-activated receptor 2 induces VEGF independently of HIF-1. *PLoS One* **7**, e46087

112. North, T. E., Goessling, W., Walkley, C. R., Lengerke, C., Kopani, K. R., Lord, A. M., Weber, G. J., Bowman, T. V., Jang, I. H., Grosser, T., Fitzgerald, G. A., Daley, G. Q., Orkin, S. H., and Zon, L. I. (2007) Prostaglandin E2 regulates vertebrate haematopoietic stem cell homeostasis. *Nature* **447**, 1007-1011

113. Chan, A. T., Ogino, S., and Fuchs, C. S. (2007) Aspirin and the risk of colorectal cancer in relation to the expression of COX-2. *N Engl J Med* **356**, 2131-2142

114. Chen, E. P., and Smyth, E. M. (2011) COX-2 and PGE2-dependent immunomodulation in breast cancer. *Prostaglandins Other Lipid Mediat* **96**, 14-20

115. Itadani, H., Oshima, H., Oshima, M., and Kotani, H. (2009) Mouse gastric tumor models with prostaglandin E2 pathway activation show similar gene expression profiles to intestinal-type human gastric cancer. *BMC Genomics* **10**, 615

116. Amano, H., Ito, Y., Suzuki, T., Kato, S., Matsui, Y., Ogawa, F., Murata, T., Sugimoto, Y., Senior, R., Kitasato, H., Hayashi, I., Satoh, Y., Narumiya, S., and Majima, M. (2009) Roles of a prostaglandin E-type receptor, EP3, in upregulation of matrix metalloproteinase-9 and vascular endothelial growth factor during enhancement of tumor metastasis. *Cancer Sci* **100**, 2318-2324

Chapter 3: Syngeneic animal models of tobacco-associated oral cancer reveal the activity of *in situ* anti-CTLA-4

3.1 Abstract

Head and neck squamous cell carcinoma (HNSCC) is the sixth most common cancer worldwide. Tobacco use is the main risk factor for HNSCC, and tobacco-associated HNSCCs have poor prognosis and response to available treatments. Recently approved anti-PD-1 immune checkpoint inhibitors showed limited activity (≤20%) in HNSCC, highlighting the need to identify new therapeutic options. For this, mouse models that accurately mimic the complexity of the HNSCC mutational landscape and tumor immune environment are urgently needed. Here, we report a mouse HNSCC model system that recapitulates the human tobacco-related HNSCC mutanome, in which tumors grow when implanted in the tongue of immunocompetent mice. These HNSCC lesions have similar immune infiltration and response rates to anti-PD-1 (≤20%) immunotherapy as human HNSCCs. Remarkably, we find that >70% of HNSCC lesions respond to intratumoral anti-CTLA-4. This syngeneic HNSCC mouse model provides a platform to accelerate the development of immunotherapeutic options for HNSCC.

3.2 Introduction

Tobacco smoking claims the lives of more than 6 million people every year worldwide and is the leading cause of cancer deaths in the U.S (1,2). Tobacco use has been associated with at least 17 types of cancer, primarily in the lung, as well as with carcinomas arising in the oral cavity, pharynx, and larynx, often referred to as squamous cell carcinomas of the head and neck (HNSCC)(1,2). HNSCC is a significant public health issue, with more than 65,400 new cases resulting in 14,600 deaths in 2019 in the U.S. alone (3). The main risk factors include tobacco use and human papillomavirus (HPV) infection, the latter of which is predicted to diminish in the future due to successful vaccination campaigns (4,5). Depending on the stage of disease, HNSCC is typically treated with surgery, radiotherapy, chemotherapy, or a combination of these interventions. These standard therapies result in a five-year survival of approximately 63%, but patients with more advanced stages have higher rates of mortality (5 year survival <50%) and require multimodality treatments, which can lead to occurrence of significant long-term side effects and lower quality of life(6,7). Despite this more aggressive regimen, up to 30-60% of HNSCC patients develop tumor recurrence, and often succumb to the disease (8). The recent elucidation of the genomic alterations underlying HNSCC progression and new immunotherapeutic strategies may provide an opportunity for the development of more effective treatment options for HNSCC.

Revolutionary breakthrough discoveries in cancer immunology have demonstrated that a patient's own immune cells can be manipulated to target, attack, and destroy cancer cells(9-11). A key emerging mechanism of tumor immune evasion involves T cell exhaustion, whereby T cell reactivity is impaired due to activation of T cell checkpoints, including PD-1 by its ligand, PD-L1 that is expressed by macrophages and some cancer cells, including HNSCC, restraining T cell activation (reviewed in (12)). Indeed, immune checkpoint blockade (ICB) by new immunotherapeutic agents such as pembrolizumab and nivolumab (anti-PD-1) have recently demonstrated potent anti-tumor activity in a subset of HNSCC patients (13-16). However, one-

year survival and response rates of anti-PD-1 in HNSCC were only 36% and 14%, respectively, which highlights the urgent need to identify novel therapeutic options to increase the effectiveness of ICB for the >80% of patients that do not have an objective response to anti-PD-1/PD-L1 treatment (13-15).

Animal models with a full functioning immune system that also properly resemble human HNSCC etiology and mutational landscape are desperately needed to accurately recapitulate the complexity of the tumor immune microenvironment (TIME), thereby accelerating the search for new immune therapeutic options. Here, we report a syngeneic murine HNSCC cell panel that recapitulates typical human tobacco-related HNSCC genomic alterations and mutational landscape, and we show that these cells form squamous carcinomas (HNSCC) when implanted orthotopically in the tongue of immune competent C57Bl/6 mice. These HNSCC lesions have immune infiltration and response rates to anti-PD-1 therapies (≤20%) similar to those of human HNSCCs, thereby providing a platform for the evaluation of new immune oncology (IO) options for HNSCC treatment.

3.3 Results

3.3.1 4MOSC models exhibit tobacco-related genomic landscapes.

Tobacco smoke contains a number of harmful carcinogens that drive tumorigenesis, the exposure to which strongly correlates with cancer incidence (17).While tobacco-associated cancers are generally characterized by high mutation frequencies (18), we have recently reported that they can be defined by very specific set of mutational signatures (19). We have also described the optimization of a carcinogen-induced oral cancer mouse model in which the compound 4-nitroquinoline-1 oxide (4NQO), a DNA adduct-forming agent that causes DNA damage and can act as a tobacco-mimetic promoting *Tp53* mutations and oral cancer initiation and progression (20). This model has been used extensively to study HNSCC progression and preventive and treatment therapeutic options (21-23). However, its direct relevance to the mutagenic process in human HNSCC has not been previously established. To begin developing syngeneic HNSCC

animal models, we first isolated 4 representatives murine HNSCC cell lines from primary 4NQO-induced tumors in the tongue of C57Bl/6 mice (designated 4MOSC1-4, short for 4NQO-induced Murine Oral Squamous Cells) (**Figure 3.1A**). The use of SigProfiler (24,25) to analyze exome DNAseq of these HNSCC cells revealed a remarkable 93.9 % similarity with human cancer signature 4, which is strictly associated with tobacco smoking, including in HNSCC, esophageal cancer, and lung cancer (19) (Pearson correlation > 0.93) (**Figure 3.1B** and individual 4MOSC cells in **Supplementary Figure S3.1**). This similarity between 4NQO-induced mutational patterns and tobacco extended to the presence of a transcriptional strand bias (**Figure 3.1C**), which reflects rate of substitution type on each nucleotide. In contrast, the mutational signature of SCC caused by DMBA, a carcinogen found in tobacco smoke that is the most widely used agent for experimental carcinogenesis studies (26), showed only 39.7% similarity with human cancer signature 4. This suggests that 4NQO-induced SCC lesions better mimic human tobacco-related human HNSCC. Indeed, these cells also exhibit typical HNSCC histology and mutations impacting *Trp53*, *Fat1-4*, *Keap1*, *Notch1-3*, *Kmt2b-d*, and others, which represent some of the most frequently altered gene pathways in HPV- human HNSCC (**Figure 3.1D-E**, and **Supplementary Data S3.1**). Of note, similar to HPV(-) HNSCC samples from TCGA, all four 4MOSC cells exhibit typical inactivating *Trp53* mutations in its core DNA binding domain, including hot spot residues (G245, and R248) that result in loss of tumor-suppression and gain of tumorigenesis and invasiveness (27).

3.3.2 4MOSC lesions mimic the human HNSCC immune microenvironment.

Transplantation of the 4MOSC cells orthotopically into the tongue of immunocompetent C57Bl/6 mice led to the formation of well-differentiated HNSCC tumors in two of the cell lines, 4MOSC1 and 4MOSC2, which exhibit typical HNSCC histology, as indicated by hematoxylin and eosin (H&E) stained sections and fluorescence cytokeratin 5 staining (**Figure 3.2A** and **Supplementary Figure. S3.2A**). 4MOSC3 and 4MOSC4 cells also formed tumors, but they regressed spontaneously after 2 weeks, likely due to their rejection by the host immune system. Thus, we

focused our studies on 4MOSC1 and 4MOSC2, with emphasis on investigating whether they have distinct biological properties reflecting human HNSCC. In this regard, since HNSCC has a high propensity to metastasize to locoregional lymph nodes (reviewed in (28)), leading to poor prognosis, we next addressed the metastatic potential of our model. Histological evaluation in H&E stained sections revealed growth of cancer cells in the lymph nodes of mice bearing 4MOSC2 but not 4MOSC1 tumors (**Figure 3.2B**). Interestingly, locoregional lymph node invasion was observed as early as 2 days post-implantation; and a higher rate of lymph node metastasis was observed 8 days after 4MOSC2 tumors were established (**Supplementary Figure. S3.2B**). 4MOSC2 tumors also exhibited much higher density of lymphatic vessels staining positive for LYVE-1 than in 4MOSC1 (**Figure 3.2C**), which is aligned with the strong correlation between intratumoral lymphangiogenesis and metastasis in human HNSCC (reviewed in (29)).

By flow cytometry analysis, we found that the immune cells infiltrating the tumor immune microenvironment (TIME) comprises of cytotoxic T cells (CD8), helper T cells (CD4), regulatory T cells (Treg), natural killer cells (NK), macrophages (M1Φ and M2Φ), as well as polymorphonuclear myeloid-derived suppressor cells (PMN-MDSC), and monocytic myeloid-derived suppressor cells (M-MDSC) (30) (**Figure 3.2D**). Notably, although the ratios of immune infiltration were similar, 4MOSC2 tumors had a considerably higher level of infiltration than 4MOSC1 (**Figure 3.2D**). Though cytotoxic CD8 T cells infiltrate both tumors at similar proportions relative to other immune cells, immunofluorescence staining showed more abundant distribution within 4MOSC2 tumor cells (**Figure 3.2E**). The more immune inflamed state of 4MOSC2 tumors is likely due to their clearly distinct chemokine and cytokine profile. Indeed, 4MOSC2 tumors express higher levels of multiple chemokines (including CXCL1 and CXCL5) and growth factors (such as G-CSF, GM-CSF) than in 4MOSC1 tumors, which may contribute to the recruitment and survival of MDSCs and inflammatory cells, as well as VEGF that may explain the higher density of lymphatic vessels **(Supplementary Figure S3.3).**

To determine whether this immune infiltration is associated with antigen-driven immunogenicity, we next investigated whether the 4MOSC tumors could generate memory immune responses. Initial exposure of mice to tumor cell antigens was achieved by first irradiating tumor cells and then injecting into the tongue of C57Bl/6 mice with or without polyinosinic-polycytidylic acid (poly IC) as an immune adjuvant. Irradiated 4MOSC1 and 4MOSC2 cells did not form tumors, and mice vaccinated with irradiated tumor cells alone or irradiated tumor cells with poly IC failed to form tumors when they were subsequently re-challenged with non-irradiated cancer cells, while naïve mice and mice with poly IC alone still formed tumors. This suggests that the mice were able to develop an immunological memory to 4MOSC antigens even in the absence of an immune adjuvant. This may be due to the fact that irradiation can induce inflammatory cell death (31), which contributes to immunogenicity. Taken together, our results suggest that these syngeneic HNSCC cell lines are highly immunogenic (**Supplementary Figure S3.4**).

These findings indicate that these mice are capable of generating adaptive immune responses against 4MOSC tumor antigens. However, 4MOSC tumors still grow and lead mice to succumb to disease, implying that these tumors can evade immunity by inducing an immune suppressive microenvironment. The expression of programmed death ligand 1 (PD-L1), the ligand for the T-cell inhibitory receptor PD-1, is often high in HNSCC patients (46-100% of tumors) (32) and has been shown to suppress cytotoxic T cells that destroy tumors and also serves as a biomarker (reviewed in (33)) predicting a better response to anti-PD-1 therapy. We found that PD-L1 is constitutively expressed on both tumor ($CD45^-$) and immune cells ($CD45^+$), but the frequency of 4MOSC1 tumor cells that expressed PD-L1 was much higher than the frequency of 4MOSC2 cells expressing PD-L1 (**Figure 3.2F**). Though most tumor-infiltrating immune cells expressed PD-L1, MDSCs, tumor-associated macrophages (TAMs) and $MHCII^+$ antigen presenting cells (APCs) infiltrating the tumor comprise of the majority of $PD\text{-}L1^{hi}CD45+$ immune cells (**Supplementary Figure S3.5**). Activated ($CD44^+$) CD8 T cells infiltrating both 4MOSC1 and 4MOSC2 tumors exhibited characteristic immune checkpoint molecules, PD-1, cytotoxic T

lymphocyte associated protein 4 (CTLA-4), T-cell immunoglobulin mucin 3 (TIM-3), and lymphocyte activation gene 3 (LAG-3) (**Figure 3.2G**). Interestingly, there were higher immune checkpoint molecules in tumor-infiltrating lymphocytes (TILs, green) than in lymph nodes (blue) or blood (red) in both tumors (**Figure 3.2G**). Similar expression patterns were seen for tumor-infiltrating CD4 T cells, but there was a higher frequency of Tregs expressing CTLA-4 compared to non-Treg CD4 T cells (**Supplementary Figure S3.6**).

3.3.3 Limited response of syngeneic HNSCC tumors to PD-1 blockade.

To interrogate whether blocking the interaction of PD-1 and PD-L1 could cause tumor regression, we first studied 4MOSC1 tumors, the syngeneic HNSCC cell line that has higher PD-L1 expression. Most mice showed an initial decreased tumor volume after anti-PD-1 treatment (**Figure 3.3A**), with a consequent increased overall survival (**Figure 3.3B**) ($p<.001$). Interestingly, however, 80% of mice that initially responded to anti-PD-1 (partial response, PR) showed tumor relapse and eventually succumbed to disease burden, while 10-20% of the mice showed complete responses (CR) (**Figure 3.3A-B,** and **Supplementary Figure S3.7A**). Due to limited tumor size and number of infiltrating cells, we could not perform a comprehensive analysis of immune cell infiltration in individual tumors at the beginning of the treatment. However, 4MOSC1 tumors from mice treated with anti-PD-1 showed clearly significant higher CD8 infiltration ($p<0.01$) compared to tumors from untreated mice by FACS analysis of tumor infiltrating leukocytes (TILs) and by immune fluorescence analysis of treated tissues (**Figure 3.3C** and **3.3D**, respectively). All responses to anti-PD-1 were abolished if CD8 T cells were eliminated from mice (**Figure 3.3E** and **Supplementary Figure S3.7B**). Together, these data indicate a CD8-dependent anti-PD-1 response in mice with 4MOSC1 tumors, but with limited durable disease control or tumor regression, which is similar to the clinical response to anti-PD-1 therapies in HNSCC patients (14,16). To our surprise, although metastasis was not observed in 4MOSC1 control mice (see above), the cervical lymph nodes of CD8-depleted mice with 4MOSC1 tumors showed tumor invasion, as indicated by cytokeratin 5 staining (**Figure 3.3F**) and visualization with H&E-staining

(**Supplementary Figure S3.7C**) suggesting that immune surveillance may prevent the metastatic spread of this tumor. In contrast, mice bearing 4MOSC2 tumors failed to respond to anti-PD-1 treatment (**Figure 3.3G** and **Supplementary Figure S3.7D**), suggesting 4MOSC2 serves as a less differentiated, high immune cell-infiltrated, metastatic, and PD-L1-low, and anti-PD-1 resistant model (**Figure 3.3G** and **Supplementary Figure S3.7D**).

The PD-1 blocking antibodies used are mouse specific, hence treatment failure is not expected to be due to neutralizing antibodies against human IgG. We next isolated 4MOSC1 cells were from mice showing limited response to anti-PD-1 as an approach to achieve a more clear perspective of immune suppressive mechanisms that may account for the recurrence and progression of 4MOSC1 tumors in mice treated with anti-PD-1. We then engrafted sensitive (parental) and anti-PD1 (αPD-1) resistant 4MOSC1 cells and treated mice with or without anti-PD-1. Among all immune cells examined, αPD-1 resistant tumors recruited significantly more $Ly6G^{hi}$ PMN-MDSCs than the parental cell line, and treatment with anti-PD-1 in these αPD-1 resistant tumors significantly increased immunosuppressive PMN-MDSCs, suggesting that MDSCs may be deterring cytotoxic immune responses. Moreover, upon anti-PD1 treatment, there were significant increases in LAG-3 and TIM-3, and greater increase in CTLA-4 in CD8 T cells isolated from the αPD-1 resistant tumors when compared to their parental tumors, while increases in LAG-3 in CD4 T cells was comparable between parental and αPD-1 resistant tumors (**Supplementary Figure S3.8**). Altogether, these data suggest that recurrence and acquired resistance to anti-PD-1 in 4MOSC1 tumors may be conferred by increased MDSC recruitment and higher expression of additional CD8 T cell inhibitory receptors.

3.3.4 Immune modulation by intratumoral (*in situ*) delivery of ICB.

A defining feature of most HNSCCs is the superficial and mucosal localization of the disease. Unlike many other cancer types, most HNSCC patients have tumors that can be readily visualized and accessed by surgeons, providing an opportunity to use intratumoral (IT) drug delivery. To investigate whether IT injection of anti-PD-1 has improves activity in our model, we

compared the effectiveness of using a lower dose anti-PD-1 treatment with standard systemic delivery. We found that mice treated with just half the dose of anti-PD-1 locally showed similar anti-tumor responses compared to mice with full dose systemic treatment (**Figure 3.4A**). Furthermore, immunofluorescence analysis revealed that IT delivery led to significantly higher PD-1 antibody distribution in tumors and cervical lymph nodes and lower distribution in the spleen as a peripheral organ when compared to systemic delivery (**Figure 3.4B**).

To investigate if there are local, differential immune signature alterations associated with IT drug delivery, we performed a comprehensive immune profiling using the nCounter PanCancer Mouse Immune Profiling gene expression platform (NanoString Technologies). Using 770 immune-related genes, we profiled immune cells infiltrating the tumor following treatment with systemic or intratumoral anti-PD-1, and compared it with another FDA-approved immunotherapy, CTLA-4 blockade. Relative to the tongues from healthy mice, mice bearing 4MOSC1 tumors have elevated expression of a majority of immune cell-associated genes. While systemic anti-PD-1 treatment increased the T cell signature, IT delivery enhanced it further while also increasing gene expression of natural killer cells and genes related to cytotoxic immune cells (**Figure 3.4C**). Interestingly, albeit used initially as a control, this analysis revealed that IT treatment with anti-CTLA-4 led to even more robust T cell, cytotoxic cell, and macrophage responses, and increased CD8 T cell tumor infiltration (**Figure 3.4C, 3.4D**). In addition, while anti-PD-1 increased Treg associated gene signatures, anti-CTLA-4 appears to diminish it, which was confirmed by flow cytometry analysis of treated tumors (**Figure 3.4C, 3.4E**). In order to further explore the role of Tregs in 4MOSC1 tumors, we utilized the *FoxP3*^{DTR} transgenic mice that have been widely used to study the immunosuppressive role of Tregs in cancer (34). Treg depletion with diphtheria toxin (DT) led to significant reduction of tumor growth, and combination of Treg depletion with anti-PD-1 led to complete responses in most mice (**Supplementary Figure S3.9**). This strongly suggests that Tregs may prevent the full therapeutic activity of anti-PD-1, and that the reduction of the

immunosuppressive activity of Tregs may represent a mechanism explaining the higher therapeutic responses to anti-CTLA-4 treatment (**Supplementary Figure S3.9**).

3.3.5 The majority of 4MOSC1 lesions respond to anti-CTLA-4.

Given that immune stimulatory effects were enhanced following anti-CTLA-4 treatment compared to anti-PD-1 treatment, we sought to determine whether mice with 4MOSC1 tumors can also respond to CTLA-4 blockade. CTLA-4 blockade systemically and IT elicited a robust anti-tumor effect, with 90% of the mice exhibiting a CR (**Figure 3.5A** and **Supplementary Figure. S3.10A**) and efficiently resisted engraftment when re-challenged with fresh 4MOSC1 cells. Similar to anti-PD-1 treatment, IT delivery resulted in significantly higher anti-CTLA-4 antibody distribution in tumors and cervical lymph nodes and lower distribution in the spleen (**Figure 3.5B**). Anti-tumor immunity of anti-CTLA-4 is also CD8 dependent, as CTLA-4 inhibition resulted in significantly increased infiltration of and IFNγ production by $CD8^+$ T cells (**Figure 3.5C, Supplementary Figure 3.11**), and its anti-tumor activity was abolished by depletion of CD8 T cells (**Supplementary Figure 3.10B**). Adding to this, when tumor-infiltrating CD8 T cells were isolated and cultured with tumor cells *in vitro*, they were able to kill the tumor cells, and CD8 T cells from anti-PD-1- and anti-CTLA-4-treated mice were able induce significantly more cancer cell death (**Figure 3.5D, 3.5E**). Of interest, 4MOSC2 tumors also failed to respond to anti-CTLA-4 treatment (**Supplementary Figure 3.10C**), providing a model that is resistant to both forms of immunotherapy for future exploration of immunotherapy resistance and the use of strategic combinatorial modalities.

3.4 Discussion

HNSCC is an immunosuppressive disease, in which the tumor deploys multiple mechanisms to evade immune surveillance and antitumor immune responses through the accumulation of immunosuppressive cytokines, impairment of cytotoxic activity and antigen-presenting function, and induction of T cell exhaustion (reviewed in (12)). Based on this knowledge, numerous immunotherapeutic strategies were developed, including ICB, cancer

vaccines, therapeutic cytokines, adoptive T-cell transfer, and adjuvants that may trigger innate immune responses such as TLR and STING agonists (reviewed in (12)). Clearly, suitable experimental systems that can model clinical responses are urgently needed to study and improve the effectiveness of immune oncology approaches in HNSCC. Here, we developed a panel of C57Bl/6-derived syngeneic cells that resemble human HNSCCs closely with unique features: (i) The HNSCC cells have nearly identical tobacco-associated mutational signatures and genomic aberrations; (ii) they can be orthotopically transplanted into the tongue of immunocompetent C57Bl/6 mice; (iii) the tumors are histologically HNSCCs with abundant lymphangiogenesis and potential for lymph node metastasis; and (iv) the tumors exhibit abundant immune infiltration and are immunogenic, the latter as judged by their ability to induce immunological memory when used to vaccinate mice. These animal models may provide an opportunity to investigate the mechanisms driving intrinsic and acquired resistance to IO agents, as well as to identify novel therapeutic options increasing the response of currently available immunotherapies in HNSCC patients.

Tobacco use is one of the major risk factors for initiation and progression of HNSCC, and serves as an important prognostic factor for survival and mortality after cancer diagnosis (reviewed in (35)). In a recent study, we analyzed somatic mutations and DNA methylation in 5243 samples comprising of cancers for which tobacco smoking confers an elevated risk, which helped define the human tobacco-associated cancer signature (19). Remarkably, although tobacco smoke is made up of thousands of chemicals, including more than 60 carcinogens (17), we found that 4NQO exposure was sufficient to mimic the tobacco carcinogenic signature. This is supported by compelling evidence demonstrating that 4NQO-induced SCC lesions exhibit near identical association (~94%) with the tobacco mutational landscapes, recapitulating human HNSCC. This is in contrast with the mutational signature caused by DMBA (<40% similarity), which although representing a widely used tobacco carcinogen (26), may not be as effective as 4NQO in reflecting the human tobacco-associated genetic signatures (19).

In this regard, currently available syngeneic HNSCC models include SCCVII cells, HPV+ SCC cells designated MEER (36) and a panel of mouse HNSCC cell lines from DMBA-treated mice (MOC1 and MOC2) (37). Though widely used, SCCVII cells are in fact derived from a spontaneously formed skin SCC lesion in C3H mice (38). MEER and MOC1/MOC2 models develop tumors in immune competent C57Bl/6 mice when implanted in the flanks, which may not reflect the HNSCC TIME, albeit MOC1/MOC2 can also grow tumors orthotopically even if their immune status has not been characterized in this anatomical location (39). These tumors are driven by *Ras* oncogenes (*Kras* in MEER and MOC2, and *Hras* in MOC1) (36,37,40), which are very potent oncogenic drivers, but infrequently (<6%) mutated in human HNSCC (41), albeit higher frequencies have been reported in some demographic groups (42). Thus, although quite useful for cancer immunology studies, these cellular systems may not mimic fully the tobacco-induced carcinogenic process driving most human HNSCCs. Despite the fact that these cell lines have dramatically different genomic alteration profiles, some of these cells respond to ICB similarly to 4MOSC1 cells, suggesting that the determinants of immune responses may be independent of the underlying driving mutations that lead to HNSCC formation. Nonetheless, neither *Hras*, *Kras*, nor *Nras* genes are mutated in the 4MOSC panel, suggesting that these cells may harbor pathway specific alterations likely more relevant to human malignancy. Taken together, the unique features of our syngeneic HNSCC animal model provide a resource to investigate novel IO pre-clinical approaches for HNSCC treatment.

Seminal studies have shed light on T cell exhaustion in human cancers, where CD8 T cells lose proliferative capacity, the ability to produce tumor necrosis factor (TNFα), interleukin-2 (IL-2), and interferon-γ (IFNγ), and upregulation of inhibitory checkpoint receptors, such as PD-1 and CTLA-4(9-11). Recently, the successes of ICB to reverse T cell exhaustion in multiple cancers illustrates the potential of therapeutic strategies targeting these negative regulatory pathways (43). In the clinic, PD-1 blockade offers 10~20% clinical improvement in HNSCC (13-15), which was modeled similarly in our study where anti-PD-1 led to regression of 4MOSC1

tumors in only ≤20% of mice. The increase in CD8 T cells seemed to provide only temporary cytotoxic activity in mice treated with anti-PD-1, as we observed reoccurrence of tumors in the majority of treated mice. Surprisingly, we saw enhanced anti-tumor responses with anti-CTLA-4 treatment, where most 4MOSC1 tumor bearing mice showed complete responses and no tumor reoccurrence. The resulting increase in CD8 T cells following anti-CTLA-4 treatment confirmed that targeting checkpoints may revitalize immunological effect of exhausted T cells, at least at the cellular level. One explanation for these strikingly different responses could be that PD-1 blockade may induce compensatory upregulation of $FoxP3^+$ Treg cells (44,45), as it occurred in our anti-PD-1-treated mice but not in anti-CTLA-4-treated mice. In fact, CTLA-4 inhibition led to significantly lower levels of $FoxP3^+$ Treg cells in the tumors. In this regard, while both blocking antibodies can lead to cytotoxic CD8 T cell responses, anti-CTLA-4 may provide additional anti-tumor immunity by depleting Tregs that mediate an immune-suppressive environment (reviewed in (46)). Moreover, PD-1 blockade predominantly activates T cells within the tumor, whereas anti-CTLA-4 may activate T cells primarily in the lymph nodes (46), in which high levels of anti-CTLA-4 can be achieved by IT delivery. These and yet to be identified mechanisms may underlie the increased response to anti-CTLA-4 in some anti-PD-1 refractory HNSCC lesions, whose elucidation may provide biomarkers for the selection of patients that may benefit from anti-CTLA-4 treatment after failing to anti-PD-1 therapy.

In this regard, the recent CONDOR trial demonstrated no benefit to adding tremelimumab, a humanized monoclonal antibody against CTLA-4, to durvalumab, which blocks PD-L1, in patients with relapsed HNSCC (47). However these are unique biological agents, as tremelimumab may display lower clinical activity than the most frequently used anti-CTLA-4 antibody, ipilimumab (48). In addition, the use of ICB in earlier stages of disease may have improved activity compared to relapsed/metastatic setting as there is potentially less immune editing and immune evasion in earlier stages of disease. In addition, one limitation of using anti-CTLA-4 for a variety of cancers in the clinic is its toxicity (49). Systemic delivery of IO agents have

been shown to be responsible for severe immune related adverse events (irAEs), such as colitis, dermatitis, uveitis, and hypophysitis (49). These adverse events are very toxic, at times irreversible and can even be life-threatening. With this in mind, IT injection may enhance tumor-specific T cell responses while reducing significant systemic exposure to healthy tissue and off-target toxicities (50,51). In addition, IT immunotherapy usually causes *in situ* priming of antitumor immunity, which may allow a patient's own tumor cells to be used as a therapeutic vaccine (50,51). In our study, a lower dose of IT anti-PD-1 showed similar therapeutic effects as systemic delivery of a higher dose, and IT anti-CTLA-4 led to complete regression of most 4MOSC1 tumors that are primarily refractory to anti-PD-1. Additionally, IT injection led to higher distribution of the antibody in the tumor and cervical lymph nodes, but less in the spleen as a surrogate for distribution in peripheral organs. This suggests that the IT route, which is feasible in HNSCC, may serve as a more effective and less toxic therapeutic strategy for this tumor type, a possibility that may have readily applicable clinical implications, and hence warrant further investigation.

Certainly, some HNSCC tumors have minimal immune infiltration, and may require a multipronged approach to facilitate immune recruitment and activation of the anti-tumor immune response (52,53). Other HNSCC lesions are completely refractory to ICB, even if highly immune infiltrated. In this regard, mice implanted with 4MOSC2 failed to respond to anti-PD-1 and anti-CTLA-4 therapy, likely due to the presence of abundant immune suppressive MDSC (30) in the TIME, which may restrict DC and/or $CD8^+$ T cell function in addition to promoting T cell exhaustion. Therefore, this 4MOSC model system is ideal for investigating mechanisms of immunotherapy resistance, as well as testing novel multimodal immunotherapies and/or optimization of potential combinations of ICB with chemo- and radiotherapies. Altogether, our findings suggest that our novel syngeneic HNSCC animal models, which strongly mimic tobacco-associated HNSCC and typical clinical situations, may provide experimental tools to investigate interplays between HNSCC and the immune system as well as provide unique opportunities to identify more effective

therapeutic strategies for tobacco-associated HNSCC, which are associated with poor prognosis and reduced response to most currently available treatment options.

3.5 Methods

3.5.1 Reagents

4NQO (4-Nitroquinoline-1-oxide) was purchased from Sigma-Aldrich, dissolved in propylene glycol (Sigma-Aldrich) as a stock solution (4 mg/mL) and stored at 4°C. PD-1 antibody (clone J43, catalog #BE0033-2), CTLA-4 antibody (clone 9H10, catalog #BP0131), isotype antibody (catalog # BE0091) and CD8 depletion antibody (Clone YTS 169.4, catalog #BE0117) were obtained from Bio X Cell (West Lebanon, NH, USA). Fluorochrome-conjugated antibodies were purchased from BioLegend and BD Biosciences.

3.5.2 Establishment of cell lines and tissue culture

Female C57Bl/6 mice (4–6 weeks of age and weighing 16–18g) were purchased from Charles River Laboratories (Worcester, MA, USA). 4NQO was diluted in the drinking water to a final concentration of 50 µg/mL to animals and was changed weekly. After 16 weeks, all animal cages were reverted to regular water until week 22. Animals were euthanized on week 22 for tissue retrieval. Single lesions were dissected, digested and cells were isolated to establish 4MOSC cell lines.

3.5.3 DNA sequencing, genomic, and tobacco signature analysis.

Raw sequencing data were aligned to the mm10 reference genome using BWA(54). Somatic mutations were identified by comparing the sequencing data from each cancer sample to the sequencing data from a normal tissue derived from the tail of one of the mice (all mice were genetically identical). To ensure robustness of the results, a consensus variant calling strategy was leveraged in which somatic mutations were identified using three independent bioinformatics tools: Strelka2 (55), Varscan2 (56), and GATK4 Mutect2 (57). Any mutation found in two out of the three variant callers was considered a bona fide somatic mutation. Additional filtering to remove any residual germline contamination was applied and any mutation found in Mouse

Genome Project or shared among all four cancers was discarded. Somatic mutational profiles were derived using the immediate sequencing context by evaluating the base 5' and the base 3' to each single point mutation. Additionally, transcriptional strand bias was evaluated by considering all protein coding genes. Mutational signatures were extracted using our previously developed computational framework SigProfiler (24,25). SigProfiler can be downloaded freely from: https://www.mathworks.com/matlabcentral/fileexchange/38724-sigprofiler.

Gene mutation analyses were performed comparing our 4 syngeneic cells to a HNSCC provisional dataset containing 243 HPV-negative tumor samples from the publicly available consortium, The Cancer Gene Atlas (TCGA) (40). Mutational plots of p53 mutations observed in characterized HNSCC samples from TCGA and 4 of our syngeneic cell lines were summarized using the 'lolipop' mutation diagram generator (58).

3.5.4 *In vivo* mouse experiments and analysis

All the animal studies using HNSCC tumor xenografts and oral carcinogenesis studies were approved by the Institutional Animal Care and Use Committee (IACUC) of University of California, San Diego, with protocol ASP #S15195. Mice at Moores Cancer Center, UCSD are housed in micro-isolator and individually ventilated cages supplied with acidified water and fed 5053 Irradiated Picolab Rodent Diet 20 from Lab Diet. Temperature for laboratory mice in our facilitiy is mandated to be between 65-75°F (~18-23°C) with 40-60% humidity. All animal manipulation activities are conducted in laminar flow hoods. All personnel are required to wear scrubs and/or lab coat, mask, hair net, dedicated shoes and disposable gloves upon entering the animal rooms. 4MOSC1 and 4MOSC2 cells were transplanted (1 million per mouse) into the tongue of female C57Bl/6 mice (4–6 weeks of age and weighing 16–18g). When tumors were formed (on day 5-6), the mice were first randomized into groups. For drug treatment, the mice were treated by either intraperitoneal (IP) or intratumoral (IT) injection with isotype control antibody, PD-1 antibody, or CTLA-4 antibody (IP 10mg/kg, IT 5mg/kg, three times a week) for three weeks. The mice were then euthanized after the completion of the treatment (or when

control-treated mice succumbed to tumor burdens, as determined by the ASP guidelines) and tumors were dissected for flow cytometric analysis or histologic and immunohistochemical evaluation.

For *Foxp3*^{DTR} mice, we use *Foxp3*-GFP-DTR mice (C57BL/6-Tg(Foxp3-DTR/EGFP); from JAX in C57BL/6 background) (6–8 weeks of age and weighing 18–22g). To deplete Tregs, mice were injected intraperitoneally with 500 ng of diphtheria toxin (DT; Sigma-Aldrich), diluted in PBS.

3.5.5 Chemokine expression profile

Tongue tumors were dissected and lysed in RIPA lysis buffer supplemented with protease and phosphatase inhibitors. Samples were run on the Mouse Chemokine Array 44-Plex (EVE Technologies, Canada).

3.5.6 Immunofluorescence and image quantification

Briefly, tissues (tongue, cervical lymph nodes and spleen) were harvested, fixed, and paraffin embedded. Slides were stained for CK5 (Fitzgerald, 20R-CP003) (1:500) and CD8 (abcam, ab22378) (1:400) antibodies. Quantification of immune-infiltration was done using QuPath, an open source software for digital pathology image analysis (59). For the quantification, at least 3 regions of interest (ROI) were selected for each condition and the percentage of positive cells for the CD8 marker was calculated. In order to quantify the immune-fluorescent-stained Foxp3 and CD8 positive cells in the *Foxp3*^{DTR} mice, we quantified the number of positive cells in each ROI. CD8 antibody (catalog # ab22378) (1:400) was purchased from Abcam (Cambridge, United Kingdom) and FoxP3 antibody (catalog #D608R) (1:200) was purchased from Cell Signaling Technology (Danvers, MA).

3.5.7 TIL isolation and flow cytometry

Tumors were dissected, minced, and re-suspended in complete media (DMEM with 10% FBS and 1% antibiotics) supplemented with Collagenase-D (1mg/mL; Roche) and incubated at 37°C for 30 minutes with shaking to form a single-cell suspension. Tissue suspensions were washed with fresh media and passed through a 100-μm strainer. Samples were washed with PBS

and immediately processed for live/dead cell discrimination using BD Horizon™ Fixable Viability Stain 510. Cell surface staining was done for 30 minutes at 4 degrees with the following antibodies (all from BioLegend, San Diego, CA): CD45 (30-F11) (1:100), CD3 (145-2C11) (1:400), CD8a (53-6.7) (1:100), CD4 (RM4-4) (1:400), NK1.1 (PK136) (1:400), CD24 (M1/69) (1:100), MHCII (M5/114.15.2) (1:800), Ly6-G (1A8) (1:400), Ly6-C (HK1.4) (1:100), F4/80 (T45-2342) (1:100), CD103 (2E7) (1:100), CD11b (M1/70) (1:200), CD11c (HL3) (1:100), PD-1 (29F.1A12) (1:100), TIM-3 (B8.2C12) (1:100), and CD44 (IM7) (1:100). Intracellular staining for inhibitory receptors LAG-3 and CTLA-4 was done using the BD Cytofix/Cytoperm kit and stained with the LAG-3 (C9B7W) (1:100) and CTLA-4 (UC10-4B9) (1:100) antibodies. Intracellular staining for FOXP3 was performed using the eBioscience FOXP3/Transcription Factor Buffer Set from Invitrogen and stained with the FOXP3 (MF23) antibody. All flow cytometry data acquisition was done using BD LSRFortessa and analyzed using FlowJo software. TIL count was determined using BD Trucount™ tubes. Immune cells were identified by the following characteristics: cytotoxic T cells ($CD45^+Thy1.2^+CD8^+$), helper T cells (CD45+Thy1.2+CD4+), Treg ($CD45^+Thy1.2^+CD4^+FoxP3^+$), NK cells ($CD45^+Thy1.2^-NK1.1^+$), macrophages ($CD45^+Thy1.2^-NK1.1^-CD11b^+CD11c^-LY6C^{low}LY6G^{low}CD24^+F4/80^+$), PMN-MDSCs ($CD45^+Thy1.2^-NK1.1^-CD11b^+CD11c^-LY6C^{low}LY6G^+$), and M-MDSCs ($CD45^+Thy1.2^-NK1.1^-CD11b^+CD11c^-LY6C^+LY6G^{low}$). A representative flow cytometry gating strategy is depicted in **Supplementary Figure S3.12**.

3.5.8 Antigen specific T-cell cytotoxicity assay

4MOSC1 tumors were mechanically and enzymatically digested as described above and tumor-derived T cells were isolated by the Murine $CD8a^+$ T Cell Isolation Kit from Miltenyi Biotec (Bergisch Gladbach, Germany). 4MOSC1 cells were plated in keratinocyte media in the 24-well µ-plate from ibidi (Grafelfing, Germany) and when cells grew to 60% confluency, T cells were added at a 1:10 cancer cell to T cells ratio. The viability dye, DRAQ7, was added in the culture medium to discriminate cancer cell killing by T cells, and T cells were labelled with Vybrant Dil

Cell-Labeling Solution from Invitrogen (Carlsbad, CA). Overnight live-imaging was captured in real time by the Zeiss LSM 880 confocal with Airyscan FAST.

3.5.9 NanoString analyses

RNA was isolated from tumor samples using the RNeasy Micro Kit (Qiagen 74004). Hybridization of samples was done according to the NanoString Hybridization Protocol for nCounter XT CodeSet Gene Expression Assays. Samples were run on the nCounter SPRINT Profiler with the nCounter PanCancer Mouse Immune Profiling gene expression platform. Analysis of gene expression was done using the Advanced Analysis module on the nSolver software.

3.5.10 Statistics and Reproducibility

Statistical data analyses, variation estimation and validation of test assumptions were carried out with GraphPad Prism version 7 statistical analysis program (GraphPad Software, San Diego, CA). All analyses were performed in triplicate or greater and the means obtained were used for independent t-tests, ANOVA, or longitudinal data analysis method. The asterisks denote statistical significance (non-significant or ns, $P>0.05$; *$P<0.05$; **$P<0.01$; and ***$P<0.001$). All the data are reported as mean ± standard error of the mean (S.E.M.). For all experiments, each experiment was repeated independently with similar results for at least 3 times.

3.5.11 Data Availability

The whole exome sequencing data of murine 4NQO-induced syngeneic cell lines have been deposited in the NCBI Sequence Read Archive (SRA) database under the accession code PRJNA575532. The whole exome sequencing data referenced during the study are available in a public repository from the NCBI SRA website. The source data underlying Figures 1b-e and Supplementary Figure 1 are provided as Supplementary Data 1-4 in Microsoft Excel format. All the other data supporting the findings of this study are available within the article and its supplementary information files and from the corresponding author upon reasonable request. A reporting summary for this article is available as a Supplementary Information file.

Chapter 3, in full, has been accepted for publication of the material in “Novel syngeneic animal model of tobacco-associated oral cancer reveals the activity of in situ anti-CTLA-4” in *Nature Communications*, 2019. Zhiyong Wang, Victoria H Wu, Michael M Allevato, Mara Gilardi, Yudou He, Juan Luis Callejas-Valera, Lynn Vitale-Cross, Daniel Martin, Panomwat Amornphimoltham, James Mcdermott, Bryan S Yung, Yusuke Goto, Alfredo A Molinolo, Andrew B Sharabi, Ezra EW Cohen, Qianming Chen, J Guy Lyons, Ludmil B Alexandrov, J. Silvio Gutkind. The dissertation author was the primary investigator and author of this paper.

3.6 Figures

Figure 3.1. Development of a novel syngeneic mouse model for oral cancer

(A) Experimental scheme of 4NQO syngeneic model. C57Bl/6 Mice were given 4NQO (50 µg/mL) in the drinking water for 16 weeks and then regular water until week 22. Cells were isolated from the lesions, cultured, and then implanted into the tongue of wild-type C57Bl/6 mice. The Scheme was drawn by Atsuko Yagi and Michael M. Allevato. (B) Mutational signatures associated with tobacco smoking. The somatic mutational profiles of the four lesions from mice exposed to 4NQO were correlated to known mutational signatures in human cancer (Pearson correlation > 0.93). Top, Signature 4 extracted from cancers associated with tobacco smoking, this signature was found only in cancer types in which tobacco smoking increases risk and mainly in those derived from epithelia directly exposed to tobacco smoke19; Middle, the pattern of a mutational signature of lesions from mice exposed to 4NQO, compilation of all 4 samples analyzed; Bottom, the pattern of a mutational signature of lesions from mice exposed to DMBA. The similarity between signature tobacco smoking associated HNSCC and signature 4NQO is 93.9%; and the similarity between signature tobacco smoking associated HNSCC and signature DMBA is only 39.7%. (C) Percentage of somatic substitutions located in translated or untranslated in tobacco smoking associated HNSCC patients (left), 4NQO derived lesions (middle) and DMBA derived lesions (right). (D) Graphical matrix representation of the individual mutations in 4 syngeneic cell lines (4MOSCs) isolated from lesions from mice exposed to 4NQO. Listed are the alterations most frequently observed in human HNSCC and the corresponding percentage of mutations. Mutations (red), or no mutations (blue) are listed in rows and four different cell lines are in column. (E) Mutational Plot of *TP53* mutations in 243 HPV-negative tumor samples from TCGA (top) and of 4 syngeneic cell lines (4MOSCs) (bottom). Frequency of mutation is depicted by height of lollipop, blue circles represent mutations unique to human or mouse, and red circles depict mutations in common between human and mouse HNSCCs.

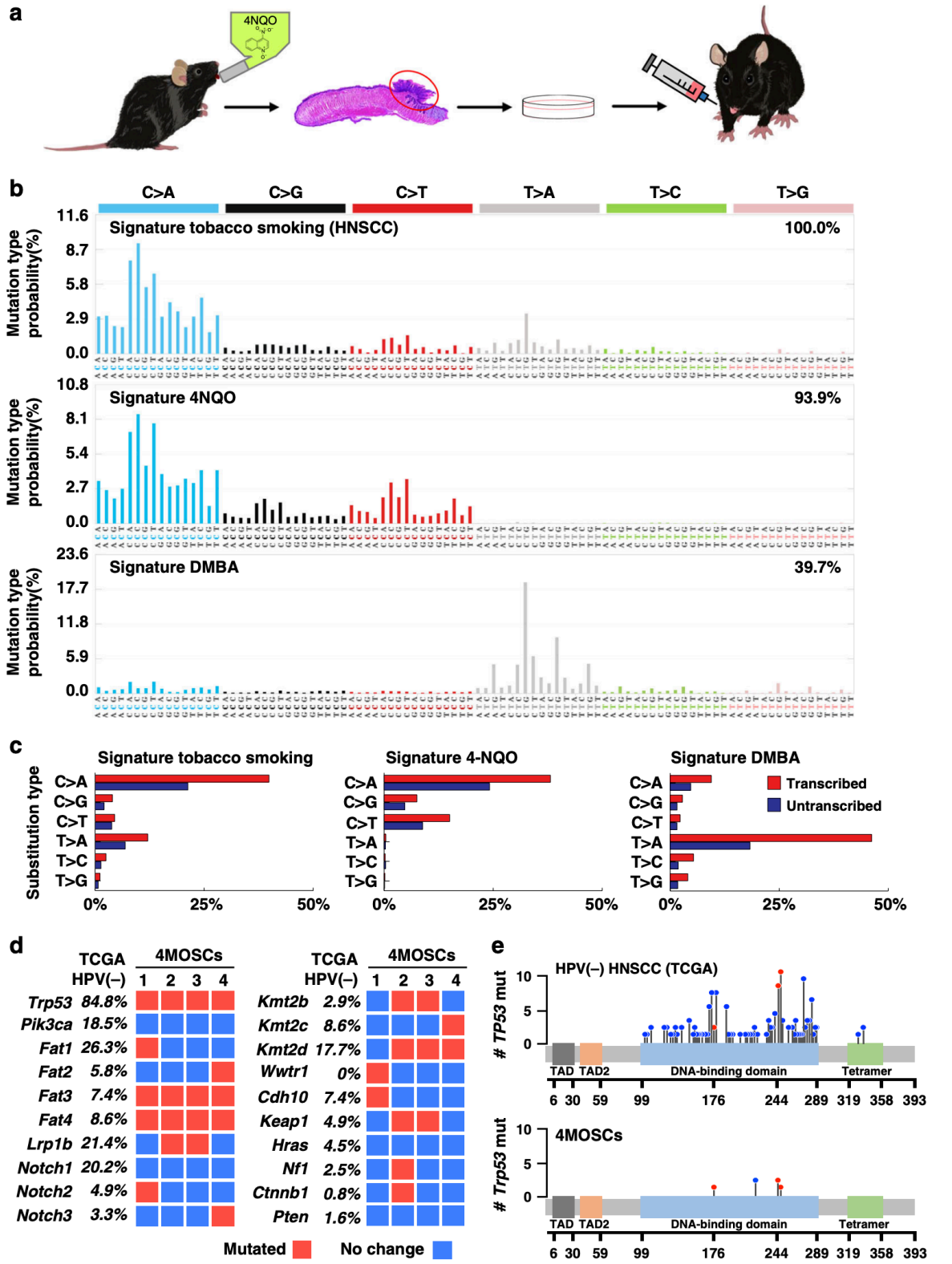
a
4NQO
b
C>A
C>G
C>T
T>A
T>C
T>G
Signature tobacco smoking (HNSCC)
100.0%
Signature 4NQO
93.9%
Signature DMBA
39.7%
Mutation type probability(%)
c
Signature tobacco smoking
Signature 4-NQO
Signature DMBA
Substitution type
Transcribed
Untranscribed
0%
25%
50%
d
TCGA HPV(–)
4MOSCs
1 2 3 4
Trp53 84.8%
Pik3ca 18.5%
Fat1 26.3%
Fat2 5.8%
Fat3 7.4%
Fat4 8.6%
Lrp1b 21.4%
Notch1 20.2%
Notch2 4.9%
Notch3 3.3%
Kmt2b 2.9%
Kmt2c 8.6%
Kmt2d 17.7%
Wwtr1 0%
Cdh10 7.4%
Keap1 4.9%
Hras 4.5%
Nf1 2.5%
Ctnnb1 0.8%
Pten 1.6%
Mutated
No change
e
HPV(–) HNSCC (TCGA)
# TP53 mut
TAD TAD2
DNA-binding domain
Tetramer
6 30 59 99 176 244 289 319 358 393
4MOSCs
Trp53 mut

Figure 3.2. Characterization of 4NQO-induced murine oral squamous cell model.

(A) Left panel, C57Bl/6 mice were implanted with $1x10^6$ of either 4MOSC1 or 4MOSC2 cells into the tongue. Tongue lesions when the tumor volume reached approximately 100 mm^3. Middle panel, representative H&E-staining of histological tissue sections from mouse tongues with 4MOSC1 or 4MOSC2 tumors. Right, representative pictures of tumors stained to show expression of cytokeratin 5 (CK5, green) and DAPI (blue) (n = 3 mice per group). (B) Top panel, representative H&E stain of a non-metastatic cervical lymph node from mice with 4MOSC1 tumors. Bottom panel, representative H&E stain of a metastatic cervical lymph node from mice with 4MOSC2 tumors. Metastatic growth of 4MOSC2 cells into the lymph node is depicted with a dotted line in the bottom area (n = 5 mice per group). (C) Representative tumor tissue sections stained for LYVE1 by immunohistochemistry in 4MOSC1 or 4MOSC2 tumors (n = 3 mice per group). (D) Absolute number of immune cells infiltrating 4MOSC1 or 4MOSC2 tumors. Shown is the average number of live cells infiltrating per mm^3 of tumor (n = 3 mice per group). (E) Immunofluorescent staining of CK5 and CD8 to show squamous cell character of the lesion and CD8 infiltration in mice with 4MOSC1 or 4MOSC2 tumors, respectively (n = 3 mice per group) (CK5, green; CD8, red; DAPI, blue). (F-G) 4MOSC1 or 4MOSC2 tumors were isolated from mice and mechanically and enzymatically digested. Single cell suspension was then stained with CD45, Nk1.1, CD3, CD8, CD44, PD-L1, PD-1, CTLA-4, LAG-3 and TIM-3 fluorescent labeled antibodies and analyzed by flow cytometry. Shown are representative flow cytometry plots of (f) the frequency of tumor cells (CD45 negative) expressing PD-L1 and (G) the frequency of $CD8^+/CD44^+$ cells expressing inhibitory receptors PD-1, CTLA-4, LAG-3 and TIM-3 in individual tumors (n = 4 mice per group). Contour plots of lymphocytes from tumor (green), and corresponding cervical lymph nodes (blue), and blood (red) are overlaid and the frequencies of tumor $CD8^+/CD44^+$ T cells expressing each inhibitory receptor are shown (n = 4 mice per group).

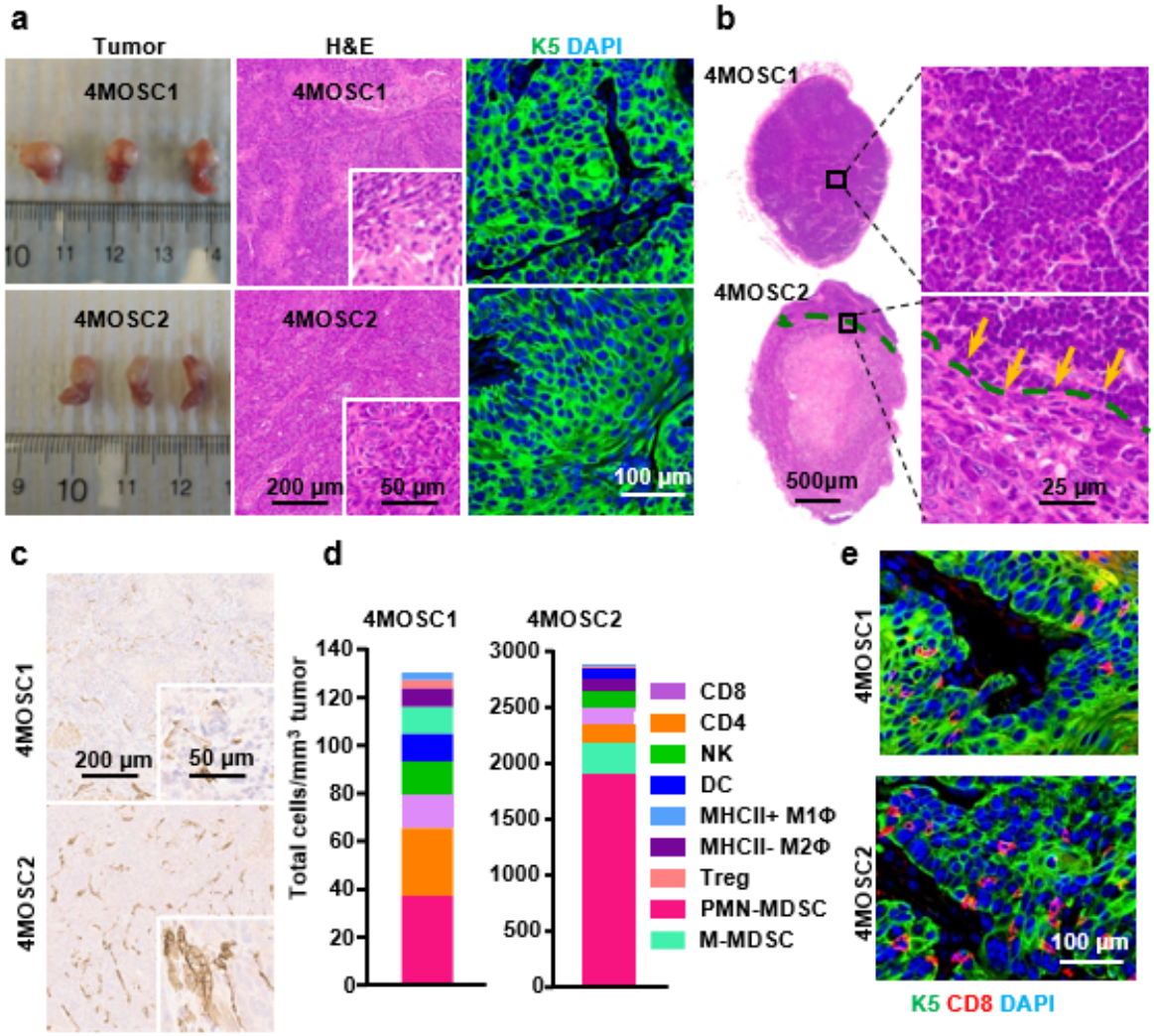
a
Tumor
H&E
K5 DAPI
4MOSC1
4MOSC2
200 μm
50 μm
100 μm
b
4MOSC1
4MOSC2
500μm
25 μm
c
4MOSC1
4MOSC2
200 μm
50 μm
d
4MOSC1
4MOSC2
Total cells/mm3 tumor
CD8
CD4
NK
DC
MHCII+ M1Φ
MHCII- M2Φ
Treg
PMN-MDSC
M-MDSC
e
4MOSC1
4MOSC2
100 μm
K5 CD8 DAPI
f
4MOSC1
PD-L1
CD45
8.95
4MOSC2
PD-L1
CD45
0.86
g
4MOSC1
CTLA-4
PD-1
0.45
34.7
5.12
59.7
LAG-3
TIM-3
15.7
58.6
18.8
6.91
4MOSC2
CTLA-4
PD-1
0.86
21.7
11.7
65.7
LAG-3
TIM-3
15.1
26.3
47.7
10.8
Tumor
Lymph nodes
Blood

Figure 3.3. Variable responses to anti-PD-1 in mice with 4MOSC1 tumors.

Variable responses to anti-PD-1 in mice with 4MOSC1 tumors. (A) C57Bl/6 mice were implanted with $1x10^6$ of 4MOSC1 cells into the tongue. After tumors reached ~30 mm^3, mice were treated IP with 10mg/kg of isotype control or anti-PD-1 (n = 10 per group). Individual growth curves of 4MOSC1 tumor-bearing mice are shown. (B) A Kaplan-Meier curve showing the survival of mice from panel a. The death of animals occurred either naturally, when tumor compromised the animal welfare, or when tumor volume reached 100 mm^3 (n = 10 mice per group; Log-Rank/Mantel-Cox test.). (C) Absolute number of live $CD45^+CD3^+CD8^+$ T cells infiltrating 4MOSC1 tumors with or without anti-PD-1 treatment. Shown is the average of the number of live CD8 T cells infiltrating per mm^3 of tumor (n = 4 mice per group; two-sided Student's *t*-test; data are represented as mean± SEM). (D) Immunofluorescent staining of CD8 highlights an increase in CD8 T cell recruitment with anti-PD-1 treatment. Shown is the average CD8 positivity was by 3 regions of interest (ROI) per mouse.(n = 3 mice per group; two-sided Student's *t*-test; data are represented as mean± SEM). (E) Dependency of anti-PD-1 on CD8 T cells. C57Bl/6 mice were treated with CD8 T cell depleting antibody daily for 3 days before tumor implantation and then once a week after. Mice were then implanted with $1x10^6$ of 4MOSC1 cells into the tongue. After tumors reached ~30 mm^3, mice were treated IP with 10mg/kg isotype control or 10mg/kg anti-PD-1 (n = 5 per group). Individual growth curves of 4MOSC1 tumor-bearing mice are shown. (F) Immunofluorescence staining of CK5 and Ki67 in cervical lymph nodes of control or CD8-depleted 4MOSC1-bearing mice. Metastatic lesions in the lymph nodes showed abundant $Ki\text{-}67^+$ proliferating tumor cells (n = 5 mice per group). (g) C57Bl/6 mice were implanted with $1x10^6$ of 4MOSC2 cells into the tongue. After tumors reached ~30 mm^3, mice were treated IP with 10mg/kg isotype control or 10mg/kg anti-PD-1 (n = 5 per group). Individual growth curves of 4MOSC2 tumor-bearing mice are shown.

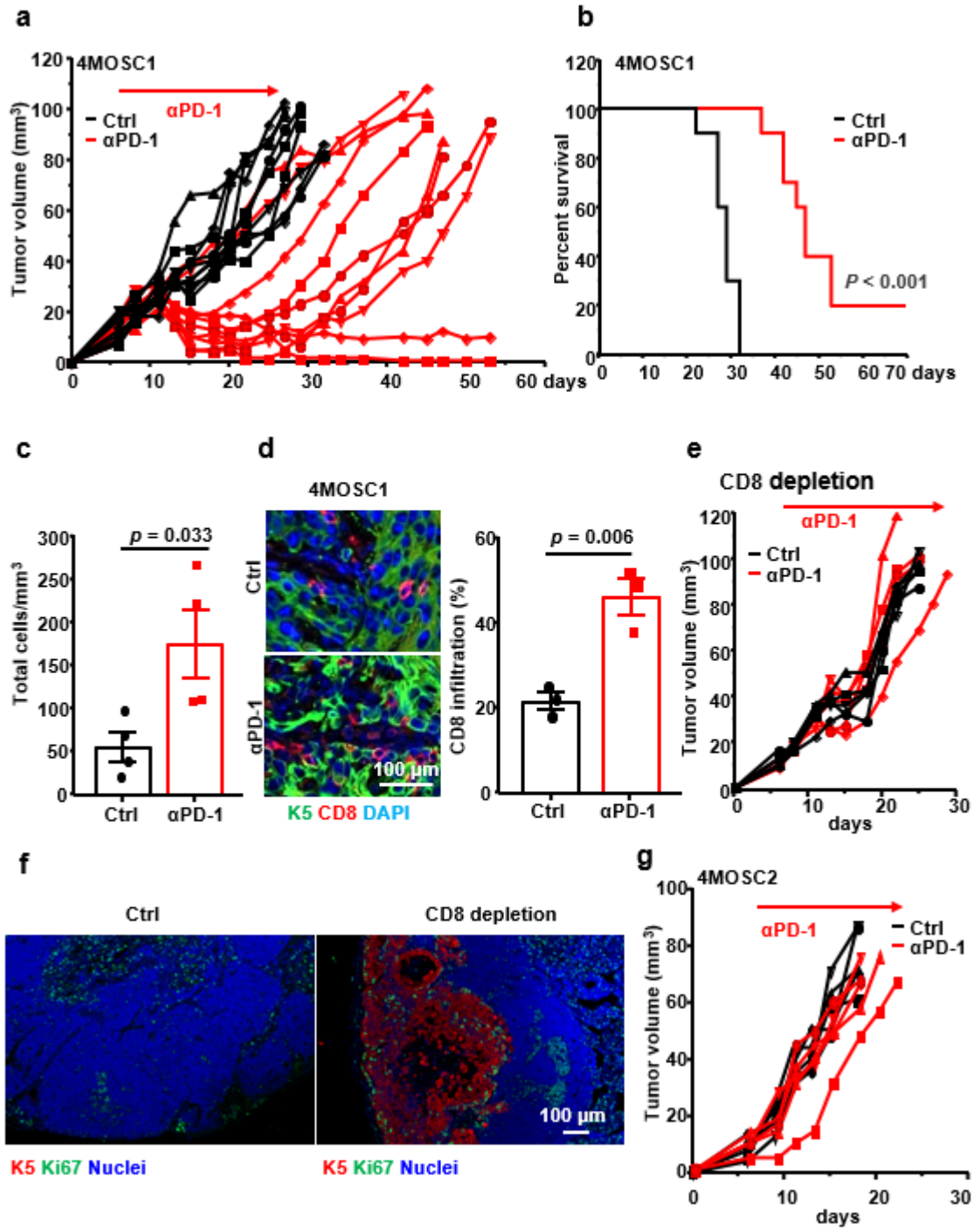
a
4MOSC1
Ctrl
αPD-1
αPD-1
Tumor volume (mm³)
60 days
b
4MOSC1
Ctrl
αPD-1
Percent survival
P < 0.001
60 70 days
c
p = 0.033
Total cells/mm³
Ctrl
αPD-1
d
4MOSC1
Ctrl
αPD-1
100 μm
K5 CD8 DAPI
p = 0.006
CD8 infiltration (%)
Ctrl
αPD-1
e
CD8 depletion
αPD-1
Ctrl
αPD-1
Tumor volume (mm³)
days
f
Ctrl
CD8 depletion
100 μm
K5 Ki67 Nuclei
K5 Ki67 Nuclei
g
4MOSC2
αPD-1
Ctrl
αPD-1
Tumor volume (mm³)
days

Figure 3.4. Efficacy of intratumoral delivery of immune oncology agents.

(A) Left panel, C57Bl/6 mice were implanted with $1x10^6$ of 4MOSC1 cells into the tongue. After tumors reached ~30 mm^3, mice were either treated IP or by intratumoral (IT) delivery of PBS, IP with 10mg/kg or IT with 5mg/kg anti-PD-1. Shown is the average volume of each tumor (n = 4 mice per group; two-sided Student's *t*-test; data are represented as mean± SEM). Right panel, representative pictures of tongues from mice in panel A with tumors depicted with a dotted line. (B) Distribution of anti-PD-1 antibody in mice with 4MOSC1 tumors using IP or IT delivery of the treatment. Staining for anti-hamster IgG showed the localization of anti-PD-1 antibody in the tongue, lymph nodes and spleen of treated mice (n = 4 mice per group). (C) RNA from each tumor was isolated and comprehensive immune profiling was analyzed using the NanoString nCounter PanCancer Mouse Immune Profiling gene expression platform. The Advanced Analysis module of the nSolver software was used to analyze genes associated with listed immune cells and given a score. Shown is the Z-score of each cell profile score (n = 3 mice per group). (D) Absolute number of live $CD45^+CD3^+CD8^+$ T cells infiltrating 4MOSC1 tumors with or without anti-PD-1 or anti-CTLA-4 treatment. Shown is the average of the number of live CD8 T cells infiltrating per mm^3 of tumor (n = 3 mice per group; two-sided Student's *t*-test; data are represented as mean± SEM). (E) Frequency of live $CD45^+CD3^+CD4^+$ $FoxP3^+$ Tregs infiltrating 4MOSC1 tumors with or without anti-PD-1 or anti-CTLA-4 treatment. Left panel, a representative flow cytometry plot from one mouse showing the frequency of Tregs ($CD4^+FoxP3^+$) out of $CD4^+$ cells is shown. Right panel, the frequency of Tregs out of $CD4^+$ cells was quantified following treatment with anti-PD-1 or anti-CTLA-4 (n = 5 mice per group; two-sided Student's *t*-test; data are represented as mean± SEM).

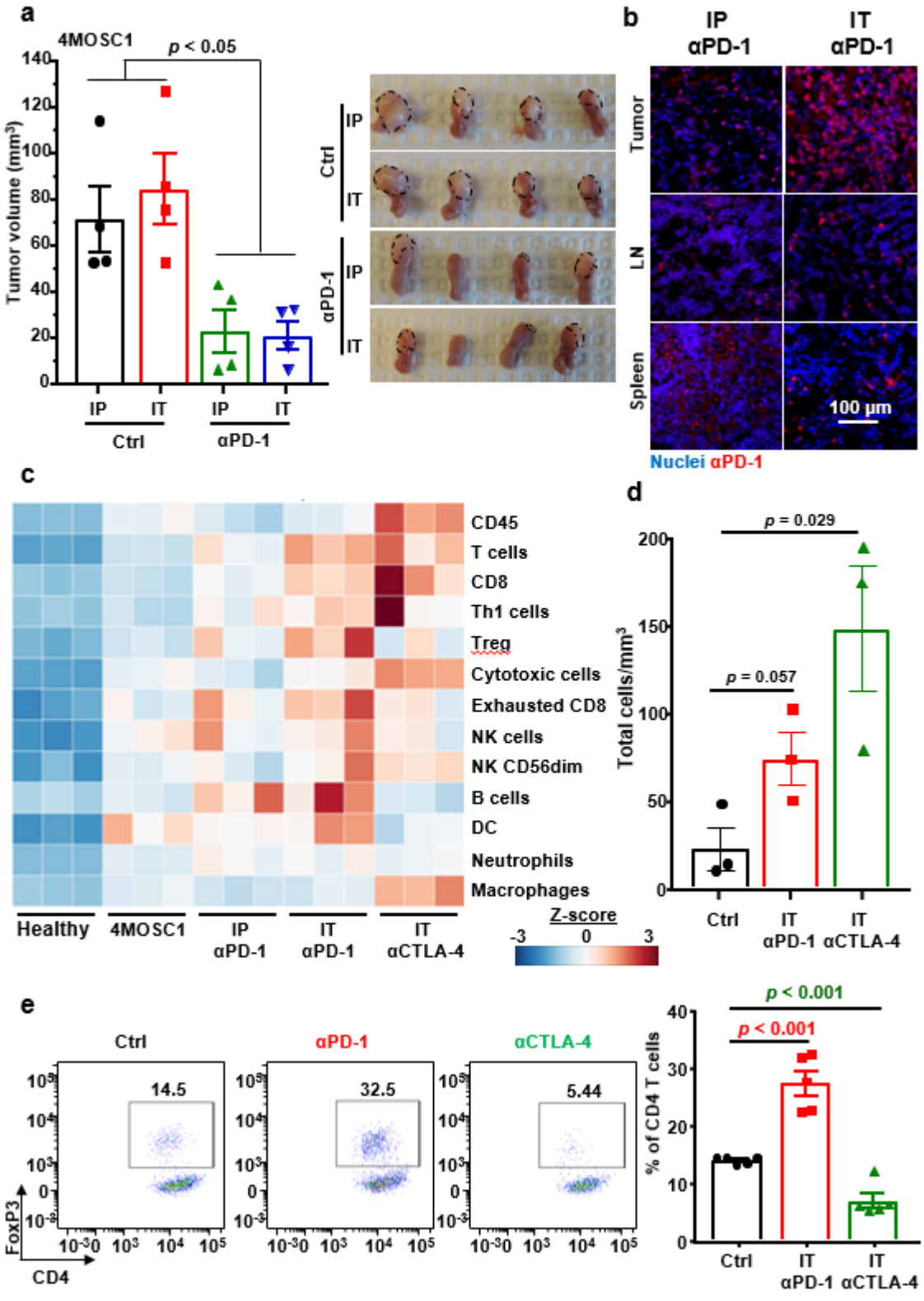
a
4MOSC1
p < 0.05
Tumor volume (mm³)
140
120
100
80
60
40
20
0
IP
IT
IP
IT
Ctrl
αPD-1
Ctrl
αPD-1
IP
IT
IP
IT
b
IP
αPD-1
IT
αPD-1
Tumor
LN
Spleen
100 μm
Nuclei αPD-1
c
CD45
T cells
CD8
Th1 cells
Treg
Cytotoxic cells
Exhausted CD8
NK cells
NK CD56dim
B cells
DC
Neutrophils
Macrophages
Healthy
4MOSC1
IP αPD-1
IT αPD-1
IT αCTLA-4
Z-score
-3
0
3
d
p = 0.029
p = 0.057
Total cells/mm³
200
150
100
50
0
Ctrl
IT αPD-1
IT αCTLA-4
e
Ctrl
αPD-1
αCTLA-4
14.5
32.5
5.44
FoxP3
CD4
p < 0.001
p < 0.001
% of CD4 T cells
40
30
20
10
0
Ctrl
IT αPD-1
IT αCTLA-4

Figure 3.5. Mice with 4MOSC1 tumors show nearly complete response to anti-CTLA-4

(A) C57Bl/6 mice were implanted with $1x10^6$ of 4MOSC1 cells into the tongue. After the tumors reached ~30 mm^3, mice were treated 10mg/kg of isotype control or anti-CTLA-4 for IP administration (left), and 5mg/kg of isotype controlor anti-CTLA-4 for IT administration (right). Individual growth curves of 4MOSC1 tumor-bearing mice plotting primary tumor growth are shown (n = 10 mice per group). (B) Shown is the immunofluorescent staining of the distribution of anti-CTLA-4 antibody for mice with 4MOSC1 tumors using IP or IT delivery of the treatment. Staining for anti-hamster IgG (red) showed the localization of anti-CTLA-4 antibody in the tongue, lymph nodes and spleen of treated mice. DAPI staining for nuclei is shown in blue (n = 4 mice per group) (C) Immunofluorescent staining of CD8 highlights an increase in CD8 T cell recruitment with anti-CTLA-4 treatment. Quantification of CD8 T cells with or without anti-CTLA-4 treatment was done by immunofluorescent staining of tumor (CK5) in the tongue. Shown is the average CD8 positivity by 3 regions of interest (ROI) per mouse, quantified by Qupath software for each condition (n = 3 mice per group two-sided Student's *t*-test; data are represented as mean± SEM). (D-E) Antigen specific T cell cytotoxic assay. C57Bl/6 mice were implanted with $1x10^6$ of 4MOSC1 cells into the tongue, and when they reached approximately 30 mm^3, mice were treated IT with isotype control, anti-PD-1, or anti-CTLA-4 every other day for 3 treatments total. CD8 T cells from each group were isolated and co-cultured with pre-plated 4MOSC1 cells. DMSO (10%) was used to treat 4MOSC1 as a positive control, and DRAQ7 was added in the culture medium to mark dead cells (red). (D) Real time live-imaging experiments were performed using the 880 confocal fast scan (Zeiss), and representative images of tumor cell killing (CD8 T cells from anti-CTLA-4 group) are shown at the indicated times. (E) Quantification of dead cancer cells at the end of experiment. (n = 3 mice per group; two sided Student's *t*-test; data are represented as mean± SEM).

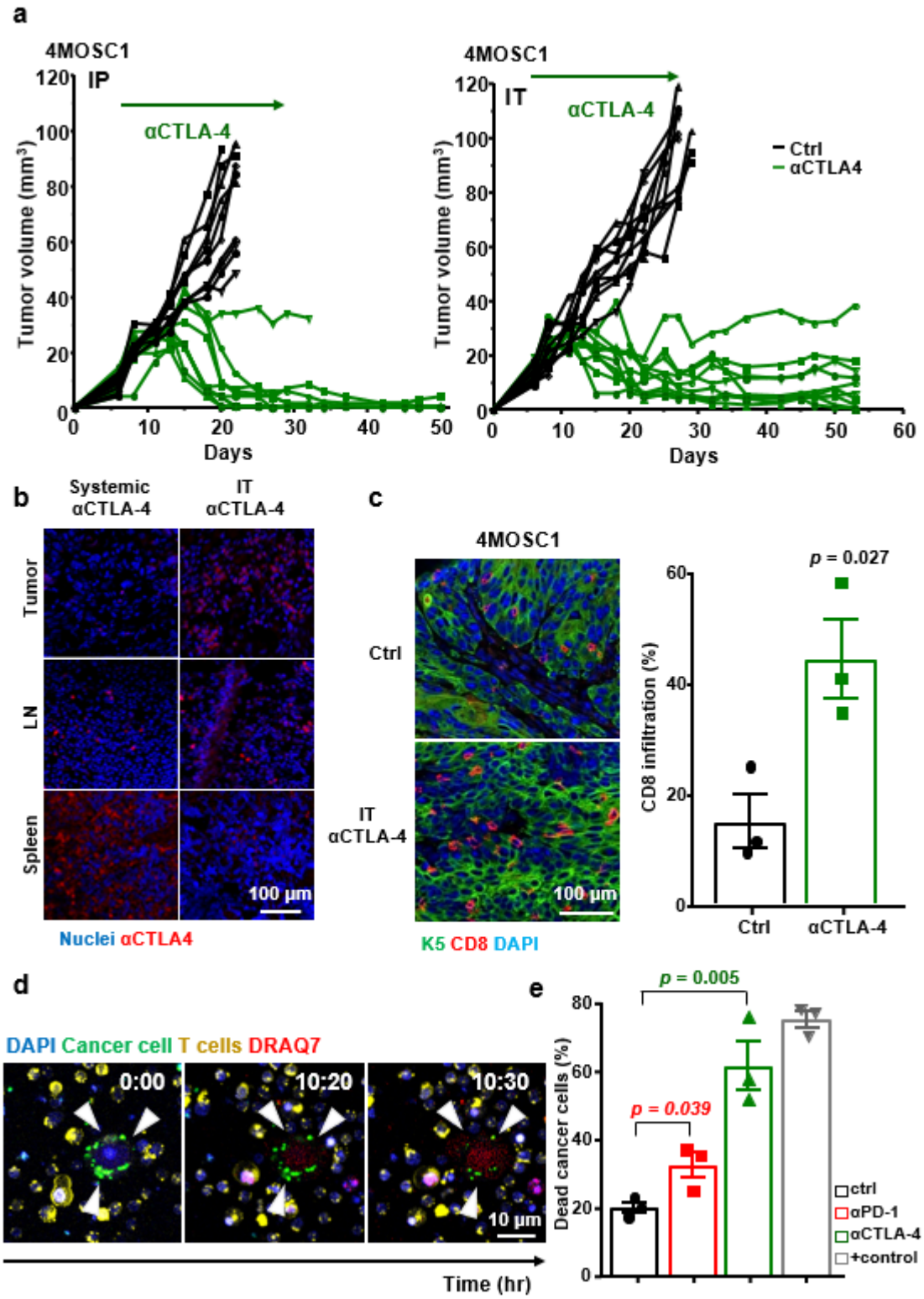
a
4MOSC1
IP
αCTLA-4
Tumor volume (mm³)
Days
4MOSC1
IT
αCTLA-4
Ctrl
αCTLA4
b
Systemic αCTLA-4
IT αCTLA-4
Tumor
LN
Spleen
100 μm
Nuclei αCTLA4
c
4MOSC1
Ctrl
IT αCTLA-4
100 μm
K5 CD8 DAPI
p = 0.027
CD8 infiltration (%)
Ctrl
αCTLA-4
d
DAPI Cancer cell T cells DRAQ7
0:00
10:20
10:30
10 μm
Time (hr)
e
p = 0.005
p = 0.039
Dead cancer cells (%)
ctrl
αPD-1
αCTLA-4
+control

3.7 Supplementary Figures

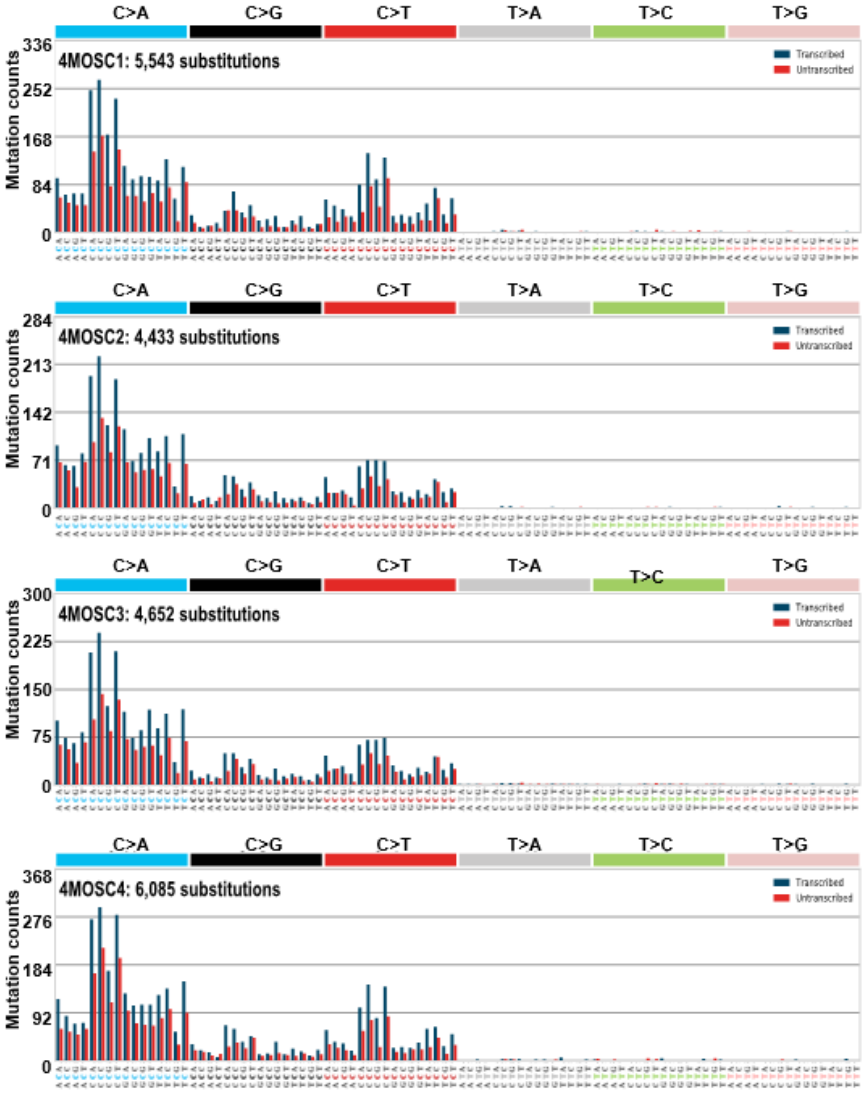

Figure S3.1 Transcriptional Bias for each individual 4MOSC cell lines.

The somatic mutational profiles of the four 4MOSCs were correlated to (Pearson correlation > 0.93), known mutational signatures in human cancer. The pattern of Signature 4 extracted from cancers associated with tobacco smoking was marked as dark blue columns.

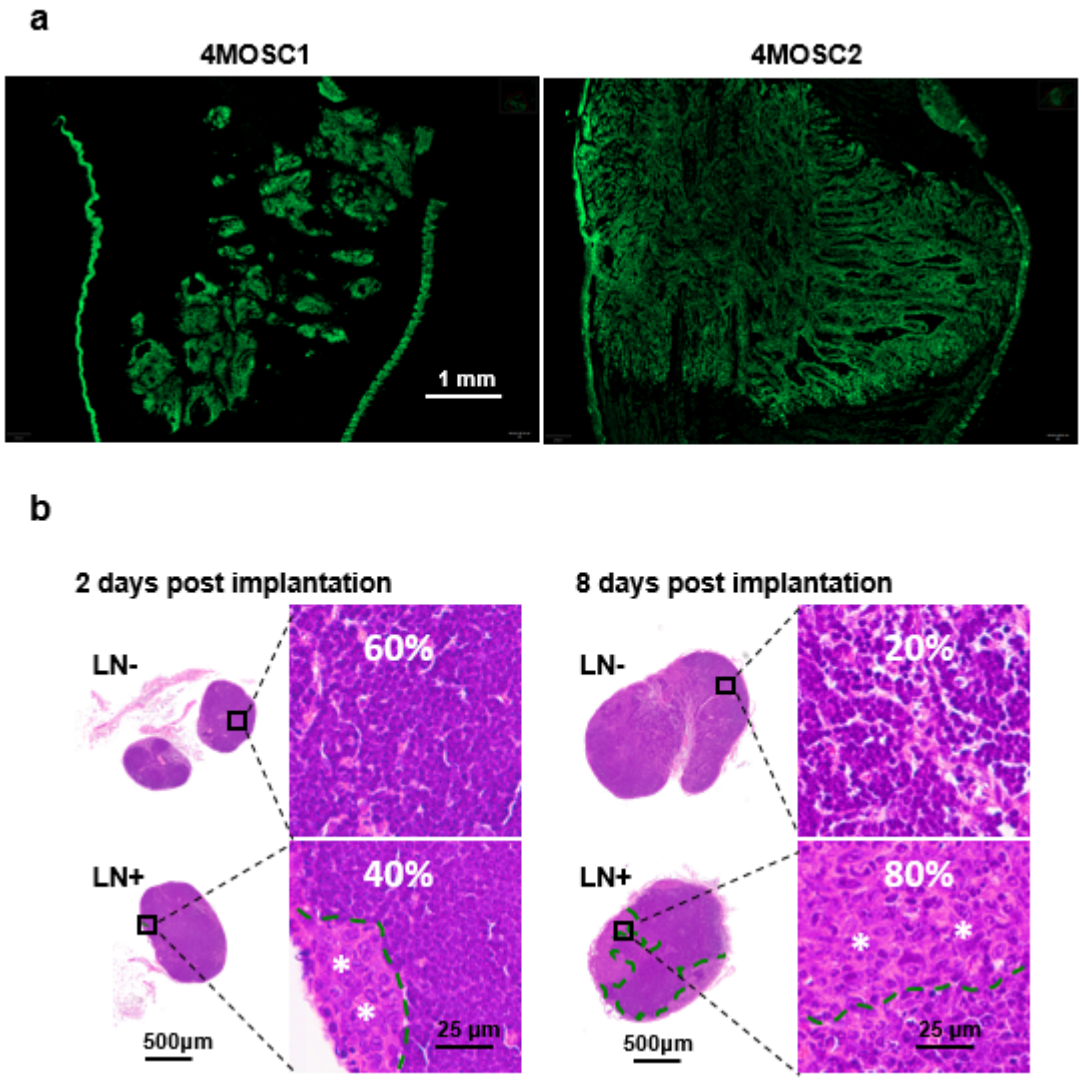

Figure S3.2. Squamous cell character

(**A**) Representative pictures of whole tongue tumors stained to show expression of cytokeratin 5 (CK5, green); left, 4MOSC1; right, 4MOSC2 (n = 3 mice per group). (**B**) Metastatic growth of 4MOSC2 cells into the lymph node. C57Bl/6 mice were implanted with $1x10^6$ of 4MOSC2 cells into the tongue. On 2 and 8 days post-implantation, cervical lymph nodes from each mouse were harvested and evaluated by H&E staining. Left, representative H&E stain of a non-metastatic (top) and a metastatic (bottom) cervical lymph node. Right, images at high magnification depict the histologic features of representative area from each individual cervical lymph node. Metastatic area is depicted with a green dotted line, with the tumor cells marked by * (n = 5 mice per group).

Supplementary Figure 3

Fold difference
1
1 to 2
2.1 to 4
4.1 to 10
> 10

	Relative value		Concentration (pg/ml)		
4MOSC	1	2	4MOSC1	4MOSC2	Sig.
CCL11	2.9		292±10	100±10	***
CCL12	1.2		314±63	268±30	ns
CCL17	7.1		361±255	51±10	ns
CCL19		2.4	48.2±6.6	118±13	**
CCL2	3.1		1339±98	430±54	***
CCL20	1.7		1.2±0.2	0.7±0.1	*
CCL21	1.7		1205±114	719±41	**
CCL22	4.4		73.6±6.2	16.8±0.9	***
CCL3	1.6		312±17	198±10	***
CCL4	2.9		295±26	102±5	***
CCL5	4.9		84.8±6.1	17.4±2.6	***
CX3CL1	1.4		132±14	96.9±6.3	ns
CXCL1		1.7	654±110	1137±75	**
CXCL10		4.0	694±82	2801±1156	ns
CXCL2		1.9	4398±835	8171±234	**
CXCL5		8.5	361±21	3052±375	***
EPO	1.5		2.4±0.2	1.6±0.1	**
G-CSF		13.7	355±73	4877±68	***
GM-CSF		13.6	52±14	704±51	***
IFNβ1		2.5	80.6±7.8	204±99	ns
IFNγ	1.6		4.8±1.0	3.1±0.4	ns
IL-10		1.3	2.7±0.4	3.6±0.3	ns
IL-11	1.9		460±138	244±51	ns
IL-12 (p40)	1.3		2.8±0.3	2.2±0.3	ns
IL-12 (p70)	1.2		4.2±0.8	3.6±0.2	ns
IL-13	1.2		4.7±0.2	3.9±0.3	ns
IL-15	1.1		6.0±0.3	5.7±0.4	ns
IL-16	1.5		795±52	543±63	*
IL-17	1.8		1.8±0.2	1.0±0.1	**
IL-1a		1.8	216±13	383±33	**
IL-1b		1.3	48.6±8.9	65.6±5.2	ns
IL-2			6.5±0.4	6.5±0.7	ns
IL-20	1.1		7.5±0.3	7.1±0.3	ns
IL-3	2.8		4.0±2.2	1.4±0.2	ns
IL-4	10.3		3.1±0.6	0.3±0.1	***
IL-5	6.2		8.1±1.3	1.3±0.2	***
IL-6	1.8		127±32	69.7±8.8	ns
IL-7		2.1	2.6±0.2	5.4±0.1	***
IL9	1.2		11.1±2.4	9.4±2.8	ns
LIF	1.6		88.9±7.2	54.9±5.3	**
M-CSF	1.2		28.2±3.2	24.5±3.0	ns
TIMP-1	1.8		6242±927	3510±757	ns
TNFα	1.3		13.9±1.4	10.6±1.1	ns
VEGF		26.8	1.4±0.2	37.5±6.5	***

Figure S3.3. Chemokine expression profile of the 4MOSC tumors.

C57Bl/6 mice were implanted with $1x10^6$ of either 4MOSC1 or 4MOSC2 cells into the tongue. Eleven days post-implantation, tongue tumors were dissected and lysed. Tumor lysates were normalized to 1 mg/mL and analyzed to quantify concentrations of multiple chemokines, cytokines, and growth factors. Left, relative values of each chemokine in 4MOSC1 and 4MOSC2; fold differences were calculated by dividing the tumor with the higher concentration by the tumor with the lower concentration, and the tumor with the lower concentration was defined as 1-fold. Right, absolute concentration of each chemokine in 4MOSC1 and 4MOSC2 (n = 5 mice per group; not significant or ns, $p > 0.05$; *, $p < 0.05$; **, $p < 0.01$; and ***, $p < 0.001$ when comparing 4MOSC1 with 4MOSC2 with two sided Student's *t*-test; data are represented as mean± SEM).

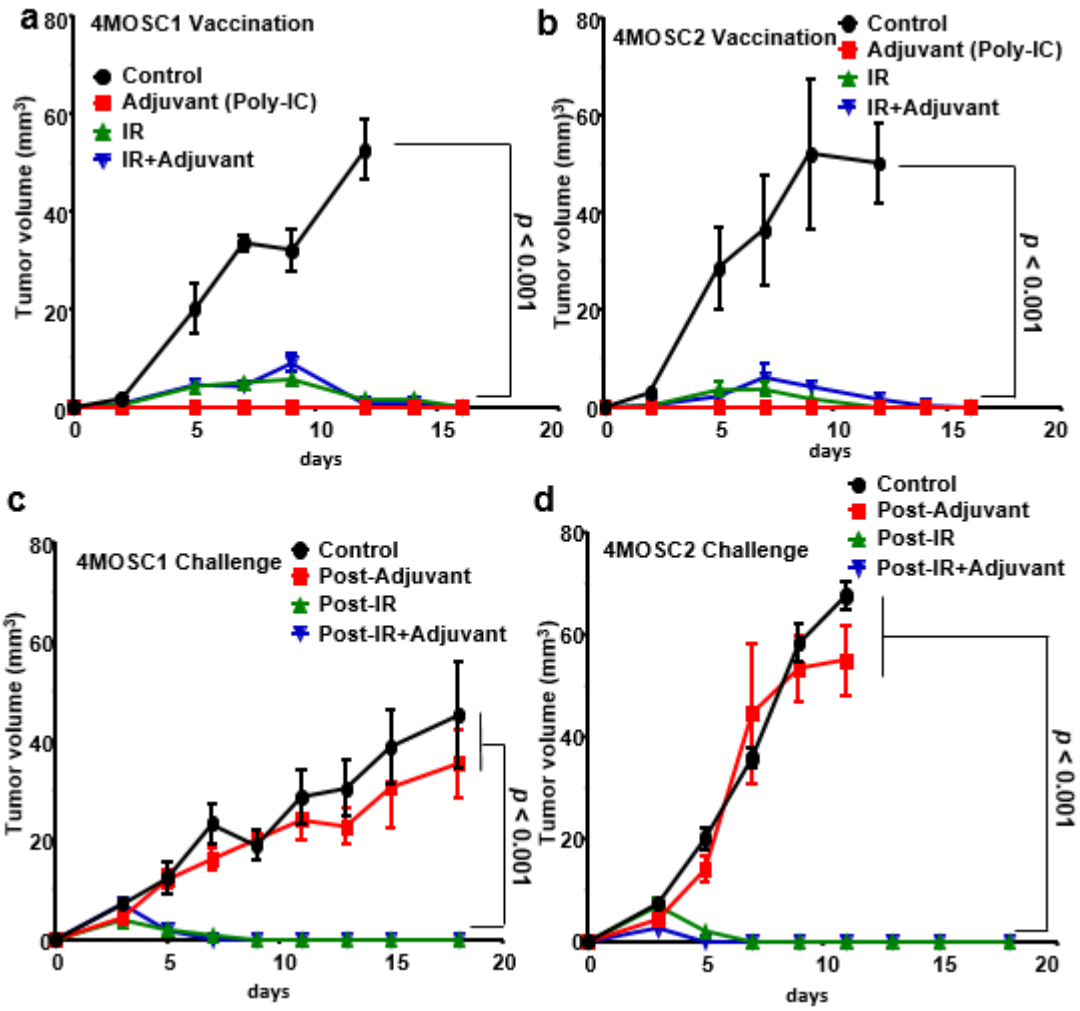

Figure S3.4. Immunogenicity of 4MOSCs.

(**A-B**) Memory immune responses induced by vaccination with irradiated 4MOSC cells. 4MOSC1 or 4MOSC2 cells were irradiated with 45 Gy and $1x10^6$ cell were injected into the tongue of C57Bl/6 mice, with (green) or without (blue) polyinosinic-polycytidylic acid (poly IC). Mice injected with non-irradiated 4MOSC cells (black) or mice only treated by poly IC (red) were used as controls. The average tumor volume of each group is shown (n = 5 mice per group, the tumor growth curves were compared by the longitudinal data analysis method; data are represented as mean± SEM). (C**-D**) Vaccinated mice (green and blue) were re-challenged with $1x10^6$ live 4MOSC cells 6 weeks after. Naïve mice (black) and mice post poly IC treatment (red) were used as controls. The average tumor volume of each group is shown (n = 5 mice per group, the tumor growth curves were compared by the longitudinal data analysis method; data are represented as mean± SEM).

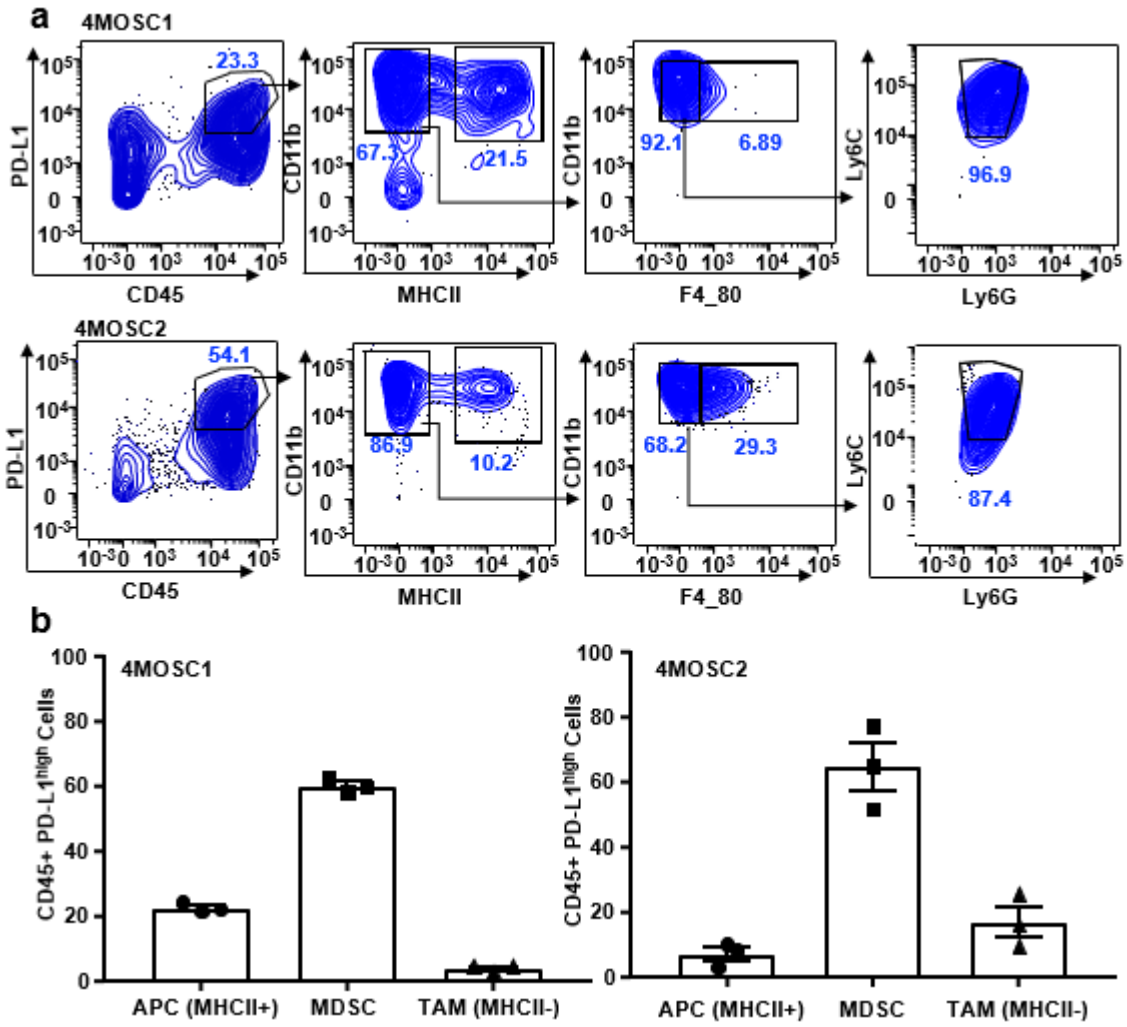

Figure S3.5. PD-L1 is expressed on tumor and tumor-infiltrating myeloid immune cells.

Frequency of live 4MOSC1 or 4MOSC2 tumors expressing PD-L1. (**A**) Shown are representative flow cytometry plots of PD-L1 expression on 4MOSC cells, CD45+ immune cells, $MHCII^{+}$ antigen presenting cells (APC), $F4/80^{+}$ $MHCII^{-}$ tumor-associated macrophages (TAMs), and $Ly6C^{+}Ly6G^{+}$ MDSCs. (**B**) The averaged frequency of each immune cell population expressing $PD\text{-}L1^{high}$ in 4MOSC1 and 4MOSC2 is shown (n = 3 mice per group; data are represented as mean± SEM).

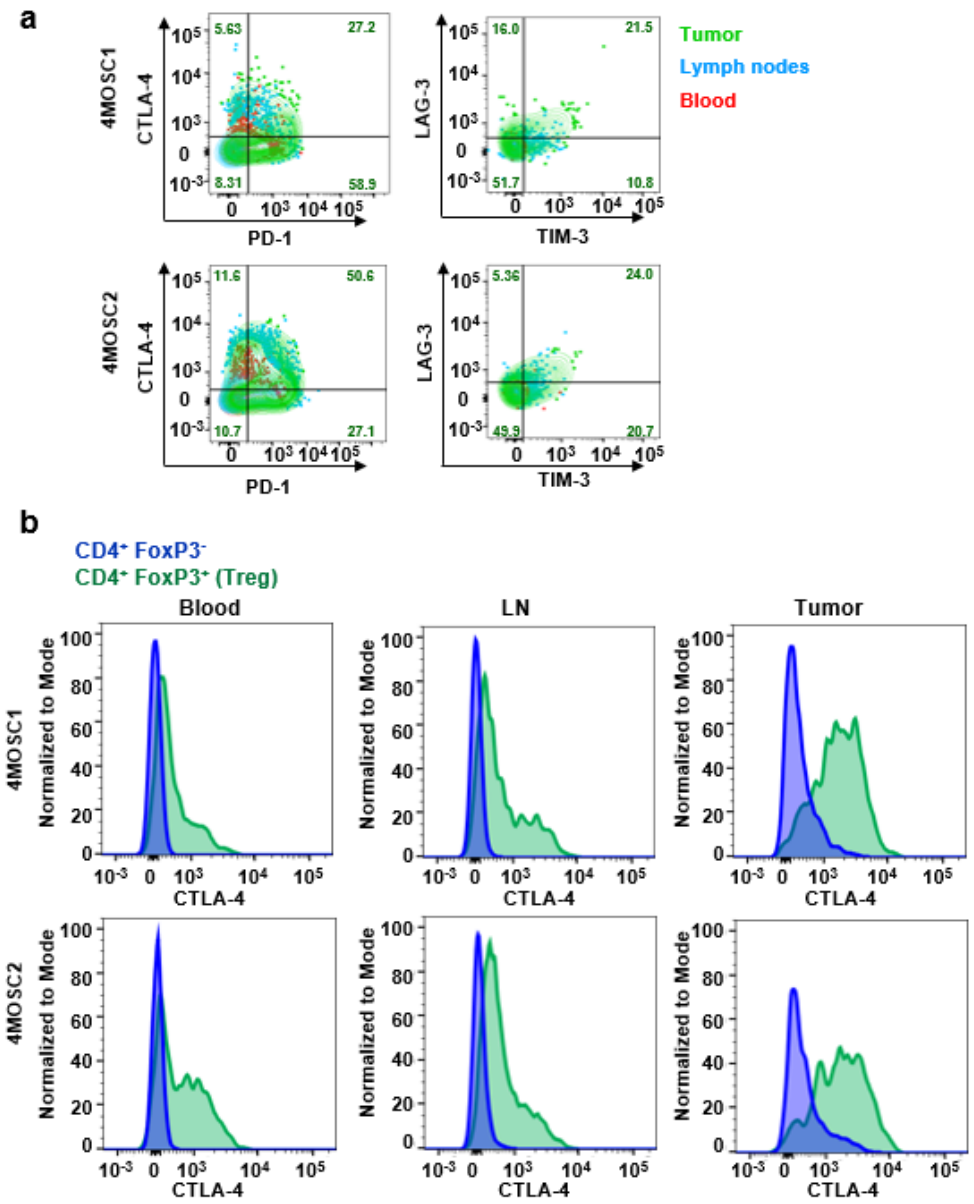

Figure S3.6. Characterization of inhibitory receptor expression on tumor-infiltrating CD4 T cells in 4MOSCs.

Frequency of live 4MOSC1 or 4MOSC2 tumors expressing inhibitory receptors. (**A**) Shown are representative flow cytometry plots of the frequency of $CD4^+$ cells expressing inhibitory receptors PD-1, CTLA-4, LAG-3 and TIM-3 (n = 4 mice per group). Contour plots of lymphocytes from tumor (green), and corresponding cervical lymph nodes (blue), and blood (red) are overlaid and the frequencies of tumor $CD4^+$ T cells expressing each inhibitory receptor are shown. (**B**) The expression of CTLA-4 on CD4 T cells, Tregs ($CD4^+FoxP3^+$) or non-Tregs ($CD4^+FoxP3^-$) are represented by overlaid histograms in blood, LN, and tumor (n = 4 mice per group).

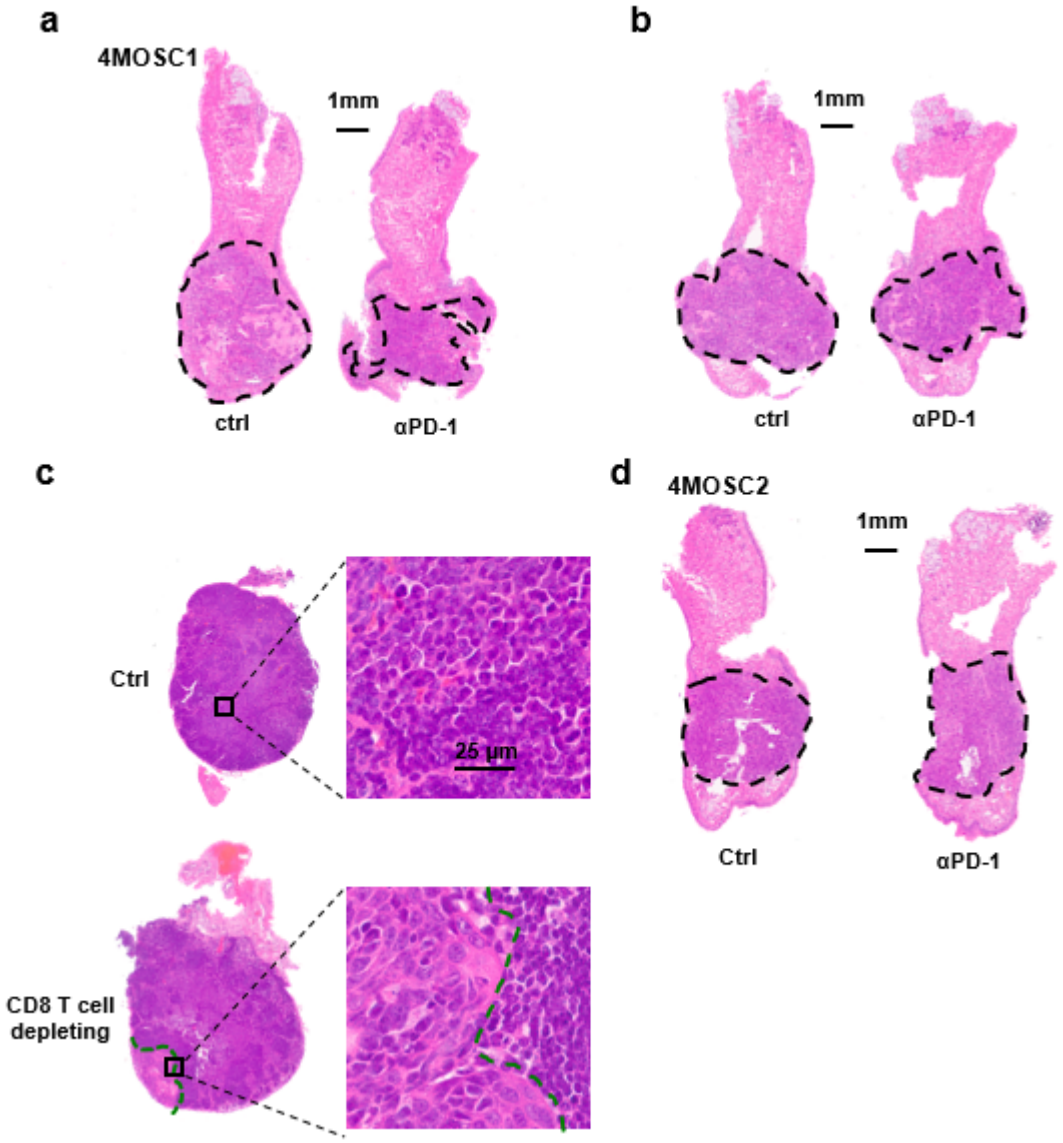

Figure S3.7. Histopathological analysis of tongues and cervical lymph nodes from 4MOSC1 or 4MOSC2 tumor-bearing mice.

(**A-B**) Representative H&E stains of mouse tumors from the experiment in panel 3.3A (n = 10 mice per group) and 3.3E (n = 5 mice per group). The H&E stained tissue section of an HNSCC tumor is depicted with a dotted line. (**C**) Top panel, representative H&E stain of a non-metastatic cervical lymph node from mice with 4MOSC1 tumors. Bottom panel, representative H&E stain of a metastatic cervical lymph node from mice with 4MOSC1 tumors after treatment with CD8 T cell-depleting antibody. Metastatic growth of 4MOSC1 cells into the lymph node is depicted with a dotted line in the left area. ((n = 5 mice per group)) (**D**) Representative H&E stains of mouse tumors from the experiment in panel 3.3G. The H&E stained tissue section of an HNSCC tumor is depicted with a dotted line (n = 5 mice per group).

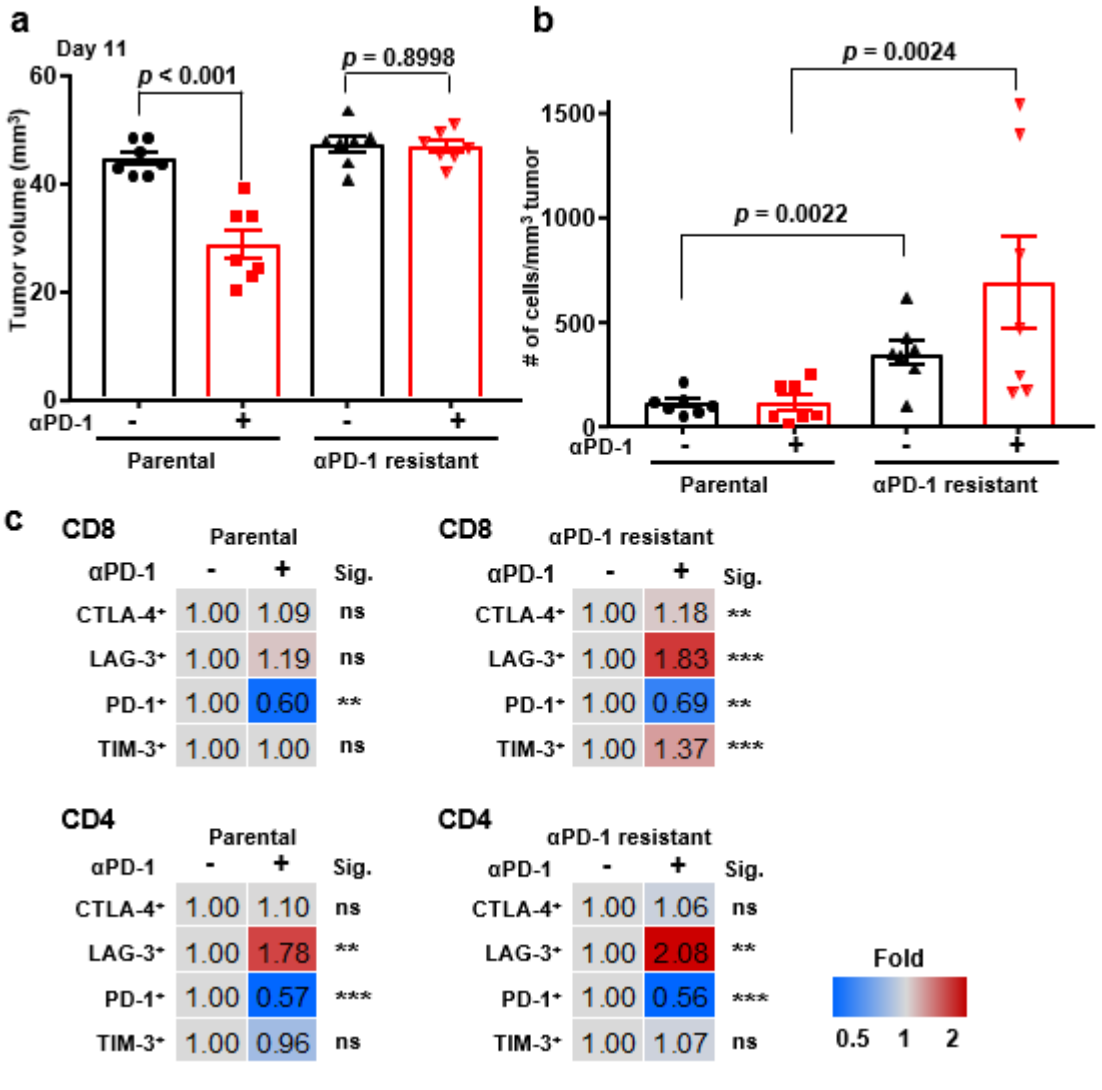

Figure S3.8. Difference of immune infiltration and immune checkpoints in parental 4MOSC1 and αPD-1-resistant 4MOSC1.

Anti-PD-1-resistant 4MOSC1 cell lines were established by first isolating cells from anti-PD-1-treated mice showing no response and re-injecting into C57Bl/6 mice. This process was repeated for a total of 3 rounds to generate the resistant cell line. C57Bl/6 mice were implanted with $1x10^6$ parental or anti-PD1-resistant 4MOSC1cells. After the tumors reached ~30 mm^3, mice were treated IP with 10mg/kg of isotype control or 10mg/kg of anti-PD-1 every other day for 3 treatments total. (**A**) Shown is the average volume of each tumor at the endpoint of the experiment with error bars representing standard error (n = 7 mice per group; two sided Student's *t*-test; data are represented as mean ± SEM). (**B**) Quantification of tumor-infiltrating PMN-MDSCs ($Ly6G^{hi}$) was performed by flow cytometry (n = 7 mice per group; two sided Student's *t*-test; data are represented as mean ± SEM). (**C**) Shown is the average fold change of the frequency of tumor-infiltrating CD4 and CD8 T cells expressing inhibitory receptors from anti-PD-1-treated parental and resistant 4MOSC1 (n = 7 mice per group; not significant or ns, $p > 0.05$; *, $p < 0.05$; and ***, $p < 0.001$, two sided Student's *t*-test).

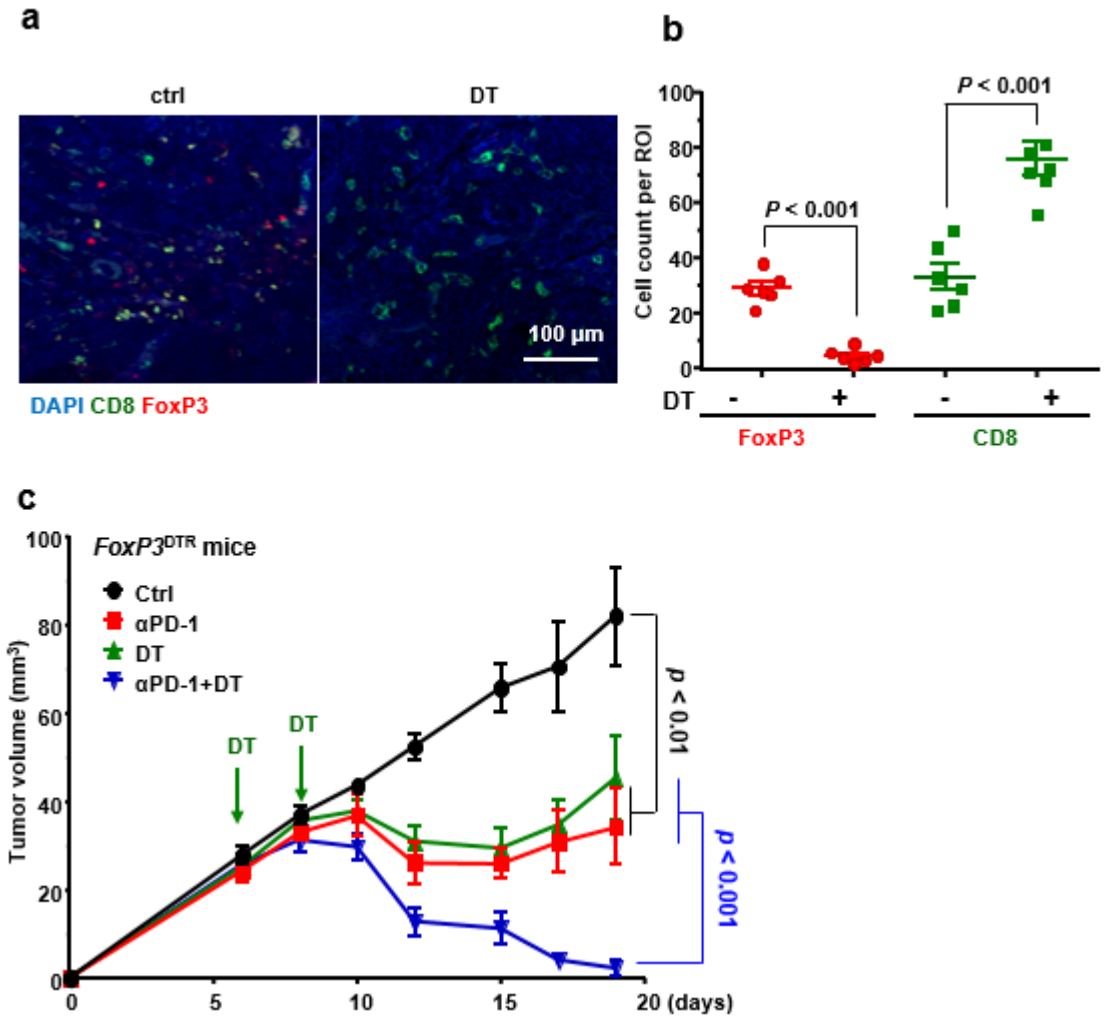

Figure S3.9. Treg-mediated suppression of anti-PD-1 activity in 4MOSC1 tumors in *FoxP3*^{DTR} mice.

(**A**) *FoxP3*^{DTR} mice were implanted with 1x10^6 of 4MOSC1 cells into the tongue, and when they reached approximately 30 mm^3, mice were treated IP with PBS or diphtheria toxin (DT). Immunofluorescent staining of isolated tumors with FoxP3 and CD8 confirm transient elimination of Tregs with DT and increase in CD8 T cells. (**B**) Shown is the quantification of the FoxP3 and CD8 positive cells by 3 regions of interests (ROI) per mouse, quantified by Qupath software for mice untreated and treated with DT. (n = 6 mice per group; two sided Student's *t*-test; data are represented as mean± SEM). (**C**) *FoxP3*^{DTR} mice with 4MOSC1 tongue tumors were treated IP with 10mg/kg of isotype control (black), 10mg/kg of anti-PD-1 (red), diphtheria toxin (green) or both (blue). (n = 5 mice per group; the tumor growth curves were compared by the longitudinal data analysis method; data are represented as mean± SEM).

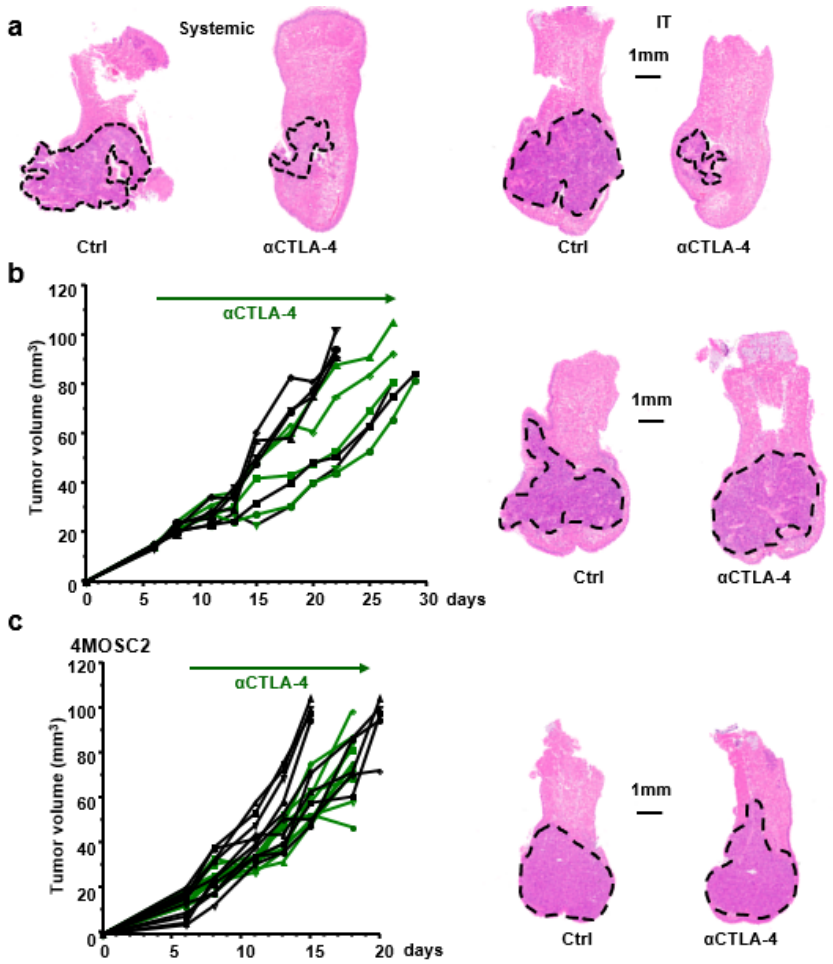

Figure S3.10. Histological analysis of tongues from 4MOSC1 or 4MOSC2 tumor-bearing mice treated with anti-CTLA-4.

(**A**) Representative H&E stains of mouse tumors from the experiment in panel 3.4A. The H&E stained tissue section of an HNSCC tumor is depicted with a dotted line (n = 10 mice per group). (**B**) Left panel, anti-CTLA-4 dependency on CD8 T cells. C57Bl/6 mice were treated with a CD8 T cell-depletion antibody, and transplanted with $1x10^6$ 4MOSC1 cells into the tongue. After the tumors reached ~30 mm^3, mice were treated IT with 5 mg/kg of isotype control (black) or anti-CTLA-4 (green) (n = 5 per group). Individual growth curves of 4MOSC1 tumor-bearing mice plotting primary tumor growth were recorded. Right panel, representative H&E of mouse tumors from the experiment in left panel. The H&E stained tissue section of an HNSCC tumor is depicted with a dotted line. (**C**) Left panel, antitumor efficacy of anti-CTLA-4 for mice with 4MOSC2 tumors. C57Bl/6 mice were transplanted with $1x10^6$ 4MOSC2 cells into the tongue. After the tumors reached ~30 mm^3, mice were treated IT with 5 mg/kg of isotype control (black) or anti-CTLA-4 (green) (n = 10 mice per group). Individual growth curves of 4MOSC2 tumor-bearing mice plotting primary tumor growth were recorded. Right panel, representative H&E of mouse tumors from the experiment in left panel. The H&E stained tissue section of an HNSCC tumor is depicted with a dotted line.

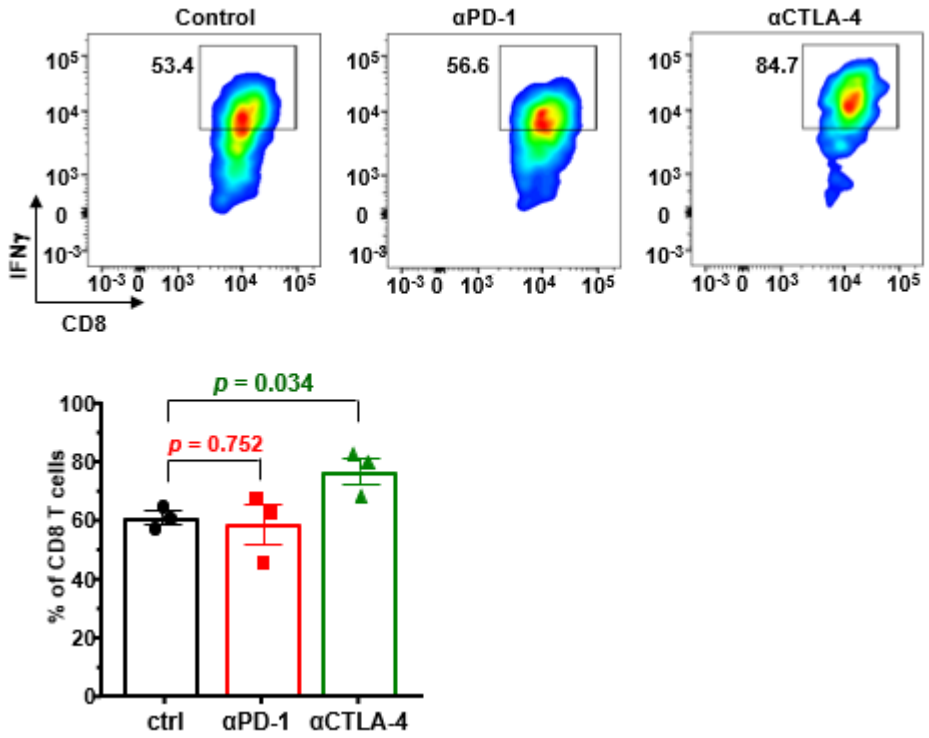

Figure S3.11. Increased expression of IFNg in CD8 T cells by anti-CTLA-4 treatment.

Frequency of $CD45^+$, $Thy1.2^+$, $CD8^+$ expressing IFNg. Top panel, a representative flow cytometry plot from one mouse showing the frequency of $IFNg^+$ out of $CD8^+$ cells is shown. Bottom panel, the frequency of $IFNg^+CD8^+$ cells was quantified following treatment with anti-PD-1 or anti-CTLA-4 (n = 3 mice per group; two sided Student's *t*-test; data are represented as mean± SEM).

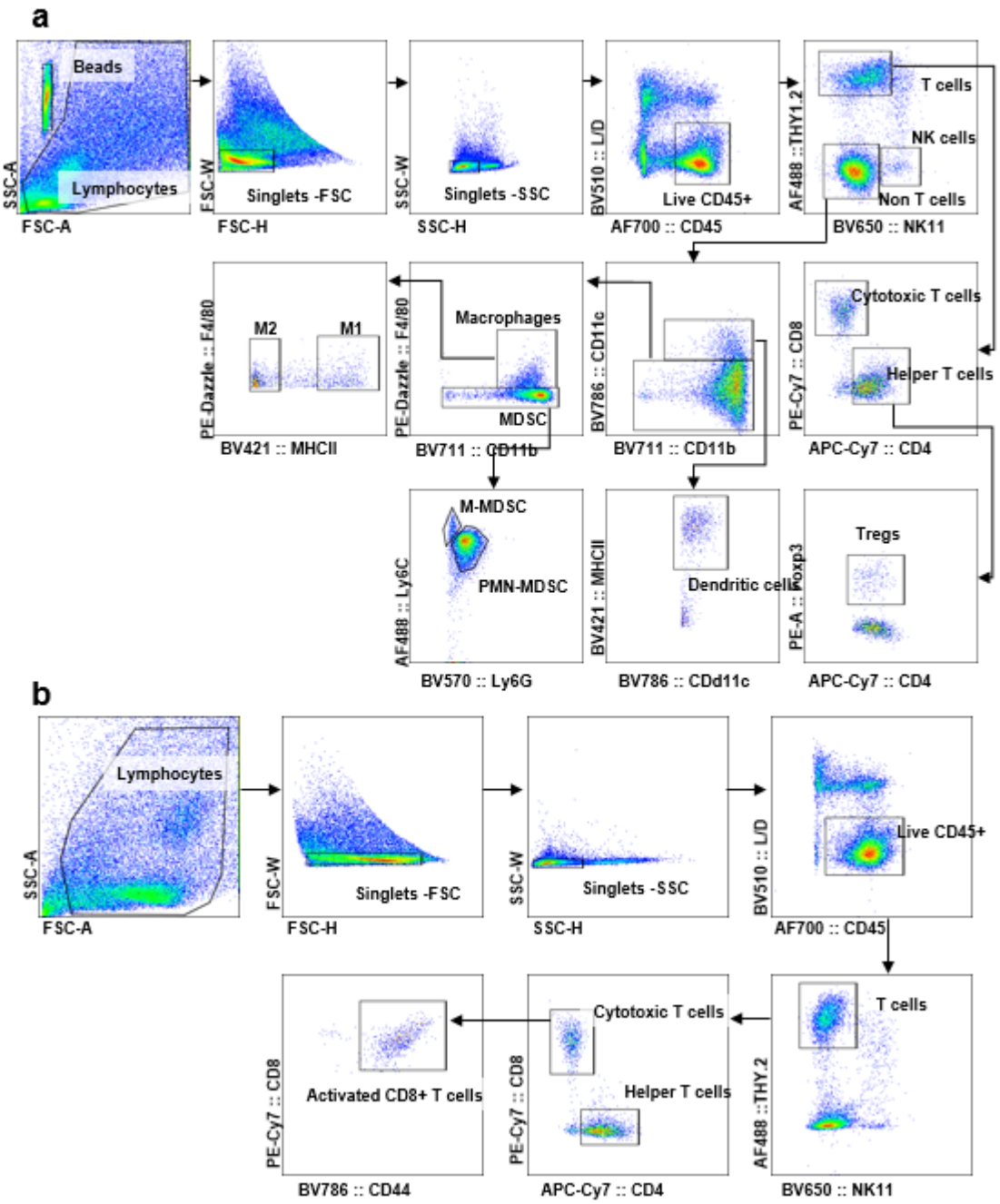

Figure S3.12. Representative flow cytometry gating strategies.

Representative flow cytometry plots to gate (**A**) tumor-infiltrating immune cells used to quantify immune cells in Figure 3.2F, 3.3C, 3.4D, 3.4E, Supplementary Figures S3.8A, S3.8B, and S3.11, and (**B**) T cell inhibitory receptors used to characterize T cells used in Figures 3.2G, Supplementary Figures S3.6A, S3.6B, and S3.8C are shown. Gating for PD-1, TIM-3, LAG-3, and CTLA-4 on activated CD8 T cells ($CD45^+THY1.2^+CD8^+CD44^+$) was determined by fluorescence minus one controls.

3.8 References

1. Lim, S. S., Vos, T., Flaxman, A. D., Danaei, G., Shibuya, K., Adair-Rohani, H., Amann, M., Anderson, H. R., Andrews, K. G., Aryee, M., Atkinson, C., Bacchus, L. J., Bahalim, A. N., Balakrishnan, K., Balmes, J., Barker-Collo, S., Baxter, A., Bell, M. L., Blore, J. D., Blyth, F., Bonner, C., Borges, G., Bourne, R., Boussinesq, M., Brauer, M., Brooks, P., Bruce, N. G., Brunekreef, B., Bryan-Hancock, C., Bucello, C., Buchbinder, R., Bull, F., Burnett, R. T., Byers, T. E., Calabria, B., Carapetis, J., Carnahan, E., Chafe, Z., Charlson, F., Chen, H., Chen, J. S., Cheng, A. T., Child, J. C., Cohen, A., Colson, K. E., Cowie, B. C., Darby, S., Darling, S., Davis, A., Degenhardt, L., Dentener, F., Des Jarlais, D. C., Devries, K., Dherani, M., Ding, E. L., Dorsey, E. R., Driscoll, T., Edmond, K., Ali, S. E., Engell, R. E., Erwin, P. J., Fahimi, S., Falder, G., Farzadfar, F., Ferrari, A., Finucane, M. M., Flaxman, S., Fowkes, F. G., Freedman, G., Freeman, M. K., Gakidou, E., Ghosh, S., Giovannucci, E., Gmel, G., Graham, K., Grainger, R., Grant, B., Gunnell, D., Gutierrez, H. R., Hall, W., Hoek, H. W., Hogan, A., Hosgood, H. D., 3rd, Hoy, D., Hu, H., Hubbell, B. J., Hutchings, S. J., Ibeanusi, S. E., Jacklyn, G. L., Jasrasaria, R., Jonas, J. B., Kan, H., Kanis, J. A., Kassebaum, N., Kawakami, N., Khang, Y. H., Khatibzadeh, S., Khoo, J. P., Kok, C., Laden, F., Lalloo, R., Lan, Q., Lathlean, T., Leasher, J. L., Leigh, J., Li, Y., Lin, J. K., Lipshultz, S. E., London, S., Lozano, R., Lu, Y., Mak, J., Malekzadeh, R., Mallinger, L., Marcenes, W., March, L., Marks, R., Martin, R., McGale, P., McGrath, J., Mehta, S., Mensah, G. A., Merriman, T. R., Micha, R., Michaud, C., Mishra, V., Mohd Hanafiah, K., Mokdad, A. A., Morawska, L., Mozaffarian, D., Murphy, T., Naghavi, M., Neal, B., Nelson, P. K., Nolla, J. M., Norman, R., Olives, C., Omer, S. B., Orchard, J., Osborne, R., Ostro, B., Page, A., Pandey, K. D., Parry, C. D., Passmore, E., Patra, J., Pearce, N., Pelizzari, P. M., Petzold, M., Phillips, M. R., Pope, D., Pope, C. A., 3rd, Powles, J., Rao, M., Razavi, H., Rehfuess, E. A., Rehm, J. T., Ritz, B., Rivara, F. P., Roberts, T., Robinson, C., Rodriguez-Portales, J. A., Romieu, I., Room, R., Rosenfeld, L. C., Roy, A., Rushton, L., Salomon, J. A., Sampson, U., Sanchez-Riera, L., Sanman, E., Sapkota, A., Seedat, S., Shi, P., Shield, K., Shivakoti, R., Singh, G. M., Sleet, D. A., Smith, E., Smith, K. R., Stapelberg, N. J., Steenland, K., Stockl, H., Stovner, L. J., Straif, K., Straney, L., Thurston, G. D., Tran, J. H., Van Dingenen, R., van Donkelaar, A., Veerman, J. L., Vijayakumar, L., Weintraub, R., Weissman, M. M., White, R. A., Whiteford, H., Wiersma, S. T., Wilkinson, J. D., Williams, H. C., Williams, W., Wilson, N., Woolf, A. D., Yip, P., Zielinski, J. M., Lopez, A. D., Murray, C. J., Ezzati, M., AlMazroa, M. A., and Memish, Z. A. (2012) A comparative risk assessment of burden of disease and injury attributable to 67 risk factors and risk factor clusters in 21 regions, 1990-2010: A systematic analysis for the Global Burden of Disease Study 2010. *Lancet* **380**, 2224-2260

2. Agudo, A., Bonet, C., Travier, N., Gonzalez, C. A., Vineis, P., Bueno-de-Mesquita, H. B., Trichopoulos, D., Boffetta, P., Clavel-Chapelon, F., Boutron-Ruault, M. C., Kaaks, R., Lukanova, A., Schutze, M., Boeing, H., Tjonneland, A., Halkjaer, J., Overvad, K., Dahm, C. C., Quiros, J. R., Sanchez, M. J., Larranaga, N., Navarro, C., Ardanaz, E., Khaw, K. T., Wareham, N. J., Key, T. J., Allen, N. E., Trichopoulou, A., Lagiou, P., Palli, D., Sieri, S., Tumino, R., Panico, S., Boshuizen, H., Buchner, F. L., Peeters, P. H., Borgquist, S., Almquist, M., Hallmans, G., Johansson, I., Gram, I. T., Lund, E., Weiderpass, E., Romieu, I., and Riboli, E. (2012) Impact of cigarette smoking on cancer risk in the European prospective investigation into cancer and nutrition study. *J Clin Oncol* **30**, 4550-4557

3. Siegel, R. L., Miller, K. D., and Jemal, A. (2019) Cancer statistics, 2019. *CA Cancer J Clin* **69**, 7-34

4. Gillison, M. L., Chaturvedi, A. K., Anderson, W. F., and Fakhry, C. (2015) Epidemiology of human papillomavirus-positive head and neck squamous cell carcinoma. *J Clin Oncol* **33**, 3235-3242

5. Stokley, S., Curtis, C. R., Jeyarajah, J., Harrington, T., Gee, J., and Markowitz, L. (2013) Human papillomavirus vaccination coverage among adolescent girls, 2007-2012, and postlicensure vaccine safety monitoring, 2006-2013 - United States. *Mmwr-Morbid Mortal W* **62**, 591-595

6. Fung, C., and Grandis, J. R. (2010) Emerging drugs to treat squamous cell carcinomas of the head and neck. *Expert Opin Emerg Drugs* **15**, 355-373

7. Kozakiewicz, P., and Grzybowska-Szatkowska, L. (2018) Application of molecular targeted therapies in the treatment of head and neck squamous cell carcinoma. *Oncol Lett* **15**, 7497-7505

8. Cohen, E. E., LaMonte, S. J., Erb, N. L., Beckman, K. L., Sadeghi, N., Hutcheson, K. A., Stubblefield, M. D., Abbott, D. M., Fisher, P. S., Stein, K. D., Lyman, G. H., and Pratt-Chapman, M. L. (2016) American Cancer Society Head and Neck Cancer Survivorship Care Guideline. *CA Cancer J Clin* **66**, 203-239

9. Okazaki, T., Chikuma, S., Iwai, Y., Fagarasan, S., and Honjo, T. (2013) A rheostat for immune responses: the unique properties of PD-1 and their advantages for clinical application. *Nat Immunol* **14**, 1212-1218

10. Pardoll, D. M. (2012) The blockade of immune checkpoints in cancer immunotherapy. *Nat Rev Cancer* **12**, 252-264

11. Wei, S. C., Duffy, C. R., and Allison, J. P. (2018) Fundamental Mechanisms of Immune Checkpoint Blockade Therapy. *Cancer Discov* **8**, 1069-1086

12. Ferris, R. L. (2015) Immunology and Immunotherapy of Head and Neck Cancer. *J Clin Oncol* **33**, 3293-3304

13. Ferris, R. L., Blumenschein, G., Jr., Fayette, J., Guigay, J., Colevas, A. D., Licitra, L., Harrington, K., Kasper, S., Vokes, E. E., Even, C., Worden, F., Saba, N. F., Iglesias Docampo, L. C., Haddad, R., Rordorf, T., Kiyota, N., Tahara, M., Monga, M., Lynch, M., Geese, W. J., Kopit, J., Shaw, J. W., and Gillison, M. L. (2016) Nivolumab for Recurrent Squamous-Cell Carcinoma of the Head and Neck. *N Engl J Med* **375**, 1856-1867

14. Seiwert, T. Y., Burtness, B., Mehra, R., Weiss, J., Berger, R., Eder, J. P., Heath, K., McClanahan, T., Lunceford, J., Gause, C., Cheng, J. D., and Chow, L. Q. (2016) Safety and clinical activity of pembrolizumab for treatment of recurrent or metastatic squamous cell carcinoma of the head and neck (KEYNOTE-012): an open-label, multicentre, phase 1b trial. *Lancet Oncol* **17**, 956-965

15. Chow, L. Q. M., Haddad, R., Gupta, S., Mahipal, A., Mehra, R., Tahara, M., Berger, R., Eder, J. P., Burtness, B., Lee, S. H., Keam, B., Kang, H., Muro, K., Weiss, J., Geva, R., Lin, C. C., Chung, H. C., Meister, A., Dolled-Filhart, M., Pathiraja, K., Cheng, J. D., and Seiwert, T. Y. (2016) Antitumor activity of pembrolizumab in biomarker-unselected patients with recurrent and/or metastatic head and neck squamous cell carcinoma: Results from the phase Ib KEYNOTE-012 expansion cohort. *Journal of Clinical Oncology* **34**, 3838-3845

16. Cohen, E. E. W., Soulieres, D., Le Tourneau, C., Dinis, J., Licitra, L., Ahn, M. J., Soria, A., Machiels, J. P., Mach, N., Mehra, R., Burtness, B., Zhang, P., Cheng, J., Swaby, R. F., Harrington, K. J., and investigators, K.-. (2019) Pembrolizumab versus methotrexate, docetaxel, or cetuximab for recurrent or metastatic head-and-neck squamous cell

carcinoma (KEYNOTE-040): a randomised, open-label, phase 3 study. *Lancet* **393**, 156-167

17. Hecht, S. S. (2003) Tobacco carcinogens, their biomarkers and tobacco-induced cancer. *Nat Rev Cancer* **3**, 733-744

18. Kandoth, C., McLellan, M. D., Vandin, F., Ye, K., Niu, B., Lu, C., Xie, M., Zhang, Q., McMichael, J. F., Wyczalkowski, M. A., Leiserson, M. D. M., Miller, C. A., Welch, J. S., Walter, M. J., Wendl, M. C., Ley, T. J., Wilson, R. K., Raphael, B. J., and Ding, L. (2013) Mutational landscape and significance across 12 major cancer types. *Nature* **502**, 333-339

19. Alexandrov, L. B., Ju, Y. S., Haase, K., Van Loo, P., Martincorena, I., Nik-Zainal, S., Totoki, Y., Fujimoto, A., Nakagawa, H., Shibata, T., Campbell, P. J., Vineis, P., Phillips, D. H., and Stratton, M. R. (2016) Mutational signatures associated with tobacco smoking in human cancer. *Science* **354**, 618-622

20. Czerninski, R., Amornphimoltham, P., Patel, V., Molinolo, A. A., and Gutkind, J. S. (2009) Targeting mammalian target of rapamycin by rapamycin prevents tumor progression in an oral-specific chemical carcinogenesis model. *Cancer Prev Res (Phila)* **2**, 27-36

21. Vitale-Cross, L., Czerninski, R., Amornphimoltham, P., Patel, V., Molinolo, A. A., and Gutkind, J. S. (2009) Chemical carcinogenesis models for evaluating molecular-targeted prevention and treatment of oral cancer. *Cancer Prev Res (Phila)* **2**, 419-422

22. Vitale-Cross, L., Molinolo, A. A., Martin, D., Younis, R. H., Maruyama, T., Patel, V., Chen, W., Schneider, A., and Gutkind, J. S. (2012) Metformin prevents the development of oral squamous cell carcinomas from carcinogen-induced premalignant lesions. *Cancer Prev Res (Phila)* **5**, 562-573

23. Tang, X. H., Urvalek, A. M., Osei-Sarfo, K., Zhang, T., Scognamiglio, T., and Gudas, L. J. (2015) Gene expression profiling signatures for the diagnosis and prevention of oral cavity carcinogenesis-genome-wide analysis using RNA-seq technology. *Oncotarget* **6**, 24424-24435

24. Alexandrov, L. B., Nik-Zainal, S., Wedge, D. C., Aparicio, S. A., Behjati, S., Biankin, A. V., Bignell, G. R., Bolli, N., Borg, A., Borresen-Dale, A. L., Boyault, S., Burkhardt, B., Butler, A. P., Caldas, C., Davies, H. R., Desmedt, C., Eils, R., Eyfjord, J. E., Foekens, J. A., Greaves, M., Hosoda, F., Hutter, B., Ilicic, T., Imbeaud, S., Imielinski, M., Jager, N., Jones, D. T., Jones, D., Knappskog, S., Kool, M., Lakhani, S. R., Lopez-Otin, C., Martin, S., Munshi, N. C., Nakamura, H., Northcott, P. A., Pajic, M., Papaemmanuil, E., Paradiso, A., Pearson, J. V., Puente, X. S., Raine, K., Ramakrishna, M., Richardson, A. L., Richter, J., Rosenstiel, P., Schlesner, M., Schumacher, T. N., Span, P. N., Teague, J. W., Totoki, Y., Tutt, A. N., Valdes-Mas, R., van Buuren, M. M., van 't Veer, L., Vincent-Salomon, A., Waddell, N., Yates, L. R., Australian Pancreatic Cancer Genome, I., Consortium, I. B. C., Consortium, I. M.-S., PedBrain, I., Zucman-Rossi, J., Futreal, P. A., McDermott, U., Lichter, P., Meyerson, M., Grimmond, S. M., Siebert, R., Campo, E., Shibata, T., Pfister, S. M., Campbell, P. J., and Stratton, M. R. (2013) Signatures of mutational processes in human cancer. *Nature* **500**, 415-421

25. Alexandrov, L., Kim, J., Haradhvala, N. J., Huang, M. N., Ng, A. W. T., Boot, A., Covington, K. R., Gordenin, D. A., Bergstrom, E., Lopez-Bigas, N., Klimczak, L. J., McPherson, J. R., Morganella, S., Sabarinathan, R., Wheeler, D. A., Mustonen, V., Getz, G., Rozen, S. G., and Stratton, M. R. (2018) The Repertoire of Mutational Signatures in Human Cancer. *bioRxiv*

26. Nassar, D., Latil, M., Boeckx, B., Lambrechts, D., and Blanpain, C. (2015) Genomic landscape of carcinogen-induced and genetically induced mouse skin squamous cell carcinoma. *Nat Med* **21**, 946-954

27. Freed-Pastor, W. A., and Prives, C. (2012) Mutant p53: one name, many proteins. *Genes Dev* **26**, 1268-1286

28. Patel, V., Marsh, C. A., Dorsam, R. T., Mikelis, C. M., Masedunskas, A., Amornphimoltham, P., Nathan, C. A., Singh, B., Weigert, R., Molinolo, A. A., and Gutkind, J. S. (2011) Decreased lymphangiogenesis and lymph node metastasis by mTOR inhibition in head and neck cancer. *Cancer Res* **71**, 7103-7112

29. Doci, C. L., Mikelis, C. M., Lionakis, M. S., Molinolo, A. A., and Gutkind, J. S. (2015) Genetic Identification of SEMA3F as an Antilymphangiogenic Metastasis Suppressor Gene in Head and Neck Squamous Carcinoma. *Cancer Res* **75**, 2937-2948

30. Bronte, V., Brandau, S., Chen, S. H., Colombo, M. P., Frey, A. B., Greten, T. F., Mandruzzato, S., Murray, P. J., Ochoa, A., Ostrand-Rosenberg, S., Rodriguez, P. C., Sica, A., Umansky, V., Vonderheide, R. H., and Gabrilovich, D. I. (2016) Recommendations for myeloid-derived suppressor cell nomenclature and characterization standards. *Nature communications* **7**, 12150

31. Sharabi, A. B., Lim, M., DeWeese, T. L., and Drake, C. G. (2015) Radiation and checkpoint blockade immunotherapy: radiosensitisation and potential mechanisms of synergy. *Lancet Oncol* **16**, e498-509

32. Zandberg, D. P., and Strome, S. E. (2014) The role of the PD-L1:PD-1 pathway in squamous cell carcinoma of the head and neck. *Oral Oncol* **50**, 627-632

33. Sun, C., Mezzadra, R., and Schumacher, T. N. (2018) Regulation and Function of the PD-L1 Checkpoint. *Immunity* **48**, 434-452

34. Kim, J. M., Rasmussen, J. P., and Rudensky, A. Y. (2007) Regulatory T cells prevent catastrophic autoimmunity throughout the lifespan of mice. *Nat Immunol* **8**, 191-197

35. Leemans, C. R., Braakhuis, B. J., and Brakenhoff, R. H. (2011) The molecular biology of head and neck cancer. *Nat Rev Cancer* **11**, 9-22

36. Williams, R., Lee, D. W., Elzey, B. D., Anderson, M. E., Hostager, B. S., and Lee, J. H. (2009) Preclinical models of HPV+ and HPV- HNSCC in mice: an immune clearance of HPV+ HNSCC. *Head Neck* **31**, 911-918

37. Chalivendra, V., Kanchi, K. L., Onken, M. D., Winkler, A. E., Mardis, E., and Uppaluri, R. (2015) Genomic analysis to define molecular basis of aggressiveness in a mouse model of oral cancer. *Genom Data* **3**, 61-62

38. Yan, R. D., and Durand, R. E. (1991) The response of hypoxic cells in SCCVII murine tumors to treatment with cisplatin and x rays. *Int J Radiat Oncol Biol Phys* **20**, 271-274

39. Judd, N. P., Winkler, A. E., Murillo-Sauca, O., Brotman, J. J., Law, J. H., Lewis, J. S., Jr., Dunn, G. P., Bui, J. D., Sunwoo, J. B., and Uppaluri, R. (2012) ERK1/2 regulation of CD44 modulates oral cancer aggressiveness. *Cancer Res* **72**, 365-374

40. Cancer Genome Atlas, N. (2015) Comprehensive genomic characterization of head and neck squamous cell carcinomas. *Nature* **517**, 576-582

41. Hoadley, K. A., Yau, C., Hinoue, T., Wolf, D. M., Lazar, A. J., Drill, E., Shen, R., Taylor, A. M., Cherniack, A. D., Thorsson, V., Akbani, R., Bowlby, R., Wong, C. K., Wiznerowicz, M., Sanchez-Vega, F., Robertson, A. G., Schneider, B. G., Lawrence, M. S., Noushmehr, H., Malta, T. M., Cancer Genome Atlas, N., Stuart, J. M., Benz, C. C., and Laird, P. W. (2018)

Cell-of-Origin Patterns Dominate the Molecular Classification of 10,000 Tumors from 33 Types of Cancer. *Cell* **173**, 291-304 e296

42. Su, S. C., Lin, C. W., Liu, Y. F., Fan, W. L., Chen, M. K., Yu, C. P., Yang, W. E., Su, C. W., Chuang, C. Y., Li, W. H., Chung, W. H., and Yang, S. F. (2017) Exome Sequencing of Oral Squamous Cell Carcinoma Reveals Molecular Subgroups and Novel Therapeutic Opportunities. *Theranostics* **7**, 1088-1099

43. Zarour, H. M. (2016) Reversing T-cell Dysfunction and Exhaustion in Cancer. *Clin Cancer Res* **22**, 1856-1864

44. Koyama, S., Akbay, E. A., Li, Y. Y., Herter-Sprie, G. S., Buczkowski, K. A., Richards, W. G., Gandhi, L., Redig, A. J., Rodig, S. J., Asahina, H., Jones, R. E., Kulkarni, M. M., Kuraguchi, M., Palakurthi, S., Fecci, P. E., Johnson, B. E., Janne, P. A., Engelman, J. A., Gangadharan, S. P., Costa, D. B., Freeman, G. J., Bueno, R., Hodi, F. S., Dranoff, G., Wong, K. K., and Hammerman, P. S. (2016) Adaptive resistance to therapeutic PD-1 blockade is associated with upregulation of alternative immune checkpoints. *Nature communications* **7**, 10501

45. Kamada, T., Togashi, Y., Tay, C., Ha, D., Sasaki, A., Nakamura, Y., Sato, E., Fukuoka, S., Tada, Y., Tanaka, A., Morikawa, H., Kawazoe, A., Kinoshita, T., Shitara, K., Sakaguchi, S., and Nishikawa, H. (2019) PD-1(+) regulatory T cells amplified by PD-1 blockade promote hyperprogression of cancer. *Proceedings of the National Academy of Sciences of the United States of America* **116**, 9999-10008

46. Buchbinder, E. I., and Desai, A. (2016) CTLA-4 and PD-1 Pathways: Similarities, Differences, and Implications of Their Inhibition. *American journal of clinical oncology* **39**, 98-106

47. Siu, L. L., Even, C., Mesia, R., Remenar, E., Daste, A., Delord, J. P., Krauss, J., Saba, N. F., Nabell, L., Ready, N. E., Brana, I., Kotecki, N., Zandberg, D. P., Gilbert, J., Mehanna, H., Bonomi, M., Jarkowski, A., Melillo, G., Armstrong, J. M., Wildsmith, S., and Fayette, J. (2019) Safety and Efficacy of Durvalumab With or Without Tremelimumab in Patients With PD-L1-Low/Negative Recurrent or Metastatic HNSCC: The Phase 2 CONDOR Randomized Clinical Trial. *JAMA Oncol* **5**, 195-203

48. Li, X., Wang, J., Yao, Y., Yang, L., Li, Z., Yu, C., Zhao, P., Yu, Y., and Wang, L. (2017) Comparative efficacy and safety of immune checkpoint inhibitor-related therapies for advanced melanoma: a Bayesian network analysis. *Oncotarget* **8**, 83637-83649

49. Bertrand, A., Kostine, M., Barnetche, T., Truchetet, M. E., and Schaeverbeke, T. (2015) Immune related adverse events associated with anti-CTLA-4 antibodies: systematic review and meta-analysis. *BMC Med* **13**, 211

50. Aznar, M. A., Tinari, N., Rullan, A. J., Sanchez-Paulete, A. R., Rodriguez-Ruiz, M. E., and Melero, I. (2017) Intratumoral Delivery of Immunotherapy-Act Locally, Think Globally. *J Immunol* **198**, 31-39

51. Marabelle, A., Tselikas, L., de Baere, T., and Houot, R. (2017) Intratumoral immunotherapy: using the tumor as the remedy. *Ann Oncol* **28**, xii33-xii43

52. Mandal, R., Senbabaoglu, Y., Desrichard, A., Havel, J. J., Dalin, M. G., Riaz, N., Lee, K. W., Ganly, I., Hakimi, A. A., Chan, T. A., and Morris, L. G. (2016) The head and neck cancer immune landscape and its immunotherapeutic implications. *JCI Insight* **1**, e89829

53. Thorsson, V., Gibbs, D. L., Brown, S. D., Wolf, D., Bortone, D. S., Ou Yang, T. H., Porta-Pardo, E., Gao, G. F., Plaisier, C. L., Eddy, J. A., Ziv, E., Culhane, A. C., Paull, E. O., Sivakumar, I. K. A., Gentles, A. J., Malhotra, R., Farshidfar, F., Colaprico, A., Parker, J.

S., Mose, L. E., Vo, N. S., Liu, J., Liu, Y., Rader, J., Dhankani, V., Reynolds, S. M., Bowlby, R., Califano, A., Cherniack, A. D., Anastassiou, D., Bedognetti, D., Rao, A., Chen, K., Krasnitz, A., Hu, H., Malta, T. M., Noushmehr, H., Pedamallu, C. S., Bullman, S., Ojesina, A. I., Lamb, A., Zhou, W., Shen, H., Choueiri, T. K., Weinstein, J. N., Guinney, J., Saltz, J., Holt, R. A., Rabkin, C. E., Cancer Genome Atlas Research, N., Lazar, A. J., Serody, J. S., Demicco, E. G., Disis, M. L., Vincent, B. G., and Shmulevich, L. (2018) The Immune Landscape of Cancer. *Immunity* **48**, 812-830 e814

54. Li, H., and Durbin, R. (2009) Fast and accurate short read alignment with Burrows-Wheeler transform. *Bioinformatics* **25**, 1754-1760

55. Kim, S., Scheffler, K., Halpern, A. L., Bekritsky, M. A., Noh, E., Kallberg, M., Chen, X., Kim, Y., Beyter, D., Krusche, P., and Saunders, C. T. (2018) Strelka2: fast and accurate calling of germline and somatic variants. *Nat Methods* **15**, 591-594

56. Koboldt, D. C., Zhang, Q., Larson, D. E., Shen, D., McLellan, M. D., Lin, L., Miller, C. A., Mardis, E. R., Ding, L., and Wilson, R. K. (2012) VarScan 2: somatic mutation and copy number alteration discovery in cancer by exome sequencing. *Genome Res* **22**, 568-576

57. Cibulskis, K., Lawrence, M. S., Carter, S. L., Sivachenko, A., Jaffe, D., Sougnez, C., Gabriel, S., Meyerson, M., Lander, E. S., and Getz, G. (2013) Sensitive detection of somatic point mutations in impure and heterogeneous cancer samples. *Nat Biotechnol* **31**, 213-219

58. Jay, J. J., and Brouwer, C. (2016) Lollipops in the Clinic: Information Dense Mutation Plots for Precision Medicine. *PLoS One* **11**, e0160519

59. Bankhead, P., Loughrey, M. B., Fernandez, J. A., Dombrowski, Y., McArt, D. G., Dunne, P. D., McQuaid, S., Gray, R. T., Murray, L. J., Coleman, H. G., James, J. A., Salto-Tellez, M., and Hamilton, P. W. (2017) QuPath: Open source software for digital pathology image analysis. *Sci Rep* **7**, 16878

Chapter 4: A chemogenetic approach reveals a GPCR-Gαs-PKA signaling axis promoting T cell dysfunction and cancer immunotherapy failure

4.1 Abstract

Recent advances in immune checkpoint blockade (ICB) inhibiting programmed death-1 (PD-1) and cytotoxic T-lymphocyte antigen-4 (CTLA-4) have revolutionized the standard of care for cancer treatment. However, the limited response rates to ICB across multiple cancer types suggest that new approaches and targets are clearly needed in order to achieve durable responses (cure). G protein-coupled receptors (GPCRs) are the most intensively studied drug targets, primarily due to their druggability and relevance to most physiological processes and disease conditions. Here, we used a new computational pipeline to cross-integrate hundreds of thousands of CD8 T cells from multiple single cell RNA-seq datasets from 13 distinct cancer types, which revealed a significant enrichment of $G\alpha_s$-coupled GPCRs on exhausted T cells. These include EP_2, EP_4, $A_{2A}R$, β_1AR, and β_2AR, all of which promote T cell dysfunction by inhibiting cytotoxicity and cytokine secretion. Using a novel synthetic biology approach, we developed a chemogenetic CD8-restricted $G\alpha_s$-DREADD (Designer Receptor Exclusively Activated by A Designer Drug) transgenic mouse model in which activation of $G\alpha_s$ signaling is temporally and spatially controlled. By utilizing this $G\alpha_s$-DREADD model, we discovered that the $G\alpha_s$-signaling axis represents a previously uncharacterized signaling axis that dampens the anti-tumor CD8 T cell activity and leads to ICB immunotherapy failure. Our findings reveal that $G\alpha_s$-coupled GPCRs may represent new targetable immune checkpoints that can be combined with ICB as part of novel multimodal precision approaches to enhance the response to immunotherapies.

4.2 Introduction

Breakthrough discoveries over the past few decades have begun to unravel the complexity of the anti-tumor immune response, leading to the introduction of immunotherapies into the clinic (1-7). Successful response to immunotherapy largely depends upon the immune infiltration of cytotoxic T lymphocytes (CTLs), such as CD8 T cells, into the tumor microenvironment (TME). However, the complex immunosuppressive network at the TME may still dampen the antitumor function of CTLs through immune checkpoints, namely programmed death-1 (PD-1) and cytotoxic T-lymphocyte-associated protein 4 (CTLA-4), driving them towards terminal differentiation into exhausted T cells (anergy) (5,7,8). As a result, immune checkpoint blockade (ICB) by antibodies targeting PD-1 (e.g., nivolumab, pembrolizumab, cemiplimab), its ligand programmed death-ligand 1 (PD-L1) (e.g., atezolizumab, avelumab, durvalumab), and CTLA-4 (ipilimumab & tremelimumab) have been approved for multiple cancer types (9-15). As monotherapies, these checkpoint inhibitors have shown remarkable efficacy in the clinic. Despite this, responsiveness to immunotherapy is restricted to certain tumor types, and most patients who initially respond do not have subsequent durable tumor control (16). Accordingly, this raises the possibility that additional immune checkpoints on CD8 T cells may exist, which prevent ICB from achieving its full potential and leads to primary or acquired resistance. In this regard, tumors may deploy multiple immune evasion strategies to bypass anti-tumor immune responses that may need to be blocked concomitantly with ICB in order achieve durable tumor remission.

G-protein coupled receptors (GPCRs) represent the largest family of cell surface receptors involved in signal transmission, and are the target of >30% of all FDA-approved drugs (17). GPCRs have remained the longstanding most pharmacologically favorable drug targets primarily due to their druggability and relevance to most physiological processes and highly prevalent disease conditions (17,18). However, the role of GPCRs in immune oncology is understudied; while aberrant GPCR signaling has been implicated in cancer, their roles and expression patterns on immune cells infiltrating tumors and as a target for immunotherapies are less understood (19-

21). There are 800 known human GPCRs and over 300 non-olfactory GPCRs, and their signaling cascades are primarily determined by activation of one or multiple heterotrimeric $G\alpha$ proteins (e.g., $G\alpha_s$, $G\alpha_{i/o}$, $G\alpha_{q/11}$, and $G\alpha_{12/13}$) (22). Intriguingly, the nature of the immune cell infiltrating the TME is largely dictated by chemokines and their GPCRs that guide and recruit different pro- or anti-tumoral immune cells to the tumor, largely orchestrating the balance between cytotoxicity and immunosuppression (21). Most chemokine receptors are coupled to $G\alpha_i$, inhibiting cyclic AMP (cAMP) production, while $G\alpha_s$-coupled receptors activate adenylyl cyclases, thereby stimulating the production of cAMP and downstream protein kinase A (PKA) signaling. With this, the interplay between signaling circuitries from GPCRs expressed on CTLs may ultimately dictate the ability to elicit effective cancer immune responses. Notably, CXCR3, a $G\alpha_i$-coupled GPCR on T cells binds three chemokines, CXCL9/10/11, to promote the migration of T cells into the tumor (23). These chemokines are known to be induced by IFNα, β, and γ, and are part of the interferon gene signature, which have predictive value for a favorable response to pembrolizumab (24). In contrast to these anti-tumor chemokine receptors that guide the migration of cytotoxic T cells to the tumor, other GPCRs expressed on T cells may override chemokine-coordinated intratumoral CTL migration, and instead display immune suppressive functions.

One of the few immune suppressive GPCRs investigated in cancer immunology is the adenosine A_{2A} receptor ($A_{2A}R$, encoded by *ADORA2A*), which is currently being explored in combination with ICB in early Phase1/1b trials for solid and liquid tumors (25). $A_{2A}R$ is a $G\alpha_s$-coupled GPCR on CTLs, which binds adenosine that accumulates in the TME and has been associated with T cell dysfunction (26,27). However, the downstream mechanisms by which $A_{2A}R$ mediates its immunosuppressive role in T cells is not well understood. This also raises the possibility that the TME may take advantage of GPCR-initiated signaling from other GPCRs to inhibit anti-tumoral T cell responses, which may contribute to incomplete responses to ICB.

By the use of a novel computational pipeline to integrate large datasets of intratumoral T cell single cell RNA sequencing (scRNA-seq) combined with a synthetic biology approach, we show here that activation of $G\alpha_s$-coupled GPCRs and the $G\alpha_s$ signaling axis is sufficient to drive a hyporesponsive T cell state. Indeed, activation of $G\alpha_s$ signaling contributes to a general CD8 T cell dysfunction by inhibiting cytotoxicity, cytokine secretion, and promoting T cell exhaustion. Our findings reveal that concomitant inhibition of $G\alpha_s$-coupled GPCRs with ICB may be necessary to reactivate the anti-tumor immune response, thereby providing a novel multi-modal immunotherapy approach for cancer treatment.

4.3 Results

4.3.1 $G\alpha_s$-coupled GPCR expression and T cell dysfunction

Given the multiple roles GPCRs play in inflammation, immune cell trafficking, and the binding of a myriad of ligands abundant in the TME, we first sought to delineate the landscape of GPCR expression patterns on different T cell subtypes in the tumor. Building on our previous analysis shedding light on the onco-GPCRome and aberrant GPCR signaling and activity on tumor cells (21), we began by investigating the landscape of GPCR expression on each tumor-infiltrating CD8 T cell subtype. In order to condense the heterogeneous population of tumor infiltrating immune cells and distinguish commonalities in GPCR expression on CD8 T cells across cancer types, we collected data and performed an integrated analysis of scRNA-seq datasets from 13 cancer types (i.e. cutaneous melanoma (CM), colorectal cancer (CRC), pancreatic ductal adenocarcinoma (PDAC), hepatocellular carcinoma (HCC), intrahepatic cholangiocarcinoma (ICC), basal cell carcinoma (BCC), uveal melanoma (UM), non-small cell lung cancer (NSCLC), breast carcinoma (BC), squamous cell carcinoma (SCC), ovarian cancer (OC), renal cell carcinoma (RCC), basal and squamous cell carcinomas (BCC, SCC), ovarian cancer (OC), renal cell carcinoma (RCC), and endometrial adenocarcinoma (EA)) (**Figure 4.1a and Table 4.1**). Using the Seurat scRNA-seq integration method, we jointly analyzed 112,610 total CD8 T cells, which were stratified into

naïve (N), proliferating (P), cytotoxic (C), effector memory (EM), pre-exhausted (PE), and terminally exhausted (TE) based on previously described annotations and expression of landmark genes (28) (**Figure 4.1b, 4.1c, S4.1a, S4.1b**). When we analyzed the relative expression of 386 GPCR genes, many GPCRs showed a distinct expression pattern in each CD8 T cell subtype (**Figure 4.1d**). Specifically within TE CD8 T cells, we found that *CXCR6*, *PTGER4*, *GPR65*, *GPR171*, and *P2RY10* were among the top GPCRs expressed, with expression patterns similar to those of signature exhaustion genes (**Figure 4.1e**).

Recent studies have demonstrated a significant correlation between PD-1-high-expressing, highly dysfunctional and exhausted T cells with survival and response status to immunotherapies in NSCLC and melanoma (29,30). Previously, a distinct transcriptional gene module was calculated to quantify T cell dysfunction linked to *LAG3* expression (e.g., *TIGIT*, *PDCD1*, *LAG3*, and *CXCL13*) in human melanoma patients (29). These modules consist of transcriptional scores of both genes and transcription factors (TFs) that can reliably predict dysfunctional programs. Here, we aimed to identify GPCRs most relevant to this dysfunction program (**Figure 4.1f**). First, we generated dysfunction scores for all CD8 T cells from our integrated analyses. As expected, amongst the different CD8 subtypes, TE CD8 T cells across 13 cancer types displayed the highest dysfunction scores, and in addition pre-exhausted and proliferating CD8s also had elevated dysfunction scores (**Figure 4.1g**).

We next investigated which GPCR genes are the most associated with the T cell dysfunction score. *CXCR6*, a marker previously shown to be expressed on PD-1^{hi} effector and exhausted CD8 T chronic viral infection, was the GPCR most significantly correlated with T cell dysfunction (31,32) (**Figure 4.1h**). In total, 35 GPCRs were shown to be significantly correlated with the dysfunction score, with *GPR56*, *CCRL2*, *GIPR*, and *F2R* among the top candidates to contribute to T cell exhaustion (**Figure 4.1h and Table 4.2**). We next aimed to distinguish patterns of expression based on heterotrimeric G protein coupling information to gain functional context and information regarding GPCR expression as a functional gene set. Based on the International

Union of Basic and Clinical Pharmacology (IUPHAR) classification, we grouped all GPCRs into G protein programs based on their primary G protein coupling to $G\alpha_{12/13}$, $G\alpha_i$, $G\alpha_{q/11}$, or $G\alpha_s$. Intriguingly, when we calculated the mean correlation of each pathway with T cell dysfunction, we found that the $G\alpha_s$ program was the most enriched with T cell dysfunction while the $G\alpha_i$ program was the least correlated (**Figure 4.1i**). Specifically, when we looked at all the GPCRs that are $G\alpha_s$-coupled, the GPCRs with significant Spearman correlations were all positively correlated with T cell dysfunction, including *GIPR*, *ADORA2A*, *PTGER4*, *GPR65*, and *TSHR* (**Figure 4.1j**). These data raise the possibility of a GPCR-$G\alpha_s$-signaling program that correlates with T cell dysfunction in tumor-infiltrating CD8 T cells.

4.3.2 Agonists for endogenously expressed $G\alpha_s$-coupled GPCRs diminishes effector T cell function

Next, we investigated whether tumor-associated T cell dysfunction-associated $G\alpha_s$-coupled GPCRs were also associated with T cell exhaustion phenotypes. First, we explored the relevance of these $G\alpha_s$-GPCRs in murine models of T cell exhaustion in addition to T cell dysfunction. For these studies we analyzed bulk transcriptomic data from the murine lymphocytic choriomeningitis chronic viral infection model (LCMV), which represents the experimental model system most central to recent, landmark discoveries defining T cell exhaustion (33,34) (**Figure 4.2a**). In this model, an acute strain of LCMV infection (Armstrong) generates robust, proliferative, and activated effector CD8 T cells that are able to resolve infection (35). Contrastingly, the chronic strain of LCMV infection (clone 13) leads to persistent antigen exposure, generating a transcriptionally and epigenetically distinct exhausted T cell state, with sustained expression of inhibitory receptors (e.g., PD-1, CTLA-4, TIM3, LAG3) as well as hierarchical loss of effector functions (35). We combined 3 RNA-sequencing datasets of fluorescent-activated cell sorting (FACS)-purified effector CD8 T cells from acute LCMV infection and exhausted T cells from chronic LCMV infection, and used DESeq2 to directly compare differential expression of GPCRs

between the two CD8 subtypes. Differential expression analysis revealed that multiple $G\alpha_s$-coupled GPCRs are upregulated in exhausted T cells compared to effector T cells, including *Glp1r*, *Ptger2*, *Ptger4*, and *Gpr65*, receptors that were also significantly correlated with T cell dysfunction in human tumor infiltrating CD8 T cells (**Figure 4.1g**, above, and **Figure 4.2b and Table 4.3**). This suggests that the $G\alpha_s$-coupled GPCRs that are expressed on both exhausted tumor-infiltrating CD8 T cells as well as exhausted CD8 T cells from chronic viral infection are intrinsically similar.

Recently, as part of a large scale analysis of signaling via representatives of the four G protein subfamilies that using TGF-α shedding responses and NanoBiT-G-protein dissociation assay, we determined coupling across 148 human GPCRs for 11 specific human G proteins and used a machine learning approach to augment a GPCR coupling predictions for Class A GPCRs (36). Here, we curated gene sets stratifying G protein coupling as designated by either IUPHAR, the TGF-α shedding assay, or our coupling predictor. We then performed a gene set enrichment analysis of GPCRs significantly upregulated in exhausted or effector T cells in LCMV infection and aimed to determine enrichment to specific G protein coupling pathways. Intriguingly, we found that the $G\alpha_s$-coupling gene set by IUPHAR had the most significant enrichment with upregulated GPCRs on exhausted T cells (**Figure 4.2c**). Additional gene sets were also significantly enriched for upregulated GPCRs on exhausted T cells, including GNAQ predicted coupling, $G_{q/11}$ primary IUPHAR coupling, and GNA14 predicted coupling (**Figure 4.2c**). Altogether, this suggests that in addition to T cell dysfunction, the expression of these $G\alpha_s$-coupled GPCRs may also play a role in driving T cell exhaustion.

To gain a better understanding of how the expression of these $G\alpha_s$-GPCRs modulate CD8 T cells, we first sought to model impairment of T cell function resulting from persistent TCR signaling by modulating T cell activation *in vitro* (**Figure 4.2e**). CD8+ T cells from splenocytes of wild type (WT) mice were activated fully with anti-CD3 and anti-CD28 for 48 hours. Subsequently,

activated T cells were subjected to additional restimulation with anti-CD3 and anti-CD28 (chronic stimulation) to model reactivation of T cells upon TCR engagement at the tumor. As a control, CD8 T cells were also expanded in culture with interleukin 2 (IL-2) (activated) without additional restimulation. Characteristic of terminally exhausted cells, the expression of PD-1, CTLA-4, TIM3, and LAG3 on CD8 T cells were all significantly elevated in chronically versus acutely stimulated CD8s, concomitant with a decrease in IFNγ and TNFα, confirming in this assay that chronically activated CD8 T cells begin acquiring an exhaustion-like phenotype (**Supplemental Figure S4.2a**).

Next, to simulate exposure of $G\alpha_s$ ligands at the tumor microenvironment, we added ligands stimulating various $G\alpha_s$-GPCRs that correlate with T cell dysfunction and/or exhaustion: prostaglandin E2 (P) for EP_2 (*PTGER2*) and EP_4 (*PTGER4*) receptors, CGS-21680 (C) for $A_{2A}R$ (*ADORA2A*), and dobutamine (D) for β1- and β2-adrenergic receptors (β_1AR-*ADRB1)*, (β_2AR-*ADRB2*). After 48 hours of the initial activation, CD8 T cells were replated for an additional 48 hours of activation with or without $G\alpha_s$ ligands, and measured the functional capacity by flow cytometric analysis of IFNγ, TNFα, and granzyme B. The combination of continuous stimulation and the addition of PGE2, dobutamine, or CGS-21680 all significantly reduced IFNγ and TNFα polyfunctionality as well as granzyme B positivity (**Figure 4.2f, 4.2g**). A similar reduction was seen in the proliferative capacity of CD8 T cells, as indicated by the reduction in Ki-67 positivity as a marker for actively dividing cells (**Supplemental Figure S4.2b**). Moreover, stimulation with PGE2 and dobutamine significantly elevated PD-1 and Tim-3 expression (**Figure 4.2g**). The simultaneous reduction in T cell function and proliferation and increase of inhibitory receptor expression suggests that $G\alpha_s$ ligands augment the dysfunctional phenotypes in CD8 T cells polarizing towards exhaustion.

In order to evaluate the functional suppression by $G\alpha_s$ ligands on cytotoxic T cell killing, we activated purified T cells from OT-1 transgenic mice, whose TCRs are specific for the ovalbumin (OVA) peptide, SIINFEKL ($OVA_{257-264}$), and co-cultured them with MC38 tumor cells expressing OVA (MC38-OVA) at a 1:5 effector to target ratio (**Figure 4.2h**). $G\alpha_s$ ligands significantly diminished the ability of OT-1 CD8 T cells to kill MC38-OVA as measured by viability of tumor cells after 2 days (**Figure 4.2i**). Altogether, our in vitro experiments identify an inhibitory effect of ligands for $G\alpha_s$-GPCRs on T cell function and cytotoxic killing.

In order to pinpoint the underlying mechanisms of $G\alpha_s$-mediated CD8 T cell dysfunction, we next characterized the pathways downstream of $G\alpha_s$/cAMP that drive immune suppression. We focused on PGE2, as this inflammatory mediator led to the most pronounced inhibition of function out of all the $G\alpha_s$ ligands that we tested. Addition of PGE2 and forskolin (fsk), a direct adenylyl cyclase-cAMP activator, during chronic stimulation led to a significant increase of the cAMP response element-binding protein (pCREB), which becomes phosphorylated following a rise in intracellular cAMP and activation of PKA (**Figure 4.2j**). While addition of EP_2 or EP_4 inhibitors (EP_2i and EP_4i, respectively) significantly decreased PGE2-induced activation of pCREB, this rescue effect was not seen for fsk-induced activation of pCREB, supporting the receptor mediated effects of PGE2 on PKA (**Figure 4.2k**). Similarly, addition of EP_2i or EP_4i antagonists restored production of IFNγ and TNFα secretion following inhibition by PGE2, but did not have significant effect on fsk-related inhibition (**Figure 4.2i**). Interestingly, the addition of EP_2 and EP_4 antagonists together more significantly reduced PGE2-mediated IFNγ and TNFα inhibition as compared to each antagonist alone, suggesting that concomitant blockade of $G\alpha_s$ activation by multiple $G\alpha_s$ receptors may afford better rescue from immune suppressive effects on CD8 T cells.

To explore whether removal of $G\alpha_s$ could alleviate PGE2-mediated inhibition of T cell function, we generated conditional CD8-specific *Gnas* knockout mice (**Figure 4.2l**). Mice

expressing a tamoxifen-inducible Cre driven by the E8i promoter were crossed with mice with loxP sites flanking *Gnas* exon one, which we refer to as CD8-*Gnas KO* (**Figure 4.2l**). CD8 T cells were isolated and chronically stimulated following administration of tamoxifen. As expected, CD8 T cells with fully functional $G\alpha_s$ generated significantly less IFNγ and TNFα after treatment with PGE2 (**Figure 4.2m**), which was nearly abolished in CD8 T cells from CD8-*Gnas KO* mice (**Figure 4.2m**). Together, this strongly suggests that *Gnas* and its downstream signaling is necessary for PGE2-mediated inhibitory effects on CD8 T cells.

4.3.3 Chemogenetic approach to determine mechanisms of immune suppression by $G\alpha_s$ stimulation

In recent years, studies on tissue-specific G protein signaling has been revolutionized by the development of DREADDs (designer receptors exclusively activated by designer drugs) (37,38). These synthetic GPCRs are modified human muscarinic receptors that have been engineered to be non-responsive to their endogenous ligand and extremely responsive to very low (nM) concentrations of a designer drug, allowing to control G protein activation in a tissue specific fashion. Classically, the synthetic drug, clozapine-N-oxide (CNO) has been used to activate DREADDs. However, in order to bypass sluggish kinetics and potential off-targeted effects elicited by CNO, we utilized the recently developed deschloroclozapine (DCZ), which has been shown to afford higher affinity and more selective agonist activity for DREADDs (39). To specifically interrogate the function of the $G\alpha_s$ signaling axis in CD8 T cell anti-tumor function, we took advantage of recently generated mice with CD8 T cell-restricted Cre recombinase temporally controlled with tamoxifen (40) (*E8i-CreERT2*), and achieved expression of $G\alpha_s$-DREADD by crossing *E8i-CreERT2* mice with *ROSA26-LSL-Gs-DREADD* mice (**Figure 4.3a and Supplemental Figure S4.3a**). The resulting mice, which we refer to as CD8-GsD, were dosed every day for 3 days with tamoxifen and $G\alpha_s$-DREADD expression and activation was subsequently verified (**Figure 4.3b**). By quantitative PCR, mice without tamoxifen did not show

demonstrable $G\alpha_s$-DREADD expression in either CD4 or CD8 T cells (**Figure 4.3c**). However, in mice treated with tamoxifen, there was a clear expression of $G\alpha_s$-DREADD expression in CD8 T cells but not in CD4 T cells as controls (**Figure 4.3c**). This confirmed tamoxifen-inducible recombination by the CRE recombinase for CD8-resctricted $G\alpha_s$-DREADD expression.

To confirm activation of the $G\alpha_s$-DREADD, mice were first dosed with tamoxifen, and then 0.01 mg/kg of DCZ was administered intraperitoneally (**Figure 4.3b**). Activation of the $G\alpha_s$-DREADD was confirmed by induction of pCREB. After administration of tamoxifen and DCZ, mice were subsequently bled to assess pCREB induction by flow cytometry. Whereas the frequency of $pCREB^+$ in $NK1.1^+$ NK cells, $CD11b^+$ myeloid cells, and $CD4^+$ T cells were low and not different in DCZ treated versus non-treated mice, the frequency of $CD8^+$ $pCREB^+$ cells significantly increased in DCZ-treated mice (**Figure 4.3d**). Moreover, mice treated with DCZ did not show significant changes in frequency of CD8, CD4, NK cells, or CD11b myeloid cells in the peripheral blood (**Supplemental Figure S4.3b**). Aligned with this, when we isolated peripheral blood from mice dosed with tamoxifen, addition of DCZ in vitro also increased pCREB exclusively in CD8 T cells (**Figure 4.3e**). Altogether, these results confirm tamoxifen-inducible, CD8-specific expression and activation of $G\alpha_s$-DREADD by DCZ in CD8-GsD mice.

Next, we sought to determine whether activation of $G\alpha_s$-signaling on CD8 T cells isolated from CD8-GsD mice by DCZ treatment behaved similarly to CD8 T cells from WT mice responding to ligands for $G\alpha_s$-coupled GPCRs. CD8 T cells isolated from CD8-GsD mice treated with or without tamoxifen were activated for 48 hours and chronically stimulated with or without DCZ (**Figure 4.3f**). Aligned with our data from ligands for $G\alpha_s$-coupled GPCRs, only in mice with tamoxifen-induced expression of $G\alpha_s$-DREADD, CD8-$G\alpha_s$ activation led to a significant decrease of IFNγ and TNFα, as well as Ki-67 and granzyme B (**Figure 4.3g and 4.3h and Supplementary Figure S4.3b**). Similarly, activation of $G\alpha_s$ in CD8 T cells led to a significant increase in PD-1 and Tim-3 expression (**Figure 4.3h**)

In order to gain an understanding of downstream transcriptional modulations stimulated by $G\alpha_s$ signaling in CD8 T cells, we first assessed gene expression of dual-specificity phosphatase 1 (*Dusp1*), a CREB target that has previously been shown to be a negative regulator of T cell activation and function through inactivation of JNK and reduced NFATc1 (41-43) (**Figure 4.3i**). Stimulation of the $G\alpha_s$-DREADD significantly increased expression of *Dusp1*, in addition to *Tigit* and *Tox*, both of which have been shown to be highly expressed on terminally exhausted CD8 T cells (44,45) (**Figure 4.3j**). Altogether, activation of $G\alpha_s$-DREADD on CD8 T cells was sufficient to exacerbate exhaustion-related phenotypes, as indicated by decreased cytotoxic function in tandem with increased expression of exhaustion-related genes.

To assess biological relevance of the inhibitory $G\alpha_s$ signaling in CD8 T cells in the tumor setting, we utilized the ovalbumin (OVA) tumor model system to investigate the effect of $G\alpha_s$ signaling on recruitment and function of antigen-specific CD8 T cells to the tumor. In order to study native T cell trafficking and function, we took advantage of an orthotopic head and neck cancer syngeneic mouse model, 4MOSC1, which our lab recently published and recapitulates human head and neck cancer mutational signatures with ~93% similarity (46,47). Mice were given 3 doses of tamoxifen before tumor implantation with 4MOSC1-OVA, and DCZ was given every day starting 1 day after tumor implantation (**Figure 4.3k**). Mice were sacrificed at an early time point to quantify the tumor-infiltrating SIINFEKL-tetramer+ CD8 T cells. At the tumor, there was a significant decrease of antigen-specific CD8 T cells infiltrating the tumor, and IFNγ and TNFα from the bulk CD8 population were both significantly decreased (**Figure 4.3l and 4.3m**). Our in vitro and in vivo data collectively indicate sufficiency of $G\alpha_s$-activation to drive exhaustion-related phenotypes and prevent trafficking of tumor-specific CD8 T cells.

4.3.4 $G\alpha_s$-signaling diminishes CD8 T cell anti-tumor responses and leads to immunotherapy failure

The availability of a unique mouse model system enabling the activation of GPCRs in specific immune cell populations prompted us to investigate the effect of CD8-specific Gαs-signaling on the immunotherapy response and tumor killing *in vivo*. CD8-GsD mice were dosed with tamoxifen and on day 0, $5x10^5$ 4MOSC1 cells or $1x10^5$ MC38-OVA cells were implanted into the tongue and flank of mice, respectively (**Figure 4.4a**). DCZ (0.01 mg/kg) was given daily to mice starting 1 day after tumor implantation. Whereas in the absence of agonist stimulation CD8-GsD mice with 4MOSC1 partially responded to anti-PD-1, similar to WT mice as we recently reported (46), activation of the $G\alpha_s$-DREADD by DCZ administration to mice abolished any anti-tumoral responses (**Figure 4.4b**). Additionally, though anti-PD-1 afforded a survival advantage in tumor-bearing mice, activation of the $G\alpha_s$ signaling axis in CD8 T cells led to survival rates not significantly different from untreated mice (**Figure 4.4b**). Similarly, in mice with MC38-OVA tumor cells, anti-PD-1 provided significant anti-tumor activity in CD8-GsD in absence of stimulation, but DCZ led to failed responsiveness and worse overall survival (**Figure 4.4c**).

Previously, we have shown that CTLA-4 blockade in the 4MOSC1 model leads to more durable, long-term anti-tumor responses and robust cytotoxic T cell responses compared to PD-1 blockade (46). Therefore, we next sought to determine whether activation of $G\alpha_s$ signaling in CD8 T cells was sufficient to limit the long-term anti-tumor immunity from CTLA-4 blockade. In the absence of DREADD ligand stimulation, 90% of CD8-$G\alpha_s$-DREADD mice responded to anti-CTLA-4 with durable tumor regression in line with previous data in WT mice (46) (**Figure 4.4d**). In CD8-GsD mice, though all mice initially responded to treatment, mice treated with the combination of anti-CTLA-4 and DCZ showed incomplete responses or tumor relapse even after the last dose of DCZ, leading to poorer survival compared with $G\alpha_s$-DREADD-expressing, non-activated mice (**Figure 4.4d**). Altogether, our data indicates that activation of the $G\alpha_s$ signaling axis on CD8 T cells limits T cell responses to anti-PD-1 and functionally impairs long-term immunity provided by anti-CTLA-4.

4.3.5 Elevated $G\alpha_s$-signaling program in cancer patients is associated with decreased response to ICB therapy

PD-1/PD-L1 blockade has been a major breakthrough for cancer immunotherapy, but the co-expression of $G\alpha_s$-GPCRs may still prevent TCR-mediated T cell activation even with anti-PD-1 therapy. Therefore, to begin exploring the clinical relevance of $G\alpha_s$-GPCR expression, we first investigated the correlation of expression between PD-1 and various $G\alpha_s$-GPCRs. In the TCGA skin cutaneous melanoma cohort, we found that *GPR65*, *PTGER2*, *PTGER4*, *ADRB2*, and *ADORA2A* were all significantly positively correlated with PD-1 expression in bulk tumors (**Figure 4.5a**). This suggests that at the bulk tumor level, PD-1 expression is likely concurrent with the expression of these GPCRs. We next asked whether the expression of these GPCRs could predict immunotherapy response in patients. To this end, we analyzed a cohort of 32 patients with metastatic melanoma (total biopsies = 48) treated either anti-PD-1 or anti-CTLA-4, or combination therapy, where single-cell RNAseq was performed on the tumors pre- and post- therapy. In this cohort, we observed that the expression levels of *GPR65*, *PTGER2*, *PTGER4*, *ADRB2*, and *ADORA2A* align with non-responders to immunotherapy, with *PTGER2* and *ADORA2A* expressed significantly higher in CD8 T cells from non-responders compared to responders, and *GPR65* nearing significance (**Figure 4.5b, 4.5c**). We next found that 4 of 5 of these $G\alpha$s-GPCRs (*PTGER4*, *GPR65*, *ADORA2A*, and *PTGER2*) have a significant predictive power to identify melanoma patients who would not respond to immunotherapy. In this analysis, *PTGER2* ranked at the top with the highest are under the curve (AUC) of 0.78 (**Figure 4.5c**).

To test the extent of the role of immune suppression in immunotherapy response by $G\alpha$s-GPCRs pathway across pan-cancer, we next computed the correlation between mean $G\alpha$s-GPCRs pathway levels in a cancer type and immunotherapy objective response rate (ORR) observed across 16 cancer types (48-50) We computed the mean $G\alpha$s-GPCRs pathway levels using TCGA expression profiles and immunotherapy response rate across 16 cancer types (51).

Remarkably, aligned with our hypothesis, we found that the mean levels of Gαs-GPCRs pathway levels in a cancer type is most negatively correlated with the immunotherapy ORR out of all the G protein signaling programs (**Figure 4.5d**).

In summary, we propose here a $G\alpha_s$-GPCR signaling axis that when activated in CD8 T cells, is sufficient to decrease cytotoxic function, exacerbate exhaustion-related phenotypes, and abolish responses to immunotherapy (**Figure 4.6**). The expression of various $G\alpha_s$-GPCRs is also correlated with PD-1 expression and has significant predictive value to predict non-responses to immunotherapy. Taken together, our data strongly suggests the need for concomitant blockade of $G\alpha_s$-GPCRs with other inhibitory receptors, including PD-1 and CTLA-4, in order to garner more effective and durable response to immunotherapy.

4.4 Discussion

Failed response to PD-1 and CTLA-4 blockade, or even combination therapy, in a large fraction of cancer patients indicate the existence of alternative mechanisms of functional suppression of T cell function after ICB therapy that need to be suppressed to enhance the therapeutic response to ICB (16). By the use of newly developed computational pipelines enabling the integration of scRNAseq datasets from hundreds of thousands of intratumoral immune cells and transcriptomic information delineating response to ICB, combined with the development of a chemogenetic approach to stimulate CD8-restricted $G\alpha_s$-GPCRs, we have now uncovered a CD8-T cell GPCR-$G\alpha_s$-signaling axis promoting T cell dysfunction and immunotherapy failure.

GPCR signaling networks in the TME orchestrate anti-cancer immune defense mechanisms, as demonstrated by chemokines and chemokine receptors displayed on both anti-tumoral and pro-tumoral immune cells (21). As such, increased chemokines that recruit CTLs, like CXCL9, CXLC10, and CXCL11, is associated with enhanced tumor-infiltrating CD8 T cells, better cancer prognosis and decreased metastasis and can predict a favorable response to anti-PD-1 treatment (24). On the other hand, metabolites and inflammatory mediators accumulating

in the TME can bind GPCRs that exert immunosuppressive effects. These include the nucleoside, adenosine, from the breakdown of ATP by ectonucleotidases CD39 and CD73, as well as the inflammatory mediator, PGE2, that is enzymatically derived from the cyclooxygenase (COX) isoforms, COX1 and COX2, which are upregulated in most solid cancers (52,53). Both adenosine and PGE2 stimulate multiple GPCRs that are expressed in many immune cell types, and, interestingly, exert their potent immunosuppressive activity by acting primarily on $G\alpha_s$-coupled receptors, $A_{2A}R$ (*ADORA2A*) and EP_2 (*PTGER2*) and EP_4 (*PTGER4*), respectively (54-56). Stimulation of A_{2A} receptor provides a broad immunosuppressive signal through multiple cell types that express $A_{2A}R$, including T cells, NK cells, DCs, and neutrophils (56). With this, blocking antibodies anti-CD73 and anti-CD39 are under current evaluation for combination with ICB as well as improvement of adoptive cell therapy efficacy (26,27,56). On the other hand, PGE2 has been linked to increased recruitment of MDSCs, increased expression of PD-1, and decreased CD8 T cell activation and NK cell recruitment and its ability to orchestrate the adaptive immune response, among others (21,57-59). Hence, nonsteroidal anti-inflammatory drugs (NSAIDs) that block COX2 and/or COX1 and COX2, and EP receptors represent promising targets for combination with ICB (60). However, the precise role of these receptors, $A_{2A}R$, EP_2, and EP_4 in CD8 T cell function in the TME is much less understood, as their corresponding receptors are expressed in multiple cell types and most studies to date have relied on global gene knock out strategies and systemic inhibition of receptors or biosynthetic pathways involved in ligand production. This may limit the ability to define key regulated events in CD8 T cells that may explain the beneficial effects of blockade of these GPCRs and predict responses when combined with ICB, as well as overlook the existence of redundant or compensatory mechanisms that may render these therapeutic interventions ineffective.

Given the complexity of receptor expression in multiple immune and tumor cells in the TME and difficulty of unraveling the function of these $G\alpha s$-linked GPCRs in CD8 T cells, we took

a synthetic biology approach to build chemogenetic DREADDs and gain spatial and temporal control of $G\alpha_s$ signaling specifically in CD8 T cells. The uniqueness of the CD8-GsD mouse model afforded us the opportunity to interrogate functions of $G\alpha_s$/cAMP/PKA irrespective of the GPCR that provides the activation. We found that activation of $G\alpha_s$-linked GPCRs in CD8 T cells is sufficient to limit antigen-specific CD8 T cell recruitment, abolish cytotoxic function, and abrogate the anti-tumor responses to both anti-PD-1 and anti-CTLA-4. Specifically, ligands for $G\alpha_s$-GPCRs significantly diminished functionality (accumulation of IFNγ, TNFα, granzyme B) and proliferation (Ki-67), two measures of effector-like functions. Additionally, $G\alpha_s$ stimulation also augmented expression of terminal exhaustion-related receptors, such as PD-1 and Tim-3, when activating $G\alpha_s$-DREADD, as a model system, and endogenous $G\alpha_s$-GPCRs with PGE2 and dobutamine. In contrast, stimulation with CGS-21860 led to a modest increase of PD-1 and Tim-3. It is possible that $A_{2A}R$ receptor desensitization may limit its ability to polarize CD8 T cells towards a more exhausted phenotype, albeit $A_{2A}R$ activation promoted CD8 T cell dysfunction in our *in vitro* system (e.g., decrease IFNγ, TNFα, and granzyme B), which aligned with the effects of global $A_{2A}R$ genetic or pharmacological inhibition *in vivo* (61-63).

Transcriptionally, $G\alpha_s$ stimulation also led to an increase of exhaustion-related genes, like *Tox* and *Tigit*, suggesting that $G\alpha_s$ activation may increase the exhaustion profiles of pre-exhausted CD8 T cells. Although the underlying mechanisms by which $G\alpha_s$-PKA may exert these functions are yet to be fully elucidated, it is likely that in the TME, $G\alpha_s$-PKA can directly inhibit T cell migration and contribute to the expression of CD8 T cell exhaustion programs. For example, our recent study has linked PKA-induced phosphorylation of P-REX1, a chemotactic Rac guanine nucleotide exchange factor (GEF), preventing cellular migration(64). Moreover, upon phosphorylation by PKA, P-CREB can subsequently regulate the expression of a multitude of genes, many of which have been implicated in disease (65). Specifically in T cells, CRE elements binding of CREB have been found in promoter and enhancer regions of TNFα, TCRα, TCR Vβ,

CD3δ, CD8α, IL-2, CD25/IL-2Rα, and IL-2R (66-73), among others, though their positive or negative regulation by PKA in the context of cancer has been largely underexplored. Altogether, the implication of $G\alpha_s$-linked GPCRs as negative regulators and heightening the terminal exhaustion of CD8 T cells in the TME provides a strong foundation for the future exploration of the GPCR- $G\alpha_s$-PKA axis as a novel target for precision cancer immunotherapy in combination with ICB.

In this regard, although the abundance of ligands in the TME and GPCR expression on tumor-infiltrating CD8 T cells is likely tumor-type specific, our pan-cancer computational analysis provides a shared landscape of GPCRs broadly associated with intratumoral exhausted CD8 T cells, which includes *ADORA2A*, *PTGER2*, *PTGER4*, *ADRB1*, *ADRB2*, and *GPR65*, all of which may converge to the initiation of CD8 T cell exhaustion programs by the activation of the $G\alpha_s$-PKA pathway (**Figure 4.6**). This finding supports a direct role of adenosine and PGE2 on CD8 T cells, and can explain the ability of their inhibiting agents to heighten the anti-tumor response to anti-PD-1. Furthermore, this analysis raises the possibility that elevated circulating adrenaline and noradrenaline, which are typical of physical and emotional stress conditions such as those frequently observed in cancer patients may limit the response to ICB. This may have a direct clinical impact, as it may provide a rationale for the use of readily available β-adrenergic blockers, such as propranolol, in patients with elevated circulating adrenaline/noradrenaline and *ADRB1* or *ADRB2* expression in intratumoral CD8 T cells (74,75). Perhaps most intriguingly from our analysis, GPR65, a proton-sensing GPCR, emerged as a $G\alpha_s$-GPCR significantly correlated with T cell dysfunction as well as significantly expressed on exhausted versus effector CD8 T cells in the LCMV viral-induced T cell dysfunction model. Indeed, multiple studies have shown that hypoxia and acidosis resulting from the export of protons and lactic acid by the tumor as a consequence of enhanced anaerobic metabolism even in the presence of oxygen, referred to as the “Warburg effect” is a hallmark of most solid tumors (76). Hypoxia has been associated with

immune exclusion from tumors, and therefore expression of GPR65 on CD8 T cells may provide a mechanism of intrinsic resistance of tumor cells to cytotoxic CD8 T cells, which can be disrupted, for example, by the future development of GPR65 inhibitors. Thus, our studies may provide a valuable resource for the future development and exploration of targeting CD8 T cell specific GPCRs as part of combination immunotherapies based on expression patterns in pre-treatment tissue biopsies.

Another unexpected finding from our study is that all of the $G\alpha_s$-GPCRs that we identified as part of our pan-cancer analysis were significantly correlated with *PDCD1* (PD-1) expression, and that 5 out of the 6 $G\alpha_s$-GPCRs that we analyzed had significant predictive power to predict responses to immunotherapy in melanoma patients. Taken together, this provides a strong rationale to target PD-1 concomitant with $G\alpha_s$-GPCR blockade. However, our data suggests that many of these $G\alpha_s$-GPCRs expressed on CD8 T cells may be functionally redundant, which raises the question of whether to target individual $G\alpha_s$-GPCRs based on the patient-specific expression profile, or simultaneously. While the latter appears to be daunting, inhibitors for this handful of GPCRs are already approved or under clinical evaluation and preclinical development. Our data showing the alleviation of PGE2-mediated suppression of cytotoxic function by knocking out *Gnas* suggests that as an alternative approach, perhaps targeting the shared downstream mechanisms, specifically cAMP/PKA, may provide a more feasible approach to targeting the $G\alpha_s$-immune checkpoint thus circumventing the emerging receptor-ligand redundancy. In this case, the possibility exists to deliver GPCR and $G\alpha_s$-PKA inhibitors as single agents or in combination intratumorally, thereby favoring immune-mediated tumor control while bypassing potential systemic toxicities. As the prospect of cancer immunotherapies will likely rely on combinatorial strategies blocking additional targets, studies interrogating downstream signaling mechanisms of T cell dysfunction and exhaustion will become important for uncovering these targets. Our work here investigating the pan-cancer GPCR repertoire of tumor infiltrating CD8 T cells combined with

the use of synthetic biology approaches to reveal the specific immune suppressive functions of $G\alpha_s$-signaling in CD8 T cells can open new doors to achieve multitargeted $G\alpha_s$-GPCRs inhibition or $G\alpha_s$/cAMP/PKA pathway modulation with the overall goal of enhancing responses to immunotherapies.

4.5 Methods

4.5.1 Cell lines, antibodies and other reagents

The 4MOSC1 cell lines were previously generated in-house by our lab. The MC38-OVA cell line was generated by retroviral transduction with pMSCV-OVA (gifted by Andrew Sharabi). 4MOSC1-OVA was generated by levntiviral transduction with the pLenti-CMV GFP DEST vector. 4MOSC1 cell lines were grown in keratinocyte media with growth supplement, cholera toxin, EGF, and antibiotics. MC38-OVA were grown in DMEM supplemented with 10% feal bovine serum (FBS), 1% antibiotics/antimycotics and 1ug/mL blasticidin. All cell lines were grown at 37°C and 5% CO_2. PD-1 antibody (clone J43, catalog #BE0033-2; clone RMP1-14, catalog #BE0146), CTLA-4 antibody (clone 9H10, catalog #BP0131), isotype antibody (Armenian hamster IgG isotype control, catalog #BE0091; Rat IgG isotype control, catalog #BE0251; Syrian hamster IgG isotype control, catalog #BE0087), and CD8 depletion antibody (Clone YTS 169.4, catalog #BE0117) were obtained from Bio X Cell (West Lebanon, NH, USA). Deschloroclozapine (DCZ) was purchased from Tocris (catalog #7193).

4.5.2 Mice

All the animal experiments used in this study were approved by the Institutional Animal Care and Use Committee (IACUC) of the University of California, San Diego, with protocol ASP #S15195. Mice at Moores Cancer Center, UCSD are housed in micro-isolator and individually ventilated cages supplied with acidified water and fed 5053 Irradiated Picolab Rodent Diet 20 from lab diet. Temperature for laboratory mice in our facility is mandated to be between 65–75 ° F (~18–23 °C) with 40–60% humidity. All animal manipulation activities are conducted in laminar

flow hoods. All personnel are required to wear scrubs and/or lab coat, mask, hair net, dedicated shoes, and disposable gloves upon entering the animal rooms. All animal studies conducted in this study were approved by the Institutional Animal Care and Use Committee (IACUC) of the University of California, San Diego, with protocol ASP #S15195.

The *E8i-CreERT2* mice were obtained from Dr. Dario Vignali, University of Pittsburgh (40).The *ROSA26-Gs-DREADD-LSL* mice were obtained from Dr. Rebecca Berdeaux, The University of Texas, Houston (77). *ROSA26-Gs-DREADD* mice were generated by crossing *E8i-CreERT2* mice with *ROSA26-Gs-DREADD-LSL*. Information regarding genotyping of CD8-GsD mice is listed in **Table 4.4**.

The *Gnas-exon 1*$^{fl/fl}$ mice were obtained from Dr. Ramiro Iglesias-Bartolome, National Institutes of Health [77]. *E8i-Gnas-exon 1*$^{-/-}$ mice were generated by crossing *E8i-CreERT2* with *Gnas-exon 1*$^{fl/fl}$.

OT-1 mice (C57BL/6-Tg(TcraTcrb)1100Mjb/J, stock no: 003831) were purchased from the Jackson Laboratory and bred in house.

4.5.3 Tamoxifen and DCZ treatment

Tamoxifen was purchased from Sigma-Aldrich. Where indicated, CD8-GsD mice were dosed with tamoxifen at 75 mg/kg body weight. A stock solution of 15 mg/mL was prepared by dissolving 75mg of tamoxifen in 5 mL of miglyol and dissolved at 37°C. After dissolving, the solution was stored at -20°C protected from light. Mice were given 1.5 mg in 100ul by intraperitoneal injection (i.p).) for 3 consecutive days before tumor implantation or cell isolation.
Deschloroclozapine (DCZ) was purchased from Tocris. Mice were dosed with DCZ at 0.01 mg/kg. A stock solution of 10 mg/mL was prepared by dissolving 10mg of DCZ into 1mL of DMSO. Subsequently, a working concentration of 0.002 mg/mL of DCZ in PBS was prepared, and mice were given 0.0002 mg of DCZ in 100µl i.p. daily.

4.5.4 In vivo mouse tumor models.

For 4MOSC1 and 4MSOC1-SIINFEKL tumor xenograft, WT female C57Bl/6 mice were purchased from Charles River Laboratories (Worcester, MA, USA). WT mice or age-matched CD8-GsD mice were first given tamoxifen i.p. every day for 3 days. On the fourth day, $5x10^5$ tumor cells were injected into the tongue of mice and when tumors reached ~30 mm^3 (4-5 days post-implantation), mice were treated by i.p. injection of either isotype control antibody, anti-PD-1 (clone J43), or anti-CTLA-4 (clone 9H10) (i.p. 10 mg/kg three times a week). Where indicated, DCZ (i.p. 0.1 mg/kg) was started on the fifth day and given daily.

For MC38-OVA tumor xenograft studies, WT female C57Bl/6 mice were purchased from Charles River Laboratories (Worcester, MA, USA). WT mice or age-matched CD8-GsD mice were first given tamoxifen i.p. every day for 3 days. On the fourth day, $1x10^5$ cells were injected subcutaneously into the flanks of mice. When tumors reached ~100 mm^3 (8-10 days post-implantation), mice were treated by i.p. injection of either isotype control antibody or anti-PD-1 (clone RMP1-14) (i.p. 10 mg/kg three times a week). Where indicated, DCZ treatment was started on the fifth day and given daily.

All mice were euthanized after the completion of the treatment (or when control-treated mice succumbed to tumor burdens, as determined by the ASP guidelines) and tumors were dissected for flow cytometric analysis.

4.5.5 In vitro T cell cultures and isolations

Splenocytes were isolated from 5-6 week-old mice and mechanically disrupted. Red blood cells were lysed by RBC lysis buffer (BioLegend) according to manufacturer's instructions. CD8 T cells were isolated by EasySep CD8 Isolation Kit by negative selection. For activation, they were then cultured at $1x10^6$ cells per well in 1mL in 24-well plates with Dynabeads Mouse T-Activator CD3/CD28 beads at a 1:1 cells to beads ratio with 25U/mL hIL-2 (PeproTech) for 48 hours. Naïve CD8 T cells were cultured with 25U/mL hIL-2 alone. After 48 hours, activated cells were collected and counted and either split into the "acute" or "chronic" activation groups. For acute activation, CD8s were cultured at $5x10^4$ cells per well in 200ul in 96-well round bottom

plates with 25 U/mL hIL-2 without beads. For chronic activation, CD8s were cultured at the same cell density with 25 U/mL hIL-2 and with CD3/CD28 beads at a 1:2.5 cells to beads ratio. Where indicated, GPCR agonists were added at the following concentrations: 1μM 16, 16-di-methyl prostaglandin E2 (PGE2) (Tocris), 5μM dobutamine hydrocholoride (dobutamine) (Tocris), 5μM CGS 21680 hydrochloride (CGS 21680) (Tocris). For PGE2 experiments, where indicated, inhibitors were added at the following concentrations: 500nM cAMPS-Rp (Tocris), 500nM ESI 09 (Tocris), 1μM forskolin (Tocris), 1μM PF 04418948 (EP_2 inhibitor; EP_2i) (Tocris), 1μM ONO AE3 208 (EP_4 inhibitor; EP_4i) (Tocris); PGE2 and inhibitors were added in the last 24 hours of culture. Inhibitors were first added for 30 min and then 1μM of PGE2 was added in the last 24 hours of culture.

For CD8-GsD in vitro experiments, 2μM of 4-hydroxytamoxifen (Sigma-Aldrich) was included in culture. Additionally, DCZ was added at a concentration of 0.002 mg/mL.

4.5.6 In vitro co-culture tumor killing assay

Splenocytes were isolated from OT-1 mice and activated with 100nM of OVA Peptide (257-264) (GenScript) and 50U/mL of hIL-2 (PeproTech) for 48 hours. After 48 hours, fresh media with 50U/mL IL-2 was added to culture and incubated for an additional 24 hours. Cells were then collected and replated and expanded at $1x10^6$ cells/mL.

For the killing assay, tumor cells (target) were plated at 50,000 cells per well in a 24-well plate. OT-1 T cells (effector) were then added at a 1:5 target:effector ratio. Where indicated, GPCR agonists were added at the following concentrations: 1uM 16, 16-di-methyl prostaglandin E2 (PGE2) (Tocris), 5μM dobutamine hydrocholoride (dobutamine) (Tocris), 5μM CGS 21680 hydrochloride (CGS 21680) (Tocris). The co-culture was left for 36 hours and cell viability was assessed by flow cytometric staining with Zombie Aqua Viability Dye (BioLegend). Percent killing was calculated by (1-(# live tumor cells in test group/# live tumor cells in tumor alone group)) * 100.

4.5.7 Flow cytometry

For viability stain of CD8 T cells *in vitro*, cells were washed once with PBS and stained with Zombie Aqua Viability Dye (BioLegend) according to manufacturer's instructions. Cell surface staining was done for 30 min at 4°C. For intracellular and transcription factor staining, cells were stimulated with 1x Cell Activation Cocktail with Brefeldin A (BioLegend) in media for 4-6 hours at 37°C prior to viability staining. After cell surface staining, cells were fixed with FOXP3/Transcription factor buffer set and stained with intracellular antibodies for 45 min at room temperature.

4.5.8 Detection of pCREB

For CD8-GsD pCREB activation experiments in vivo, CD8-GsD mice were first given tamoxifen i.p. every day for 3 days. DCZ (i.p. 0.01 mg/kg) was started on the fifth day and given daily for 5 days. Blood was collected from mice with retro-orbital bleeding and lyse and fixed with Lyse/Fix Buffer (BD Biosciences). Cells were then permeabilized with Perm Buffer II (BD Biosciences) and stained with the anti-CREB (pS133)/ATF-1 (pS63) antibody (BD Biosciences) according to manufacturer's instructions.

For CD8-GsD pCREB activation experiments *in vitro*, CD8-GsD mice were first given tamoxifen i.p. every day for 3 days. On the fourth day, blood was collected from mice with retro-orbital bleeding. Red blood cells were lysed by RBC lysis buffer (BioLegend) according to manufacturer's instructions. 0.002 mg/mL of DCZ was added to culture for 15 min, and cells were fixed by CytoFix buffer (BD Biosciences) according to manufacturer's instructions. Cells were then permeabilized with Perm Buffer II (BD Biosciences) and stained with extracellular antibodies and with the anti-CREB (pS133)/ATF-1 (pS63) antibody (BD Biosciences) according to manufacturer's instructions.

For PGE2 pCREB activation experiments in vitro, CD8 T cells from chronical activation scheme were serum-starved for 1 hour. 1μM of PGE2 was then added for 15 min in the presence or absence of inhibitors and cells were fixed by CytoFix buffer (BD Biosciences) according to

manufacturer's instructions. Cells were then permeabilized with Perm Buffer II (BD Biosciences) and stained with extracellular antibodies and with the anti-CREB (pS133)/ATF-1 (pS63) antibody (BD Biosciences) according to manufacturer's instructions.

4.5.9 Quantitative PCR

RNA was extracted from naïve, activated, chronically stimulated, and chronically stimulated CD8 T cells treated with DCZ by the RNeasy Mini kit following manufacturer's instructions (Qiagen). 100ng of RNA was converted to cDNA using SuperScript™ VILO™ cDNA Synthesis Kit (ThermoFisher Scientific). qPCR was performed using the SYBR™ Select Master Mix (ThermoFisher Scientific). *Actb* was used for normalization. The following primers were used for qPCR: *Dusp1* fwd 5'- GTTGTTGGATTGTCGCTCCTT, *Dusp1* rev 5'- TTGGGCACGATATGCTCCAG, *Tox* fwd 5'- GCTCCCGTTCCATCCACAAA, *Tox* rev 5'- TCCCAATCTCTTGCATCACAGA, *Tigit* fwd 5'- GAATGGAACCTGAGGAGTCTCT, *Tigit* rev 5'- AGCAATGAAGCTCTCTAGGCT, *Actb* fwd 5'- GGCTGTATTCCCCTCCATCG, *Actb* rev 5'- CCAGTTGGTAACAATGCCATGT.

4.5.10 Bioinformatics analysis

For single cell RNA-seq integration, we used the Seurat scRNA-seq integration method (78). The combined counts matrix was filtered to remove non-protein-coding genes, and the cell type annotations in the metadata were used to subset for CD8 T cells, totaling 112,610 cells and 32,315 genes. To account for technical differences between datasets, we used the standard Seurat v4.0.1 integration workflow for batch-correction. Log-normalization and identification of variable features were performed for each individual dataset, and integration features were selected and used for anchor identification. The resulting anchors were used to integrate the data and produce the corrected expression matrix while retaining all of the genes from the original matrix. Scaling and dimension reduction were performed using PCA and UMAP, respectively, which were also used as an embedding for visualization of the distribution of cells. To examine the relative expression of GPCRs between CD8 T cell subtypes, the average expression of each

GPCR was calculated for each of the 6 groups: naive, cytotoxic, effector memory, proliferative, pre-exhausted, and terminally exhausted. Cells were pre-annotated from original datasets. The average expression values were then row-normalized for each GPCR and visualized on a circular heatmap using *circlize v0.4.12* and *ComplexHeatmap v2.6.2.* Package versions: *circlize v0.4.12, ComplexHeatmap 2.6.2, ggplot2 3.3.3, Seurat 4.0.1*.

For calculation of T cell dysfunction score, the average expression of all genes in the T cell dysfunction gene set was calculated and plotted for each CD8 T cell from the integrated CD8 dataset. Spearman correlations for each GPCR and the dysfunction score were calculated by correlating expression of the GPCR with mean expression of the dysfunction gene set for each CD8 T cell from the melanoma dataset (GSE120575) (79).

For differential expression analysis, 3 datasets of LCMV RNA-seq data were batch corrected with ComBat. Subsequently, DESeq2 was used to analyze all effector CD8 T cells versus all exhausted CD8 T cells.

For gene set enrichment analysis, we created GPCRs gene-sets on the basis of their G-protein coupling mechanisms. We considered either G-protein family level transduction mechanisms from IUPHAR or individual G-protein couplings form recent experimental TGFα shedding assay that we augmented through machine learning-based predictions (36,80). For each G-protein family coupling from IUPHAR, we created gene-sets based on primary and secondary mechanisms either in isolation or combined. For experimental TGFα shedding assay, we considered as couplings the binding with LogRAi values greater than -1.0. We defined the predicted couplings by considering either a looser (0.5) or a more stringent (0.9) cutoff of the coupling probabilities outputted from PRECOG (80). For each individual G-protein couplings, we created gene-sets by considering the experimental and predicted couplings either in isolation or in combination. We created gene sets in the .gmt format, by considering corresponding Entrez IDs, and we performed gene set enrichment analysis through *ClusterProfiler (81)* giving as an

input the list of genes ranked according to Log2Fold change values from differential expression analysis.

For analysis of objective response rates (ORR), expression profiles of tumors from 2277 patients across 14 cancer types treated with immune checkpoint inhibitors were collected (49-51). Mean expression of each GPCR was calculated and were classified based on coupling information from IUPHAR.

4.5.11 Statistical analysis

Graphs were plotted using GraphPad Prism v9.2.0 (GraphPad Software Inc.) and R (). Where indicated, data is expressed as mean ± s.e.m. The following tests were performed (see Fig. legends for details): correlation, unpaired two-tailed student's t-test, Log-rank (Mantel-Cox) for Kaplan-Meier survival curves. Statistical significance was determined by: *, $p < 0.05$, ** $p < 0.01$, *** $p < 0.001$, **** $p < 0.0001$.

Chapter 4, in full, is in preparation for submission for publication in "A chemogenetic approach reveals a GPCR-Gαs-PKA signaling axis promoting T cell dysfunction and cancer immunotherapy failure". Victoria H. Wu, Bryan S. Yung, Farhoud Faraji, Robert Saddawi-Konefka, Zhiyong Wang, Miranda Song, Meghana S. Pagadala, Alexander T. Wenzel, Sanju Sinha, Marin Matic, Francesco Raimondi, Thomas S. Hoang, Rebecca Berdeux, Hannah Carter, Eytan Ruppin, Jill P. Mesirov, J. Silvio Gutkind. The dissertation author was the primary investigator and author of this paper.

4.6 Figures

Figure 4.1. $G\alpha_s$-coupled GPCRs are correlated with T cell dysfunction and enriched in terminally exhausted T cells.

a, Schematic of integrated analysis of 13 single cell RNA-seq datasets (n = 217 patients, n = 217,000 T cells). Full name of cancer types and their abbreviations are listed in the text and in Supplemental Table S1A. **b,** Integration of all CD8 expressing cells and the stratification into 5 different CD8 subtypes (n = 112,610 CD8 T cells analyzed). **c,** Visualization of integrated CD8 T cells using dimensionality reduction. **d,** The CD8 onco-GPCRome. Normalized average expression of 367 GPCR genes organized by receptor family and aligned with annotated landmark genes from different CD8 subtypes. **e,** Visualization of landmark genes for terminally exhausted CD8 T cells with the top 5 most highly expressed GPCRs in the terminally exhausted CD8 population. **f,** Schematic explaining analysis of correlation of GPCRs and G protein genes with the T cell dysfunction score (29). **g**, Quantification of T cell dysfunction score across all subtypes of CD8 T cells. **h,** Spearman correlation of 119 GPCR genes with the T cell dysfunction score and the statistical p-values were calculated and plotted from tumor-infiltrating CD8 T cells from human melanoma (GSE120575) (79). Blue dots indicate GPCRs with Spearman correlations with $p < 0.01$ and grey dots indicate GPCRs with Spearman correlations with $p > 0.01$. A full list of p-values and Spearman correlation values is listed in Supplemental Table S1D. **i,** The mean correlation values of GPCRs was calculated based on their G protein coupling designation from IUPHAR. These values were then ranked and plotted, and included $G\alpha_i$, $G\alpha_{12/13}$, $G\alpha_{q/11}$, and $G\alpha_s$ G protein couplings. **j,** Spearman correlation of 367 GPCR genes with the T cell dysfunction score was the statistical p-values were calculated, and the $G\alpha_s$-coupled GPCRs (primary coupling as designated by IUPHAR) were plotted. Blue dots indicate GPCRs with Spearman correlations with $p < 0.01$ and grey dots indicate GPCRs with Spearman correlations with $p > 0.01$.

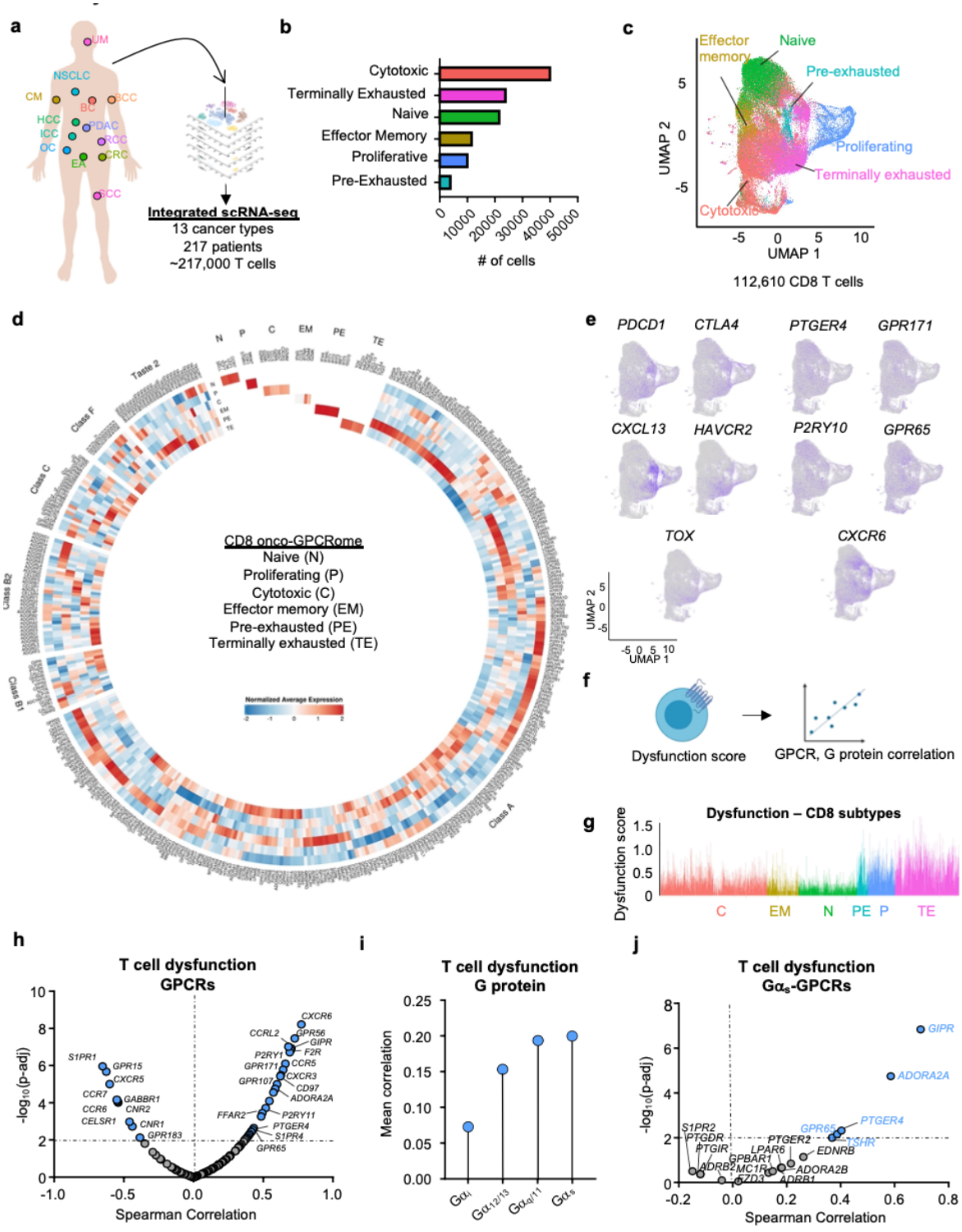
a
UM
NSCLC
CM
BCC
BC
HCC
PDAC
ICC
RCC
OC
CRC
EA
CCC
Integrated scRNA-seq
13 cancer types
217 patients
~217,000 T cells
b
Cytotoxic
Terminally Exhausted
Naive
Effector Memory
Proliferative
Pre-Exhausted
0
10000
20000
30000
40000
50000
# of cells
c
Effector memory
Naive
Pre-exhausted
Proliferating
Terminally exhausted
Cytotoxic
UMAP 2
UMAP 1
112,610 CD8 T cells
d
N
P
C
EM
PE
TE
Taste 2
Class F
Class C
Class B2
Class B1
Class A
CD8 onco-GPCRome
Naive (N)
Proliferating (P)
Cytotoxic (C)
Effector memory (EM)
Pre-exhausted (PE)
Terminally exhausted (TE)
Normalized Average Expression
e
PDCD1
CTLA4
PTGER4
GPR171
CXCL13
HAVCR2
P2RY10
GPR65
TOX
CXCR6
UMAP 2
UMAP 1
f
Dysfunction score
GPCR, G protein correlation
g
Dysfunction – CD8 subtypes
Dysfunction score
C
EM
N
PE
P
TE
h
T cell dysfunction
GPCRs
-log10(p-adj)
Spearman Correlation
S1PR1
GPR15
CXCR5
CCR7
GABBR1
CCR6
CNR2
CELSR1
CNR1
GPR183
CXCR6
CCRL2
GPR56
GIPR
F2R
P2RY1
GPR171
CCR5
GPR107
CXCR3
CD97
ADORA2A
FFAR2
P2RY11
PTGER4
S1PR4
GPR65
i
T cell dysfunction
G protein
Mean correlation
Gαi
Gα12/13
Gαq/11
Gαs
j
T cell dysfunction
Gαs-GPCRs
-log10(p-adj)
Spearman Correlation
GIPR
ADORA2A
S1PR2
PTGDR
PTGIR
ADRB2
GPR65
PTGER4
TSHR
PTGER2
LPAR6
EDNRB
GPBAR1
MC1R
ADORA2B
EZD3
ADRB1

Figure 4.2. Enrichment of $G\alpha_s$-coupling in exhausted T cells augments an exhaustion-like dysfunctional state in chronically activated CD8 T cells.

a, Schematic of curated RNA-seq datasets from different subtypes of T cells sorted out from the murine chronic infection model, LCMV. **b,** Differential expression analysis of effector versus exhausted CD8 T cells from curated bulk RNA-seq datasets in LCMV infection. Orange dots represent significantly ($p < 0.05$) upregulated GPCRs in effector CD8 T cells (eff); purple dots represent significantly ($p < 0.05$) upregulated GPCRs in exhausted CD8 T cells (exh); grey dots represent GPCRs not significantly ($p > 0.05$) upregulated in effector or exhausted T cells. **c,** Gene set enrichment analysis (GSEA) showing normalized enrichment scores (NES) of GPCRs significantly upregulated in either effector or exhausted T cells. Gene sets encompassing coupling information from IPUHAR, a TGF-α shedding assay, and a coupling predictor [33] were included in this analysis. Significantly enriched G protein gene sets are indicated by asterisks. **d**, GSEA mountain plots illustrating significant enrichment of exhausted CD8 T cells with Gs primary and secondary transduction mechanisms from IUPHAR ("Gs_iuphar_all") and GNAQ predicted couplings with probability > 0.9 ("GNAQ_predicted_09") gene sets. **e,** Experimental scheme illustrating *in vitro* chronic stimulation assay of CD8 T cells. **f,** Representative flow cytometry plots showing expression of IFNγ and TNFα in chronically stimulated CD8 T cells after treatment with 1 μM PGE2 (P), 5 μM Dobutamine (D), or 5 μM CGS-21860 (C). **g,** Quantification of IFNγ and TNFα, granzyme B, Ki-67, PD-1 and Tim-3 in CD8 T cells treated with $G\alpha_s$ agonists The average frequency and s.e.m. are shown (n = 6 per group). **h,** Schematic illustrating *in vitro* co-culture tumor killing assay. **i,** Percent killing by OT-1 T cells in the presence or absence of $G\alpha_s$ agonists. The average frequency and s.e.m. are shown (n = 3 per group). **j,** Specificity of phospho-CREB (pCREB) induction (**j**) and IFNγ and TNFα (**k**) inhibition to PGE2. PGE2 or forskolin (fsk) was added to chronically stimulated CD8 T cells in the presence or absence of EP2 inhibitor (EP_2i) or EP4 inhibitor (EP_4i) The average frequency and s.e.m. are shown (n = 6 per group). **l,** Cartoon depicting generation of *CD8-Gnas KO* mice. **m,** Quantification of IFNγ and TNFα in CD8 T cells from *CD8-Gnas*$^{+/+}$ or *CD8-Gnas KO* mice (n = 3 per group). Statistical significance was determined by two-tailed unpaired Student's *t*-test; *, $p < 0.05$, ** $p < 0.01$, *** $p < 0.001$, **** $p < 0.0001$. All experiments were performed at least 3 times with similar results.

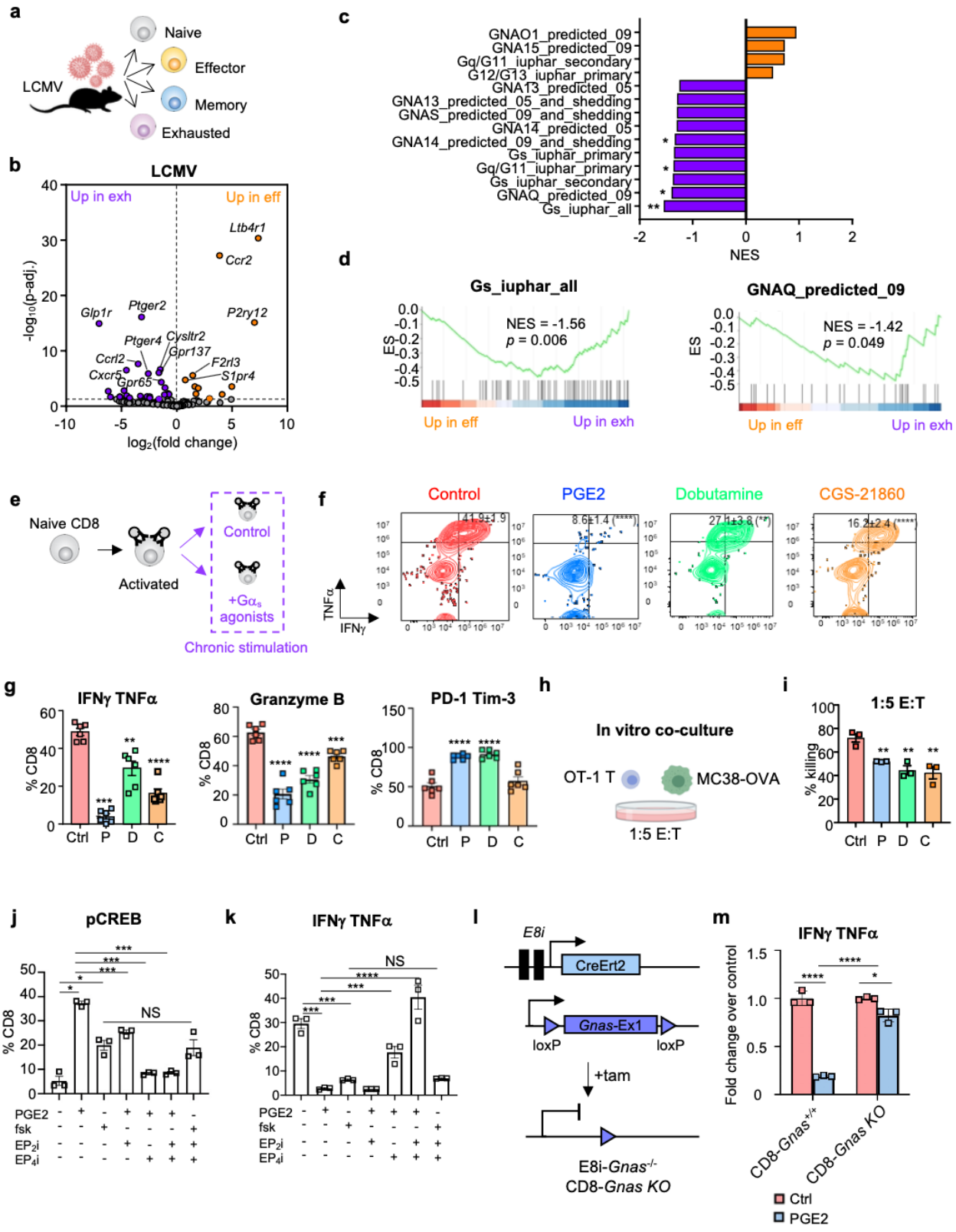
a
LCMV
Naive
Effector
Memory
Exhausted
b
LCMV
Up in exh
Up in eff
Ltb4r1
Ccr2
Glp1r
Ptger2
P2ry12
Ptger4
Cysltr2
Gpr137
Ccrl2
Cxcr5
Gpr65
F2rl3
S1pr4
-log10(p-adj.)
log2(fold change)
c
GNAO1_predicted_09
GNA15_predicted_09
Gq/G11_iuphar_secondary
G12/G13_iuphar_primary
GNA13_predicted_05
GNA13_predicted_05_and_shedding
GNAS_predicted_09_and_shedding
GNA14_predicted_05
GNA14_predicted_09_and_shedding
Gs_iuphar_primary
Gq/G11_iuphar_primary
Gs_iuphar_secondary
GNAQ_predicted_09
Gs_iuphar_all
NES
d
Gs_iuphar_all
NES = -1.56
p = 0.006
GNAQ_predicted_09
NES = -1.42
p = 0.049
ES
Up in eff
Up in exh
e
Naive CD8
Activated
Control
+Gαs agonists
Chronic stimulation
f
Control
PGE2
Dobutamine
CGS-21860
41.9±1.9
8.6±1.4 (****)
27.1±3.8 (**)
16.2±2.4 (****)
TNFα
IFNγ
g
IFNγ TNFα
Granzyme B
PD-1 Tim-3
% CD8
Ctrl P D C
h
In vitro co-culture
OT-1 T
MC38-OVA
1:5 E:T
i
1:5 E:T
% killing
j
pCREB
NS
PGE2
fsk
EP2i
EP4i
k
IFNγ TNFα
l
E8i
CreErt2
Gnas-Ex1
loxP
+tam
E8i-Gnas-/-
CD8-Gnas KO
m
IFNγ TNFα
Fold change over control
CD8-Gnas+/+
CD8-Gnas KO
Ctrl
PGE2

Figure 4.3. Mechanisms of immune suppression by $G\alpha_s$ stimulation in CD8 T cells uncovered by chemogenetically engineered $G\alpha_s$-DREADD.

a, Schematic illustrating generation of *E8i*^{CreErt2}*Rosa26*^{LSLGsDREADD} (CD8-GsD) mice. **b,** Experimental scheme showing confirmation of expression and activation of CD8-specific $G\alpha_s$-DREADD by tamoxifen and deschloroclozapine (DCZ), respectively. **c,** Confirmation of $G\alpha_s$-DREADD expression in CD4 or CD8 T cells purified from peripheral blood of CD8-GsD mice dosed with or without tamoxifen. The average relative expression and s.e.m. are shown (n = 8 per group). **d,** Confirmation of CD8-restricted $G\alpha_s$-DREADD activation following tamoxifen and DCZ treatment in CD11b+, NK1.1+, CD4+, or CD8+ cells from peripheral blood. The average frequency and s.e.m. are shown (n = 6 per group). **e,** Representative histograms showing P-CREB induction from 0.002 mg/mL DCZ *in vitro*. **f,** Experimental scheme showing in vitro chronic stimulation assay with CD8 T cells purified from CD8-GsD mice. **g,** Representative flow cytometry plots of IFNγ and TNFα (left panel) and quantification (right panel) in chronically stimulated CD8 T cells with or without 0.002 mg/mL DCZ. The average relative expression and s.e.m. are shown (n = 3 per group). **h,** Quantification of granzyme B, Ki-67, and P-1 and Tim-3 in chronically stimulated CD8 T cells treated with or without 0.002 mg/mL DCZ. The average frequency and s.e.m. are shown (n = 3 per group). **i,** Cartoon illustrating CREB activity downstream of cAMP/PKA. **j,** Quantitative PCR data showing relative expression of CREB and exhaustion-associated genes. The average frequency and s.e.m. are shown (n = 3 per group). **k,** Experimental scheme of CD8-GsD mice implanted with 4MSOC1-SIINFEKL. **l, m,** Representative flow cytometry plots (left panel) and quantification (right panel) of OVA-tetramer positive (**l**) or IFNγ and TNFα double positive (**m**) CD8 T cells in CD8-GsD implanted with 4MOSC1-OVA treated with or without 0.01 mg/kg DCZ. The average frequency and s.e.m. are shown (n = 3 per group). Statistical significance was determined by two-tailed unpaired Student's *t*-test; NS, $p > 0.05$; *, $p < 0.05$, ** $p < 0.01$, *** $p < 0.001$, **** $p < 0.0001$. All experiments were performed at least 3 times with similar results.

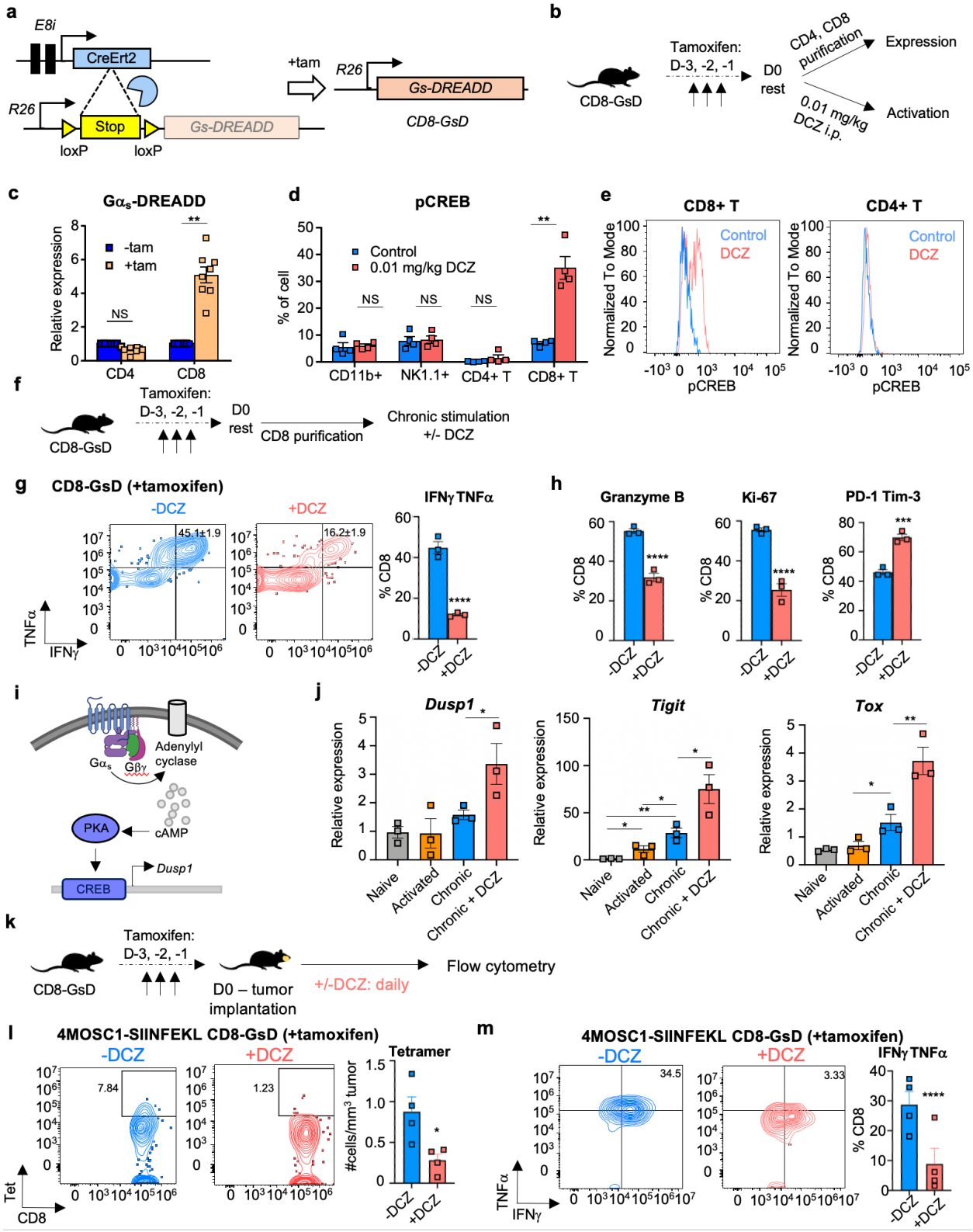
a
E8i
CreErt2
R26
Stop
loxP
loxP
Gs-DREADD
+tam
R26
Gs-DREADD
CD8-GsD
b
CD8-GsD
Tamoxifen:
D-3, -2, -1
D0
rest
CD4, CD8
purification
Expression
0.01 mg/kg
DCZ i.p.
Activation
c
Gαs-DREADD
Relative expression
-tam
+tam
NS
**
CD4
CD8
d
pCREB
% of cell
Control
0.01 mg/kg DCZ
NS
NS
NS
**
CD11b+
NK1.1+
CD4+ T
CD8+ T
e
CD8+ T
CD4+ T
Normalized To Mode
Control
DCZ
pCREB
f
CD8-GsD
Tamoxifen:
D-3, -2, -1
D0
rest
CD8 purification
Chronic stimulation
+/- DCZ
g
CD8-GsD (+tamoxifen)
-DCZ
+DCZ
45.1±1.9
16.2±1.9
TNFα
IFNγ
IFNγ TNFα
% CD8
****
-DCZ
+DCZ
h
Granzyme B
Ki-67
PD-1 Tim-3
% CD8
****
***
i
Adenylyl
cyclase
Gαs
Gβγ
PKA
cAMP
Dusp1
CREB
j
Dusp1
Tigit
Tox
Relative expression
Naive
Activated
Chronic
Chronic + DCZ
k
CD8-GsD
Tamoxifen:
D-3, -2, -1
D0 – tumor
implantation
+/-DCZ: daily
Flow cytometry
l
4MOSC1-SIINFEKL CD8-GsD (+tamoxifen)
-DCZ
+DCZ
7.84
1.23
Tet
CD8
Tetramer
#cells/mm3 tumor
m
4MOSC1-SIINFEKL CD8-GsD (+tamoxifen)
-DCZ
+DCZ
34.5
3.33
TNFα
IFNγ
IFNγ TNFα
% CD8
****

Figure 4.4. CD8-restricted $G\alpha_s$ stimulation leads to immunotherapy failure.

a, Experimental scheme of CD8-GsD mice implanted with tumors and treated with DCZ, anti-PD-1, or anti-CTLA4. **b, c,** Tumor growth curve (**b**) and survival curves (**c**) of CD8-GsD mice implanted with 4MOSC1 tumors treated with or without immunotherapy. Mice were given 3 doses of tamoxifen, and $5x10^5$ 4MOSC1 cells were implanted into the tongue. Where indicated, 0.01 mg/kg DCZ was administered daily starting one day after tumor implantation. When tumors reached ~30 mm^3, mice were treated with either hamster IgG (left panel) (n = 6 mice per group), 10 mg/kg anti-PD-1 (middle panel) (n = 10 mice per group), or 10mg/kg anti-CTLA4 (right panel) (n = 7 mice per group). **d e,** Tumor growth curve (**d**) and survival curves (**e**) of CD8-GsD mice implanted with MC38-OVA tumors treated with or without immunotherapy. Mice were given 3 doses of tamoxifen, and $1x10^5$ MC38-OVA cells were implanted into the flanks of mice. Where indicated, 0.1 mg/kg DCZ was administered daily starting one day after tumor implantation. When tumors reached ~100 mm^3, mice were treated with either hamster IgG (left panel) or 10 mg/kg anti-PD-1 (middle panel). Statistical significance of survival data was calculated by the log-rank test.

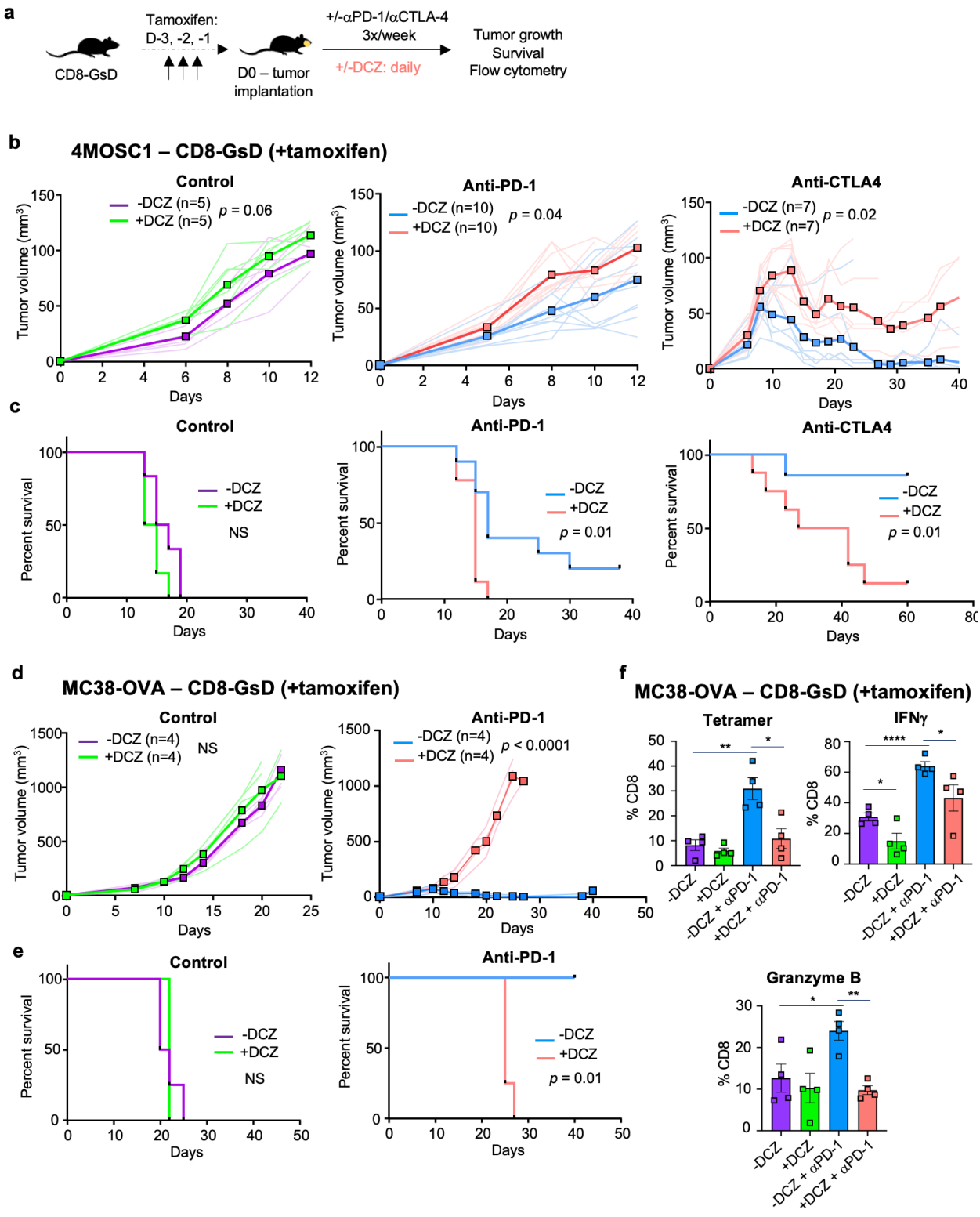
a
CD8-GsD
Tamoxifen:
D-3, -2, -1
D0 – tumor implantation
+/-αPD-1/αCTLA-4
3x/week
+/-DCZ: daily
Tumor growth
Survival
Flow cytometry
b
4MOSC1 – CD8-GsD (+tamoxifen)
Control
-DCZ (n=5)
+DCZ (n=5)
p = 0.06
Anti-PD-1
-DCZ (n=10)
+DCZ (n=10)
p = 0.04
Anti-CTLA4
-DCZ (n=7)
+DCZ (n=7)
p = 0.02
Tumor volume (mm3)
Days
c
Control
Anti-PD-1
Anti-CTLA4
Percent survival
-DCZ
+DCZ
NS
p = 0.01
Days
d
MC38-OVA – CD8-GsD (+tamoxifen)
Control
-DCZ (n=4)
+DCZ (n=4)
NS
Anti-PD-1
p < 0.0001
Tumor volume (mm3)
Days
e
Control
Anti-PD-1
Percent survival
-DCZ
+DCZ
NS
p = 0.01
Days
f
MC38-OVA – CD8-GsD (+tamoxifen)
Tetramer
IFNγ
Granzyme B
% CD8
-DCZ
+DCZ
-DCZ + αPD-1
+DCZ + αPD-1

Figure 4.5. Overexpression of $G\alpha_s$-GPCRs in cancer patients associated with poor survival and decreased response to ICB.

a, Correlation of various $G\alpha_s$-GPCRs to *PDCD1* in melanoma tumors from the TCGA Skin Cutaneous Melanoma cohort (n = 469 patients). Spearman correlations and p-values are listed. **b,** t-distributed stochastic neighbor embedding (tsne) visualization of responders (R) and (NR) to immunotherapy in melanoma patients from GSE120575 (top left panel). Expression patterns of various $G\alpha_s$-GPCRs are shown accordingly. **c,** Area under the curve (AUC) analysis of predictive power of $G\alpha_s$-GPCRs in predictive response to immunotherapy (top left panel). Expression of the GPCRs were calculated as $\log_2$(TPM+1) and expression levels between R and NR was compared. *p*-values are listed. **d,** Predicted correlation of objective response rate (ORR) to ICB for each G protein coupling pathway across 17 cancer types.

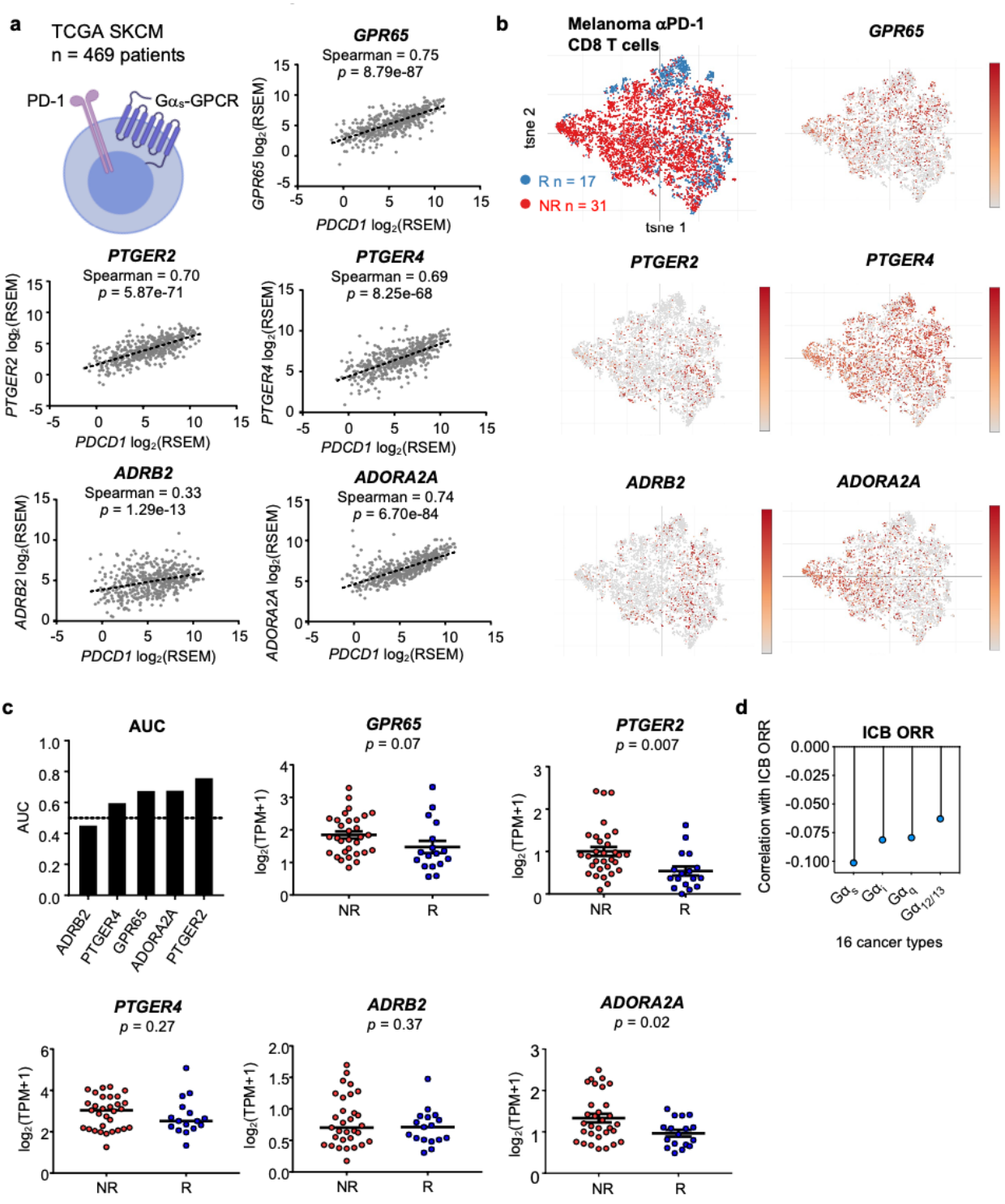
a
TCGA SKCM
n = 469 patients
PD-1
Gαs-GPCR
GPR65
Spearman = 0.75
p = 8.79e-87
PTGER2
Spearman = 0.70
p = 5.87e-71
PTGER4
Spearman = 0.69
p = 8.25e-68
ADRB2
Spearman = 0.33
p = 1.29e-13
ADORA2A
Spearman = 0.74
p = 6.70e-84
PDCD1 log2(RSEM)
b
Melanoma αPD-1
CD8 T cells
R n = 17
NR n = 31
tsne 1
tsne 2
GPR65
PTGER2
PTGER4
ADRB2
ADORA2A
c
AUC
ADRB2
PTGER4
GPR65
ADORA2A
PTGER2
p = 0.07
p = 0.007
p = 0.27
p = 0.37
p = 0.02
log2(TPM+1)
NR
R
d
ICB ORR
Correlation with ICB ORR
Gαs
Gαi
Gαq
Gα12/13
16 cancer types

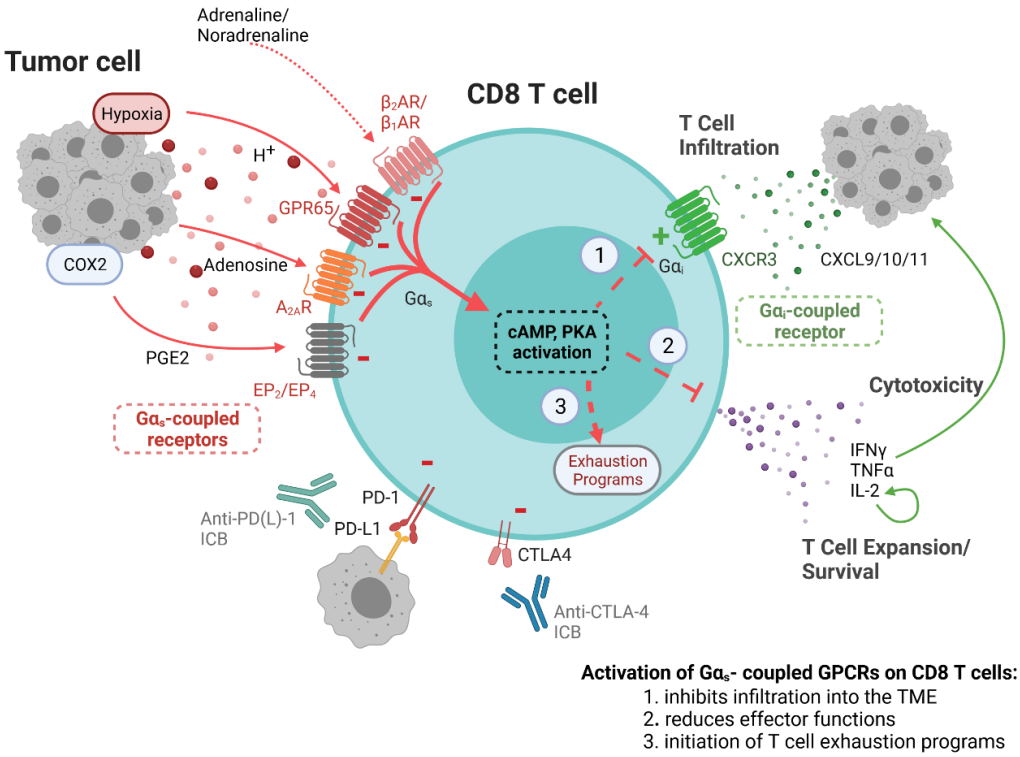

Figure 4.6. Cartoon illustrating the $G\alpha_s$-signaling axis as an immune checkpoint in cancer.

$G\alpha_s$-GPCRs, like EP_2, EP_4, $A_{2A}R$, β_1AR, and β_2AR, expressed on CD8 T cells that ligands in the TME activates cAMP and PKA and augments T cell exhaustion-related programs and diminishes T cell proliferation, cytotoxicity, and infiltration into the tumor. These receptors may need to be blocked in combination with PD-1 and CTLA-4 to overcome T cell dysfunction and exhaustion.

4.7 Supplementary figures

S4.1a. Number of patients per cancer

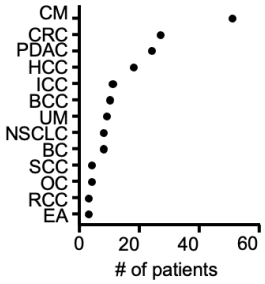

S4.1b. Integration for CD8 annotated by source

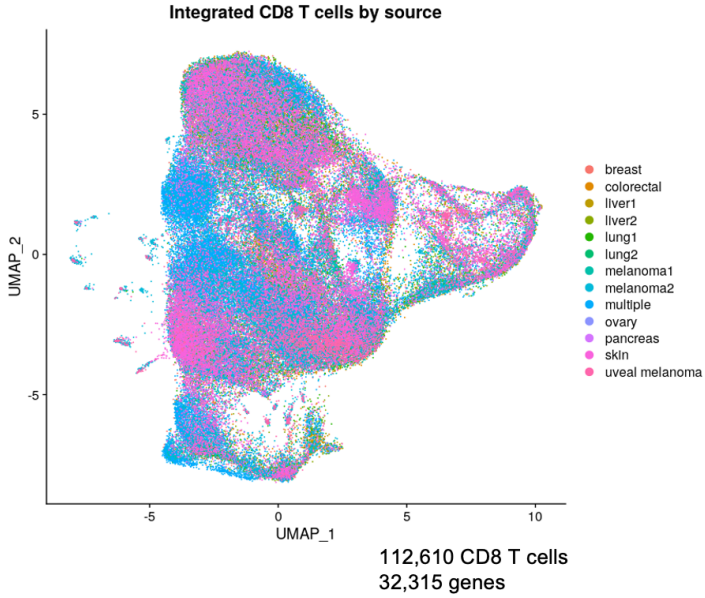

Figure S4.1. S4.1a, Number of patients per cancer type in each dataset used in the single cell RNA-seq integration. **S4.1b,** Visualization of 112,610 CD8 T cells after integration from 13 single cell RNA-seq datasets.

S4.2a. Chronic stimulation leads to acquisition of exhaustion-related phenotypes

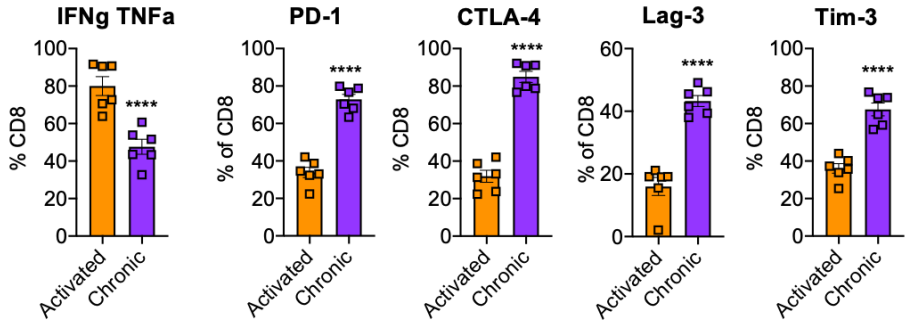

S4.2b. Decrease of proliferation by Gα_s agonists

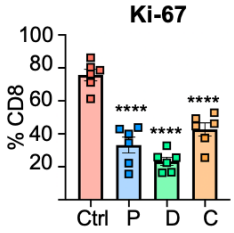

Figure S4.2. S4.2a, Upregulation of inhibitory receptors and decrease of IFNγ and TNFα in chronically versus acutely simulated CD8 T cells. **S4.2b**, Significant decrease of Ki-67 with Gα_s agonists in chronically stimulated CD8 T cells. The average frequency and s.e.m. are shown (n = 6 per group). Statistical significance was determined by two-tailed unpaired Student's *t*-test; **** $p < 0.0001$. All experiments were performed at least 3 times with similar results.

Figure S4.3. S4.3a, Genotyping confirmation for CD8-GsD mice. Primers detecting the *Gs-DREADD*, *ROSA26*, and *E8i-Cre* were used to confirm recombination by the Cre-recombinase. Information about primers and genotyping is listed in **Supplemental Table S4.4**. **S4.3b**, Effect of DCZ on circulating CD8, CD4, NK cells, and CD11b myeloid cells in the peripheral blood of CD8-GsD mice treated with tamoxifen and 5 doses of DCZ. **S4.3c**, Effect of DCZ on non-tamoxifen-treated CD8-GsD mice. Quantification of IFNγ and TNFα and PD-1 and Tim-3 in non-tamoxifen-treated CD8 T cells treated with or without DCZ. The average frequency and s.e.m. are shown (n = 3 per group). Statistical significance was determined by two-tailed unpaired Student's *t*-test; NS, $p > 0.05$. All experiments were performed at least 3 times with similar results.

S4.3a. Genotype information for CD8-GsD mice

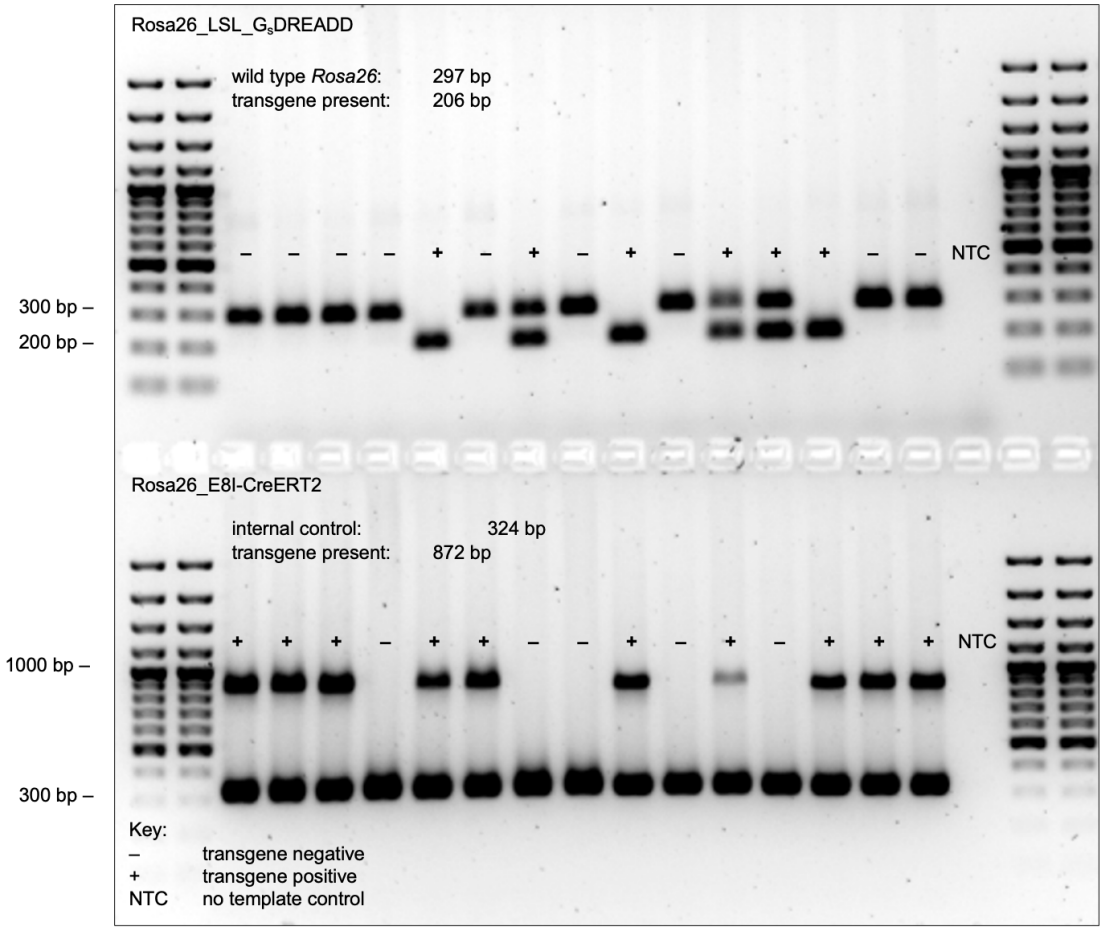

S4.3b. DCZ does not significantly alter frequency of CD8, CD4, NK cells, and CD11b myeloid cells in CD8-GsD mice dosed with tamoxifen

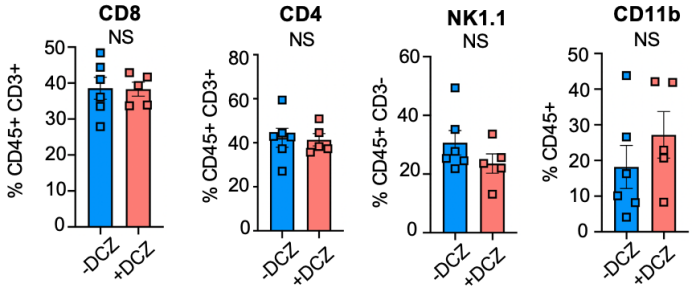

S4.3c. Effect of DCZ on non-tamoxifen dosed mice

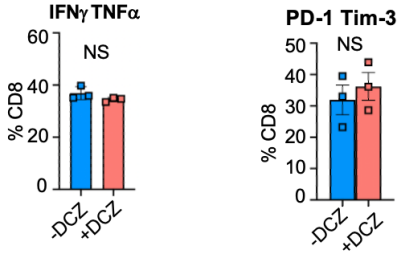

Table 4.1 Integrated dataset information and number of CD8 T cells.

Cancer Type	Abbreviation	Study	Number of patients	Total Cells	Cytotoxic	Effector memory	Naive	Pre-exhausted	Proliferative	Terminally Exhausted
Breast Carcinoma	BC	Azizi et al. 2018	8	7951	4202	230	2581	442	183	313
Basal Cell Carcinoma	BCC	Yost et al. 2019	10	9732	3717	68	3277	218	1113	1339
Cutaneous Melanoma	CM	Sade-Feldman et al. 2018; Li et al. 2019	51	18256	6157	256	2969	1025	2219	5630
Colorectal Cancer	CRC	Lee et al. 2020	27	10394	3208	83	2507	139	1282	3175
Endometrial Adenocarcinoma	EA	Wu et al. 2020	3	15008	3622	6995	1382	369	383	2257
Hepatocellular Carcinoma	HCC	Zhang et al. 2019; Lichun et al. 2019	18	4364	1682	37	1367	54	448	776
Intrahepatic Cholangiocarcinoma	ICC	Lichun et al. 2019	11	1592	451	34	424	105	292	286
Non Small Cell Lung Cancer	NSCLC	Lambrechts et al. 2018	8	22704	6792	3892	4227	1402	2132	4259
Ovarian Cancer	OC	Schelker et al. 2017	4	362	95	63	146	1	50	7
Pancreatic Ductal Adenocarcinoma	PDAC	Peng et al. 2019	24	1678	478	39	679	26	388	68
Renal Cell Carcinoma	RCC	Wu et al. 2020	3	4238	3263	65	623	22	118	147
Squamous Cell Carcinoma	SCC	Yost et al. 2019	4	12460	5571	86	1329	237	1130	4107
Uveal Melanoma	UM	Durante et al. 2020	9	3871	1041	41	358	103	560	1768

Table 4.2 Spearman correlation values and p-values of GPCR expression to T cell dysfunction score from CD8 T cells in (GSE120575).

GPCR	p-value	Spearman Correlation
CXCR6	0	0.773664785
GPR56	3.42E-08	0.726443769
CCRL2	1.15E-07	0.701910551
GIPR	1.46E-07	0.696699957
F2R	1.91E-07	0.690729483
P2RY1	9.61E-08	0.681676597
CCR5	7.82E-07	0.659248806
GPR171	1.65E-06	0.642531481
CXCR3	3.26E-06	0.62700825
CD97	3.71E-06	0.623968736
GPR107	1.01E-05	0.599978289
ADORA2A	1.79E-05	0.585757707
FZD6	2.80E-05	0.574142423
CCR1	7.96E-05	0.545484151
P2RY11	0.000195722	0.518779852
FFAR2	0.000361523	0.49379957
GPR114	0.000541283	0.485887972
GPR174	0.002293735	0.433239253
GPR137	0.002853574	0.424554928
TPRA1	0.00361604	0.414893617
GPR19	0.003731542	0.413590968
PTGER4	0.004779182	0.403169779
S1PR4	0.005670171	0.395788102
GPR65	0.006902243	0.387103778
CCR8	0.00803123	0.380264872
LPAR2	0.00868441	0.376682588
TSHR	0.009968122	0.368472481
GPR68	0.012296936	0.360290925
LPAR5	0.017546207	0.342705167
C3AR1	0.021038581	0.333369518
EMR2	0.022995284	0.328701693
CELSR3	0.024649447	0.325010855
CCR2	0.026562519	0.320994355
GPR113	0.036961438	0.302648719
P2RY10	0.039121083	0.299392097
LTB4R2	0.067463282	0.266391663
ADRA2B	0.071734968	0.262264999
EDNRB	0.072185825	0.261864242
GPR84	0.07496202	0.259439258
HRH1	0.079457824	0.255658457
CYSLTR2	0.10466158	0.237107807
P2RY2	0.113825439	0.231220877
GPR133	0.118749944	0.228205408
PTGER2	0.141255888	0.215371255
LTB4R	0.152822775	0.209400782

Table 4.2 Spearman correlation values and p-values of GPCR expression to T cell dysfunction score from CD8 T cells in (GSE120575), continued.

GPCR	p-value	Spearman Correlation
ADORA3	0.161504484	0.205328795
FPR2	0.201661947	0.187598417
P2RY6	0.20459093	0.186407557
FPR3	0.211741932	0.183549603
GPR25	0.216118356	0.181833691
ADORA2B	0.216829068	0.181557326
FPR1	0.218883082	0.180762133
ADRB1	0.219192514	0.180642789
LPAR6	0.223023049	0.178897091
GPR146	0.225028615	0.178413439
P2RY13	0.266427904	0.163635383
GPBAR1	0.313941506	0.148451706
C5AR1	0.340754916	0.140527044
GPR75	0.349369358	0.138063961
F2RL2	0.36406104	0.133630048
MC1R	0.367209084	0.132761615
SUCNR1	0.386860188	0.127753616
GPR126	0.458634665	0.109532916
CMKLR1	0.465597135	0.107852737
GPR132	0.502010667	0.099001303
CCR4	0.529212765	0.092813721
PTAFR	0.598469905	0.077724707
GPRC5B	0.606073196	0.076336421
CXCR4	0.623804675	0.072405558
GPR141	0.641799235	0.06887942
LPAR1	0.664914559	0.064144454
NMUR1	0.704771406	0.056123972
P2RY14	0.848103606	0.02833261
FZD3	0.885708511	0.021276596
CX3CR1	0.921814625	0.014546244
GPR97	0.942703168	0.010654502
CXCR2	0.943703585	0.01046817
FZD1	0.952559434	0.008819392
GPR82	0.98035165	0.003690838
EMR1	0.984809758	0.002822482
OPN3	0.988899136	0.002062583
GPR157	0.992403928	0.001411356
OPRL1	0.947866756	-0.009692929
GPR31	0.930495836	-0.012929572
GPR34	0.90024378	-0.018562744
CALCRL	0.896547908	-0.019273577
GPR35	0.847527475	-0.028441164
ADRB2	0.78639984	-0.040056448
P2RY12	0.691145329	-0.058846942

Table 4.2 Spearman correlation values and p-values of GPCR expression to T cell dysfunction score from CD8 T cells in (GSE120575), continued.

GPCR	p-value	Spearman Correlation
HRH2	0.655958207	-0.06578376
CCR9	0.57616804	-0.082725479
GPR42	0.535933898	-0.091566784
GPR18	0.521503925	-0.094550586
PTGIR	0.417967083	-0.119639562
PTGDR	0.415967224	-0.119843682
CCR10	0.39844968	-0.124687756
GPR22	0.364453643	-0.133521494
S1PR2	0.312638145	-0.148847615
FFAR3	0.302460051	-0.151976204
S1PR5	0.283918903	-0.15785474
CCKBR	0.193963394	-0.190787822
PTGDR2	0.112644508	-0.231958718
LGR6	0.103306894	-0.238011236
CYSLTR1	0.064861625	-0.268888406
GPR160	0.044980204	-0.291250543
P2RY8	0.015548723	-0.348784195
GPR183	0.007492982	-0.38341294
CNR1	0.00185255	-0.437923015
CELSR1	0.001051338	-0.458381958
CNR2	9.69E-05	-0.53983934
CCR6	9.06E-05	-0.541793313
GABBR1	8.06E-05	-0.545158489
CCR7	6.84E-05	-0.549826314
CXCR5	9.88E-06	-0.600629614
GPR15	2.10E-06	-0.624475548
S1PR1	1.09E-06	-0.651758576

Table 4.3 Differential expression results for GPCRs in effector versus exhausted CD8 T cells from LCMV infection.

GPCR	baseMean	log2FoldChange	lfcSE	stat	pvalue	padj
Ltb4r1	23.53719452	7.366352749	0.603562437	-12.20478992	2.93E-34	4.58E-31
Ccr2	1538.442821	3.864967456	0.333932809	-11.57408723	5.58E-31	6.15E-28
Ptger2	265.3203631	-3.179494494	0.35218874	9.027814156	1.75E-19	7.82E-17
P2ry12	81.66347877	7.026244727	0.802862368	-8.751493411	2.11E-18	7.54E-16
Glp1r	535.2234285	-7.02832395	0.808131463	8.697005707	3.41E-18	1.18E-15
Ccrl2	363.5038158	-3.495779175	0.553424136	6.316636643	2.67E-10	2.24E-08
Cysltr2	359.2162883	-1.489840357	0.252528007	5.899703456	3.64E-09	2.24E-07
Cxcr5	553.5609213	-4.56331361	0.779914588	5.851042768	4.89E-09	2.92E-07
Gpr137	77.2490324	-1.617063986	0.28687805	5.636764417	1.73E-08	8.71E-07
Ptger4	1517.685443	-2.569755299	0.462285885	5.558801125	2.72E-08	1.30E-06
F2rl3	169.5287489	1.443156155	0.266670831	-5.41175108	6.24E-08	2.65E-06
S1pr4	3005.562446	0.767304601	0.15362789	-4.994565775	5.90E-07	1.77E-05
Gpr65	545.4910628	-1.405991376	0.293698766	4.787188579	1.69E-06	4.42E-05
S1pr1	2249.768129	1.636880986	0.378155836	-4.328588453	1.50E-05	0.000272461
Gpr25	3.584538609	4.976264838	1.151831048	-4.320307952	1.56E-05	0.000280177
Tpra1	539.1148242	-1.065262213	0.254207569	4.190521225	2.78E-05	0.000459084
Cx3cr1	3770.962815	1.941589351	0.467244998	-4.155398899	3.25E-05	0.000520969
Gpr22	6.695499328	-4.764498668	1.23867777	3.846439148	0.000119847	0.001476825
Gpr3	6.566031026	-6.198660769	1.643208343	3.772291442	0.000161755	0.001890167
Lpar6	304.4628815	-0.780551001	0.226131742	3.451753367	0.000556957	0.00506582
Gpr146	91.44578289	1.73702762	0.509226377	-3.411110851	0.000646988	0.005670647
Lpar5	319.1772944	-0.706188631	0.211955063	3.331784677	0.00086291	0.00709197
P2ry13	32.53580054	4.104230027	1.236344713	-3.319648625	0.000901308	0.007333637
Gpr19	48.43301256	-1.113837299	0.340955705	3.26680939	0.001087669	0.008464411
Ccr6	179.4274537	-4.534399256	1.44179351	3.144971333	0.001661031	0.011746847
Celsr3	10.50392649	-3.292832059	1.073547697	3.067243371	0.002160429	0.014282285
Oprm1	7.351680985	-2.691857211	0.9001838	2.990341762	0.002786655	0.01717506
Tas1r3	21.60047447	-2.450494785	0.823129725	2.977045671	0.002910407	0.017733812
Gpr161	3.94429666	-5.144395871	1.738219742	2.959577404	0.003080613	0.01847264
Gpr63	2.401994867	-5.160578437	1.755423659	2.939790865	0.003284338	0.019427466
Hrh1	4.331755602	-6.000460238	2.056132018	2.918324401	0.00351918	0.02052308
Gprc5c	5.218574676	-4.264326188	1.556825107	2.739117046	0.006160444	0.031067255
Mrgpre	101.1292478	-2.443665558	0.896425157	2.726011803	0.006410471	0.031975632
Gpr87	2.88895307	2.964003466	1.134697031	-2.612154069	0.00899737	0.040828857
Gpr62	6.901892963	-3.047549883	1.175998018	2.59145835	0.009557011	0.042733198
F2rl1	93.62045027	-1.602694319	0.637529647	2.513913394	0.011939975	0.04990734
Nmur1	2.980218663	-5.457236005	2.184036611	2.498692549	0.01246524	0.051471395
Cxcr2	3.492233641	4.923088266	2.010314516	-2.448914449	0.014328748	0.05709679
Tbxa2r	494.7445433	-0.785827745	0.323207665	2.431340061	0.015043088	0.059284118
Cxcr3	4133.016971	-0.502104572	0.213968726	2.34662598	0.018944261	0.069232192
Mc1r	3.305641736	-4.888294117	2.157826043	2.265379145	0.023489423	0.080759693
Grm2	1.542295223	-4.475009432	2.021863526	2.213309343	0.026876326	0.088953118
S1pr5	815.4984767	1.845512043	0.835433011	-2.209048505	0.027171267	0.08970201
Htr2a	1.524459335	-4.477422146	2.044884148	2.189572524	0.028555253	0.092695128
Vipr1	16.34659634	1.702927763	0.793159173	-2.147018936	0.031791774	0.099908633
P2ry14	39.44779807	1.528841057	0.723773202	-2.112320617	0.034658959	0.106280391
Gpr162	2.843774831	-3.095467053	1.476645635	2.09628294	0.036057099	0.109194163
Grm5	1.728947251	-4.652623599	2.253388825	2.06472294	0.038949223	0.114839282
Gpr171	1027.295684	0.66277728	0.327178142	-2.025738257	0.042791614	0.122434283
Ntsr1	2.509770739	-5.193731923	2.580589743	2.01261434	0.044155217	0.125189886
Adrb2	257.3619146	-0.808494602	0.403790057	2.002264762	0.045256264	0.127385179
Npy1r	1.596654544	-4.539993178	2.29632718	1.977067213	0.048034033	0.132657678
Fzd4	3.349438634	-2.97022857	1.502601714	1.9767238	0.048072859	0.132706281
Pth2r	2.160476978	-4.981077777	2.529853868	1.968919169	0.048962374	0.13441003
Gpbar1	5.432421686	-4.169181747	2.121907048	1.9648277	0.049434183	0.13522532
Gpr156	1.441306673	-4.38708674	2.27156415	1.931306558	0.053445153	0.142462172
Gpr132	568.6693091	0.570433868	0.296369169	-1.924740926	0.054261778	0.143984103
Tshr	1.492770032	-4.434657012	2.306668964	1.922537253	0.054538191	0.144515243
Fzd9	2.168234876	-4.976407254	2.621145617	1.898561919	0.057622099	0.15018487
Oprl1	2.134781826	-3.957085486	2.124354154	1.862724008	0.062501106	0.158107398
Chrm4	5.607959733	2.019182194	1.086232713	-1.858885458	0.063043376	0.158924347
P2ry2	2.299979294	-4.362397015	2.355983621	1.851624508	0.064079761	0.160520358
Gpr26	1.902212572	-4.798454314	2.627974407	1.825913639	0.067863271	0.166628282
Oprd1	1.761425191	-4.259242599	2.362535316	1.802827061	0.071415379	0.172535802
Chrm1	2.077452523	-4.217561943	2.34321296	1.799905521	0.071875558	0.173334973
Gpr141	5.09843406	2.783612594	1.560310583	-1.784011866	0.074421737	0.177196861
Ptafr	1.852607405	2.689427112	1.527968312	-1.76013278	0.078385296	0.183443502

Table 4.3 Differential expression results for GPCRs in effector versus exhausted CD8 T cells from LCMV infection, continued.

GPCR	baseMean	log2FoldChange	lfcSE	stat	pvalue	padj
Calcrl	135.0969585	0.907830587	0.516011432	-1.759322623	0.078522726	0.183580651
Lgr6	3.909381785	-2.015054565	1.148861777	1.753957356	0.079437814	0.184960423
Gpr151	1.714447821	-2.962497454	1.72443548	1.717952042	0.085805363	0.194951974
Lgr5	1.552408003	-4.499882134	2.632819043	1.709149797	0.087423205	0.197235922
Gipr	1.500584965	-4.453635539	2.611229045	1.705570619	0.088088054	0.198000512
Adrb1	69.74469123	-1.450492439	0.86680371	1.673380515	0.094252411	0.207092946
Mc5R	1.331187558	-4.29000021	2.564176407	1.6730519	0.094317079	0.207157375
Ccr4	2.03906156	-3.496644505	2.124898417	1.645558431	0.099854703	0.215633271
C5Ar1	1.322909402	3.916880451	2.429856156	-1.611980381	0.106966209	0.225867063
Bdkrb1	2.958750668	-3.481533583	2.1609366	1.611122502	0.107153025	0.22610434
C3Ar1	2.758865603	-2.500664642	1.561804302	1.601138273	0.109346297	0.229471836
Ccr5	1461.587431	0.678796588	0.427675763	-1.587175722	0.112472852	0.233757573
Gpr135	1.940730672	-2.138718646	1.384852759	1.544365372	0.122499844	0.247868972
Sctr	1.874341074	-2.361987788	1.562540925	1.511632591	0.130627356	0.258457228
Ffar1	3.296496992	-2.692279186	1.836207856	1.466217007	0.142589177	0.27321375
Ccr8	9.281072536	-1.746277913	1.197891919	1.457792549	0.144897733	0.275866103
Gpr21	3.651267489	-1.515479909	1.057661892	1.432858573	0.151898258	0.284253984
Prokr2	1.353686013	-4.294516502	3.086940118	1.391188795	0.164168184	0.299481986
Ccr7	236.8922659	-1.71942753	1.251350495	1.374057498	0.169423833	0.305667537
Gpr45	3.480665373	-1.478557139	1.082485818	1.36589054	0.171973323	0.308116131
Xcr1	52.20761745	0.939625342	0.697256618	-1.347603331	0.177785999	0.314534139
Htr2B	1.690281729	-2.138278974	1.736138071	1.231629563	0.218087492	0.36132782
Gpr107	475.2301008	0.254749648	0.212111254	-1.201019009	0.229743828	0.374845193
Kiss1R	4.012017696	0.962565565	0.813950039	-1.182585563	0.236973437	0.383009032
Galr2	2.62964051	-1.719608876	1.55960859	1.102590026	0.270205243	0.420311797
Gpr182	3.247407773	-1.457674273	1.322155991	1.102497952	0.270245248	0.420339163
Gpr83	1.548797687	-2.138558268	1.980762284	1.079664271	0.28029171	0.430820441
Vipr2	3.661692554	-1.77423593	1.654264592	1.07252246	0.283485431	0.434054849
Hrh2	277.8349472	-0.290594641	0.271204573	1.071496098	0.283946424	0.434479497
Gpr157	2.371116606	-1.154909984	1.085721299	1.063726009	0.287452839	0.438057852
Adora3	2.397152852	-1.722451258	1.620066303	1.063198003	0.287692168	0.438351337
Cysltr1	2.060611723	-1.712871752	1.621798101	1.056155974	0.290896961	0.441906084
Pth1R	12.21828633	-0.727007075	0.726343011	1.000914257	0.316868263	0.468606236
Avpr2	7.560826321	1.101465239	1.135007082	-0.970447899	0.331823283	0.484495576
Ccr1	4.496071639	1.422180616	1.484818843	-0.95781423	0.338156443	0.491218657
F2R	1780.822545	0.409626055	0.434794513	-0.942114132	0.34613421	0.499711116
Opn3	5.5939203	1.128141149	1.204067496	-0.936941785	0.348788504	0.502305797
Gpr35	2.219265403	1.037660547	1.172233476	-0.885199551	0.376049014	0.528220436
Gpr68	1155.45706	0.213194729	0.2425924	-0.878818667	0.379499603	0.531038951
Lgr4	3.229756521	-0.933367595	1.088552818	0.857438959	0.391202336	0.542396674
Gpr18	926.8691245	-0.275724927	0.350035761	0.787705023	0.430869267	0.578915123
Cmklr1	229.5789047	0.731566151	0.935804357	-0.78175117	0.434360823	0.582429201
Adora2A	873.8334372	-0.33419414	0.430039586	0.777124131	0.437085538	0.584953566
Gpr4	2.289900582	-1.262543466	1.630778939	0.774196573	0.438814554	0.586681421
Cxcr6	6442.52664	0.4799979	0.639180982	-0.750957731	0.452678094	0.599365699
Gpr15	3.109530299	-1.182688399	1.628113524	0.726416421	0.467583528	0.613712319
Chrm3	1.650585605	-0.895583772	1.352373968	0.662230857	0.507823281	0.647510071
F2Rl2	281.5583521	0.33976902	0.547042754	-0.621101399	0.534532909	0.670489881
Ccr9	41.74488948	0.431265996	0.710286599	-0.607171805	0.543736902	0.678247359
P2Ry10	611.893337	-0.124281773	0.226903932	0.547728601	0.58387827	0.710480566
Ptger1	9.488434262	-0.461433568	0.864100391	0.534004582	0.593338364	0.718727703
Gpr179	2.22276176	-0.524161082	1.067493875	0.491020224	0.623412144	0.742685305
Lpar2	42.582688	-0.477967437	0.989002184	0.483282489	0.628895172	0.746939963
S1Pr2	293.8964164	-0.228004113	0.496109451	0.459584296	0.645814633	0.760724372
Gpr34	12.42208012	0.577897268	1.272078557	-0.454293695	0.649617453	0.764531585
Ccr3	7.987272357	0.442492314	1.054315361	-0.419696355	0.674707288	0.78441205
Gabbr1	128.996442	0.291083885	0.766884415	-0.379566828	0.704266989	0.805299803
Fzd5	60.08034612	0.343115892	0.925685458	-0.370661426	0.710889724	0.810697846
Tas1R1	3.520369766	0.325515835	1.133224037	-0.287247556	0.773922775	0.854925295
Cnr2	5.816418327	-0.316698674	1.265959819	0.25016487	0.802459851	0.875771574
Gpr183	499.5804894	-0.168342272	0.678859263	0.247978162	0.804151303	0.876529645
Cxcr4	104.6637997	-0.17025401	0.688792926	0.24717735	0.804770973	0.876814198
Gpr174	568.4134996	0.076334693	0.31950256	-0.238917314	0.8111697	0.880970972
Galr3	8.305122289	0.234449606	1.125522491	-0.208302906	0.834992462	0.897077598
Gpr52	3.264317533	-0.2403799	1.196247862	0.200944894	0.840741663	0.901189341
Gprc5A	12.80049083	0.214986397	1.101434019	-0.195187722	0.845245991	0.90389945
Gpr153	1.585201709	-0.292491371	1.645497896	0.177752504	0.85891735	0.914556313

Table 4.3 Differential expression results for GPCRs in effector versus exhausted CD8 T cells from LCMV infection, continued, continued.

GPCR	baseMean	log2FoldChange	lfcSE	stat	pvalue	padj
Gpr55	315.0789216	0.089335276	0.508990135	-0.17551475	0.860675182	0.91544054
Celsr2	12.57527014	0.139945651	0.976962147	-0.143245724	0.886096119	0.931595533
Fzd6	2.451135689	0.169199921	1.212091047	-0.139593409	0.888981249	0.933268588
Celsr1	330.5654749	-0.042371236	0.647383782	0.06544995	0.947815755	0.970027261
Gpr160	211.1207321	0.003066354	0.29336033	-0.010452518	0.991660249	0.9954286
Oprk1	0.828786518	-2.87005095	1.838550707	1.561039866	0.118514345	
Npbwr1	1.057637461	-3.936936728	3.26958646	1.204108463	0.228547659	
Fzd7	0.760988518	-2.70948321	2.736855008	0.989998813	0.322174699	
Gpr1	0.48319666	-2.889555711	3.284983111	0.879625743	0.379062088	
Cxcr1	1.014962973	-3.862131373	3.160835111	1.221870562	0.221756579	
Htr5B	0.553985973	-2.188486302	3.274360527	0.668370597	0.503897059	
Adora1	0.411095824	-2.606301259	3.286247129	0.793093507	0.427723346	
Chrm5	0.664565466	-2.889555971	3.28498311	0.879625823	0.379062045	
Gpr176	0.469867058	-1.93204873	3.275953079	0.589766912	0.555346929	
Adra2B	0.668704443	-2.487893421	3.272302441	0.760288349	0.447082245	
Sstr4	0.788761201	-3.509821455	3.277159899	1.070994875	0.284171734	
Mc3R	1.071965338	-3.962473955	3.111237917	1.273600432	0.202805059	
Ghsr	0.984566398	-2.894740908	3.258812033	0.88828103	0.374389601	
Qrfpr	0.839025465	-3.588570112	2.723787196	1.317492834	0.187673482	
P2Ry1	0.939913727	-0.405605305	1.846740159	0.219633121	0.826156894	
Gpr149	0.664565466	-2.889555971	3.28498311	0.879625823	0.379062045	
Rxfp1	0.446973256	-2.602810348	2.855109935	0.911632269	0.361962329	
Rxfp4	1.15928585	-4.06966032	3.26764607	1.245440979	0.212969698	
Gpr61	0.803784524	-2.519716402	3.271820816	0.770126649	0.441224769	
Tacr3	0.866045963	-3.646858687	3.27448776	1.113718833	0.265399827	
Ptgfr	0.973385849	-3.82306699	3.271396456	1.16863457	0.242550894	
Cnr1	0.622657458	-3.201710299	3.282747275	0.975314281	0.329404389	
Gabbr2	0.873673714	-2.956492727	2.740205208	1.078931139	0.280618426	
Htr1D	0.789790784	-0.626873581	2.311867101	0.271154679	0.786272069	
Htr6	0.404998513	-2.080119272	2.899784891	0.717335716	0.473166974	
Cckar	0.645425277	-3.190279037	3.282913836	0.97178275	0.331158639	
Fzd10	1.173940569	-1.606316833	2.066999551	0.777124906	0.437085081	
Rxfp2	0.843935531	-3.612097098	3.204930628	1.12704377	0.259723975	
Calcr	0.631697403	-2.998633171	2.741860432	1.093649092	0.27410891	
Gpr85	0.545038844	0.238555791	2.393960106	-0.099649025	0.920622971	
Grm8	1.026353916	-3.895919093	3.145648578	1.238510595	0.215526796	
Opn1Sw	1.010912808	-1.567066456	1.95612537	0.801107373	0.423069488	
Smo	0.560216611	-0.050857347	1.546190931	0.032892023	0.973760694	
Chrm2	0.546730148	-2.889555971	3.28498311	0.879625823	0.379062045	
Crhr2	0.767887687	-3.462674187	3.278051986	1.056320706	0.290821719	
Ghrhr	0.622657458	-3.201710299	3.282747275	0.975314281	0.329404389	
Adcyap1R1	0.98600823	-3.833253725	3.161088348	1.212637327	0.225268511	
Tacr1	0.280122268	-1.465426155	3.272320165	0.44782481	0.654279637	
Prokr1	1.056808064	0.281635132	2.155613025	-0.13065199	0.896050613	
Oxtr	0.628949313	-3.196595495	3.282827171	0.973732496	0.330189378	
Rho	0.950992176	-3.783809214	3.272053589	1.156401969	0.247516777	
Gprc5D	0.703461442	-3.355298821	3.280033219	1.022946598	0.306333096	
C5Ar2	1.257522135	-3.154840825	2.138600749	1.475189245	0.140161672	
Ptgir	1.190816133	2.360537344	1.61106437	-1.465203618	0.142865373	
Ffar2	0.686765994	0.350881219	1.837667091	-0.190938402	0.848573853	
P2Ry6	0.902778885	0.713326018	1.836095127	-0.388501667	0.697644821	
Cckbr	0.905974861	-3.717038645	3.273212199	1.135593545	0.256126712	
Gprc5B	0.848292275	-2.922842811	2.284210047	1.279585831	0.200690836	
Mrgprg	0.609640002	-2.889555711	3.284983111	0.879625743	0.379062088	
Mrgprf	0.61233975	-3.184721979	3.28298927	0.970067739	0.332012728	
Ednra	0.9791112	-3.823580931	3.167678921	1.207060761	0.227408745	
Hcrtr2	0.484116648	-2.889555711	3.284983111	0.879625743	0.379062088	
Ackr4	1.248222224	-2.24793289	1.854648465	1.212053353	0.225491958	
Grm1	0.590712795	-3.120615223	3.283690552	0.95033779	0.341940643	
Nmbr	1.216758415	-1.817861681	1.600147051	1.136059139	0.255931815	
Gpr6	0.805865838	-3.538879614	3.276572442	1.080055356	0.280117531	
Gprc6A	0	0	0	0	1	
Grm6	0.405577437	-2.606301259	3.286247129	0.793093507	0.427723346	
Adora2B	0.588940497	-0.54553521	2.906717068	0.187680878	0.851126821	
Glp2R	0.938185035	-3.76632054	2.690563639	1.399825853	0.161565474	
Ccr10	0.999106603	-0.308438832	2.309784874	0.13353574	0.893769701	
Crhr1	0.397816462	-1.622974607	3.27714406	0.495240544	0.620430334	

Table 4.3 Differential expression results for GPCRs in effector versus exhausted CD8 T cells from LCMV infection, continued, continued.

GPCR	baseMean	log2FoldChange	lfcSE	stat	pvalue	padj
Gcgr	0.438200667	-2.606301259	3.286247129	0.793093507	0.427723346	
Uts2R	0.440381759	-2.606301259	3.286247129	0.793093507	0.427723346	
Gpr33	0.837481753	-1.192763043	2.856164859	0.417610013	0.676232275	
Agtr1A	0.487339879	-2.606301259	3.286247129	0.793093507	0.427723346	
S1Pr3	0.785601468	-2.42983061	2.088138614	1.163634729	0.244572071	
Ltb4R2	0.371421022	-0.459633701	2.503066116	0.18362827	0.854305084	
Fzd3	0.43563284	-0.932064685	2.09634497	0.444614173	0.656598603	
Adra1A	0.844536047	-3.613701253	2.719762945	1.328682435	0.183952762	
Ednrb	0.783340232	-3.500592283	3.27734417	1.068118605	0.285467014	
Trhr	0.797057691	0.188515303	3.22904363	-0.058381157	0.953445024	
Gpr20	0.838678063	-3.59298304	3.275508894	1.09692361	0.272674787	
Sstr3	0.251898814	-0.658831886	3.175626938	0.20746514	0.835646615	
Gpr84	0.493314989	-2.889555971	3.28498311	0.879625823	0.379062045	
Casr	1.007746568	-3.872690793	2.68623714	1.441678672	0.149393043	
Drd3	0.539026337	-2.889555711	3.284983111	0.879625743	0.379062088	
Mas1	1.134995178	-2.763359338	2.784152052	0.992531761	0.320938194	
Fpr1	0.608903511	2.602823866	2.304010607	-1.129692658	0.258605752	
Fpr2	1.094262056	3.358558326	2.562016936	-1.31090403	0.189890189	
Fpr3	0.463596076	-2.606301259	3.286247129	0.793093507	0.427723346	
Sstr5	0.260380089	0.170015581	3.268773042	-0.052012048	0.958519093	
Lhcgr	0.910066634	-3.702219698	3.192675778	1.159597766	0.246212611	
Fshr	0.701121068	-3.351350557	3.280104783	1.021720579	0.306913168	
Fzd8	0.55819234	-2.188486511	3.274360526	0.668370662	0.503897018	
Hrh4	0.21919572	0.632095797	3.259435688	-0.193927985	0.84623227	
Htr4	0.900738324	-3.288252019	2.36382592	1.391071987	0.164203599	
Gpr152	0.539966234	-2.980325343	2.799138067	1.064729667	0.286998281	
Htr7	0.299711493	1.602954174	3.234774069	-0.495538217	0.620220252	
Ffar4	1.201554136	-1.579281062	2.844745366	0.555157267	0.578787095	
Adra2A	0.488127133	-1.908426053	2.876504735	0.663453124	0.507040392	
Brs3	0.80744688	-3.54153295	3.276519373	1.080882652	0.279749316	
Opn1Mw	0.743852343	-2.704291447	3.268725618	0.827322866	0.408054087	

Table 4.4 – Genotyping information for CD8-GsD mice

Transgene	Primer name	Primer name FF alias	Tm	Sequence	primer identifier	Band sizes	Comments
Rosa26_LSL_HA-GsDREADD-GFP							
Dreadd Gs	Olg-Rosa-9F	**GsD_F**	56.9	**CTCGAAGTACTCGGCGTAGG**		Knock in=206bp	targets CRE-luc
Dreadd Gs	Olg-Rosa-9R	**GsD_R**	55.3	**CTTGGCAATCCGGTACTGTT**			targets CRE-luc
oIMR9020	gt-tomato-wt-F	**Rosa26_F**	58.2	**AAGGGAGCTGCAGTGGAGTA**		WT= 297bp	targets ROSA26
oIMR9021	gt-tomato-wt-R	**Rosa26_R**	53.5	**CCGAAAATCTGTGGGAAGTC**			targets ROSA26
Rosa26_E8i-Cre-ERT2-IRES-GFP							
	E8i-Cre-IC-1	**E8i-Cre-IC-1**	62	**CTAGGCCACAGAATTGAAAGATCT**	internal control		mmu IL2 gene F
	E8i-Cre-IC-2	**E8i-Cre-IC-2**	64	**GTAGGTGGAAATTCTAGCATCATCC**	internal control	IC = 324bp	mmu IL2 gene R
	E8i-Cre-ER7-For	**E8i-Cre-ER7-For**	69	**CCACCGAGTCCTGGACAAGATCAC**	Cre F		
	E8i-Cre-IRES-Rev	**E8i-Cre-IRES-Rev**	65	**CCTCGACTAAACACATGTAAAGCATG**	Cre R	E8i-Cre = 872 bp	

Cycling conditions

Transgene	Step #	Temp °C	Time	Note
HA-GsDREADD-GFP	1	95	4 min	
	2	95	1 min	
	3	55	1 min	**30 cycles**
	4	72	1 min	
	5	72	10 min	
	6	4	hold	
Cycler program				
GENO2		**2% Agarose**		

Transgene	Step #	Temp °C	Time	Note
E8I-CreERT-GFP	1	95	3 min	
	2	95	30 se	
	3	60	1 min	**35 cycles**
	4	72	1 min	
	5	72	7 min	
	6	4	hold	
Cycler program				
GENO2		**2% Agarose**		

4.9 References

1. Maleki Vareki, S. (2018) High and low mutational burden tumors versus immunologically hot and cold tumors and response to immune checkpoint inhibitors. J Immunother Cancer 6, 157
2. Okazaki, T., and Honjo, T. (2007) PD-1 and PD-1 ligands: from discovery to clinical application. Int Immunol 19, 813-824
3. Leach, D. R., Krummel, M. F., and Allison, J. P. (1996) Enhancement of antitumor immunity by CTLA-4 blockade. Science 271, 1734-1736
4. Iwai, Y., Terawaki, S., and Honjo, T. (2005) PD-1 blockade inhibits hematogenous spread of poorly immunogenic tumor cells by enhanced recruitment of effector T cells. Int Immunol 17, 133-144
5. Freeman, G. J., Long, A. J., Iwai, Y., Bourque, K., Chernova, T., Nishimura, H., Fitz, L. J., Malenkovich, N., Okazaki, T., Byrne, M. C., Horton, H. F., Fouser, L., Carter, L., Ling, V., Bowman, M. R., Carreno, B. M., Collins, M., Wood, C. R., and Honjo, T. (2000) Engagement of the PD-1 immunoinhibitory receptor by a novel B7 family member leads to negative regulation of lymphocyte activation. J Exp Med 192, 1027-1034
6. Dong, H., Strome, S. E., Salomao, D. R., Tamura, H., Hirano, F., Flies, D. B., Roche, P. C., Lu, J., Zhu, G., Tamada, K., Lennon, V. A., Celis, E., and Chen, L. (2002) Tumor-associated B7-H1 promotes T-cell apoptosis: a potential mechanism of immune evasion. Nat Med 8, 793-800
7. Ishida, Y., Agata, Y., Shibahara, K., and Honjo, T. (1992) Induced expression of PD-1, a novel member of the immunoglobulin gene superfamily, upon programmed cell death. EMBO J 11, 3887-3895
8. Wei, S. C., Levine, J. H., Cogdill, A. P., Zhao, Y., Anang, N. A. S., Andrews, M. C., Sharma, P., Wang, J., Wargo, J. A., Pe'er, D., and Allison, J. P. (2017) Distinct Cellular Mechanisms Underlie Anti-CTLA-4 and Anti-PD-1 Checkpoint Blockade. Cell 170, 1120-1133.e1117
9. Rotte, A. (2019) Combination of CTLA-4 and PD-1 blockers for treatment of cancer. J Exp Clin Cancer Res 38, 255
10. Mellman, I., Coukos, G., and Dranoff, G. (2011) Cancer immunotherapy comes of age. Nature 480, 480-489
11. Cheng, W., Fu, D., Xu, F., and Zhang, Z. (2018) Unwrapping the genomic characteristics of urothelial bladder cancer and successes with immune checkpoint blockade therapy. Oncogenesis 7, 2
12. Polk, A., Svane, I. M., Andersson, M., and Nielsen, D. (2018) Checkpoint inhibitors in breast cancer - Current status. Cancer Treat Rev 63, 122-134
13. Ferris, R. L., Blumenschein, G., Jr., Fayette, J., Guigay, J., Colevas, A. D., Licitra, L., Harrington, K., Kasper, S., Vokes, E. E., Even, C., Worden, F., Saba, N. F., Iglesias Docampo, L. C., Haddad, R., Rordorf, T., Kiyota, N., Tahara, M., Monga, M., Lynch, M., Geese, W. J., Kopit, J., Shaw, J. W., and Gillison, M. L. (2016) Nivolumab for Recurrent Squamous-Cell Carcinoma of the Head and Neck. N Engl J Med 375, 1856-1867
14. Borghaei, H., Paz-Ares, L., Horn, L., Spigel, D. R., Steins, M., Ready, N. E., Chow, L. Q., Vokes, E. E., Felip, E., Holgado, E., Barlesi, F., Kohlhaufl, M., Arrieta, O., Burgio, M. A., Fayette, J., Lena, H., Poddubskaya, E., Gerber, D. E., Gettinger, S. N., Rudin, C. M., Rizvi, N., Crino, L., Blumenschein, G. R., Jr., Antonia, S. J., Dorange, C., Harbison, C. T., Graf

Finckenstein, F., and Brahmer, J. R. (2015) Nivolumab versus Docetaxel in Advanced Nonsquamous Non-Small-Cell Lung Cancer. N Engl J Med 373, 1627-1639

15. Larkin, J., Chiarion-Sileni, V., Gonzalez, R., Grob, J. J., Cowey, C. L., Lao, C. D., Schadendorf, D., Dummer, R., Smylie, M., Rutkowski, P., Ferrucci, P. F., Hill, A., Wagstaff, J., Carlino, M. S., Haanen, J. B., Maio, M., Marquez-Rodas, I., McArthur, G. A., Ascierto, P. A., Long, G. V., Callahan, M. K., Postow, M. A., Grossmann, K., Sznol, M., Dreno, B., Bastholt, L., Yang, A., Rollin, L. M., Horak, C., Hodi, F. S., and Wolchok, J. D. (2015) Combined Nivolumab and Ipilimumab or Monotherapy in Untreated Melanoma. N Engl J Med 373, 23-34

16. Haslam, A., and Prasad, V. (2019) Estimation of the Percentage of US Patients With Cancer Who Are Eligible for and Respond to Checkpoint Inhibitor Immunotherapy Drugs. JAMA Netw Open 2, e192535

17. Hauser, A. S., Attwood, M. M., Rask-Andersen, M., Schioth, H. B., and Gloriam, D. E. (2017) Trends in GPCR drug discovery: new agents, targets and indications. Nat Rev Drug Discov 16, 829-842

18. Santos, R., Ursu, O., Gaulton, A., Bento, A. P., Donadi, R. S., Bologa, C. G., Karlsson, A., Al-Lazikani, B., Hersey, A., Oprea, T. I., and Overington, J. P. (2017) A comprehensive map of molecular drug targets. Nat Rev Drug Discov 16, 19-34

19. Dorsam, R. T., and Gutkind, J. S. (2007) G-protein-coupled receptors and cancer. Nat Rev Cancer 7, 79-94

20. O'Hayre, M., Degese, M. S., and Gutkind, J. S. (2014) Novel insights into G protein and G protein-coupled receptor signaling in cancer. Curr Opin Cell Biol 27, 126-135

21. Wu, V., Yeerna, H., Nohata, N., Chiou, J., Harismendy, O., Raimondi, F., Inoue, A., Russell, R. B., Tamayo, P., and Gutkind, J. S. (2019) Illuminating the Onco-GPCRome: Novel G protein-coupled receptor-driven oncocrine networks and targets for cancer immunotherapy. J Biol Chem

22. Pierce, K. L., Premont, R. T., and Lefkowitz, R. J. (2002) Seven-transmembrane receptors. Nat Rev Mol Cell Biol 3, 639-650

23. Tokunaga, R., Zhang, W., Naseem, M., Puccini, A., Berger, M. D., Soni, S., McSkane, M., Baba, H., and Lenz, H. J. (2018) CXCL9, CXCL10, CXCL11/CXCR3 axis for immune activation - A target for novel cancer therapy. Cancer Treat Rev 63, 40-47

24. Ayers, M., Lunceford, J., Nebozhyn, M., Murphy, E., Loboda, A., Kaufman, D. R., Albright, A., Cheng, J. D., Kang, S. P., Shankaran, V., Piha-Paul, S. A., Yearley, J., Seiwert, T. Y., Ribas, A., and McClanahan, T. K. (2017) IFN-gamma-related mRNA profile predicts clinical response to PD-1 blockade. J Clin Invest 127, 2930-2940

25. Nieto, P., Elosua-Bayes, M., Trincado, J. L., Marchese, D., Massoni-Badosa, R., Salvany, M., Henriques, A., Mereu, E., Moutinho, C., Ruiz, S., Lorden, P., Chin, V. T., Kaczorowski, D., Chan, C.-L., Gallagher, R., Chou, A., Planas-Rigol, E., Rubio-Perez, C., Gut, I., Piulats, J. M., Seoane, J., Powell, J. E., Batlle, E., and Heyn, H. (2020) A Single-Cell Tumor Immune Atlas for Precision Oncology. bioRxiv, 2020.2010.2026.354829

26. Li, H., van der Leun, A. M., Yofe, I., Lubling, Y., Gelbard-Solodkin, D., van Akkooi, A. C. J., van den Braber, M., Rozeman, E. A., Haanen, J. B. A. G., Blank, C. U., Horlings, H. M., David, E., Baran, Y., Bercovich, A., Lifshitz, A., Schumacher, T. N., Tanay, A., and Amit, I. (2019) Dysfunctional CD8 T Cells Form a Proliferative, Dynamically Regulated Compartment within Human Melanoma. Cell 176, 775-789.e718

27. Thommen, D. S., Koelzer, V. H., Herzig, P., Roller, A., Trefny, M., Dimeloe, S., Kiialainen, A., Hanhart, J., Schill, C., Hess, C., Savic Prince, S., Wiese, M., Lardinois, D., Ho, P. C., Klein, C., Karanikas, V., Mertz, K. D., Schumacher, T. N., and Zippelius, A. (2018) A transcriptionally and functionally distinct PD-1. Nat Med 24, 994-1004

28. Zander, R., Schauder, D., Xin, G., Nguyen, C., Wu, X., Zajac, A., and Cui, W. (2019) CD4. Immunity 51, 1028-1042.e1024

29. Zander, R., Schauder, D., Xin, G., Nguyen, C., Wu, X., Zajac, A., and Cui, W. (2019) CD4 + T Cell Help Is Required for the Formation of a Cytolytic CD8 + T Cell Subset that Protects against Chronic Infection and Cancer. Immunity 51, 1028-1042.e1024

30. Wherry, E. J., Ha, S. J., Kaech, S. M., Haining, W. N., Sarkar, S., Kalia, V., Subramaniam, S., Blattman, J. N., Barber, D. L., and Ahmed, R. (2007) Molecular signature of CD8+ T cell exhaustion during chronic viral infection. Immunity 27, 670-684

31. Zajac, A. J., Blattman, J. N., Murali-Krishna, K., Sourdive, D. J., Suresh, M., Altman, J. D., and Ahmed, R. (1998) Viral immune evasion due to persistence of activated T cells without effector function. J Exp Med 188, 2205-2213

32. Wherry, E. J., and Kurachi, M. (2015) Molecular and cellular insights into T cell exhaustion. Nat Rev Immunol 15, 486-499

33. Inoue, A., Raimondi, F., Kadji, F. M. N., Singh, G., Kishi, T., Uwamizu, A., Ono, Y., Shinjo, Y., Ishida, S., Arang, N., Kawakami, K., Gutkind, J. S., Aoki, J., and Russell, R. B. (2019) Illuminating G-Protein-Coupling Selectivity of GPCRs. Cell 177, 1933-1947 e1925

34. Zhu, H., and Roth, B. L. (2014) DREADD: a chemogenetic GPCR signaling platform. Int J Neuropsychopharmacol 18

35. Roth, B. L. (2016) DREADDs for Neuroscientists. Neuron 89, 683-694

36. Nagai, Y., Miyakawa, N., Takuwa, H., Hori, Y., Oyama, K., Ji, B., Takahashi, M., Huang, X. P., Slocum, S. T., DiBerto, J. F., Xiong, Y., Urushihata, T., Hirabayashi, T., Fujimoto, A., Mimura, K., English, J. G., Liu, J., Inoue, K. I., Kumata, K., Seki, C., Ono, M., Shimojo, M., Zhang, M. R., Tomita, Y., Nakahara, J., Suhara, T., Takada, M., Higuchi, M., Jin, J., Roth, B. L., and Minamimoto, T. (2020) Deschloroclozapine, a potent and selective chemogenetic actuator enables rapid neuronal and behavioral modulations in mice and monkeys. Nat Neurosci 23, 1157-1167

37. Liu, C., Somasundaram, A., Manne, S., Gocher, A. M., Szymczak-Workman, A. L., Vignali, K. M., Scott, E. N., Normolle, D. P., John Wherry, E., Lipson, E. J., Ferris, R. L., Bruno, T. C., Workman, C. J., and Vignali, D. A. A. (2020) Neuropilin-1 is a T cell memory checkpoint limiting long-term antitumor immunity. Nat Immunol 21, 1010-1021

38. Zhang, Y., Reynolds, J. M., Chang, S. H., Martin-Orozco, N., Chung, Y., Nurieva, R. I., and Dong, C. (2009) MKP-1 is necessary for T cell activation and function. J Biol Chem 284, 30815-30824

39. Lang, R., and Raffi, F. A. M. (2019) Dual-Specificity Phosphatases in Immunity and Infection: An Update. Int J Mol Sci 20

40. Tsvetanova, N. G., Trester-Zedlitz, M., Newton, B. W., Riordan, D. P., Sundaram, A. B., Johnson, J. R., Krogan, N. J., and von Zastrow, M. (2017) G Protein-Coupled Receptor Endocytosis Confers Uniformity in Responses to Chemically Distinct Ligands. Mol Pharmacol 91, 145-156

41. Seo, H., Chen, J., González-Avalos, E., Samaniego-Castruita, D., Das, A., Wang, Y. H., López-Moyado, I. F., Georges, R. O., Zhang, W., Onodera, A., Wu, C. J., Lu, L. F., Hogan,

P. G., Bhandoola, A., and Rao, A. (2019) TOX and TOX2 transcription factors cooperate with NR4A transcription factors to impose CD8. Proc Natl Acad Sci U S A 116, 12410-12415

42. Thommen, D. S., and Schumacher, T. N. (2018) T Cell Dysfunction in Cancer. Cancer Cell 33, 547-562

43. Wang, Z., Wu, V. H., Allevato, M. M., Gilardi, M., He, Y., Luis Callejas-Valera, J., Vitale-Cross, L., Martin, D., Amornphimoltham, P., Mcdermott, J., Yung, B. S., Goto, Y., Molinolo, A. A., Sharabi, A. B., Cohen, E. E. W., Chen, Q., Lyons, J. G., Alexandrov, L. B., and Gutkind, J. S. (2019) Syngeneic animal models of tobacco-associated oral cancer reveal the activity of in situ anti-CTLA-4. Nat Commun 10, 5546

44. Wang, Z., Goto, Y., Allevato, M. M., Wu, V. H., Saddawi-Konefka, R., Gilardi, M., Alvarado, D., Yung, B. S., O'Farrell, A., Molinolo, A. A., Duvvuri, U., Grandis, J. R., Califano, J. A., Cohen, E. E. W., and Gutkind, J. S. (2021) Disruption of the HER3-PI3K-mTOR oncogenic signaling axis and PD-1 blockade as a multimodal precision immunotherapy in head and neck cancer. Nat Commun 12, 2383

45. Samstein, R. M., Lee, C. H., Shoushtari, A. N., Hellmann, M. D., Shen, R., Janjigian, Y. Y., Barron, D. A., Zehir, A., Jordan, E. J., Omuro, A., Kaley, T. J., Kendall, S. M., Motzer, R. J., Hakimi, A. A., Voss, M. H., Russo, P., Rosenberg, J., Iyer, G., Bochner, B. H., Bajorin, D. F., Al-Ahmadie, H. A., Chaft, J. E., Rudin, C. M., Riely, G. J., Baxi, S., Ho, A. L., Wong, R. J., Pfister, D. G., Wolchok, J. D., Barker, C. A., Gutin, P. H., Brennan, C. W., Tabar, V., Mellinghoff, I. K., DeAngelis, L. M., Ariyan, C. E., Lee, N., Tap, W. D., Gounder, M. M., D'Angelo, S. P., Saltz, L., Stadler, Z. K., Scher, H. I., Baselga, J., Razavi, P., Klebanoff, C. A., Yaeger, R., Segal, N. H., Ku, G. Y., DeMatteo, R. P., Ladanyi, M., Rizvi, N. A., Berger, M. F., Riaz, N., Solit, D. B., Chan, T. A., and Morris, L. G. T. (2019) Tumor mutational load predicts survival after immunotherapy across multiple cancer types. Nat Genet 51, 202-206

46. Valero, C., Lee, M., Hoen, D., Weiss, K., Kelly, D. W., Adusumilli, P. S., Paik, P. K., Plitas, G., Ladanyi, M., Postow, M. A., Ariyan, C. E., Shoushtari, A. N., Balachandran, V. P., Hakimi, A. A., Crago, A. M., Long Roche, K. C., Smith, J. J., Ganly, I., Wong, R. J., Patel, S. G., Shah, J. P., Lee, N. Y., Riaz, N., Wang, J., Zehir, A., Berger, M. F., Chan, T. A., Seshan, V. E., and Morris, L. G. T. (2021) Pretreatment neutrophil-to-lymphocyte ratio and mutational burden as biomarkers of tumor response to immune checkpoint inhibitors. Nat Commun 12, 729

47. Valero, C., Lee, M., Hoen, D., Zehir, A., Berger, M. F., Seshan, V. E., Chan, T. A., and Morris, L. G. T. (2021) Response Rates to Anti-PD-1 Immunotherapy in Microsatellite-Stable Solid Tumors With 10 or More Mutations per Megabase. JAMA Oncol 7, 739-743

48. Sinha, N., Sinha, S., Valero, C., Schäffer, A. A., Aldape, K., Litchfield, K., Chan, T. A., Morris, L. G. T., and Ruppin, E. (2021) Immune determinants of the association between tumor mutational burden and immunotherapy response across cancer types. bioRxiv, 2021.2005.2025.445197

49. Zelenay, S., van der Veen, A. G., Bottcher, J. P., Snelgrove, K. J., Rogers, N., Acton, S. E., Chakravarty, P., Girotti, M. R., Marais, R., Quezada, S. A., Sahai, E., and Reis e Sousa, C. (2015) Cyclooxygenase-Dependent Tumor Growth through Evasion of Immunity. Cell 162, 1257-1270

50. Liu, B., Qu, L., and Yan, S. (2015) Cyclooxygenase-2 promotes tumor growth and suppresses tumor immunity. Cancer Cell Int 15, 106

51. Yao, C., Sakata, D., Esaki, Y., Li, Y., Matsuoka, T., Kuroiwa, K., Sugimoto, Y., and Narumiya, S. (2009) Prostaglandin E2-EP4 signaling promotes immune inflammation through Th1 cell differentiation and Th17 cell expansion. Nat Med 15, 633-640

52. Take, Y., Koizumi, S., and Nagahisa, A. (2020) Prostaglandin E Receptor 4 Antagonist in Cancer Immunotherapy: Mechanisms of Action. Front Immunol 11, 324

53. Vigano, S., Alatzoglou, D., Irving, M., Ménétrier-Caux, C., Caux, C., Romero, P., and Coukos, G. (2019) Targeting Adenosine in Cancer Immunotherapy to Enhance T-Cell Function. Front Immunol 10, 925

54. Fong, L., Hotson, A., Powderly, J. D., Sznol, M., Heist, R. S., Choueiri, T. K., George, S., Hughes, B. G. M., Hellmann, M. D., Shepard, D. R., Rini, B. I., Kummar, S., Weise, A. M., Riese, M. J., Markman, B., Emens, L. A., Mahadevan, D., Luke, J. J., Laport, G., Brody, J. D., Hernandez-Aya, L., Bonomi, P., Goldman, J. W., Berim, L., Renouf, D. J., Goodwin, R. A., Munneke, B., Ho, P. Y., Hsieh, J., McCaffery, I., Kwei, L., Willingham, S. B., and Miller, R. A. (2020) Adenosine 2A Receptor Blockade as an Immunotherapy for Treatment-Refractory Renal Cell Cancer. Cancer Discov 10, 40-53

55. Leone, R. D., and Emens, L. A. (2018) Targeting adenosine for cancer immunotherapy. J Immunother Cancer 6, 57

56. Bottcher, J. P., Bonavita, E., Chakravarty, P., Blees, H., Cabeza-Cabrerizo, M., Sammicheli, S., Rogers, N. C., Sahai, E., Zelenay, S., and Reis e Sousa, C. (2018) NK Cells Stimulate Recruitment of cDC1 into the Tumor Microenvironment Promoting Cancer Immune Control. Cell 172, 1022-1037 e1014

57. Tomić, S., Joksimović, B., Bekić, M., Vasiljević, M., Milanović, M., Čolić, M., and Vučević, D. (2019) Prostaglanin-E2 Potentiates the Suppressive Functions of Human Mononuclear Myeloid-Derived Suppressor Cells and Increases Their Capacity to Expand IL-10-Producing Regulatory T Cell Subsets. Front Immunol 10, 475

58. Miao, J., Lu, X., Hu, Y., Piao, C., Wu, X., Liu, X., Huang, C., Wang, Y., Li, D., and Liu, J. (2017) Prostaglandin E. Oncotarget 8, 89802-89810

59. Pelly, V. S., Moeini, A., Roelofsen, L. M., Bonavita, E., Bell, C. R., Hutton, C., Blanco-Gomez, A., Banyard, A., Bromley, C. P., Flanagan, E., Chiang, S. C., Jorgensen, C., Schumacher, T. N., Thommen, D. S., and Zelenay, S. (2021) Anti-inflammatory drugs remodel the tumor immune environment to enhance immune checkpoint blockade efficacy. Cancer Discov

60. Giuffrida, L., Sek, K., Henderson, M. A., Lai, J., Chen, A. X. Y., Meyran, D., Todd, K. L., Petley, E. V., Mardiana, S., Mølck, C., Stewart, G. D., Solomon, B. J., Parish, I. A., Neeson, P. J., Harrison, S. J., Kats, L. M., House, I. G., Darcy, P. K., and Beavis, P. A. (2021) CRISPR/Cas9 mediated deletion of the adenosine A2A receptor enhances CAR T cell efficacy. Nat Commun 12, 3236

61. Ma, S. R., Deng, W. W., Liu, J. F., Mao, L., Yu, G. T., Bu, L. L., Kulkarni, A. B., Zhang, W. F., and Sun, Z. J. (2017) Blockade of adenosine A2A receptor enhances CD8. Mol Cancer 16, 99

62. Kjaergaard, J., Hatfield, S., Jones, G., Ohta, A., and Sitkovsky, M. (2018) A. J Immunol 201, 782-791

63. Adame-Garcia, S. R., Cervantes-Villagrana, R. D., Orduna-Castillo, L. B., Del Rio, J. C., Gutkind, J. S., Reyes-Cruz, G., Taylor, S. S., and Vazquez-Prado, J. (2019) cAMP-dependent activation of the Rac guanine exchange factor P-REX1 by type I protein kinase A (PKA) regulatory subunits. J Biol Chem 294, 2232-2246

64. Ramms, D. J., Raimondi, F., Arang, N., Herberg, F. W., Taylor, S. S., and Gutkind, J. S. (2021) Gαs -PKA pathway signalopathies: The emerging genetic landscape and therapeutic

potential of human diseases driven by aberrant Gαs -PKA signaling American Society for Pharmacology and Experimental Therapeutics (United States), Pharmacological Reviews

65. Falvo, J. V., Brinkman, B. M., Tsytsykova, A. V., Tsai, E. Y., Yao, T. P., Kung, A. L., and Goldfeld, A. E. (2000) A stimulus-specific role for CREB-binding protein (CBP) in T cell receptor-activated tumor necrosis factor alpha gene expression. Proc Natl Acad Sci U S A 97, 3925-3929

66. Hughes-Fulford, M., Sugano, E., Schopper, T., Li, C. F., Boonyaratanakornkit, J. B., and Cogoli, A. (2005) Early immune response and regulation of IL-2 receptor subunits. Cell Signal 17, 1111-1124

67. Solomou, E. E., Juang, Y. T., and Tsokos, G. C. (2001) Protein kinase C-theta participates in the activation of cyclic AMP-responsive element-binding protein and its subsequent binding to the -180 site of the IL-2 promoter in normal human T lymphocytes. J Immunol 166, 5665-5674

68. Yeh, J. H., Lecine, P., Nunes, J. A., Spicuglia, S., Ferrier, P., Olive, D., and Imbert, J. (2001) Novel CD28-responsive enhancer activated by CREB/ATF and AP-1 families in the human interleukin-2 receptor alpha-chain locus. Mol Cell Biol 21, 4515-4527

69. Mayall, T. P., Sheridan, P. L., Montminy, M. R., and Jones, K. A. (1997) Distinct roles for P-CREB and LEF-1 in TCR alpha enhancer assembly and activation on chromatin templates in vitro. Genes Dev 11, 887-899

70. Anderson, S. J., Miyake, S., and Loh, D. Y. (1989) Transcription from a murine T-cell receptor V beta promoter depends on a conserved decamer motif similar to the cyclic AMP response element. Mol Cell Biol 9, 4835-4845

71. Gao, M. H., and Kavathas, P. B. (1993) Functional importance of the cyclic AMP response element-like decamer motif in the CD8 alpha promoter. J Immunol 150, 4376-4385

72. Gupta, A., and Terhorst, C. (1994) CD3 delta enhancer. CREB interferes with the function of a murine CD3-delta A binding factor (M delta AF). J Immunol 152, 3895-3903

73. De Giorgi, V., Grazzini, M., Benemei, S., Marchionni, N., Botteri, E., Pennacchioli, E., Geppetti, P., and Gandini, S. (2018) Propranolol for Off-label Treatment of Patients With Melanoma: Results From a Cohort Study. JAMA Oncol 4, e172908

74. Daher, C., Vimeux, L., Stoeva, R., Peranzoni, E., Bismuth, G., Wieduwild, E., Lucas, B., Donnadieu, E., Bercovici, N., Trautmann, A., and Feuillet, V. (2019) Blockade of beta-Adrenergic Receptors Improves CD8(+) T-cell Priming and Cancer Vaccine Efficacy. Cancer Immunol Res 7, 1849-1863

75. Hanahan, D., and Weinberg, R. A. (2011) Hallmarks of cancer: the next generation. Cell 144, 646-674

76. Akhmedov, D., Mendoza-Rodriguez, M. G., Rajendran, K., Rossi, M., Wess, J., and Berdeaux, R. (2017) Gs-DREADD Knock-In Mice for Tissue-Specific, Temporal Stimulation of Cyclic AMP Signaling. Mol Cell Biol 37

77. Iglesias-Bartolome, R., Torres, D., Marone, R., Feng, X., Martin, D., Simaan, M., Chen, M., Weinstein, L. S., Taylor, S. S., Molinolo, A. A., and Gutkind, J. S. (2015) Inactivation of a Gα(s)-PKA tumour suppressor pathway in skin stem cells initiates basal-cell carcinogenesis. Nat Cell Biol 17, 793-803

78. Stuart, T., Butler, A., Hoffman, P., Hafemeister, C., Papalexi, E., Mauck, W. M., Hao, Y., Stoeckius, M., Smibert, P., and Satija, R. (2019) Comprehensive Integration of Single-Cell Data. Cell 177, 1888-1902.e1821

79. Sade-Feldman, M., Yizhak, K., Bjorgaard, S. L., Ray, J. P., de Boer, C. G., Jenkins, R. W., Lieb, D. J., Chen, J. H., Frederick, D. T., Barzily-Rokni, M., Freeman, S. S., Reuben, A., Hoover, P. J., Villani, A. C., Ivanova, E., Portell, A., Lizotte, P. H., Aref, A. R., Eliane, J. P., Hammond, M. R., Vitzthum, H., Blackmon, S. M., Li, B., Gopalakrishnan, V., Reddy, S. M., Cooper, Z. A., Paweletz, C. P., Barbie, D. A., Stemmer-Rachamimov, A., Flaherty, K. T., Wargo, J. A., Boland, G. M., Sullivan, R. J., Getz, G., and Hacohen, N. (2018) Defining T Cell States Associated with Response to Checkpoint Immunotherapy in Melanoma. Cell 175, 998-1013.e1020

80. Singh, G., Inoue, A., Gutkind, J. S., Russell, R. B., and Raimondi, F. (2019) PRECOG: PREdicting COupling probabilities of G-protein coupled receptors. Nucleic Acids Res 47, W395-W401

81. Yu, G., Wang, L. G., Han, Y., and He, Q. Y. (2012) clusterProfiler: an R package for comparing biological themes among gene clusters. OMICS 16, 284-287